Nonlinear Observers for Aircraft Maneuvering in Wind

Jeremy W. Hopwood

Dissertation submitted to the Faculty of the
Virginia Polytechnic Institute and State University
in partial fulfillment of the requirements for the degree of

Doctor of Philosophy
in
Aerospace Engineering

Craig A. Woolsey, Chair
Mark L. Psiaki
Shane D. Ross
Daniel J. Stilwell

April 21, 2025
Blacksburg, Virginia

Keywords: Nonlinear Observers, Wind Estimation, Flight Mechanics, Stochastic Stability

Nonlinear Observers for Aircraft Maneuvering in Wind

Jeremy W. Hopwood

(ABSTRACT)

Knowledge of wind velocity is fundamental across fields from atmospheric science to aeronautics, yet direct wind sensing is often constrained by operational limits. This motivates indirect wind estimation methods that infer wind from aircraft motion. However, typical model-based estimators lack rigorous stability guarantees across the full flight envelope — a major limitation for safety-critical aerospace applications. This dissertation addresses these gaps by advancing nonlinear observer design and flight dynamic modeling to estimate wind from aircraft motion with assured performance.

First, a symmetry-preserving, reduced-order state observer is introduced for the unmeasured part of a system's state, leveraging the fact that the system dynamics are invariant under the action of a Lie group. By using a moving frame to construct invariant observer mappings, both the design process and stability analysis are simplified. In cases where the system's nonlinearities comprise the Lie group's action, the nonlinear observer may even yield linear state estimation error dynamics to enable a multitude of design and optimization techniques that improve performance.

Next, a quasi-steady nonlinear flight dynamic model for multirotor aircraft is derived from blade-element and momentum theory, ensuring validity over a large operating range while remaining identifiable from flight data. The utility of this model is assessed through a high-fidelity simulation study based on wind tunnel data. Recognizing the challenges of parameter estimation in large-domain models for unstable aircraft, a two-phase data collection methodology is proposed. In the first phase, a set of linear time-invariant models is identified at multiple operating conditions to define an uncertain linear parameter-varying (LPV) model. In the second phase, a robust LPV control law with an H_∞ norm bound guarantee is synthesized, enabling automated flights with sufficiently large excitation signals for nonlinear system identification.

Finally, the nonlinear observer theory is combined with the large-domain flight dynamic models to achieve provably effective wind estimation for maneuvering aircraft. The framework is extended to uncertain aerodynamics and random turbulence by formulating the system as a stochastic differential equation. A nonlinear passivity-based wind observer is also introduced, serving as a full-order alternative to reduced-order methods. Together, these observers offer stability guarantees applicable to general maneuvering flight, demonstrated on both fixed-wing and multirotor UAVs. Overall, this dissertation contributes to safer, more autonomous aerospace systems.

Nonlinear Observers for Aircraft Maneuvering in Wind

Jeremy W. Hopwood

(GENERAL AUDIENCE ABSTRACT)

Accurate wind measurements are vital for applications ranging from weather prediction to aircraft navigation and control, yet directly measuring wind is often impractical or infeasible, especially for emerging vertical takeoff and landing vehicles. This creates a critical need for methods that indirectly estimate wind using aircraft motion data. Existing estimation methods, however, struggle to guarantee performance across the full range of flight conditions, posing risks to safety-critical aerospace applications. This dissertation addresses these shortcomings by advancing both theoretical and practical tools for estimating wind during flight. At its core is a novel nonlinear state observer that estimates the unknown states of a system by leveraging symmetry in the dynamics. This geometric insight simplifies both the observer's construction and the analysis of its performance. To complement these theoretical advances, a practical nonlinear flight dynamic model for multirotor aircraft is developed, integrating rotor aerodynamic theory with established modeling approaches suitable for real-time navigation and control. Together, these theoretical and practical contributions form a framework for wind estimation that accounts for aerodynamic uncertainty and turbulence in general maneuvering flight. Simulation and flight test demonstrations are performed on both fixed-wing and multirotor aircraft, showcasing the effectiveness of the proposed methods and their potential to enhance aircraft autonomy and reliability when under challenging operating conditions.

Dedication

To Kylie,

The wind that lifts me
And the heart that steadies me,
Raising me higher
Than I could imagine alone.

Acknowledgments

I begin by expressing my deepest gratitude to my advisor, Prof. Craig Woolsey, whose exceptional mentorship, patience, and insight have been foundational to my growth as a researcher and scholar throughout my Ph.D. journey. I am likewise profoundly thankful to my committee members Prof. Mark Psiaki, Prof. Shane Ross, and Prof. Daniel Stilwell for their thoughtful questions, constructive feedback, and steadfast support in both coursework and research during my time at Virginia Tech. I extend my sincere thanks to Dr. David Broderick, whose holistic mentorship at Central Connecticut State University sparked my interest in control theory and equipped me with the foundational mindset and skills that proved essential to my graduate studies. I am also thankful to Jared Cooper for his invaluable collaboration and sponsorship.

I was fortunate to have my research momentum kindled by the vibrant and supportive community of the Nonlinear Systems Laboratory (NSL) at Virginia Tech. I owe special thanks to James Gresham for his guidance, collaboration, and friendship during my early graduate studies. I am also grateful to Chris Gahan, whose relentless curiosity and enthusiasm made working together a constant source of inspiration and growth. My heartfelt thanks go to all my NSL colleagues, past and present, for fostering an intellectually rich and supportive environment. I am especially thankful for stimulating collaborations with former members, inluding Dr. Benjamin Simmons, Dr. Mekonen Halefom, Dr. Zakia Ahmed, Dr. Nazmus Sakib, and many others. It has been a privilege to build equally meaningful relationships with current NSL members and to play a part in their academic journeys, particularly through fruitful collaborations with Dennis Marquis, Ian Willebeek-LeMair, Patrick Corrigan, Garrett Asper, and Samuel Widman.

Finally, I am deeply indebted to my parents for their unwavering support throughout my life. They fostered a home that sparked my curiosity and nurtured a tenacity for learning, encouraging me to pursue every goal with wonder and determination. I am deeply grateful to Dr. George Steinfeld, whose wisdom and support have helped me navigate life's challenges and shaped who I am today. Most of all, I offer my deepest thanks to my wife, Kylie, for her steadfast love, patience, and belief in me. There is no one I would rather have beside me on this journey.

Contents

List of Figures

List of Tables

Chapter 1

Introduction

Knowledge of wind velocity is fundamental across disciplines ranging from atmospheric science to aeronautics, supporting critical applications such as weather forecasting and flight safety. For example, atmospheric scientists rely on wind measurements as key boundary conditions in numerical weather models, while in aeronautics, measurements of airspeed, angle of attack, and sideslip angle are vital for pilot decision-making and enabling safer, more automated flight operations. Direct measurements of wind velocity are often constrained by engineering and operational limitations. Traditional sensing methods, such as anemometers and air data probes, may not always be feasible due to payload restrictions, cost constraints, or operational limitations. This challenge has motivated the development of wind estimation techniques that infer wind velocity indirectly from aircraft motion without the need for specialized sensors. Such approaches are applicable across a broad spectrum of vehicle sizes and types, from small unmanned aerial vehicles (UAVs) to large commercial aircraft.

Wind estimation plays a critical role in several engineering and scientific applications. In aeronautics, synthetic air data systems leverage estimated wind information to reconstruct air data (i.e., airspeed, angle of attack, and sideslip angle) without relying on dedicated sensors such as multi-hole probes or vaned air data units [96], [141]. Synthetic air data systems not only provide a fallback in scenarios where sensors fail, but also give air data measurements in regions of flight where there is not enough airflow to use such sensors. Additionally, path planning algorithms can incorporate real-time wind estimates to improve efficiency and safety guarantees [92], [157], which is especially important in urban environments. Beyond aviation, wind estimation is vital to weather prediction and atmospheric science, particularly within the atmospheric boundary layer, which remains poorly sampled due to operational constraints on traditional meteorological platforms such as weather balloons [17], [55], [79], [123], [146]. For these reasons, advances in wind estimation technologies have become increasingly relevant in the Urban Air Mobility (UAM) and Advanced Air Mobility (AAM) missions, where understanding low-altitude wind conditions is essential for safe and reliable operations of future aerial vehicles [1], [128]. For example, the development of wind estimation technologies is important for relaxing flight safety margins to enable more weather-tolerant operations [85], [144].

The increasing reliance on wind estimates highlights the need for solutions that enjoy stronger mathematical guarantees; that is, assurance that the estimates of wind velocity "converge" in some sense to the true wind velocity. These guarantees can enable the integration of wind

estimates into safety monitoring systems, such as those described in references [98] and [140], providing an alternative to traditional measurement techniques. Typical model-based estimation and filtering methods lack such convergence guarantees for nonlinear systems. Nonlinear filtering techniques, such as the extended Kalman filter, often only retain stability guarantees for small perturbations about steady motion with sufficiently low noise [90]. For aircraft, there are two ways in which the small-perturbation assumption may be violated. The first is aggressive maneuvering and agile flight, which is especially applicable for UAVs that do not impose the physiological limitations of the human pilot. The second is large changes in wind conditions as especially seen in urban scenarios with the "urban canyon effect." Even if the vehicle is steadily translating in inertial space, the large changes to the aerodynamics necessitate a more careful approach in the nonlinear setting. These observations motivate the exploration of nonlinear observer techniques for wind estimation. In contrast with state estimators, nonlinear observers provide a stability guarantee on a state estimation error system.

The design of nonlinear observers with guaranteed performance across a wide range of operating conditions necessitates system models that are accurate across these same conditions. In other words, confidence in model-based wind estimates falls to the severity of approximations and assumptions made in the flight dynamic model as well as the estimation approach. This observation motivates a particular interest in expanding operating conditions for which flight dynamic models and the estimation algorithms remain accurate and mathematically valid, thereby extending such properties to the resulting wind and aircraft state estimates. Thus arise two thrusts of this dissertation in pursuit of provably effective wind estimation for aircraft maneuvering in turbulent wind.

1. Theoretical Advancements in Nonlinear Observers
Methods for designing state observers for nonlinear systems are limited with no general techniques that guarantee global convergence of the estimation error, as there are in the linear case. Provably effective state estimation strategies are inevitably limited to special classes of systems, motivating considerable attention in the past twenty-five years. In particular, the role of differential geometry in observer design has been explored in which symmetries of a nonlinear dynamical system are preserved in the state observer and its state estimation error dynamics. Existing approaches to symmetry-preserving observers only consider the full-order case in which the entire state of the system is estimated. In many scenarios, however, part of the system's state may be known with negligible error or determined as the output of an independently designed observer. Thus, reduced-order observers are an attractive alternative where only the unmeasured part of the system's state is estimated. After covering mathematical preliminaries in Chapter 2 of this dissertation, Chapter 3 presents a reduced-order observer that is also symmetry-preserving, thereby simplifying stability analysis and enabling performance optimization.

2. Flight Dynamic Modeling and System Identification
Accurate flight dynamic models are essential for model-based control and estimation of UAVs, but obtaining nonlinear models valid over a wide range of flight conditions is challenging.

Traditional control- and estimation-oriented multirotor modeling approaches struggle to capture nonlinear phenomena and thus weaken any derived control and estimation guarantees beyond small perturbations from some operating condition. In Chapter 4, a nonlinear model for multirotor flight is developed using blade-element and momentum theory in a way that balances accuracy and practicability. However, system identification of large-domain multirotor models is difficult, as these types of UAVs are inherently unstable. In particular, stabilizing controllers can introduce regressor correlation and suppress dynamics of interest, complicating data collection and parameter estimation. Furthermore, the level of input excitation required for parameter estimation can drive the system unstable — a situation that must be avoided for high-risk and high-cost vehicles. Chapter 5 addresses these challenges by formulating a two-phase system identification process using robust linear parameter-varying (LPV) control techniques. With decorrelated input excitation signals and reference trajectories, the control law bounds the worst-case vehicle's response to these input excitations. This approach enables safe, automated flight experiments providing uncorrelated data for nonlinear model identification.

Safety-Critical Wind Estimation
Bringing together the observer theory from Chapter 3 and the large-domain flight dynamic model developed in Chapter 4, Chapters 6–8 detail how nonlinear observers are employed to estimate wind velocity for maneuvering aircraft. Specifically, the integration of symmetry-preserving reduced-order (Chapter 7) and passivity-based observers (Chapter 8) with large-domain flight dynamic models ensures provably effective wind estimation, providing essential theoretical guarantees for stability and convergence — especially important for safety-critical applications. A key challenge remains in the inherent imperfections of any model, requiring the incorporation of randomness as a natural extension to account for the remaining unpredictable behavior. While state estimators like the Kalman filter properly deal with this randomness and inherently provide local stochastic stability guarantees, the explicit stochastic stability properties of nonlinear observers remain largely unexplored. To fill this gap, Chapter 7 details the extension of the symmetry-preserving reduced-order wind observer to include uncertain aerodynamics and random turbulence. The wind estimation approaches in Chapters 7–8 are demonstrated using both simulation and flight data for fixed-wing and multirotor UAVs.

This dissertation is a unique juxtaposition of theory and application that is deeply motivated by the unifying goal of wind estimation for aircraft maneuvering in turbulent wind. As such, certain chapters may be read independently of others. Overall, this dissertation is organized according to the chapter dependence chart shown in Figure 1.1.

The primary contributions presented in this dissertation relate to nonlinear observer theory, nonlinear flight dynamic modeling and system identification, and wind estimation for aircraft maneuvering in turbulent wind. Specific contributions are summarized as follows.

- Theoretical development of a symmetry-preserving reduced-order nonlinear observer for systems defined on smooth manifolds under a Lie group's action [70] (Chapter 3).

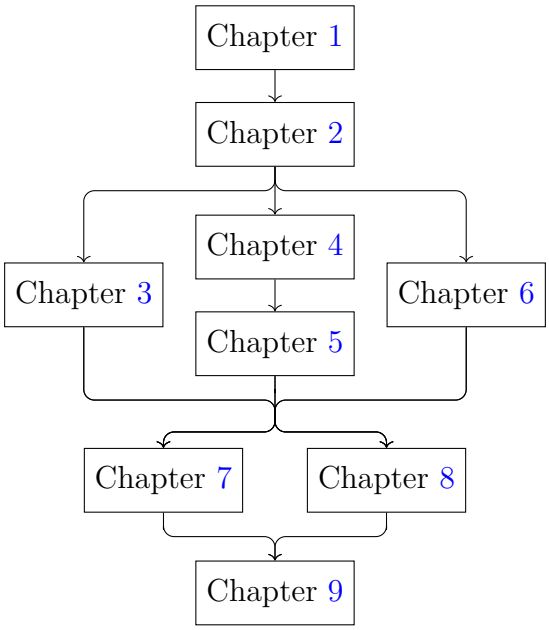

Figure 1.1: Chapter dependence chart

- Formulation and analysis of a nonlinear, quasi-steady flight dynamic model for multi-rotor aircraft [74] (Chapter 4).
- Development and application of a control methodology for obtaining sufficiently rich excitation data for large-domain system identification of unstable aircraft in a provably safe manner [76] (Chapter 5).
- Refinement and generalization of the stochastic process models used in nonlinear, model-based wind estimation [67], [71], [75] (Chapter 6).
- Application of the author's symmetry-preserving reduced-order observer to the problem of wind estimation using a deterministic system model defined on the tangent bundle of the special Euclidean group [77] (Chapter 7).
- Extension of the symmetry-preserving reduced-order wind observer to flight in turbulence with uncertain aerodynamics by extending the theoretical results of [70] to a special class of stochastic differential equations [71] (Chapter 7).
- First application of a passivity-based observer to the problem of wind estimation for maneuvering aircraft [75] (Chapter 8).

Additional contributions by the author not included in this dissertation include the following.

- Development and flight testing of a stall spin flight termination sequence for fixed-wing UAVs using parallel robust H_∞ and yaw-varying linear quadratic control laws to direct its spinning descent along a desired inertial direction [72], [73].

The author's collaborative contributions surrounding wind estimation and system identification for small UAVs are listed as follows.

- Wind estimation using an H_∞ filter to bound the worst-case effect of turbulence on the estimate error of a specified frequency band of the wind [47], [50].
- Uncertainty quantification and variance reduction in wind estimates using generalized polynomial chaos [48], [49].
- Square root information filtering for quadrotor wind estimation with a comparison to dual-Doppler LiDAR wind measurements [104].
- Maneuvering wind estimation using an unscented Kalman filter for bio-inspired approaches to chemical source localization [36].
- Model-based wind estimation incorporating unsteady aerodynamics identified from flight data [67].
- Nonlinear system identification for fixed-wing aircraft in a stall spin [65], [66].
- Remote uncorrelated piloted inputs for nonlinear system identification of UAVs [63], [64].
- Development of a flight test methodology for system identification and control law testing for small UAVs [62].

Chapter 2

Mathematical Preliminaries

2.1 Introduction

This chapter provides the mathematical preliminaries for this dissertation, which are a blend of differential geometry and probability theory in the context of designing stable observers for rigid body motion. An introduction to differential geometry is presented in Section 2.2, formalizing how systems are defined on "curvy spaces" and how calculus is written in this coordinate-free setting. Next, Section 2.3 presents the notion of a Lie group and how it acts on a dynamical system. In particular this section discusses when a system's dynamics are left unchanged by the Lie group action — that is, invariant. As the motivating application of the preliminaries in Sections 2.2 and Section 2.3, the equations of motion for a rigid body aircraft are detailed in Section 2.4.

In control and observer applications, we are interested in influencing or understanding how systems respond to perturbations from some equilibrium condition. Section 2.5 details the deterministic notions of stability that are used in this dissertation along with Lyapunov sufficient conditions. However, Sections 2.2–2.5 only deal with deterministic, unperturbed systems. More generally, we are interested in systems

$$\dot{\boldsymbol{x}} = \boldsymbol{f}(\boldsymbol{x}, \boldsymbol{\xi})$$

where $\boldsymbol{\xi}$ is some unknown disturbance. Often, this disturbance is referred to as "noise," reflecting inherent randomness or uncertainty in its value over time. Perhaps statements can be made about its frequency content (e.g., white noise has constant power spectral density) or its magnitude (e.g., $\|\boldsymbol{\xi}\|_{L_2} < \infty$). However, care must be taken when dealing with stochastic nonlinear systems of the form

$$\dot{\boldsymbol{x}} = \boldsymbol{f}(\boldsymbol{x}, \boldsymbol{u}) + \boldsymbol{D}(\boldsymbol{x}, \boldsymbol{u}) \times \text{white noise}$$

Sections 2.6 and 2.7 lay out the preliminaries surrounding what *white noise* means in this context and how it affects solutions $\boldsymbol{x}(t)$. Next, Section 2.8 presents stochastic versions of the stability concepts detailed in Section 2.5, including for the class of systems where the noise does not vanish at the desired equilibrium condition — the case encountered in observer design for stochastic systems.

2.2 Differential Geometry

This section is largely based on texts by Boothby [25], Murray *et al.* [116, Appendix A], Marsden and Ratiu [102], and Tu [147].

The state space of a dynamical system is naturally represented by a smooth manifold. Systems evolve according to physical and mathematical laws that are not generally captured by unconstrained motion in Euclidean space, $\mathbb{R}^n$. In this dissertation, it suffices to consider an n-dimensional *manifold* $\mathcal{M}$ to be a set that is everywhere locally homeomorphic to ("looks like") $\mathbb{R}^n$. To facilitate calculus (impose a differentiable structure) on $\mathcal{M}$, we consider pairs (U, ϕ) called *coordinate charts*, defined by an open set $U \subset \mathcal{M}$ and a homeomorphism $\phi : U \to V \subset \mathbb{R}^n$. Charts *parameterize* open subsets of manifolds. As a familiar example in mechanics, Euler angles locally parameterize the manifold of rigid-body orientations. Two overlapping charts (ϕ_α, U_α) and (ϕ_β, U_β) are called C^∞*-compatible* if $\phi_\beta^{-1} \circ \phi_\alpha$ is a diffeomorphism — that is, a *smooth* (C^∞ or infinitely differentiable) map with a smooth inverse. Here, "$\circ$" denotes the composition of maps. A *smooth atlas* is collection of C^∞-compatible charts $\{(\phi_\gamma, U_\gamma)\}$ where the collection of U_γ's cover $\mathcal{M}$. A *smooth* (also, C^∞ or *differentiable*) *manifold* is a manifold equipped with a smooth atlas.

Let $C^\infty(\mathcal{M})$ denote the space of smooth, $\mathbb{R}$-valued functions on the n-dimensional smooth manifold $\mathcal{M}$. A *derivation* at a point $p \in \mathcal{M}$ is a linear map $X_p : C^\infty(p) \to \mathbb{R}$ that satisfies Leibniz rule:

$$X_p(fg) = (X_p f)g(p) + f(p)(X_p g) \quad \text{for all } f, g \in C^\infty(p)$$

The *tangent space* to $\mathcal{M}$ at p, denoted $\mathsf{T}_p\mathcal{M}$, is the vector space of derivations at p. In terms of a coordinate chart (ϕ, U) with coordinates $(x_1, \ldots, x_n)$, this definition of the tangent space (now equipped with the basis $\{\frac{\partial}{\partial x_1}, \cdots, \frac{\partial}{\partial x_n}\}$) reveals that each derivation

$$X_p = X_1 \frac{\partial}{\partial x_1} + \cdots + X_n \frac{\partial}{\partial x_n}$$

is associated with the vector $\boldsymbol{X} = [X_1 \ \cdots \ X_n]^\mathsf{T} \in \mathbb{R}^n$. Thus, derivations are also called *tangent vectors* — a description that invokes a rather helpful visualization (see Figure 2.1).

Consider two smooth manifolds $\mathcal{M}$ and $\mathcal{N}$, and let $F : \mathcal{M} \to \mathcal{N}$ be a smooth map. Just as each point $p \in \mathcal{M}$ is mapped to a point $F(p) \in \mathcal{N}$, so are tangent vectors $X_p \in \mathsf{T}_p\mathcal{M}$ mapped to $\mathrm{T}_pF(X_p) \in \mathsf{T}_{F(p)}\mathcal{N}$ as illustrated in Figure 2.1. The map $\mathrm{T}_pF : \mathsf{T}_p\mathcal{M} \to \mathsf{T}_{F(p)}\mathcal{N}$ is called the *tangent map* (or *derivative map*) of F at p. For $f \in C^\infty(p)$,

$$\mathrm{T}_pF(X_p)(f) = X_p(f \circ F)$$

The chain rule for a composition of maps $H = F \circ G$ is thus written as

$$\mathrm{T}_pH = \mathrm{T}_{G(p)}F \circ \mathrm{T}_pG \tag{2.1}$$

If $F : M \to N$ is a diffeomorphism, then T_pF is an *isomorphism* (a structure-preserving, invertible map) of tangent spaces with inverse $(\mathrm{T}_pF)^{-1} = \mathrm{T}_{F(p)}F^{-1}$.

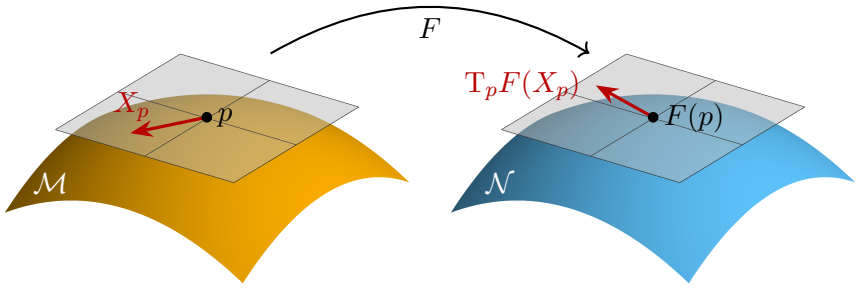

Figure 2.1: The tangent map

For the special case where F is a map from $\mathbb{R}^n$ to $\mathbb{R}^m$ (or open subsets thereof), the tangent map T_pF is simply the *Jacobian*, ∂F, which is independent of the base point p. In (global) coordinates $(x_1, \ldots, x_n)$ for $\mathbb{R}^n$, each of the m components F may be denoted $F_i(x_1, \cdots, x_n)$. As a slight abuse of notation, we often write $\boldsymbol{F}(\boldsymbol{x})$ where $\boldsymbol{x} = [x_1 \ \cdots \ x_n]^\mathsf{T}$ and $\boldsymbol{F} = [F_1 \ \cdots \ F_m]^\mathsf{T}$. Hence, we have the familiar Jacobian matrix $\frac{\partial \boldsymbol{F}}{\partial \boldsymbol{x}}$ which, as a matrix, is a linear map from $\mathbb{R}^m$ to $\mathbb{R}^n$.

The collection of all the tangent spaces along with the base manifold is called the *tangent bundle*. It is formally the disjoint union

$$\mathsf{T}\mathcal{M} = \bigsqcup_{p \in \mathcal{M}} \mathsf{T}_p\mathcal{M}$$

Even though the tangent spaces $T_p\mathcal{M}$ are already disjoint by definition, this notation explicitly[1] includes the base space $\mathcal{M}$ making $\mathsf{T}\mathcal{M}$ a $2n$-dimensional smooth manifold — n dimensions being attributed to $\mathcal{M}$ and n more to the tangent spaces.

The *natural projection* $\pi : (p, f(p)) \in \mathsf{T}\mathcal{M} \mapsto p \in \mathcal{M}$ maps the tangent bundle back to the base manifold. With this additional structure, a *vector field* f on a manifold $\mathcal{M}$ is a rule that assigns each point $p \in \mathcal{M}$ a tangent vector $f(p) \in \mathsf{T}_p\mathcal{M}$ such that $\pi \circ f = \mathrm{id}$ (the identify map). A curve $c(t)$ taking values on $\mathcal{M}$ is called an *integral curve* of the vector field f if

$$\dot{c}(t) = f(c(t)) \tag{2.2}$$

Through this viewpoint, we see that vector fields define *dynamical systems*. In local coordinates we will more compactly write

$$\dot{\boldsymbol{x}} = \boldsymbol{f}(\boldsymbol{x}) \tag{2.3}$$

where $\boldsymbol{f}$ is the local vector representation of $f : p \in \mathcal{M} \mapsto (p, f(p)) \in \mathsf{T}\mathcal{M}$ and $\boldsymbol{x}(t)$ is the vector representation of $c(t) \in \mathcal{M}$.

[1] Many authors use the notation $\mathsf{T}\mathcal{M} = \bigcup_{p \in \mathcal{M}} \mathsf{T}_p\mathcal{M}$ and note the inclusion of the base space $\mathcal{M}$. Using the disjoint union $\bigsqcup_{p \in \mathcal{M}} T_p\mathcal{M} \coloneqq \bigcup_{p \in \mathcal{M}} (\{p\} \times \mathsf{T}_p\mathcal{M})$ like Tu [147] makes this inclusion explicit.

2.3 Lie Groups and Invariance

This section is based on texts by Boothby [25], Olver [122], and Marsden and Ratiu [102].

A *Lie group* G is a group[2] that is also a smooth manifold with the requirement that the group multiplication $(g, h) \mapsto g * h$ and inverse $g \mapsto g^{-1}$ are smooth maps. Thus, Lie group elements represent both points on a manifold and actions on those points. Examples of these actions include (left) translation, conjugation, adjoint action, and the coadjoint action. More generally, a Lie group G *acts* on a set $\mathcal{X}$ via a map

$$\varphi : (g, x) \in G \times \mathcal{X} \mapsto \varphi_g(x) \in \mathcal{X}$$

satisfying the following two conditions:

i) $\varphi_e(x) = x$ for all $x \in \mathcal{X}$ where e is the identity element of G

ii) $\varphi_g \circ \varphi_h = \varphi_{g*h}$ for any $g, h \in G$

The inverse transformation φ_g^{-1} is given by the action of the inverse group element — i.e., $\boldsymbol{\varphi}_g^{-1} = \boldsymbol{\varphi}_{g^{-1}}$. The Lie group G is said to *act freely* on $\mathcal{X}$ if $\varphi_g(x) = x$ implies g is the identity element, e. The collection $\{\varphi_g\}_{g \in G}$ is called a *transformation group*. It is a group in the sense that it satisfies the four group axioms.[2] The *G-orbit* of a point $x \in \mathcal{X}$ is the set

$$\mathrm{Orb}_G(x) = \{\varphi_g(x) \mid g \in G\}$$

An *invariant* is a map $I : \mathcal{X} \to \mathbb{R}$ such that $I \circ \varphi_g = I$ for all $g \in G$. Suppose the smooth map between manifolds $\gamma : \mathcal{X} \to \mathcal{M}$ induces the transformation $\psi : G \times \mathcal{M} \to \mathcal{M}$. The map γ is called *equivariant with respect to φ and ψ* if

$$\gamma(\varphi_g(x)) = \psi_g(\gamma(x)) \quad \text{for all } x \in \mathcal{X}$$

For the special case illustrated in Figure 2.2, where $\mathcal{M} = G$ and $\psi_g : h \mapsto h * g^{-1}$, the map γ is called *equivariant* if

$$\gamma(\varphi_g(x)) = \gamma(x) * g^{-1} \tag{2.4}$$

This is the statement of equivariance that will be used in Chapter 3 for the purpose of observer design.

With an understanding of how a Lie group G acts on a smooth manifold $\mathcal{X}$, we can examine how vector fields on $\mathcal{X}$ change (or don't change) under the Lie group action. Consider a set $\mathcal{U}$ on which the Lie group G also acts via the map $\psi_g : u \in \mathcal{U} \mapsto \psi_g(u) \in \mathcal{U}$. The maps φ and ψ define a transformation group on $\mathcal{X} \times \mathcal{U}$. The dynamical control system $\dot{x} = f(x, u)$ is called *G-invariant* if

$$f(\varphi_g(x), \psi_g(u)) = \mathrm{T}_x\varphi_g\big(f(x, u)\big) \tag{2.5}$$

as depicted in Figure 2.3.

[2] A *group* is a set together with a binary operation that satisfies the four group axioms of closure, associativity, the existence of an identity, and the existence of an inverse.

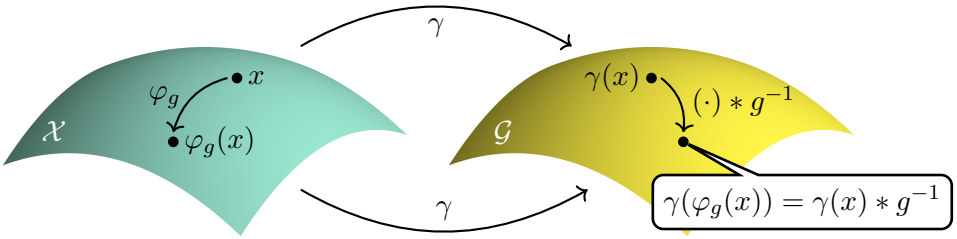

Figure 2.2: Equivariance

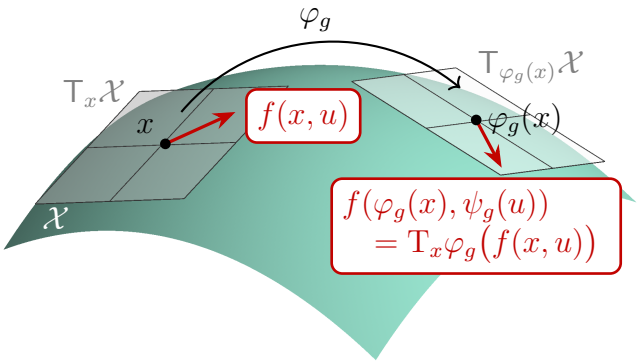

Figure 2.3: Tangent vectors of an invariant control system

As an example, consider the general linear group $\mathsf{GL}(n,\mathbb{R})$, represented by $n \times n$ invertible matrices. Suppose $\boldsymbol{A} \in \mathsf{GL}(n,\mathbb{R})$ acts on the phase space, $\mathbb{R}^n \times \mathbb{R}^n$, of a canonical Hamiltonian system via the map $\boldsymbol{\varphi_A} : (\boldsymbol{q},\boldsymbol{p}) \mapsto (\boldsymbol{Aq}, \boldsymbol{A}^{-\mathsf{T}}\boldsymbol{p}) =: (\boldsymbol{Q},\boldsymbol{P})$. Under this transformation, Hamilton's equations

$$\begin{bmatrix}\dot{\boldsymbol{q}}\\ \dot{\boldsymbol{p}}\end{bmatrix} = \underbrace{\begin{bmatrix}\mathbf{0} & \mathbb{I}\\ -\mathbb{I} & \mathbf{0}\end{bmatrix}}_{\mathbb{J}} \begin{bmatrix}\nabla_{\boldsymbol{q}} H(\boldsymbol{q},\boldsymbol{p})\\ \nabla_{\boldsymbol{p}} H(\boldsymbol{q},\boldsymbol{p})\end{bmatrix} \tag{2.6}$$

simply become

$$\begin{bmatrix}\dot{\boldsymbol{Q}}\\ \dot{\boldsymbol{P}}\end{bmatrix} = \begin{bmatrix}\mathbf{0} & \mathbb{I}\\ -\mathbb{I} & \mathbf{0}\end{bmatrix} \begin{bmatrix}\nabla_{\boldsymbol{Q}} \bar{H}(\boldsymbol{Q},\boldsymbol{P})\\ \nabla_{\boldsymbol{P}} \bar{H}(\boldsymbol{Q},\boldsymbol{P})\end{bmatrix} \tag{2.7}$$

where $\bar{H}(\boldsymbol{Q},\boldsymbol{P}) = H(\boldsymbol{q},\boldsymbol{p})$. The symmetry exemplified by Eqs. (2.6)–(2.7) is a consequence of the fact that the Jacobian matrix

$$\boldsymbol{M} := \partial\boldsymbol{\varphi_A} = \begin{bmatrix}\boldsymbol{A} & \mathbf{0}\\ \mathbf{0} & \boldsymbol{A}^{-\mathsf{T}}\end{bmatrix}$$

satisfies the relation

$$\boldsymbol{M}\mathbb{J}\boldsymbol{M}^{\mathsf{T}} = \mathbb{J}$$

Referring to general statement (2.5) of invariance, the Hamiltonian system (2.6) is invariant with respect to the transformation group $\{\boldsymbol{\varphi_A}\}_{\boldsymbol{A}\in\mathsf{GL}(n,\mathbb{R})}$, where the tangent map $\mathsf{T}_{(\boldsymbol{q},\boldsymbol{p})}\boldsymbol{\varphi_A}$

is equal to the Jacobian $\boldsymbol{M} = \partial \boldsymbol{\varphi}_{\boldsymbol{A}}$. In fact, $\boldsymbol{\varphi}_{\boldsymbol{A}}$ is a particular example of a *canonical transformation* (or *symplectic transformation*)

$$(\boldsymbol{Q}, \boldsymbol{P}) = \boldsymbol{\phi}(\boldsymbol{q}, \boldsymbol{p}) \quad \text{such that} \quad \partial \boldsymbol{\phi} \in \mathsf{Sp}(2n, \mathbb{R})$$

where $\mathsf{Sp}(2n, \mathbb{R}) = \{\boldsymbol{M} \in \mathbb{R}^{2n \times 2n} \mid \boldsymbol{M} \mathbb{J} \boldsymbol{M}^{\mathsf{T}} = \mathbb{J}\}$ is the *symplectic group*.[3]

2.4 Rigid-Body Aircraft Equations of Motion

A motivating example of a dynamical control system defined on a smooth manifold is the forced rigid body — the system considered throughout this dissertation. Let the orthonormal vectors $\{\boldsymbol{i}_1, \boldsymbol{i}_2, \boldsymbol{i}_3\}$ define an earth-fixed North-East-Down (NED) reference frame, $\mathcal{F}_{\mathrm{I}}$, which we take to be inertial over the time and space scales of motion considered. Let the orthonormal vectors $\{\boldsymbol{b}_1, \boldsymbol{b}_2, \boldsymbol{b}_3\}$ define the body-fixed frame, $\mathcal{F}_{\mathrm{B}}$, centered at the aircraft's center of gravity (CG), with $\boldsymbol{b}_1$ pointing out the front of the aircraft, $\boldsymbol{b}_2$ pointing out the right-hand side, and $\boldsymbol{b}_3$ pointing downward to complete a right-handed frame. The position of the body frame with respect to the inertial frame is given by the vector $\boldsymbol{q} = [x\ y\ z]^{\mathsf{T}} \in \mathbb{R}^3$. The attitude of the aircraft is described by the rotation matrix $\boldsymbol{R}_{\mathrm{IB}}$ that maps free vectors from $\mathcal{F}_{\mathrm{B}}$ to $\mathcal{F}_{\mathrm{I}}$. The matrix $\boldsymbol{R}_{\mathrm{IB}}$ is an element of the special orthogonal group,

$$\mathsf{SO}(3) = \{\boldsymbol{R} \in \mathbb{R}^{3\times 3} \mid \boldsymbol{R}^{-1} = \boldsymbol{R}^{\mathsf{T}},\ \det \boldsymbol{R} = 1\}$$

with the Lie group action being matrix multiplication.

The aircraft's configuration is described by points $\boldsymbol{\eta} = (\boldsymbol{q}, \boldsymbol{R}_{\mathrm{IB}})$ in the special Euclidean group,

$$\mathsf{SE}(3) = \mathbb{R}^3 \rtimes \mathsf{SO}(3)$$

where $\rtimes$ is the *semi-direct product*, which expresses how two elements of the group compose a new element [69, §9.6]. The Lie groups $\mathsf{SO}(3)$ and $\mathsf{SE}(3)$ are not just groups, but also smooth manifolds, meaning that we can define coordinate charts on the rigid-body configuration space as discussed in Section 2.2. For example, the roll-pitch-yaw Euler angles are a common local parameterization $\phi(\boldsymbol{R}_{\mathrm{IB}}) \in V = \{(\varphi, \theta, \psi) \in \mathbb{R}^3 \mid |\theta| \neq \frac{\pi}{2}\}$ of the open subset $U = \{\boldsymbol{R} \in \mathsf{SO}(3) \mid |R_{31}| \neq 0\}$, where R_{31} is the 3,1-element of the rotation matrix $\boldsymbol{R}$.

Let $\boldsymbol{v}_{\mathrm{I}} = [v_x\ v_y\ v_z]^{\mathsf{T}}$ denote the time derivative of the aircraft's position $\boldsymbol{q}$. The vector $\boldsymbol{v}_{\mathrm{I}}$ is the inertial velocity of the aircraft, expressed in the inertial frame. In the body frame, $\boldsymbol{v} = [u\ v\ w]^{\mathsf{T}} = \boldsymbol{R}_{\mathrm{IB}}^{\mathsf{T}} \boldsymbol{v}_{\mathrm{I}}$ is the translational velocity of the aircraft with respect to $\mathcal{F}_{\mathrm{I}}$ expressed in $\mathcal{F}_{\mathrm{B}}$. Thus, the translational kinematics may be written as

$$\dot{\boldsymbol{q}} = \boldsymbol{R}_{\mathrm{IB}} \boldsymbol{v} \tag{2.8}$$

Geometrically, $\dot{\boldsymbol{q}} \in \mathsf{T}_{\boldsymbol{q}} \mathbb{R}^3 \cong \mathbb{R}^3$ for any $\boldsymbol{q} \in \mathbb{R}^3$, where $\cong$ denotes an isomorphism.

[3] For a geometric treatment of symplectic transformations on Hamiltonian systems, see the text by Marsden and Ratiu [102].

Turning to rotational motion, differentiating the identity $\boldsymbol{R}_{\mathrm{IB}}^{\mathsf{T}}\boldsymbol{R}_{\mathrm{IB}} = \mathbb{I}$ reveals that $\boldsymbol{R}_{\mathrm{IB}}^{\mathsf{T}}\dot{\boldsymbol{R}}_{\mathrm{IB}}$ is skew-symmetric and that (trivially by the associativity of matrix multiplication)

$$\dot{\boldsymbol{R}}_{\mathrm{IB}} = \boldsymbol{R}_{\mathrm{IB}}(\boldsymbol{R}_{\mathrm{IB}}^{\mathsf{T}}\dot{\boldsymbol{R}}_{\mathrm{IB}})$$

Let $\boldsymbol{S}(\boldsymbol{\omega}) \coloneqq \boldsymbol{R}_{\mathrm{IB}}^{\mathsf{T}}\dot{\boldsymbol{R}}_{\mathrm{IB}}$ where $\boldsymbol{S}(\cdot)$ is the skew-symmetric cross product equivalent matrix satisfying $\boldsymbol{S}(\boldsymbol{a})\boldsymbol{b} = \boldsymbol{a} \times \boldsymbol{b}$ for 3-vectors $\boldsymbol{a}$ and $\boldsymbol{b}$. Let $\boldsymbol{S}^{-1}(\cdot)$ denote the inverse mapping; that is, $\boldsymbol{S}^{-1}(\boldsymbol{S}(\boldsymbol{a})) = \boldsymbol{a} \in \mathbb{R}^3$. It can be shown that $\boldsymbol{\omega} = [p\ q\ r]^{\mathsf{T}} \in \mathbb{R}^3$ is the angular velocity of $\mathcal{F}_{\mathrm{B}}$ with respect to $\mathcal{F}_{\mathrm{I}}$, expressed in $\mathcal{F}_{\mathrm{B}}$. Thus,

$$\dot{\boldsymbol{R}}_{\mathrm{IB}} = \boldsymbol{R}_{\mathrm{IB}}\boldsymbol{S}(\boldsymbol{\omega}) \tag{2.9}$$

are the rotational kinematics of the rigid body. The matrix $\boldsymbol{S}(\boldsymbol{\omega})$ is an element of the *Lie algebra*[4] $\mathfrak{so}(3)$ — the tangent space to the identity element, $\mathsf{T}_e\mathsf{SO}(3)$, with matrix commutation as the Lie bracket. We will sometimes write $\boldsymbol{\omega} \in \mathfrak{so}(3)$ for compactness since $\mathfrak{so}(3) \cong \mathbb{R}^3$.

Let $\boldsymbol{\nu} = (\boldsymbol{v}, \boldsymbol{\omega}) \in \mathfrak{se}(3) \cong \mathbb{R}^6$ be the *generalized velocity* of the rigid body. Putting together the translational kinematics (2.8) and rotational kinematics (2.9), the aircraft kinematics are written compactly as

$$\dot{\boldsymbol{\eta}} = \boldsymbol{f}_{\eta}(\boldsymbol{\eta}, \boldsymbol{\nu}) \tag{2.10}$$

which are defined on the tangent bundle $\mathsf{TSE}(3)$. For each generalized velocity $\boldsymbol{\nu}$ in the Lie algebra $\mathfrak{se}(3)$, the vector field $\boldsymbol{f}_{\eta}$ maps configurations $\boldsymbol{\eta} \in \mathsf{SE}(3)$ to tangent vectors in $\mathsf{T}_{\boldsymbol{\nu}}\mathsf{SE}(3)$. Thus, rigid-body motion can be viewed as a curve on $\mathsf{SE}(3)$ with velocity vectors living in corresponding tangent spaces $\mathsf{T}_{\boldsymbol{\nu}}\mathsf{SE}(3)$, evolving under the rule defined by the vector field $\boldsymbol{f}_{\eta}$.

The rigid-body dynamics may be derived using Newton's second law of motion (e.g., Etkin [40, Ch. 5]) or through a Lagrangian or Hamiltonian formalism (e.g., Goldstein [53, Ch. 5]). For a geometric perspective on the Hamiltonian dynamics of the free rigid body, the interested reader is directed to the text by Marsden and Ratiu [102, Ch. 15]. In either case, let $\boldsymbol{F}$ and $\boldsymbol{M}$ respectively denote the aerodynamic force and moment acting at the aircraft CG, expressed in $\mathcal{F}_{\mathrm{B}}$. Let $\boldsymbol{g}$ be the gravitational acceleration in $\mathcal{F}_{\mathrm{I}}$. Suppose the aircraft's mass m is constant, and let $\boldsymbol{I}$ denote the moment of inertia matrix about the CG, expressed in $\mathcal{F}_{\mathrm{B}}$. Altogether, the aircraft dynamics are

$$\dot{\boldsymbol{v}} = \boldsymbol{v} \times \boldsymbol{\omega} + \boldsymbol{R}_{\mathrm{IB}}^{\mathsf{T}}\boldsymbol{g} + \frac{1}{m}\boldsymbol{F} \tag{2.11}$$

$$\dot{\boldsymbol{\omega}} = \boldsymbol{I}^{-1}(\boldsymbol{I}\boldsymbol{\omega} \times \boldsymbol{\omega} + \boldsymbol{M}) \tag{2.12}$$

Defining the *generalized mass matrix* $\mathscr{M} = \mathbf{diag}(m\mathbb{I}, \boldsymbol{I})$ and the *generalized force* $\mathscr{F} = [\boldsymbol{F}^{\mathsf{T}}\ \boldsymbol{M}^{\mathsf{T}}]^{\mathsf{T}}$, the aircraft dynamics are written compactly as

$$\dot{\boldsymbol{\nu}} = \boldsymbol{f}_{\nu}(\boldsymbol{\eta}, \boldsymbol{\nu}) + \mathscr{M}^{-1}\mathscr{F} \tag{2.13}$$

[4] A *Lie algebra* $\mathfrak{g}$ is a vector space equipped with a bilinear, skew-symmetric operation $[\cdot,\cdot] : \mathfrak{g} \times \mathfrak{g} \to \mathfrak{g}$, called the *Lie bracket*, that satisfies the Jacobi identity, $[[u,v],w]+[[w,u],v]+[[v,w],u] = 0$ for all $u, v, w \in \mathfrak{g}$.

A geometric interpretation of Eq. (2.13) is as follows. The vector field $\boldsymbol{f}_\nu$ maps the 12-dimensional manifold $\mathsf{TSE}(3)$ to its tangent bundle, $\mathsf{T}\big(\mathsf{TSE}(3)\big)$. Since $\mathsf{T}_{(\boldsymbol{\eta},\boldsymbol{\nu})}\big(\mathsf{TSE}(3)\big)$ is a vector space, the addition of the generalized specific force $\mathscr{M}^{-1}\mathscr{F}$ to yield the aircraft's generalized body-frame acceleration $\dot{\boldsymbol{\nu}}$ is well-defined.

Altogether, the rigid-body aircraft equations of motion are

$$\begin{aligned}\dot{\boldsymbol{q}} &= \boldsymbol{R}_{\mathrm{IB}}\boldsymbol{v}\\ \dot{\boldsymbol{R}}_{\mathrm{IB}} &= \boldsymbol{R}_{\mathrm{IB}}\boldsymbol{S}(\boldsymbol{\omega})\\ \dot{\boldsymbol{v}} &= \boldsymbol{v}\times\boldsymbol{\omega} + \boldsymbol{R}_{\mathrm{IB}}^{\mathsf{T}}\boldsymbol{g} + \frac{1}{m}\boldsymbol{F}\\ \dot{\boldsymbol{\omega}} &= \boldsymbol{I}^{-1}(\boldsymbol{I}\boldsymbol{\omega}\times\boldsymbol{\omega} + \boldsymbol{M})\end{aligned} \tag{2.14}$$

with state $\boldsymbol{x} = (\boldsymbol{q}, \boldsymbol{R}_{\mathrm{IB}}, \boldsymbol{v}, \boldsymbol{\omega})$. We will use the notation $(\boldsymbol{a}, \boldsymbol{b})$ as shorthand for $[\boldsymbol{a}^{\mathsf{T}}\ \boldsymbol{b}^{\mathsf{T}}]^{\mathsf{T}}$ if $\boldsymbol{a}$ and $\boldsymbol{b}$ are column vectors. More generally, $(\boldsymbol{a}, \boldsymbol{b})$ denotes a point in the product space whose component subspaces are where $\boldsymbol{a}$ and $\boldsymbol{b}$ live, respectively. So, for example, the second element of $\boldsymbol{x}$ lives in $\mathsf{SO}(3)$. Referring to Eqs. (2.10) and (2.13), we will sometimes compactly write Eq. (2.14) as

$$\begin{aligned}\dot{\boldsymbol{\eta}} &= \boldsymbol{f}_\eta(\boldsymbol{\eta},\boldsymbol{\nu})\\ \dot{\boldsymbol{\nu}} &= \boldsymbol{f}_\nu(\boldsymbol{\eta},\boldsymbol{\nu}) + \mathscr{M}^{-1}\mathscr{F}\end{aligned} \tag{2.15}$$

explicitly breaking the system (2.14) up into kinematics and dynamics.

2.5 Lyapunov Stability Theory

Motivated by the design and stability analysis of nonlinear observers, this section lays out the preliminaries on stability for time-varying nonlinear systems. The definitions and sufficient conditions here are largely based on the text by Khalil [86]. The focus is stability of equilibria for nonlinear dynamical systems defined on open subsets of $\mathbb{R}^n$. For a geometric treatment of stability through the perspective of Section 2.2, see the text by Bullo and Lewis [28].

This dissertation is mainly focused on proving stability of the origin of a state estimation error system whose state is the difference between a state estimate and the true state. Thus, any control inputs to the nonlinear system may appear in these error dynamics. Accordingly, consider the nonlinear dynamical system

$$\dot{\boldsymbol{x}} = \boldsymbol{f}(\boldsymbol{x}, \boldsymbol{w}) \tag{2.16}$$

where $\boldsymbol{x}(t) \in \mathcal{X} \subset \mathbb{R}^n$ is the state vector and $\boldsymbol{w}(t) \in \mathcal{W}$ is a known input. The signal $\boldsymbol{w}$ is an element of the space

$$\mathcal{W}_{[0,\infty)} \coloneqq \{\omega \mid \omega : [0,\infty) \to \mathcal{W}\}$$

Assume $\boldsymbol{f}$ is locally Lipschitz in $\boldsymbol{x}$ on $\mathcal{X}\times\mathcal{W}$ so that solutions $\boldsymbol{x}(t)$ are well-defined. Without loss of generality, consider the initial time to be $t_0 = 0$ and the origin $\boldsymbol{x} = \boldsymbol{0}$ to be an *equilibrium* — that is, $\boldsymbol{f}(\boldsymbol{0}, \boldsymbol{w}) = \boldsymbol{0}$ for all $\boldsymbol{w} \in \mathcal{W}_{[0,\infty)}$.

To state the definitions of stability for this class of system, the function spaces $\mathcal{K}$ and $\mathcal{KL}$ of *comparison functions* are defined as follows. A continuous function $\alpha : [0, a) \to [0, \infty)$ is class-$\mathcal{K}$ if it is strictly increasing and $\alpha(0) = 0$. It is class-$\mathcal{K}_\infty$ if $a = \infty$ and $\alpha(y) \to \infty$ as $y \to \infty$. A continuous function $\beta : [0, a) \times [0, \infty) \to [0, \infty)$ is class-$\mathcal{KL}$ if for each fixed τ, $\beta(y, \tau)$ is class-$\mathcal{K}$ and for each fixed y, $\beta(y, \tau)$ is decreasing and $\beta(y, \tau) \to 0$ as $\tau \to \infty$.

The origin $\boldsymbol{x} = \mathbf{0}$ of the system (2.16) is

(i) *stable uniformly in* $\boldsymbol{w}$ if there exist a class-$\mathcal{K}$ function α and a constant $r > 0$ such that
$$\|\boldsymbol{x}(t)\| \leq \alpha(\|\boldsymbol{x}(0)\|) \tag{2.17}$$
for all $t \geq 0$, $\|\boldsymbol{x}(0)\| < r$, and $\boldsymbol{w} \in \mathcal{W}_{[0,\infty)}$.

(ii) *asymptotically stable uniformly in* $\boldsymbol{w}$ if there exist a class-$\mathcal{KL}$ function β and a constant $r > 0$ such that
$$\|\boldsymbol{x}(t)\| \leq \beta(\|\boldsymbol{x}(0)\|, t) \tag{2.18}$$
for all $t \geq 0$, $\|\boldsymbol{x}(0)\| < r$, and $\boldsymbol{w} \in \mathcal{W}_{[0,\infty)}$.

(iii) *globally asymptotically stable uniformly in* $\boldsymbol{w}$ if Eq. (2.18) holds for all $t \geq 0$, $\boldsymbol{x}(0) \in \mathcal{X}$, and $\boldsymbol{w} \in \mathcal{W}_{[0,\infty)}$.

(iv) *exponentially stable uniformly in* $\boldsymbol{w}$ if it is asymptotically stable uniformly in $\boldsymbol{w}$ with β satisfying
$$\beta(r, s) = kre^{-\gamma s} \tag{2.19}$$
for constants $k, \gamma > 0$;

(v) *globally exponentially stable uniformly in* $\boldsymbol{w}$ if it is globally asymptotically stable uniformly in $\boldsymbol{w}$ with β satisfying Eq. (2.19).

Lyapunov stability theory is concerned with determining sufficient conditions for the types of stability listed above. The origin $\boldsymbol{x} = \mathbf{0}$ is *uniformly stable* in the compact subset $\mathcal{D} \subset \mathcal{X}$ containing the origin if there exist a continuously differentiable function $V : \mathcal{D} \times [0, \infty) \to \mathbb{R}$ and positive definite[5] functions $W_1(\boldsymbol{x})$ and $W_2(\boldsymbol{x})$ on $\mathcal{D}$ such that
$$W_1(\boldsymbol{x}) \leq V(\boldsymbol{x}, t) \leq W_2(\boldsymbol{x}) \tag{2.20}$$
$$\frac{\partial V}{\partial t} + \frac{\partial V}{\partial \boldsymbol{x}} \boldsymbol{f}(\boldsymbol{x}, \boldsymbol{w}) \leq 0 \tag{2.21}$$
for all $t \in [0, \infty)$, $\boldsymbol{x} \in \mathcal{D}$, and $\boldsymbol{w} \in \mathcal{W}_{[0,\infty)}$. The origin $\boldsymbol{x} = \mathbf{0}$ is *uniformly asymptotically stable in* $\mathcal{D}$ if V further satisfies
$$\frac{\partial V}{\partial t} + \frac{\partial V}{\partial \boldsymbol{x}} \boldsymbol{f}(\boldsymbol{x}, \boldsymbol{w}) \leq -W_3(\boldsymbol{x}) \tag{2.22}$$

[5] A function $W(\boldsymbol{x})$ is *positive definite* (denoted $W(\boldsymbol{x}) \succ 0$) on a subset $\mathcal{D} \subset \mathcal{X}$ if $W(\mathbf{0}) = 0$ and $\boldsymbol{W}(\boldsymbol{x}) > 0$ for all $\boldsymbol{x} \in \mathcal{D} \setminus \{\mathbf{0}\}$.

for some positive definite function $W_3(\boldsymbol{x})$. Furthermore, the origin is *uniformly exponentially stable in* $\mathcal{D}$ if

$$W_1(\boldsymbol{x}) = k_1\|\boldsymbol{x}\|^a, \quad W_2(\boldsymbol{x}) = k_2\|\boldsymbol{x}\|^a, \quad \text{and} \quad W_3(\boldsymbol{x}) = k_3\|\boldsymbol{x}\|^a \tag{2.23}$$

for positive constants k_1, k_2, k_3 and a. The above conditions are sufficient for their respective global versions of stability if $\mathcal{D} = \mathcal{X}$ and V is radially unbounded — that is, $V(\boldsymbol{x}, t) \to \infty$ as $\|\boldsymbol{x}\| \to \infty$ for all $t \in [0, \infty)$.

2.6 Probability Theory

This section is based on the works of Durrett [38], Arguin [8], and Evans [42].

Stochastic systems are defined on probability spaces, which we introduce as follows. Consider an abstract set of outcomes Ω, called the *sample space*. This language is motivated by the aim to quantify how likely subsets of the sample space (called *events*) occur. However, not every collection of subsets of Ω makes sense. There can be infinitely many "bad" subsets for a given problem. To formalize what are considered "good" collections of events, a *σ-algebra* is defined to be a collection $\mathcal{F}$ of subsets of Ω such that

(i) $\mathcal{F}$ contains both the empty set $\varnothing$ and the entire sample space Ω;

(ii) if a subset A is in $\mathcal{F}$, then so is its complement A^{c};

(iii) all countable unions and intersections of subsets $A_i \in \mathcal{F}$ are in $\mathcal{F}$.

Most common is the Borel σ-algebra $\mathcal{B}^n$, which is the collection of all intersections and unions of open and closed subsets, respectively, of $\mathbb{R}^n$. Given a sample space Ω and a σ-algebra $\mathcal{F}$, the pair $(\Omega, \mathcal{F})$ is a *measurable space*. Once a *measure* $\mathbb{P}$ is assigned to $(\Omega, \mathcal{F})$, the triple $(\Omega, \mathcal{F}, \mathbb{P})$ is called a *measure* space.[6] A *probability space* is simply a measure space whose measure satisfies the following three axioms:

(i) $\mathbb{P}(A) \in [0, 1]$ for all $A \in \mathcal{F}$.

(ii) $\mathbb{P}(\varnothing) = 0$ and $\mathbb{P}(\Omega) = 1$.

(iii) $\mathbb{P}$ is *additive*. That is, for any sequence of disjoint (mutually exclusive) events $A_1, A_2, \ldots$,

$$\mathbb{P}(A_1 \cup A_2 \cup \cdots) = \mathbb{P}(A_1) + \mathbb{P}(A_2) + \cdots$$

In this case, the measure $\mathbb{P}$ is called a *probability measure*. Altogether, the triple $(\Omega, \mathcal{F}, \mathbb{P})$ is a called *probability space*. It is said an event $A \in \mathcal{F}$ occurs *almost surely* if $\mathbb{P}(A) = 1$ and that two events $A, B \in \mathcal{F}$ are *independent* if $\mathbb{P}(A \cup B) = \mathbb{P}(A)\mathbb{P}(B)$. Two sub-$\sigma$-algebras $\mathcal{A}, \mathcal{B} \subset \mathcal{F}$ are independent if all events $A \in \mathcal{A}$ and $B \in \mathcal{B}$ are independent.

[6] For an introduction to measure theory, see the text by Tao [143].

Often, elements of the sample space Ω do not have concrete meaning nor are we interested in their particular values. Instead, we are generally interested in the consequence of these outcomes. Consider two measurable spaces $(\Omega, \mathcal{F})$ and $(\mathcal{X}, \mathcal{A})$. The map $\boldsymbol{X} : \Omega \to \mathcal{X}$ is called a *random variable* if $\boldsymbol{X}$ is $\mathcal{F}$-measurable. That is, for all events $A \in \mathcal{A}$,

$$\{\omega \in \Omega \mid \boldsymbol{X}(\omega) \in \mathcal{A}\} = \boldsymbol{X}^{-1}(A) \in \mathcal{F}$$

We also say that

$$\sigma(\boldsymbol{X}) = \{\boldsymbol{X}^{-1}(B) \mid B \in \mathcal{B}^n\} \tag{2.24}$$

is the *σ-algebra generated by $\boldsymbol{X}$*. It is the smallest σ-algebra on which $\boldsymbol{X}$ is measurable. In the common case that $\mathcal{X} = \mathbb{R}^n$, we have $\sigma(\boldsymbol{X}) = \mathcal{B}^n$. If a probability measure is assigned to the measurable space $(\Omega, \mathcal{F})$ on which a $\mathbb{R}^n$-valued random variable $\boldsymbol{X}(\omega)$ is defined, then the distribution of that random variable is uniquely defined. The *distribution function* of $\boldsymbol{X}$ is the function $F_{\boldsymbol{X}} : \mathbb{R}^n \to [0, 1]$ given by

$$F_{\boldsymbol{X}}(\boldsymbol{x}) = \mathbb{P}(\{\boldsymbol{X} \leq \boldsymbol{x}\}) \tag{2.25}$$

for all $\boldsymbol{x} \in \mathbb{R}^n$, where $\{\boldsymbol{X} \leq \boldsymbol{x}\}$ denotes the event $\{\omega \in \Omega \mid \boldsymbol{X}(\omega) \leq \boldsymbol{x}\}$. In the special case that $F_{\boldsymbol{X}}$ is Lebesgue-continuous (that is, $\mathbb{P}(N) = 0$ for every set N of Lebesgue measure zero), then $F_{\boldsymbol{X}}$ has a *density function* f that uniquely satisfies

$$F_{\boldsymbol{X}}(x_1, \ldots, x_n) = \int_{-\infty}^{x_n} \cdots \int_{-\infty}^{x_1} f(x_1, \ldots, x_n) \, \mathrm{d}x_1 \cdots \mathrm{d}x_n \tag{2.26}$$

Consider a $\mathcal{X}$-valued random variable $\boldsymbol{X}$ on a probability space $(\Omega, \mathcal{F}, \mathbb{P})$. The *expected value* of $\boldsymbol{X}$ is defined as

$$\mathbb{E}(\boldsymbol{X}) \coloneqq \int_{\Omega} \boldsymbol{X}(\omega) \, \mathrm{d}\mathbb{P}(\omega) \tag{2.27}$$

In the special (yet often-considered) case that $\mathcal{X} = \mathbb{R}^n$ and the distribution function is Lebesgue-continuous with density f, we have

$$\mathbb{E}(\boldsymbol{X}) = \int_{\mathbb{R}^n} \boldsymbol{x} f(\boldsymbol{x}) \, \mathrm{d}\boldsymbol{x} \tag{2.28}$$

as the familiar statement of the expected value.

A $\mathcal{X}$-valued *random process* on a probability space $(\Omega, \mathcal{F}, \mathbb{P})$ is an infinite sequence of random variables

$$\boldsymbol{X} = \{\boldsymbol{X}_t \mid t \in \mathbb{T}\}$$

where $\mathbb{T}$ may be discrete (e.g., $\mathbb{T} = \mathbb{N}$) or continuous (e.g., $\mathbb{T} = [0, \infty)$). One may view random processes as sequences of random variables; that is, $\boldsymbol{X}_t(\cdot)$ is a random variable for each fixed $t \in \mathbb{T}$. Or equivalently, $\boldsymbol{X}_{(\cdot)}(\omega)$ is a function on $\mathbb{T}$ for each fixed $\omega \in \Omega$ and is called a *sample path*. We will often use the notation $\boldsymbol{X}(t, \omega)$ to emphasize the functional dependence on both t and ω.

The most fundamental continuous-time random process is the *Wiener process*. As a mathematical representation of *Brownian motion*, it is the continuous-time limit of a random walk. More formally, a $\mathbb{R}^n$-valued random process $\boldsymbol{W} = [W^1 \ \cdots \ W^n]^\mathsf{T}$ is a *standard Wiener process* if

(i) $\boldsymbol{W}(0) = \mathbf{0}$ almost surely;

(ii) $W^i(t) - W^i(s) \sim \mathcal{N}(0, t-s)$ for all $t \geq s \geq 0$ for each $i = 1, \ldots, n$;[7]

(iii) the increments $W^i(t_1) - W^i(0)$, $W^i(t_2) - W^i(t_1)$, $\cdots$, $W^i(t_m) - W^i(t_{m-1})$ are independent for all $0 < t_1 < t_2 < \cdots < t_m$ for each $i = 1, \ldots, n$ and any t_m;

(iv) the σ-algebras $\sigma(\{W^i(t) \mid t \geq 0\})$, $i = 1, \ldots, n$, are independent.

We identify almost all $\omega \in \Omega$ with a continuous function $\boldsymbol{W}_{(\cdot)}(\omega) : [0, \infty) \to \mathbb{R}^n$. Therefore, in this dissertation we will always consider the probability space defined by

$$\begin{aligned}
\Omega &= C([0,\infty), \mathbb{R}^n) \equiv \text{space of } \mathbb{R}^n\text{-valued continuous functions on } [0,\infty) \\
\mathcal{F} &= \mathcal{B}(C([0,\infty), \mathbb{R}^n)) \equiv \text{Borel sigma algebra on } C([0,\infty), \mathbb{R}^n) \\
\mathbb{P} &= \text{Gaussian probability measure satisfying items (i)–(iv) above}
\end{aligned}$$

on which the random process $\boldsymbol{W}_t(\omega) = \omega(t)$ is defined.

Remark 2.1. *The Wiener process has non-zero quadratic variation*

$$[W]_t \coloneqq \lim_{|P| \to 0} \sum_{k=0}^{m-1} (W(t_{k+1}) - W(t_k))^2 = t$$

where $P = \{0 < t_1 < t_2 < \cdots < t\}$ *is a partition of size* $|P| \coloneqq \max\{t_{k+1} - t_k \mid k = 0, \ldots, m-1\}$.

Although the Wiener process W is almost surely continuous, it is almost surely nowhere differentiable in the classical sense. However, it does admit a *distributional derivative*, which defines continuous-time *white noise* [10, Ch. 3]. Loosely, this means the distribution of $\dot{W}$ exists in some sense even though the derivative of each sample path does not. This perspective comes from the theory of *generalized random processes*, where randomness is understood through how the process acts on smooth functions.

Let $\varphi \in C^\infty$ be a test function (i.e., a smooth function with compact support). The Wiener process W can be viewed as a generalized random process through

$$\Phi(\varphi) = \int_0^\infty \varphi(t) W(t) \, \mathrm{d}t$$

which defines a (random) linear functional on the space of test functions.[8] In this framework,

[7] that is, sampled from a Gaussian distribution with mean zero and variance $t - s$.

[8] As described by Arnold [10], generalized random processes can be interpreted physically by considering how sensors inherently average over time, thus never measuring pointwise values but instead integrals against smooth functions.

the mean and covariance of W are given by

$$m(\varphi) \coloneqq \mathbb{E}\left(\Phi(\varphi)\right) = 0$$
$$C(\varphi,\psi) \coloneqq \mathbb{E}\big((\Phi(\varphi) - m(\varphi))(\Phi(\psi) - m(\psi))\big) = \int_0^\infty \int_0^\infty \varphi(t)\psi(s)\min(t,s)\,\mathrm{d}t\,\mathrm{d}s$$

The distributional derivative $\dot{\Phi}$ is defined by the relation

$$\dot{\Phi}(\varphi) = -\Phi(\dot{\varphi}) \implies \int_0^\infty \varphi(t)\dot{W}(t)\,\mathrm{d}t = -\int_0^\infty \dot{\varphi}(t)W(t)\,\mathrm{d}t$$

Therefore, the mean and covariance of the generalized random process $\dot{\Phi}(\varphi)$ are

$$\dot{m}(\varphi) \coloneqq \mathbb{E}\big(\dot{\Phi}(\varphi)\big) = -\int_0^\infty \dot{\varphi}(t)\mathbb{E}\left(W(t)\right)\,\mathrm{d}t = 0 \tag{2.29}$$

and

$$\begin{aligned}\dot{C}(\varphi,\psi) \coloneqq \mathbb{E}\big(\dot{\Phi}(\varphi)\dot{\Phi}(\psi)\big) &= \int_0^\infty \int_0^\infty \dot{\varphi}(t)\dot{\psi}(s)\mathbb{E}\big(W(t)W(s)\big)\,\mathrm{d}t\,\mathrm{d}s \\ &= \int_0^\infty \int_0^\infty \dot{\varphi}(t)\dot{\psi}(s)\min(t,s)\,\mathrm{d}t\,\mathrm{d}s \\ &= \int_0^\infty \int_0^\infty \varphi(t)\psi(s)\delta(t-s)\,\mathrm{d}t\,\mathrm{d}s \end{aligned} \tag{2.30}$$

Through the lens of generalized random processes, Eqs. (2.29) and (2.30) express the familiar characterization of white noise as a zero-mean process with covariance given by the Dirac delta function $\delta(t-s)$.

2.7 Itô Calculus and Stochastic Differential Equations

This section introduces "how calculus is done" with the Wiener process. It is largely based on material by Arnold [10] and Evans [42] with additional inspiration from Øksendal [121] and Pavliotis [125].

A random process $\boldsymbol{G} : [0,\infty)\times\Omega$ on the probability space $(\Omega,\mathcal{F},\mathbb{P})$ is called *non-anticipating* if $\boldsymbol{G}(t)$ is measurable with respect to the σ-algebra $\mathcal{F}_t = \sigma(\{\boldsymbol{G}(s) \mid s \le t\})$. A random process $\bar{\boldsymbol{G}}$ is called a *step process* if there exists a partition $P = \{0 < t_1 < t_2 < \cdots < t_m = T\}$ such that

$$\bar{\boldsymbol{G}}(t) \equiv \bar{\boldsymbol{G}}_k \quad \text{for all} \quad t_k \le t < t_{k+1} \quad (k = 0,1,\ldots,m-1)$$

The *Itô integral of a non-anticipating step process* $\bar{\boldsymbol{G}}$ with respect to the Wiener process $\boldsymbol{W}$ is

$$\int_0^T \bar{\boldsymbol{G}}\mathrm{d}\boldsymbol{W} = \sum_{k=0}^{m-1} \bar{\boldsymbol{G}}_k(\boldsymbol{W}(t_{k+1}) - \boldsymbol{W}(t_k))$$

More generally, consider a random process $\boldsymbol{G}$ *approximated by a sequence of non-anticipating step processes* $\{\bar{\boldsymbol{G}}^j \mid j = 1, \ldots, m\}$; that is,

$$\lim_{m\to\infty} \int_0^T \|\boldsymbol{G}(t) - \bar{\boldsymbol{G}}^m(t)\|^2 \, \mathrm{d}t = 0 \quad \text{almost surely}$$

The *Itô integral of* $\boldsymbol{G}$ with respect to the Wiener process $\boldsymbol{W}$ is

$$\int_0^T \boldsymbol{G}\mathrm{d}\boldsymbol{W} = \int_0^T \boldsymbol{G}(t)\mathrm{d}\boldsymbol{W}_t = \lim_{m\to\infty} \int_0^T \bar{\boldsymbol{G}}^m \mathrm{d}\boldsymbol{W} \tag{2.31}$$

The construction of this integral is very similar to the Riemann–Stieltjes integral with the difference being that the intermediate value of the integrand in a Riemann sum approximation is not arbitrary; rather, it is taken as the initial point $\boldsymbol{G}(t_k)$ so that the result is also non-anticipating. For example, the integral

$$\int_0^t W\mathrm{d}W = \frac{W^2}{2} - \frac{t}{2}$$

would not be well-defined in the deterministic setting.

Due in part to the fact that the Wiener process has non-zero quadratic variation (see Remark 2.1), the usual chain rule of calculus does not hold. Consider a random process $\boldsymbol{X}$ that satisfies

$$\boldsymbol{X}_t = \boldsymbol{X}_0 + \int_0^t \boldsymbol{f}(t)\mathrm{d}t + \int_0^t \boldsymbol{G}(s)\mathrm{d}\boldsymbol{W}_s \tag{2.32}$$

The first integral is the usual integral, but the second is understood in the sense of Itô. This equation is often written in differential form as

$$\mathrm{d}\boldsymbol{X} = \boldsymbol{f}\mathrm{d}t + \boldsymbol{G}\mathrm{d}\boldsymbol{W}$$

However, the "differential" $\mathrm{d}\boldsymbol{X}$ is always to be interpreted as shorthand for the integral equation (2.32). It was shown by Itô that for a standard Wiener process W,

$$\begin{aligned} \mathrm{d}(W^2) &= 2W\mathrm{d}W + \mathrm{d}t \\ \mathrm{d}(tW) &= W\mathrm{d}t + t\mathrm{d}W \end{aligned}$$

To illustrate the consequence of this fact, consider the scalar case where $\mathrm{d}X = f\mathrm{d}t + \sigma\mathrm{d}W$, and let $Y = h(t, X)$. It holds that

$$\begin{aligned} \mathrm{d}Y &= \frac{\partial h}{\partial t}\mathrm{d}t + \frac{\partial h}{\partial X}\mathrm{d}X + \frac{1}{2}\frac{\partial^2 h}{\partial X^2}(\mathrm{d}X)^2 \\ &= \left(\frac{\partial h}{\partial t} + \frac{\partial h}{\partial X}f + \frac{1}{2}\frac{\partial^2 h}{\partial X^2}\sigma^2\right)\mathrm{d}t + \frac{\partial h}{\partial X}\sigma\mathrm{d}W \end{aligned}$$

Notice that without the Hessian $\partial^2 h/\partial X^2$, we would have the chain rule or ordinary calculus.

In higher dimensions, differentials of $\boldsymbol{Y} = \boldsymbol{h}(t, \boldsymbol{X})$ satisfy *Itô's lemma* (also, *Itô's rule* or *Itô's formula*),

$$\mathrm{d}\boldsymbol{Y} = \left(\frac{\partial h}{\partial t} + \frac{\partial h}{\partial \boldsymbol{X}} \boldsymbol{f} + \frac{1}{2} \operatorname{Tr} \left[\frac{\partial^2 h}{\partial \boldsymbol{X}^2} \boldsymbol{\sigma} \boldsymbol{\sigma}^{\mathsf{T}} \right] \right) \mathrm{d}t + \frac{\partial h}{\partial \boldsymbol{X}} \boldsymbol{\sigma} \mathrm{d}\boldsymbol{W} \tag{2.33}$$

which generalizes the chain rule to functions of random processes (2.32).

More generally, we consider random processes $\boldsymbol{X}_t$ satisfying

$$\boldsymbol{X}_t = \boldsymbol{X}_0 + \int_0^t \boldsymbol{f}(\boldsymbol{X}_s, s) \mathrm{d}s + \int_0^t \boldsymbol{\sigma}(\boldsymbol{X}_s, s) \mathrm{d}\boldsymbol{W}_s \tag{2.34}$$

where $\boldsymbol{f} : \mathbb{R}^n \times [0, \infty) \to \mathbb{R}^n$ is the *drift vector field*, $\boldsymbol{\sigma} : \mathbb{R}^n \times [0, \infty) \to \mathbb{R}^{n \times m}$ is the *diffusion* (or *dispersion*) *matrix field*, and $\boldsymbol{W}$ is a $\mathbb{R}^m$-valued standard Wiener process on the probability space $(\Omega, \mathcal{F}, \mathbb{P})$. The random process (2.34) is known as a *strong solution* to the *stochastic differential equation* (SDE)

$$\mathrm{d}\boldsymbol{X}_t = \boldsymbol{f}(\boldsymbol{X}_t, t) \mathrm{d}t + \boldsymbol{\sigma}(\boldsymbol{X}_t, t) \mathrm{d}\boldsymbol{W}_t \tag{2.35}$$

provided that for all $t \in [0, \infty)$,

(i) $\boldsymbol{X}_t$ is almost surely continuous and $\mathcal{F}_t$-measurable;

(ii) $\boldsymbol{f}_t \coloneqq \boldsymbol{f}(\boldsymbol{X}_t, t)$ satisfies $\mathbb{E}(\|\boldsymbol{f}_t\|) < \infty$;

(iii) $\boldsymbol{\sigma}_t \coloneqq \boldsymbol{\sigma}(\boldsymbol{X}_t, t)$ satisfies $\mathbb{E}(\|\boldsymbol{\sigma}_t\|^2) < \infty$;

(iv) $\boldsymbol{X}_t(\omega) = \boldsymbol{X}_0(\omega) + \int_0^t \boldsymbol{f}(\boldsymbol{X}_s(\omega), s) \mathrm{d}s + \int_0^t \boldsymbol{\sigma}(\boldsymbol{X}_s(\omega), s) \mathrm{d}\boldsymbol{W}_s(\omega)$ for almost all $\omega \in \Omega$.

We now give two simple examples of stochastic differential equations. The scalar SDE

$$\mathrm{d}X_t = aX_t \mathrm{d}t + bX_t \mathrm{d}W_t$$

has the unique strong solution

$$X_t(\omega) = X_0(\omega) e^{(a - b^2/2)t + bW_t(\omega)}$$

which is known as *geometric Brownian motion*. Another common example is the *Langevin equation*,

$$\mathrm{d}\boldsymbol{X}_t = \boldsymbol{A}\boldsymbol{X}_t \mathrm{d}t + \boldsymbol{\sigma} \mathrm{d}\boldsymbol{W}_t$$

which has the unique strong solution

$$\boldsymbol{X}_t(\omega) = e^{\boldsymbol{A}t} \boldsymbol{X}_0(\omega) + \int_0^t e^{\boldsymbol{A}(t-s)} \boldsymbol{\sigma} \mathrm{d}\boldsymbol{W}_s(\omega)$$

called the *Ornstein-Uhlenbeck process*.

A core concept in analysis of stochastic differential equations is how probability densities change over time. This motivates the definition of a linear operator called the *infinitesimal generator* $\mathscr{L}$ of the random process $\boldsymbol{X}_t$. Exactly how $\mathscr{L}$ defines the evolution of probability densities is beyond the scope of this dissertation;[9] instead, we focus on the fact that the infinitesimal generator also defines the expected rate-of-change of a function. More formally,

$$\mathscr{L}V(\boldsymbol{x},t) = \lim_{t \searrow 0} \frac{\mathbb{E}\left(V(\boldsymbol{X}_t,t)|\boldsymbol{X}_0 = \boldsymbol{x}\right) - V(\boldsymbol{x},t)}{t}$$

for any bounded $V : \mathbb{R}^n \times [0,\infty)$. If V is twice differentiable in its first argument and once differentiable in its second argument (that is, an element of $C^{(2,1)}$), then

$$\mathscr{L}V(\boldsymbol{x},t) = \frac{\partial V(\boldsymbol{x},t)}{\partial t} + \frac{\partial V(\boldsymbol{x},t)}{\partial \boldsymbol{x}}\boldsymbol{f}(\boldsymbol{x},t) + \frac{1}{2}\operatorname{Tr}\left(\boldsymbol{\sigma}(\boldsymbol{x},t)\boldsymbol{\sigma}^{\mathsf{T}}(\boldsymbol{x},t)\frac{\partial^2 V(\boldsymbol{x},t)}{\partial \boldsymbol{x}^2}\right) \tag{2.36}$$

In light of Section 2.5, the choice of function "V" is deliberate. In stochastic stability analysis (soon detailed in Section 2.8), $\mathscr{L}V$ is indeed analogous to $\dot{V}$ (which represented the rate of change of a Lyapunov function in Section 2.5) in the deterministic case.

Like with ordinary differential equations, we often wish to numerically construct solutions to SDEs. It is important that these solutions are not only accurate in their sample paths, but also probabilistically accurate. Consider the SDE

$$\mathrm{d}\boldsymbol{X}_t = \boldsymbol{f}(\boldsymbol{X}_t)\mathrm{d}t + \boldsymbol{\sigma}(\boldsymbol{X}_t)\mathrm{d}\boldsymbol{W}_t$$

and a time discretization $\{0 = t_0 < t_1 < \cdots < t_N = T\}$. For fixed $\omega \in \Omega$, denote

$$\begin{aligned}\Delta t_k &:= t_{k+1} - t_k \\ \boldsymbol{x}_k &:= \boldsymbol{X}_{t_k}(\omega) \\ \Delta \boldsymbol{w}_k &:= \boldsymbol{W}_{t_{k+1}}(\omega) - \boldsymbol{W}_{t_k}(\omega)\end{aligned}$$

The discrete-time approximation

$$\boldsymbol{x}_{k+1} - \boldsymbol{x}_k = \boldsymbol{f}(\boldsymbol{x}_k)\Delta t_k + \boldsymbol{\sigma}(\boldsymbol{x}_k)\Delta \boldsymbol{w}_k$$

is called the *Euler-Maruyama* method (akin to the Euler method for ODEs). The key here is that

$$\Delta \boldsymbol{w}_k \sim \mathcal{N}(\boldsymbol{0}, \Delta t_k \mathbb{I})$$

To obtain higher-order approximations to solutions $\boldsymbol{X}_t$ one can perform Taylor series-like expansions to incorporate higher-order effects. Here, however, we must be careful to respect the laws of Itô calculus. In doing so one realizes that standard Runge-Kutta numerical methods do not hold for stochastic differential equations.[10]

[9] The interested reader is directed to the text by Pavliotis [125].

[10] See the text by Kloeden and Platen [89] for a thorough treatment of numerical methods for SDEs.

2.8 Stability of Stochastic Differential Equations

This section presents prerequisite notions of stochastic stability with Lyapunov-like sufficient conditions. Consider the SDE

$$\mathrm{d}\boldsymbol{X} = \boldsymbol{f}(\boldsymbol{X}, t)\mathrm{d}t + \boldsymbol{G}(\boldsymbol{X}, t)\boldsymbol{\sigma}(t)\mathrm{d}\boldsymbol{W} \tag{2.37}$$

where $\boldsymbol{\sigma}\boldsymbol{\sigma}^{\mathsf{T}}$ is the *infinitesimal covariance* of the scaled Wiener process $\boldsymbol{\sigma}\boldsymbol{W}$ and the usual conditions on $\boldsymbol{f}$ and $\boldsymbol{G}$ hold so that strong solutions almost surely starting from $\boldsymbol{x}_0 \in \mathbb{R}^n$ are well-defined. In this section, we make a distinction between the random process $\boldsymbol{X}(t)$ and its sample paths $\boldsymbol{x}(t) = \boldsymbol{X}_t(\omega)$ for fixed $\omega \in \Omega$.

First, suppose the origin is a *true equilibrium*, meaning $\boldsymbol{f}(\boldsymbol{0}, t) = \boldsymbol{0}$ and $\boldsymbol{G}(\boldsymbol{0}, t) = \boldsymbol{0}$ for all $t \in [t_0, \infty)$. In this case, we say the noise vanishes at the origin. The following preliminaries for this class of system are based on the works of Khasminskii [88] and Arnold [10]. The origin of the SDE (2.37) is said to be

(i) *stable in probability* if

$$\lim_{\|\boldsymbol{x}_0\| \to 0} \mathbb{P}\Big\{ \sup_{t \in [t_0, \infty)} \|\boldsymbol{X}(t)\| > \epsilon \Big\} = 0 \tag{2.38}$$

(ii) *asymptotically stable in probability* if

$$\lim_{\|\boldsymbol{x}_0\| \to 0} \mathbb{P}\Big\{ \lim_{t \to \infty} \boldsymbol{X}(t) = \boldsymbol{0} \Big\} = 1 \tag{2.39}$$

(iii) *asymptotically stable in the large* if

$$\mathbb{P}\Big\{ \lim_{t \to \infty} \boldsymbol{X}(t) = \boldsymbol{0} \Big\} = 1 \tag{2.40}$$

for all $\boldsymbol{x}_0 \in \mathbb{R}^n$.

Like with deterministic systems, we can state Lyapunov sufficient conditions for these notions of stochastic stability. Consider a function $V \in C^{(2,1)}$, $V : \mathbb{R}^n \times [0, \infty)$. Suppose there exist positive definite functions $W_1(\boldsymbol{x})$ and $W_2(\boldsymbol{x})$ on a compact subset $\mathcal{D} \subset \mathbb{R}^n$ such that

$$W_1(\boldsymbol{x}) \leq V(\boldsymbol{x}, t) \leq W_2(\boldsymbol{x}) \tag{2.41}$$

$$\mathscr{L}V(\boldsymbol{x}, t) \leq 0 \tag{2.42}$$

for all $t \in [0, \infty)$ and $\boldsymbol{x} \in \mathcal{D}$. The origin is *asymptotically stable in probability* if V further satisfies

$$\mathscr{L}V(\boldsymbol{x}, t) \leq -W_3(\boldsymbol{x}) \tag{2.43}$$

for some positive definite function $W_3(\boldsymbol{x})$ on $\mathcal{D}$. The origin is *asymptotically stable in the large* if $\mathcal{D} = \mathbb{R}^n$ and V is radially unbounded.

For many systems, however, noise does not vanish at the origin. In other words, the fact that $\boldsymbol{G}(\mathbf{0}, t) \neq \mathbf{0}$ means one cannot apply the above notions of stochastic stability. In this dissertation, we consider the particular perspective of *noise-to-state stability* (NSS) as presented by Mateos-Núñez and Cortés [103], which is a statement on the probabilistic convergence of the state to some ultimate bound whose size depends on the magnitude of the driving noise. The SDE (2.37) is *noise-to-state stable* if for any $\epsilon \in (0, 1]$ there exist a class-$\mathcal{K}$ function α and a class-$\mathcal{KL}$ function β such that

$$\mathbb{P}\left\{ \|\boldsymbol{X}(t)\|^p > \beta(\|\boldsymbol{x}_0\|, t - t_0) + \alpha\Big(\operatorname*{ess\,sup}_{s\in[t_0,t)} \|\boldsymbol{\sigma}(s)\|_{\mathrm{F}} \Big) \right\} \leq \epsilon \tag{2.44}$$

for some integer $p > 0$. Here, $\|\cdot\|_{\mathrm{F}}$ denotes the Frobenius norm. The system is *pth moment noise-to-state stable* if there exist a class-$\mathcal{K}$ function α and a class-$\mathcal{KL}$ function β such that

$$\mathbb{E}\big(\|\boldsymbol{X}(t)\|^p\big) \leq \beta(\|\boldsymbol{x}_0\|, t - t_0) + \alpha\Big(\operatorname*{ess\,sup}_{s\in[t_0,t)} \|\boldsymbol{\sigma}(s)\|_{\mathrm{F}} \Big) \tag{2.45}$$

If there exist an integer $p > 0$, a C^2 Lyapunov function $V(\boldsymbol{x})$, a continuous positive definite function $W(\boldsymbol{x})$, class $\mathcal{K}_\infty$ functions α_1, α_2, and a class-$\mathcal{K}$ function ρ such that for all $\boldsymbol{x} \in \mathbb{R}^n$ and $t \in [t_0, \infty)$,

$$\alpha_1(\|\boldsymbol{x}\|^p) \leq V(\boldsymbol{x}) \leq \alpha_2(\|\boldsymbol{x}\|^p) \tag{2.46}$$

$$\mathscr{L}V(\boldsymbol{x}, t) \leq -W(\boldsymbol{x}) + \rho(\|\boldsymbol{\sigma}(t)\|_{\mathrm{F}}) \tag{2.47}$$

where

$$V(\boldsymbol{x}) \leq \alpha_3(W(\boldsymbol{x})) \tag{2.48}$$

for some concave class-$\mathcal{K}_\infty$ function α_3, then the system is noise-to-state stable in probability. Specifically, for any $\epsilon \in (0, 1]$,

$$\mathbb{P}\left\{ \|\boldsymbol{X}(t)\|^p > \alpha_1^{-1}\left(\frac{2}{\epsilon}\mu\Big(\alpha_2\big(\|\boldsymbol{x}_0\|^p\big), t\Big)\right) + \alpha_1^{-1}\left(\frac{2}{\epsilon}\alpha_3\Big(2\rho\big(\operatorname*{ess\,sup}_{s\in[t_0,t)} \|\boldsymbol{\sigma}(s)\|_{\mathrm{F}}\big)\Big)\right) \right\} \leq \epsilon \tag{2.49}$$

where the class-$\mathcal{KL}$ function $\mu(a, \tau)$ is defined by the unique solution $y(t)$ to the ODE

$$\frac{\mathrm{d}y}{\mathrm{d}\tau} = -\frac{1}{2}\alpha_3^{-1}\big(y(\tau)\big), \quad y(0) = a \tag{2.50}$$

Furthermore, if α_1 is convex, then the system is pth moment noise-to-state stable in probability such that

$$\mathbb{E}\big(\|\boldsymbol{X}(t)\|^p\big) \leq \alpha_1^{-1}\left(2\mu\Big(\alpha_2\big(\|\boldsymbol{x}_0\|^p\big), t\Big)\right) + \alpha_1^{-1}\left(2\alpha_3\Big(2\rho\big(\operatorname*{ess\,sup}_{s\in[t_0,t)} \|\boldsymbol{\sigma}(s)\|_{\mathrm{F}}\big)\Big)\right) \tag{2.51}$$

The above convexity conditions are not required in Lyapunov stability theorems for deterministic systems but are needed here to leverage *Jensen's inequality*, stating that any convex function α of a random variable X satisfies $\alpha(\mathbb{E}(X)) \leq \mathbb{E}(\alpha(X))$ [26, Ch. 3].

Chapter 3

Symmetry-Preserving Reduced-Order Observers

3.1 Introduction

Methods for designing state observers for nonlinear systems are limited, and there are no general techniques that guarantee global convergence of the estimation error as there are in the linear case [130, Ch. 15]. Provably effective state estimation strategies are inevitably limited to special classes of systems. Here, we leverage symmetries in a dynamical system's structure to aid observer design and stability analysis.

As seen in Chapter 2, symmetries are described by the invariance of a system under a Lie group's action. From a Lagrangian perspective, Aghannan and Rouchon [2] leveraged the symmetry inherent in the coordinate-free Euler-Lagrange equations to design a nonlinear observer given measurements of the system's configuration. This idea of leveraging symmetries in the dynamics was generalized by Bonnabel *et al.* to include general nonlinear systems under a Lie group's action [24] as well as systems defined on Lie groups [22]. Thus was laid the foundation for the invariant extended Kalman filter [23], which was shown by Barrau and Bonnabel [20] to be a stable observer. From a closely-related but unique perspective, Mahony *et al.* [100] developed a nonlinear observer for kinematic systems with complete symmetry — that is, systems defined on homogeneous spaces. This work was generalized by Van Goor *et al.* [150] with the equivariant Kalman filter, which applies to general equivariant systems.

Existing approaches to symmetry-preserving observers only consider the *full-order* case, however, in which the entire state of the system is estimated. In many scenarios, part of the system's state may be known with negligible error or may be obtained as the output of an observer whose design is independent of the rest of the system's state. For example, attitude observers for aircraft or spacecraft often do not rely on the rigid body's translational dynamics (e.g., Lefferts *et al.* [94] and Mahony *et al.* [99]). Another example is the problem of wind estimation from aircraft motion (e.g., González-Rocha *et al.* [56] and Chen *et al.* [32]), where the main goal is to obtain estimates of wind and air-relative velocity — not to re-estimate the aircraft's position, attitude, and angular velocity. More generally, the problem of disturbance estimation falls into this category where the internal state of the system is known but the disturbance is not (e.g., Chen and Woolsey [33]). In these scenarios, *reduced-*

order observers, in the sense of Karagiannis and Astolfi [84] and Astolfi *et al.* [12], are of particular interest where only the unmeasured part of the system's state is estimated. The aim of observer design is to render a particular set, characterized by zero state estimation error, positively invariant and globally asymptotically attractive.

This chapter is based on reference [70] and presents a reduced-order observer that is also symmetry-preserving. As detailed in Section 3.2, the state space is separated into measured and unmeasured parts, with the measured part of the state being defined on a smooth manifold. Considering a system that is invariant under the action of a Lie group G, the notion of a moving frame [101], [122] is described in Section 3.3. The moving frame is used as the primary tool to construct a symmetry-preserving reduced-order pre-observer[1] in Section 3.4. The equivariance of the moving frame is leveraged to construct an equivariant map from measurements to the observer's state space. This property is used to prove the dynamics of the state estimate are also invariant under the Lie group's action. Section 3.5 details how this equivariance is further leveraged to find sufficient conditions for the pre-observer to be a stable observer. An application of the observer to rigid body velocity estimation is presented in Section 3.6.

3.2 Problem Statement

Consider a system whose state is given by an unmeasured part, $\boldsymbol{x} \in \mathcal{X} \subset \mathbb{R}^n$, and a measured part, $\boldsymbol{y} \in \mathcal{Y}$. Here, $\mathcal{X}$ is an open subset of $\mathbb{R}^n$ containing the origin and $\mathcal{Y}$ is a p-dimensional smooth manifold. The dynamics of this system are given by

$$\dot{\boldsymbol{x}} = \boldsymbol{f}(\boldsymbol{x}, \boldsymbol{y}, \boldsymbol{u}) \tag{3.1a}$$

$$\dot{\boldsymbol{y}} = \boldsymbol{h}(\boldsymbol{x}, \boldsymbol{y}, \boldsymbol{u}) \tag{3.1b}$$

where $\boldsymbol{u} \in \mathcal{U}$ is the known "input" to the system. It is not necessarily just composed of control inputs, but rather is a known signal on which a particular Lie group acts. Here, the dynamics of the measured part of the state, $\boldsymbol{y}$, may be expressed intrinsically, that is, without specifying a local coordinate chart.

In the language of Karagiannis and Astolfi [84], the dynamical system

$$\dot{\boldsymbol{z}} = \boldsymbol{\alpha}(\boldsymbol{z}, \boldsymbol{y}, \boldsymbol{u}) \tag{3.2}$$

where $\boldsymbol{z} \in \mathbb{R}^{q(\geq n)}$, is called a (global) *reduced-order observer* for $\boldsymbol{x}$ if there exists a smooth manifold

$$\mathcal{Z} = \{(\boldsymbol{x}, \boldsymbol{y}, \boldsymbol{z}) \in \mathcal{X} \times \mathcal{Y} \times \mathbb{R}^q \mid \boldsymbol{\theta}(\boldsymbol{z}, \boldsymbol{y}) = \boldsymbol{\phi}(\boldsymbol{x}, \boldsymbol{y})\} \tag{3.3}$$

defined by smooth mappings $\boldsymbol{\theta}$ and $\boldsymbol{\phi}$ that are left invertible with respect to their first argument, such that $\mathcal{Z}$ is positively invariant and (globally) asymptotically attractive. The estimate of $\boldsymbol{x}$ is then given by

$$\hat{\boldsymbol{x}} = \boldsymbol{\phi}^{(\mathrm{L},\cdot)}(\boldsymbol{\theta}(\boldsymbol{z}, \boldsymbol{y}), \boldsymbol{y}) \tag{3.4}$$

[1] Briefly, a pre-observer is an observer for which there is not (yet) any claim about error convergence.

where $\boldsymbol{\phi}^{(\mathrm{L},\cdot)}$ denotes the functional left inverse of $\boldsymbol{\phi}$ with respect to its first argument — i.e., $\boldsymbol{\phi}^{(\mathrm{L},\cdot)}(\boldsymbol{\phi}(\boldsymbol{x},\boldsymbol{y}),\boldsymbol{y}) = \boldsymbol{x}$.

Our aim is to construct the vector field $\boldsymbol{\alpha}$ and mappings $\boldsymbol{\phi}$ and $\boldsymbol{\theta}$ by leveraging symmetries in the dynamics (3.1). Therefore, we consider systems of the form (3.1) that possess symmetries; that is, they are invariant under a Lie group's action.

Assumption 3.1. *The system (3.1) is G-invariant with respect to the transformation group $\{(\boldsymbol{\varphi}_g(\boldsymbol{x}), \boldsymbol{\varrho}_g(\boldsymbol{y}), \boldsymbol{\psi}_g(\boldsymbol{u}))\}_{g\in G}$, where G is an r-dimensional Lie group and $\boldsymbol{\varphi}_g(\boldsymbol{x})$ is linear in $\boldsymbol{x}$.*

This assumption implies that

$$\mathrm{T}_{\boldsymbol{x}}\boldsymbol{\varphi}_g\big(\boldsymbol{f}(\boldsymbol{x},\boldsymbol{y},\boldsymbol{u})\big) = \boldsymbol{f}(\boldsymbol{\varphi}_g(\boldsymbol{x}), \boldsymbol{\varrho}_g(\boldsymbol{y}), \boldsymbol{\psi}_g(\boldsymbol{u})) \tag{3.5}$$

$$\mathrm{T}_{\boldsymbol{y}}\boldsymbol{\varrho}_g\big(\boldsymbol{h}(\boldsymbol{x},\boldsymbol{y},\boldsymbol{u})\big) = \boldsymbol{h}(\boldsymbol{\varphi}_g(\boldsymbol{x}), \boldsymbol{\varrho}_g(\boldsymbol{y}), \boldsymbol{\psi}_g(\boldsymbol{u})) \tag{3.6}$$

in reference to Section 2.3.

3.3 The Moving Frame

Similar to Bonnabel *et al.* [24], the primary tool which we use to construct a reduced-order observer for systems (3.1) satisfying Assumption 3.1 is the moving frame [122]. In the words of Mansfield and Zhao [101], the moving frame aims at the following:

> "Given the Lie group action, derive the invariants and their relationships algorithmically, that is, without prior knowledge of 100 years of differential geometry, and with minimal effort."

The moving frame is intimately tied to how G-orbits relate to the composition of Lie group actions. For the observer considered here, we only need to consider the transformation on the measured part of the state, $\boldsymbol{\varrho}_g(\boldsymbol{y})$. Therefore, it is sufficient to consider a *moving frame* to be a mapping $\gamma : \mathcal{Y} \to G$ that has the equivariance property (2.4), now written in terms of the measured part of the state as

$$\gamma(\boldsymbol{\varrho}_g(\boldsymbol{y})) * g = \gamma(\boldsymbol{y}) \tag{3.7}$$

As illustrated in Figure 3.1, a *moving frame* is a map $\gamma : \mathcal{Y} \to G$ that has the equivariance property (2.4). It may be associated with a $(p-r)$-dimensional coordinate cross-section $\mathcal{K}$ that transversely intersects G-orbits on $\mathcal{Y}$.

We construct a moving frame according to the methods presented by Olver [122], which are also given in tutorial format by Mansfield and Zhao [101]. Suppose the r-dimensional Lie group G *acts freely* on the p-dimensional manifold $\mathcal{Y}$; that is, $\boldsymbol{\varrho}_g(\boldsymbol{y}) = \boldsymbol{y}$ implies g is the identity element, e. For fixed $\boldsymbol{y} \in \mathcal{Y}$, the map $\boldsymbol{\varrho}_{(\cdot)}(\boldsymbol{y}) : G \to \mathcal{Y}$ is non-surjective, only mapping to points on the G-orbit of $\boldsymbol{y}$ (the red dashed line in Figure 3.1). However, one can identify the r-dimensional part $\bar{\boldsymbol{\varrho}}_{(\cdot)}(\boldsymbol{y})$ of the map $\boldsymbol{\varrho}_{(\cdot)}(\boldsymbol{y})$ that is invertible (i.e., bijective). As depicted in Figure 3.1, one can select a constant $\boldsymbol{k}$ in the image of $\bar{\boldsymbol{\varrho}}$ that defines the

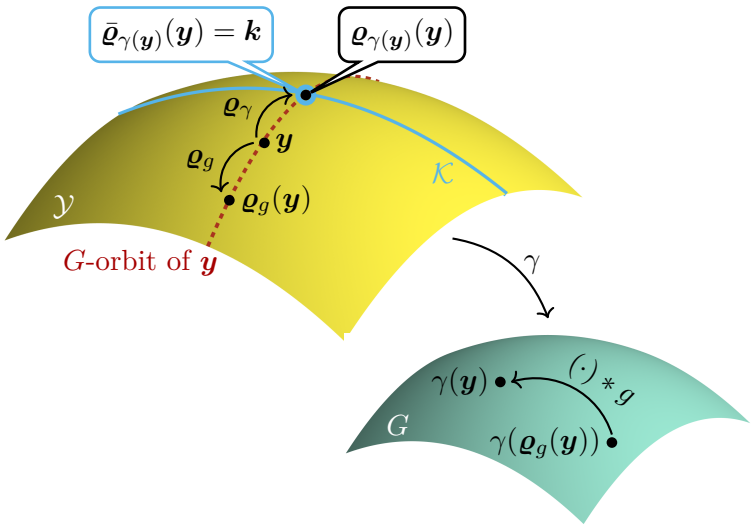

Figure 3.1: Equivariance of the moving frame γ and its construction via the cross-section $\mathcal{K}$

unique point at which the G-orbit of a generic point $\boldsymbol{y}$ intersects the $(p-r)$-dimensional cross-section

$$\mathcal{K} = \{\boldsymbol{y} \in \mathcal{Y} \mid \bar{\boldsymbol{\varrho}}_e(\boldsymbol{y}) = \boldsymbol{k}\}$$

In other words, the moving frame is obtained by solving the *normalization equation*

$$\bar{\boldsymbol{\varrho}}_h(\boldsymbol{y}) = \boldsymbol{k} \tag{3.8}$$

for $h \in G$. The solution $h = \gamma(\boldsymbol{y})$ defines the moving frame $\gamma : \mathcal{Y} \to G$.

3.4 Invariant Reduced-Order Pre-Observer

It can now be described what it means for a reduced-order observer to be symmetry-preserving under the transformation group considered in Assumption 3.1. We postulate the form of an observer for the unmeasured part of the state, $\boldsymbol{x}$, that preserves invariance of the state estimate dynamics. Inspired by Bonnabel *et al.* [24] and Karagiannis and Astolfi [84], consider the following definition.

Definition 3.1 (G-invariant reduced-order pre-observer)**.** *The dynamical system*

$$\dot{\boldsymbol{z}} = \boldsymbol{\alpha}(\boldsymbol{z}, \boldsymbol{y}, \boldsymbol{u}) \tag{3.9}$$

with output

$$\hat{\boldsymbol{x}} = \boldsymbol{z} + \boldsymbol{\beta}(\boldsymbol{y}) \tag{3.10}$$

for some smooth map $\boldsymbol{\beta} : \mathcal{Y} \to \mathcal{X}$ is a G-invariant reduced-order pre-observer *if the system*

$$\dot{\hat{\boldsymbol{x}}} = \boldsymbol{\alpha}(\hat{\boldsymbol{x}} - \boldsymbol{\beta}(\boldsymbol{y}), \boldsymbol{y}, \boldsymbol{u}) + \mathrm{T}_{\boldsymbol{y}}\boldsymbol{\beta}\big(\boldsymbol{h}(\boldsymbol{x}, \boldsymbol{y}, \boldsymbol{u})\big) \tag{3.11}$$

is G-invariant and the manifold

$$\mathcal{Z} = \{(\boldsymbol{z}, \boldsymbol{x}, \boldsymbol{y}) \in \mathcal{X} \times \mathcal{X} \times \mathcal{Y} \mid \boldsymbol{z} = \boldsymbol{x} - \boldsymbol{\beta}(\boldsymbol{y})\} \tag{3.12}$$

is positively invariant. A G-invariant pre-observer is a G-invariant observer *if $\mathcal{Z}$ is asymptotically attractive.*

This prescription of the *zero-error manifold* $\mathcal{Z}$ is not quite as general as the case described by Astolfi *et al.* [12]. We instead consider the condition that defines $\mathcal{Z}$ to be linear in $\boldsymbol{z}$ and $\boldsymbol{x}$ (and for $\boldsymbol{z}$ to be the same dimension as $\boldsymbol{x}$). In other words, we choose $\boldsymbol{\theta}(\boldsymbol{z}, \boldsymbol{y}) = \boldsymbol{z}$ and $\boldsymbol{\phi}(\boldsymbol{x}, \boldsymbol{y}) = \boldsymbol{x} - \boldsymbol{\beta}(\boldsymbol{y})$ in Eq. (3.3). This simplification reveals an intuitive choice for $\boldsymbol{\beta}$ in the following lemma based on the underlying geometry.

Lemma 3.1. *Suppose there exists a moving frame $\gamma : \mathcal{Y} \to G$ that only depends on $\boldsymbol{y} \in \mathcal{Y}$, and let $\boldsymbol{\ell} : \mathcal{Y} \to \mathcal{X}$ be a smooth map (called the* gain map*). If*

$$\boldsymbol{\beta}(\boldsymbol{y}) = \boldsymbol{\varphi}_{\gamma(\boldsymbol{y})^{-1}}\Big(\boldsymbol{\ell}\big(\boldsymbol{\varrho}_{\gamma(\boldsymbol{y})}(\boldsymbol{y})\big)\Big) \tag{3.13}$$

then the following commutative identities (illustrated in Figure 3.2) hold for all $g \in G$ and $\boldsymbol{y} \in \mathcal{Y}$:

$$\boldsymbol{\beta}(\boldsymbol{\varrho}_g(\boldsymbol{y})) = \boldsymbol{\varphi}_g(\boldsymbol{\beta}(\boldsymbol{y})) \tag{3.14}$$

$$\mathrm{T}_{\boldsymbol{\varrho}_g(\boldsymbol{y})}\boldsymbol{\beta} \circ \mathrm{T}_{\boldsymbol{y}}\boldsymbol{\varrho}_g = \mathrm{T}_{\boldsymbol{\beta}(\boldsymbol{y})}\boldsymbol{\varphi}_g \circ \mathrm{T}_{\boldsymbol{y}}\boldsymbol{\beta} \tag{3.15}$$

In other words, $\boldsymbol{\beta}$ commutes with the transformation group.

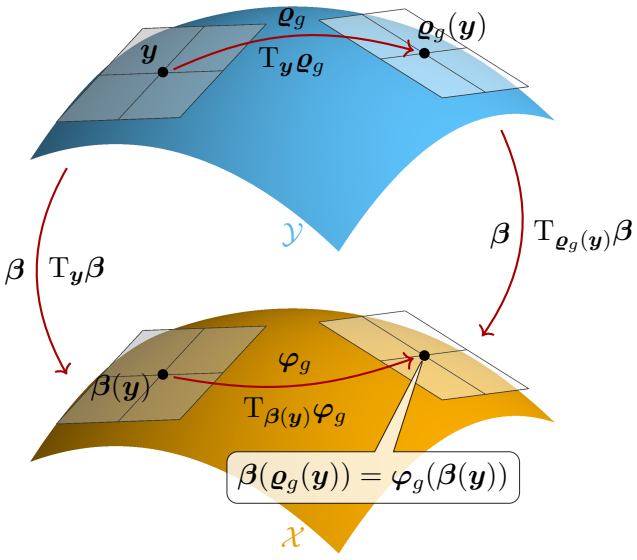

Figure 3.2: Commutative relationship between $\boldsymbol{\beta}$ and the transformation group

Proof. Beginning with the definition of $\boldsymbol{\beta}$, we have

$$\boldsymbol{\beta}(\boldsymbol{\varrho}_g(\boldsymbol{y})) = \boldsymbol{\varphi}_{\gamma(\boldsymbol{\varrho}_g(\boldsymbol{y}))^{-1}}\Big(\boldsymbol{\ell}\big(\boldsymbol{\varrho}_{\gamma(\boldsymbol{\varrho}_g(\boldsymbol{y}))}(\boldsymbol{\varrho}_g(\boldsymbol{y}))\big)\Big)$$

By the equivariance property (2.4) of the moving frame,

$$\boldsymbol{\beta}(\boldsymbol{\varrho}_g(\boldsymbol{y})) = \boldsymbol{\varphi}_{(\gamma * g^{-1})^{-1}}\Big(\boldsymbol{\ell}\big(\boldsymbol{\varrho}_{\gamma * g^{-1}}(\boldsymbol{\varrho}_g(\boldsymbol{y}))\big)\Big)$$

Using the composition properties for group elements and group actions,

$$\begin{aligned}\boldsymbol{\beta}(\boldsymbol{\varrho}_g(\boldsymbol{y})) &= \boldsymbol{\varphi}_{g*\gamma^{-1}}\Big(\boldsymbol{\ell}\big(\boldsymbol{\varrho}_{\gamma * g^{-1} * g}(\boldsymbol{y})\big)\Big)\\ &= \boldsymbol{\varphi}_g\Big(\boldsymbol{\varphi}_{\gamma^{-1}}\big(\boldsymbol{\ell}\big(\boldsymbol{\varrho}_{\gamma}(\boldsymbol{y})\big)\big)\Big)\\ &= \boldsymbol{\varphi}_g(\boldsymbol{\beta}(\boldsymbol{y}))\end{aligned}$$

Finally, (3.15) follows directly from the properties of the tangent map. □

Using Lemma 3.1, a G-invariant pre-observer is readily constructed for a system satisfying Assumption 3.1.

Theorem 3.1. *Suppose Assumption 3.1 and the conditions of Lemma 3.1 hold. Let the vector field* $\boldsymbol{\alpha}(\cdot, \boldsymbol{y}, \boldsymbol{u}) : \mathcal{X} \to \mathsf{T}\mathcal{X}$ *be defined by*

$$\boldsymbol{\alpha}(\boldsymbol{z}, \boldsymbol{y}, \boldsymbol{u}) = \boldsymbol{f}(\boldsymbol{z} + \boldsymbol{\beta}(\boldsymbol{y}), \boldsymbol{y}, \boldsymbol{u}) - \mathrm{T}_{\boldsymbol{y}}\boldsymbol{\beta}\big(\boldsymbol{h}(\boldsymbol{z} + \boldsymbol{\beta}(\boldsymbol{y}), \boldsymbol{y}, \boldsymbol{u})\big) \tag{3.16}$$

Then, the dynamical system

$$\dot{\boldsymbol{z}} = \boldsymbol{\alpha}(\boldsymbol{z}, \boldsymbol{y}, \boldsymbol{u}) \tag{3.17}$$

with output

$$\hat{\boldsymbol{x}} = \boldsymbol{z} + \boldsymbol{\beta}(\boldsymbol{y}) \tag{3.18}$$

is a G-invariant, reduced-order pre-observer.

Proof. We begin by showing invariance of the state estimate dynamics (3.11). Define

$$\boldsymbol{F}(\hat{\boldsymbol{x}}, \boldsymbol{x}, \boldsymbol{y}, \boldsymbol{u}) = \boldsymbol{\alpha}(\hat{\boldsymbol{x}} - \boldsymbol{\beta}(\boldsymbol{y}), \boldsymbol{y}, \boldsymbol{u}) + \mathrm{T}_{\boldsymbol{y}}\boldsymbol{\beta}\big(\boldsymbol{h}(\boldsymbol{x}, \boldsymbol{y}, \boldsymbol{u})\big)$$

Then,

$$\mathrm{T}_{\hat{\boldsymbol{x}}}\boldsymbol{\varphi}_g\big(\boldsymbol{F}(\hat{\boldsymbol{x}}, \boldsymbol{x}, \boldsymbol{y}, \boldsymbol{u})\big) = \mathrm{T}_{\hat{\boldsymbol{x}}}\boldsymbol{\varphi}_g\big(\boldsymbol{f}(\hat{\boldsymbol{x}}, \boldsymbol{y}, \boldsymbol{u})\big) - \big(\mathrm{T}_{\hat{\boldsymbol{x}}}\boldsymbol{\varphi}_g \circ \mathrm{T}_{\boldsymbol{y}}\boldsymbol{\beta}\big)\big(\boldsymbol{h}(\hat{\boldsymbol{x}}, \boldsymbol{y}, \boldsymbol{u}) - \boldsymbol{h}(\boldsymbol{x}, \boldsymbol{y}, \boldsymbol{u})\big)$$

The assumed linearity of $\boldsymbol{\varphi}_g$ implies $\mathrm{T}_{\boldsymbol{x}}\boldsymbol{\varphi}_g$ does not depend on the choice of base point $\boldsymbol{x}$. Therefore, $\mathrm{T}_{\hat{\boldsymbol{x}}}\boldsymbol{\varphi}_g = \mathrm{T}_{\boldsymbol{\beta}(\boldsymbol{y})}\boldsymbol{\varphi}_g$, and Lemma 3.1 can be used along with the invariance of $\boldsymbol{f}$ to obtain

$$\mathrm{T}_{\hat{\boldsymbol{x}}}\boldsymbol{\varphi}_g\big(\boldsymbol{F}(\hat{\boldsymbol{x}}, \boldsymbol{x}, \boldsymbol{y}, \boldsymbol{u})\big) = \boldsymbol{f}(\boldsymbol{\varphi}_g(\hat{\boldsymbol{x}}), \boldsymbol{\varrho}_g(\boldsymbol{y}), \boldsymbol{\psi}_g(\boldsymbol{u})) - \big(\mathrm{T}_{\boldsymbol{\varrho}_g(\boldsymbol{y})}\boldsymbol{\beta} \circ \mathrm{T}_{\boldsymbol{y}}\boldsymbol{\varrho}_g\big)\big(\boldsymbol{h}(\hat{\boldsymbol{x}}, \boldsymbol{y}, \boldsymbol{u}) - \boldsymbol{h}(\boldsymbol{x}, \boldsymbol{y}, \boldsymbol{u})\big)$$

Since $\boldsymbol{h}$ is also G-invariant, we have

$$\mathrm{T}_{\hat{\boldsymbol{x}}}\boldsymbol{\varphi}_g\big(\boldsymbol{F}(\hat{\boldsymbol{x}},\boldsymbol{x},\boldsymbol{y},\boldsymbol{u})\big) = \boldsymbol{f}(\boldsymbol{\varphi}_g(\hat{\boldsymbol{x}}),\boldsymbol{\varrho}_g(\boldsymbol{y}),\boldsymbol{\psi}_g(\boldsymbol{u})) - \mathrm{T}_{\boldsymbol{\varrho}_g(\boldsymbol{y})}\boldsymbol{\beta}\big(\boldsymbol{h}(\boldsymbol{\varphi}_g(\hat{\boldsymbol{x}}),\boldsymbol{\varrho}_g(\boldsymbol{y}),\boldsymbol{\psi}_g(\boldsymbol{u})) - \boldsymbol{h}(\boldsymbol{\varphi}_g(\boldsymbol{x}),\boldsymbol{\varrho}_g(\boldsymbol{y}),\boldsymbol{\psi}_g(\boldsymbol{u}))\big)$$

By Lemma 3.1, recognize that

$$\boldsymbol{\varphi}_g(\hat{\boldsymbol{x}}) = \boldsymbol{\varphi}_g(\boldsymbol{z}) + \boldsymbol{\beta}(\boldsymbol{\varrho}_g(\boldsymbol{y}))$$

Then, it follows that

$$\mathrm{T}_{\hat{\boldsymbol{x}}}\boldsymbol{\varphi}_g\big(\boldsymbol{F}(\hat{\boldsymbol{x}},\boldsymbol{x},\boldsymbol{y},\boldsymbol{u})\big) = \boldsymbol{\alpha}(\boldsymbol{\varphi}_g(\hat{\boldsymbol{x}}) - \boldsymbol{\beta}(\boldsymbol{\varrho}_g(\boldsymbol{y})),\boldsymbol{\varrho}_g(\boldsymbol{y}),\boldsymbol{\psi}_g(\boldsymbol{u})) + \mathrm{T}_{\boldsymbol{\varrho}_g(\boldsymbol{y})}\boldsymbol{\beta}\big(\boldsymbol{h}(\boldsymbol{\varphi}_g(\boldsymbol{x}),\boldsymbol{\varrho}_g(\boldsymbol{y}),\boldsymbol{\psi}_g(\boldsymbol{u}))\big)$$

Therefore,

$$\mathrm{T}_{\hat{\boldsymbol{x}}}\boldsymbol{\varphi}_g\big(\boldsymbol{F}(\hat{\boldsymbol{x}},\boldsymbol{x},\boldsymbol{y},\boldsymbol{u})\big) = \boldsymbol{F}(\boldsymbol{\varphi}_g(\hat{\boldsymbol{x}}),\boldsymbol{\varphi}_g(\boldsymbol{x}),\boldsymbol{\varrho}_g(\boldsymbol{y}),\boldsymbol{\psi}_g(\boldsymbol{u}))$$

That is, the system (3.16)–(3.18) is G-invariant. Next, we show the zero error manifold $\mathcal{Z}$ given in (3.12) is positively invariant. Since $\boldsymbol{z} - \boldsymbol{x} + \boldsymbol{\beta}(\boldsymbol{y}) = \boldsymbol{0}$ on $\mathcal{Z}$, we verify that

$$\begin{aligned}
&\boldsymbol{\alpha}(\boldsymbol{x} - \boldsymbol{\beta}(\boldsymbol{y}),\boldsymbol{y},\boldsymbol{u}) - \boldsymbol{f}(\boldsymbol{x},\boldsymbol{y},\boldsymbol{u}) + \mathrm{T}_{\boldsymbol{y}}\boldsymbol{\beta}\big(\boldsymbol{h}(\boldsymbol{x},\boldsymbol{y},\boldsymbol{u})\big)\\
&\quad = \boldsymbol{f}(\boldsymbol{x},\boldsymbol{y},\boldsymbol{u}) - \mathrm{T}_{\boldsymbol{y}}\boldsymbol{\beta}\big(\boldsymbol{h}(\boldsymbol{x},\boldsymbol{y},\boldsymbol{u})\big) - \boldsymbol{f}(\boldsymbol{x},\boldsymbol{y},\boldsymbol{u}) + \mathrm{T}_{\boldsymbol{y}}\boldsymbol{\beta}\big(\boldsymbol{h}(\boldsymbol{x},\boldsymbol{y},\boldsymbol{u})\big)\\
&\quad = \boldsymbol{0}
\end{aligned}$$

Thus, referring to (3.17), trajectories originating in $\mathcal{Z}$ remain in $\mathcal{Z}$. It follows that (3.16)-(3.18) is a G-invariant reduced-order pre-observer. □

As an improvement over the general reduced-order observer described in Section 3.2, Theorem 3.1 leverages symmetry to construct a reduced-order pre-observer. The functions $\boldsymbol{\theta}$, $\boldsymbol{\phi}$, and $\boldsymbol{\alpha}$ in Eqs. (3.2)–(3.4) are formulated using the moving frame γ. The equivariance of the moving frame is the key property that makes this pre-observer G-invariant.

3.5 Invariant Reduced-Order Observer

We now aim to find sufficient conditions for the pre-observer in Theorem 3.1 to be a G-invariant reduced-order *observer*. That is, we seek conditions under which $\mathcal{Z}$ is asymptotically attractive. Like Bonnabel *et al.* [24], consider error coordinates that are G-invariant. Specifically, take

$$\boldsymbol{\eta}(\boldsymbol{z},\boldsymbol{x},\boldsymbol{y}) = \boldsymbol{\varphi}_{\gamma(\boldsymbol{y})}(\boldsymbol{z}) + \boldsymbol{\ell}(\boldsymbol{\varrho}_{\gamma(\boldsymbol{y})}(\boldsymbol{y})) - \boldsymbol{\varphi}_{\gamma(\boldsymbol{y})}(\boldsymbol{x}) \tag{3.19}$$

The invariant coordinates $\boldsymbol{\eta}$ are non-zero if and only if $(\boldsymbol{z},\boldsymbol{x},\boldsymbol{y}) \notin \mathcal{Z}$. Thus, $\boldsymbol{\eta} \to \boldsymbol{0}$ as $t \to \infty$ implies $\mathcal{Z}$ is asymptotically attractive. Let $\boldsymbol{X} = \boldsymbol{\varphi}_{\gamma(\boldsymbol{y})}(\boldsymbol{x})$, $\boldsymbol{Y} = \boldsymbol{\varrho}_{\gamma(\boldsymbol{y})}(\boldsymbol{y})$, and $\boldsymbol{U} = \boldsymbol{\psi}_{\gamma(\boldsymbol{y})}(\boldsymbol{u})$. Using the moving frame to define these transformed points means $(\boldsymbol{X},\boldsymbol{Y},\boldsymbol{U})$ constitutes

a complete set of invariants [122, Ch. 8]. As will be shown shortly, the stability of the pre-observer (3.17) depends only on $\boldsymbol{\eta}$ and the invariants $\boldsymbol{X}$, $\boldsymbol{Y}$, and $\boldsymbol{Z}$ (see Remark 3.1).

To derive sufficient conditions for asymptotic stability, we will make use of the following result.

Lemma 3.2. *Let $\boldsymbol{\lambda} : \mathcal{Y} \to \mathcal{X}$ be the map*

$$\boldsymbol{\lambda}(\boldsymbol{y}; \boldsymbol{\xi}) = \boldsymbol{\varphi}_{\gamma(\boldsymbol{y})}(\boldsymbol{\xi})$$

where $\boldsymbol{\xi} \in \mathcal{X}$ is held constant. Then,

$$\mathrm{T}_{(\boldsymbol{y};\boldsymbol{\varphi}_{g^{-1}}(\boldsymbol{\zeta}))}\boldsymbol{\lambda}\big(\boldsymbol{h}(\boldsymbol{x},\boldsymbol{y},\boldsymbol{u})\big) = \mathrm{T}_{(\boldsymbol{\varrho}_g(\boldsymbol{y});\boldsymbol{\zeta})}\boldsymbol{\lambda}\big(\boldsymbol{h}(\boldsymbol{\varphi}_g(\boldsymbol{x}),\boldsymbol{\varrho}_g(\boldsymbol{y}),\boldsymbol{\psi}_g(\boldsymbol{u}))\big) \tag{3.20}$$

for any $g \in G$ and $\boldsymbol{\zeta} \in \mathcal{X}$.

The following proof of Lemma 3.2 is illustrated in Figure 3.3.

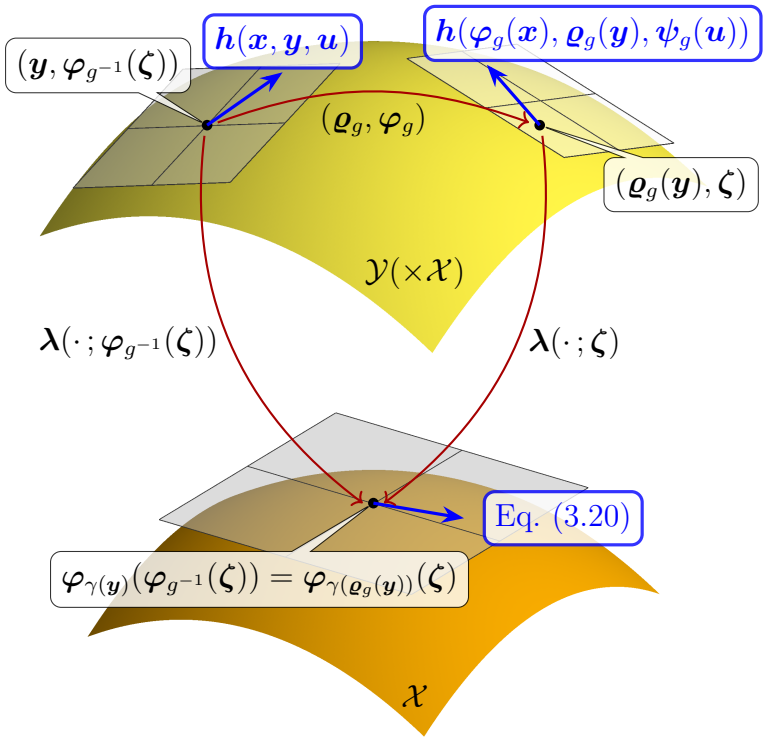

Figure 3.3: Invariance of $\boldsymbol{\lambda}$ and its tangent map

Proof. First, we recognize $\boldsymbol{\lambda}$ is invariant since

$$\begin{aligned}
\boldsymbol{\lambda}(\boldsymbol{\varrho}_g(\boldsymbol{y}); \boldsymbol{\varphi}_g(\boldsymbol{\xi})) &= \boldsymbol{\varphi}_{\gamma(\boldsymbol{\varrho}_g(\boldsymbol{y}))}(\boldsymbol{\varphi}_g(\boldsymbol{\xi})) \\
&= \boldsymbol{\varphi}_{\gamma(\boldsymbol{y})*g^{-1}}(\boldsymbol{\varphi}_g(\boldsymbol{\xi})) \\
&= \boldsymbol{\varphi}_{\gamma(\boldsymbol{y})}(\boldsymbol{\xi}) \\
&= \boldsymbol{\lambda}(\boldsymbol{y}; \boldsymbol{\xi})
\end{aligned}$$

for any $\boldsymbol{\xi} \in \mathcal{X}$, where we again use the equivariance of the moving frame γ. Therefore,

$$\boldsymbol{\lambda}(\boldsymbol{y}; \boldsymbol{\varphi}_{g^{-1}}(\boldsymbol{\zeta})) = \boldsymbol{\lambda}(\boldsymbol{\varrho}_g(\boldsymbol{y}); \boldsymbol{\zeta})$$

for any $\boldsymbol{\zeta} \in \mathcal{X}$. Since $\boldsymbol{\lambda}(\boldsymbol{\varrho}_g(\boldsymbol{y}); \boldsymbol{\zeta})$ is a composition of maps, it follows that

$$\mathrm{T}_{(\boldsymbol{y};\boldsymbol{\varphi}_{g^{-1}}(\boldsymbol{\zeta}))}\boldsymbol{\lambda} = \mathrm{T}_{(\boldsymbol{\varrho}_g(\boldsymbol{y});\boldsymbol{\zeta})}\boldsymbol{\lambda} \circ \mathrm{T}_{\boldsymbol{y}}\boldsymbol{\varrho}_g$$

Applying this tangent map to the G-invariant vector field $\boldsymbol{h}$, we obtain

$$\begin{aligned}\mathrm{T}_{(\boldsymbol{y};\boldsymbol{\varphi}_{g^{-1}}(\boldsymbol{\zeta}))}\boldsymbol{\lambda}\big(\boldsymbol{h}(\boldsymbol{x},\boldsymbol{y},\boldsymbol{u})\big) &= \big(\mathrm{T}_{(\boldsymbol{\varrho}_g(\boldsymbol{y});\boldsymbol{\zeta})}\boldsymbol{\lambda} \circ \mathrm{T}_{\boldsymbol{y}}\boldsymbol{\varrho}_g\big)\big(\boldsymbol{h}(\boldsymbol{x},\boldsymbol{y},\boldsymbol{u})\big) \\ &= \mathrm{T}_{(\boldsymbol{\varrho}_g(\boldsymbol{y});\boldsymbol{\zeta})}\boldsymbol{\lambda}\big(\boldsymbol{h}(\boldsymbol{\varphi}_g(\boldsymbol{x}), \boldsymbol{\varrho}_g(\boldsymbol{y}), \boldsymbol{\psi}_g(\boldsymbol{u}))\big)\end{aligned}$$

which verifies Eq. (3.20). □

Finally, sufficient conditions for (3.17) to be a G-invariant reduced-order observer are given as follows.

Theorem 3.2. *Suppose the assumptions of Theorem 3.1 hold. The G-invariant pre-observer (3.17) is a G-invariant observer if the origin $\boldsymbol{\eta} = \mathbf{0}$ of the* invariant error system

$$\begin{aligned}\dot{\boldsymbol{\eta}} = \boldsymbol{f}(\boldsymbol{X}+\boldsymbol{\eta},\boldsymbol{Y},\boldsymbol{U}) - \boldsymbol{f}(\boldsymbol{X},\boldsymbol{Y},\boldsymbol{U}) \\ - \mathrm{T}_{\boldsymbol{Y}}\boldsymbol{\beta}\big(\boldsymbol{h}(\boldsymbol{X}+\boldsymbol{\eta},\boldsymbol{Y},\boldsymbol{U}) - \boldsymbol{h}(\boldsymbol{X},\boldsymbol{Y},\boldsymbol{U})\big) + \mathrm{T}_{(\boldsymbol{Y};\boldsymbol{\eta})}\boldsymbol{\lambda}\big(\boldsymbol{h}(\boldsymbol{X},\boldsymbol{Y},\boldsymbol{U})\big)\end{aligned} \tag{3.21}$$

is asymptotically stable uniformly in $\boldsymbol{X}$, $\boldsymbol{Y}$, and $\boldsymbol{U}$.

Proof. By definition, the pre-observer (3.17) is an observer if the zero error manifold $\mathcal{Z}$ is positively invariant and asymptotically attractive or, equivalently, if the state estimation error dynamics have a globally asymptotically stable equilibrium at the origin $\boldsymbol{\eta} = \mathbf{0}$. It remains for us to show that the estimation error dynamics are given by the invariant error system (3.21). Since $\boldsymbol{\varphi}_g(\boldsymbol{x})$ is linear in $\boldsymbol{x}$, we can write

$$\boldsymbol{\eta} = \boldsymbol{\varphi}_{\gamma(\boldsymbol{y})}(\boldsymbol{z} + \boldsymbol{\beta}(\boldsymbol{y})) - \boldsymbol{\varphi}_{\gamma(\boldsymbol{y})}(\boldsymbol{x})$$

Thus, the time derivative of $\boldsymbol{\eta}$ satisfies

$$\begin{aligned}\dot{\boldsymbol{\eta}} = \mathrm{T}_{(\boldsymbol{z}+\boldsymbol{\beta}(\boldsymbol{y}))}\boldsymbol{\varphi}_{\gamma(\boldsymbol{y})}\Big(\boldsymbol{\alpha}(\boldsymbol{z},\boldsymbol{y},\boldsymbol{u}) + \mathrm{T}_{\boldsymbol{y}}\boldsymbol{\beta}\big(\boldsymbol{h}(\boldsymbol{x},\boldsymbol{y},\boldsymbol{u})\big)\Big) \\ - \mathrm{T}_{\boldsymbol{x}}\boldsymbol{\varphi}_{\gamma(\boldsymbol{y})}\big(\boldsymbol{f}(\boldsymbol{x},\boldsymbol{y},\boldsymbol{u})\big) + \mathrm{T}_{(\boldsymbol{y};\boldsymbol{z}+\boldsymbol{\beta}(\boldsymbol{y})-\boldsymbol{x})}\boldsymbol{\lambda}\big(\boldsymbol{h}(\boldsymbol{x},\boldsymbol{y},\boldsymbol{u})\big)\end{aligned}$$

Substituting the definition of $\boldsymbol{\alpha}$ from Theorem 3.1 and again using the linearity of $\boldsymbol{\varphi}_g(\cdot)$, we have

$$\begin{aligned}\dot{\boldsymbol{\eta}} = \mathrm{T}_{(\boldsymbol{z}+\boldsymbol{\beta}(\boldsymbol{y}))}\boldsymbol{\varphi}_{\gamma(\boldsymbol{y})}\big(\boldsymbol{f}(\boldsymbol{z}+\boldsymbol{\beta}(\boldsymbol{y}),\boldsymbol{y},\boldsymbol{u})\big) - \mathrm{T}_{\boldsymbol{x}}\boldsymbol{\varphi}_{\gamma(\boldsymbol{y})}\big(\boldsymbol{f}(\boldsymbol{x},\boldsymbol{y},\boldsymbol{u})\big) \\ - \big(\mathrm{T}_{\boldsymbol{\beta}(\boldsymbol{y})}\boldsymbol{\varphi}_{\gamma(\boldsymbol{y})} \circ \mathrm{T}_{\boldsymbol{y}}\boldsymbol{\beta}\big)\big(\boldsymbol{h}(\boldsymbol{z}+\boldsymbol{\beta}(\boldsymbol{y}),\boldsymbol{y},\boldsymbol{u}) - \boldsymbol{h}(\boldsymbol{x},\boldsymbol{y},\boldsymbol{u})\big) + \mathrm{T}_{(\boldsymbol{y};\boldsymbol{z}+\boldsymbol{\beta}(\boldsymbol{y})-\boldsymbol{x})}\boldsymbol{\lambda}\big(\boldsymbol{h}(\boldsymbol{x},\boldsymbol{y},\boldsymbol{u})\big)\end{aligned}$$

Applying the invariance of $\boldsymbol{f}$ and $\boldsymbol{h}$ through the use of Lemma 3.1 yields

$$\begin{aligned}\dot{\boldsymbol{\eta}} = \boldsymbol{f}\big(\boldsymbol{\varphi}_{\gamma(\boldsymbol{y})}(\boldsymbol{z}+\boldsymbol{\beta}(\boldsymbol{y})),\boldsymbol{Y},\boldsymbol{U}\big) - \boldsymbol{f}\big(\boldsymbol{X},\boldsymbol{Y},\boldsymbol{U}\big) \\ - \mathrm{T}_{\boldsymbol{Y}}\boldsymbol{\beta}\Big(\boldsymbol{h}\big(\boldsymbol{\varphi}_{\gamma(\boldsymbol{y})}(\boldsymbol{z}+\boldsymbol{\beta}(\boldsymbol{y})),\boldsymbol{Y},\boldsymbol{U}\big) - \boldsymbol{h}\big(\boldsymbol{X},\boldsymbol{Y},\boldsymbol{U}\big)\Big) \\ + \mathrm{T}_{(\boldsymbol{y};\boldsymbol{z}+\boldsymbol{\beta}(\boldsymbol{y})-\boldsymbol{x})}\boldsymbol{\lambda}\big(\boldsymbol{h}(\boldsymbol{x},\boldsymbol{y},\boldsymbol{u})\big)\end{aligned}$$

Notice the last term in the above equation can also be written as

$$\mathrm{T}_{(\boldsymbol{y};\boldsymbol{\varphi}_{\gamma(\boldsymbol{y})^{-1}}(\boldsymbol{\eta}))}\boldsymbol{\lambda}\big(\boldsymbol{h}(\boldsymbol{x},\boldsymbol{y},\boldsymbol{u})\big)$$

Therefore, we can use Lemma 3.2 along with a substitution of

$$\boldsymbol{z} = \boldsymbol{\varphi}_{\gamma(\boldsymbol{y})^{-1}}(\boldsymbol{\eta}) - \boldsymbol{\beta}(\boldsymbol{y}) + \boldsymbol{x}$$

to obtain Eq. (3.21). □

Theorem 3.2 states sufficient conditions for the reduced-order pre-observer constructed in Theorem 3.1 to be an asymptotically stable observer. In particular, the error system (3.21) is G-invariant, meaning stability can be equivalently analyzed under arbitrary transformation by the Lie group's action.

Remark 3.1. *The error system* (3.21) *depends only on the invariant error* $\boldsymbol{\eta}$ *and the invariants* $\boldsymbol{X}$, $\boldsymbol{Y}$, *and* $\boldsymbol{U}$, *which can be reduced to a set of* $n+p-r$ *functionally independent invariants,* $\boldsymbol{I}(\boldsymbol{x},\boldsymbol{y},\boldsymbol{u})$ *[122, Ch. 8]. This observation is consistent with the full-order case considered by Bonnabel* et al. *[24, Theorem 3].*

3.6 Example: Rigid-Body Velocity Observer

Consider a rigid aircraft instrumented with an accelerometer, gyroscope, magnetometer, and GNSS receiver such that its position $\boldsymbol{q}$ and attitude rotation matrix $\boldsymbol{R}_{\mathrm{IB}}$ are known without error. Furthermore, assume the angular velocity $\boldsymbol{\omega}$ and body-frame specific force $\boldsymbol{a}$ (obtained from filtered accelerometer readings) are available as inputs for the observer design. However, suppose that the body velocity $\boldsymbol{v}$ is not directly measured. The aim is to design a reduced-order velocity observer for the system

$$\begin{aligned}\underbrace{\dot{\boldsymbol{v}}}_{\dot{\boldsymbol{x}}} &= \underbrace{\boldsymbol{v}\times\boldsymbol{\omega} + \boldsymbol{R}_{\mathrm{IB}}^{\mathsf{T}}\boldsymbol{g} + \boldsymbol{a}}_{\boldsymbol{f}(\boldsymbol{x},\boldsymbol{y},\boldsymbol{u})} \\ \underbrace{\begin{pmatrix}\dot{\boldsymbol{q}}\\ \dot{\boldsymbol{R}}_{\mathrm{IB}}\end{pmatrix}}_{\dot{\boldsymbol{y}}} &= \underbrace{\begin{pmatrix}\boldsymbol{R}_{\mathrm{IB}}\boldsymbol{v}\\ \boldsymbol{R}_{\mathrm{IB}}\boldsymbol{S}(\boldsymbol{\omega})\end{pmatrix}}_{\boldsymbol{h}(\boldsymbol{x},\boldsymbol{y},\boldsymbol{u})}\end{aligned} \tag{3.22}$$

Proposition 3.1. *The system (3.22) is* $\mathsf{SO}(3)$*-invariant with respect to the transformation group* $\{\boldsymbol{\varphi}_g(\boldsymbol{x}), \boldsymbol{\varrho}_g(\boldsymbol{y}), \boldsymbol{\psi}_g(\boldsymbol{u})\}_{g\in\mathsf{SO}(3)}$ *defined by*

$$\boldsymbol{\varphi}_g(\boldsymbol{x}) = \boldsymbol{R}_g\boldsymbol{v}, \quad \boldsymbol{\varrho}_g(\boldsymbol{y}) = \begin{pmatrix} \boldsymbol{q} \\ \boldsymbol{R}_{\mathrm{IB}}\boldsymbol{R}_g^{\mathsf{T}} \end{pmatrix}, \quad \boldsymbol{\psi}_g(\boldsymbol{u}) = \begin{pmatrix} \boldsymbol{R}_g\boldsymbol{\omega} \\ \boldsymbol{R}_g\boldsymbol{a} \end{pmatrix}$$

where $\boldsymbol{R}_g$ *denotes the element* $g \in G$ *for* $G = \mathsf{SO}(3)$.

Proof. We have

$$\begin{aligned} \mathrm{T}_{\boldsymbol{x}}\boldsymbol{\varphi}_g\big(\boldsymbol{f}(\boldsymbol{x},\boldsymbol{y},\boldsymbol{u})\big) &= \boldsymbol{R}_g(\boldsymbol{v}\times\boldsymbol{\omega}) + \boldsymbol{R}_g\boldsymbol{R}_{\mathrm{IB}}^{\mathsf{T}}\boldsymbol{g} + \boldsymbol{R}_g\boldsymbol{a} \\ &= \boldsymbol{R}_g\boldsymbol{v}\times\boldsymbol{R}_g\boldsymbol{\omega} + (\boldsymbol{R}_{\mathrm{IB}}\boldsymbol{R}_g^{\mathsf{T}})^{\mathsf{T}}\boldsymbol{g} + \boldsymbol{R}_g\boldsymbol{a} \\ &= \boldsymbol{f}(\boldsymbol{\varphi}_g(\boldsymbol{x}), \boldsymbol{\varrho}_g(\boldsymbol{y}), \boldsymbol{\psi}_g(\boldsymbol{u})) \end{aligned}$$

and

$$\begin{aligned} \mathrm{T}_{\boldsymbol{y}}\boldsymbol{\varrho}_g\big(\boldsymbol{h}(\boldsymbol{x},\boldsymbol{y},\boldsymbol{u})\big) &= \begin{pmatrix} \boldsymbol{R}_{\mathrm{IB}}\boldsymbol{v} \\ \boldsymbol{R}_{\mathrm{IB}}\boldsymbol{S}(\boldsymbol{\omega})\boldsymbol{R}_g^{\mathsf{T}} \end{pmatrix} \\ &= \begin{pmatrix} \boldsymbol{R}_{\mathrm{IB}}\boldsymbol{R}_g^{\mathsf{T}}\boldsymbol{R}_g\boldsymbol{v} \\ \boldsymbol{R}_{\mathrm{IB}}\boldsymbol{R}_g^{\mathsf{T}}\boldsymbol{S}(\boldsymbol{R}_g\boldsymbol{\omega}) \end{pmatrix} \\ &= \boldsymbol{h}(\boldsymbol{\varphi}_g(\boldsymbol{x}), \boldsymbol{\varrho}_g(\boldsymbol{y}), \boldsymbol{\psi}_g(\boldsymbol{u})) \end{aligned}$$

Here, we have used the property that $\boldsymbol{S}(\boldsymbol{R}\boldsymbol{\xi}) = \boldsymbol{R}\boldsymbol{S}(\boldsymbol{\xi})\boldsymbol{R}^{\mathsf{T}}$ for any $\boldsymbol{R} \in \mathsf{SO}(3)$ and $\boldsymbol{\xi} \in \mathbb{R}^3$. □

Since $\boldsymbol{R}_{\mathrm{IB}}$ is an element of the Lie group G, the moving frame is simply

$$\gamma(\boldsymbol{y}) = \boldsymbol{R}_{\mathrm{IB}}$$

Because the transformation group is also linear in the measured part of the state, we can choose the gain map $\boldsymbol{\ell}$ to be

$$\boldsymbol{\ell}(\boldsymbol{y}) = \boldsymbol{L}\boldsymbol{q}$$

where $\boldsymbol{L} \in \mathbb{R}^{3\times 3}$ is a tuning parameter. Therefore, Eq. (3.13) states that

$$\boldsymbol{\beta}(\boldsymbol{y}) = \boldsymbol{R}_{\mathrm{IB}}^{\mathsf{T}}\boldsymbol{L}\boldsymbol{q}$$

Applying Theorem 3.1, we have

$$\boldsymbol{\alpha}(\boldsymbol{z},\boldsymbol{x},\boldsymbol{y}) = \underbrace{(\boldsymbol{z} + \boldsymbol{R}_{\mathrm{IB}}^{\mathsf{T}}\boldsymbol{L}\boldsymbol{q})\times\boldsymbol{\omega} + \boldsymbol{R}_{\mathrm{IB}}^{\mathsf{T}}\boldsymbol{g} + \boldsymbol{a}}_{\boldsymbol{f}(\boldsymbol{z}+\boldsymbol{\beta}(\boldsymbol{y}),\boldsymbol{y},\boldsymbol{u})} \underbrace{+ \boldsymbol{S}(\boldsymbol{\omega})\boldsymbol{R}_{\mathrm{IB}}^{\mathsf{T}}\boldsymbol{L}\boldsymbol{q} - \boldsymbol{R}_{\mathrm{IB}}^{\mathsf{T}}\boldsymbol{L}\boldsymbol{R}_{\mathrm{IB}}(\boldsymbol{z} + \boldsymbol{R}_{\mathrm{IB}}^{\mathsf{T}}\boldsymbol{L}\boldsymbol{q})}_{-\mathrm{T}_{\boldsymbol{y}}\boldsymbol{\beta}(\boldsymbol{h}(\boldsymbol{z}+\boldsymbol{\beta}(\boldsymbol{y}),\boldsymbol{y},\boldsymbol{u}))}$$

with the estimate of $\boldsymbol{v}$ given by

$$\hat{\boldsymbol{v}} = \boldsymbol{z} + \boldsymbol{R}_{\mathrm{IB}}^{\mathsf{T}}\boldsymbol{L}\boldsymbol{q}$$

The sufficient condition given in Theorem 3.2 reduces to the requirement that the origin of the system

$$\dot{\boldsymbol{\eta}} = -\boldsymbol{L}\boldsymbol{\eta}$$

is asymptotically stable. Therefore, if $(-\boldsymbol{L})$ is Hurwitz, then the pre-observer $\dot{\boldsymbol{z}} = \boldsymbol{\alpha}(\boldsymbol{z}, \boldsymbol{y}, \boldsymbol{u})$ is a globally exponentially stable, reduced-order, $\mathsf{SO}(3)$-invariant observer.

As a numerical example, consider the maneuvering flight trajectory shown in Figure 3.4. For the initial condition $\hat{\boldsymbol{v}}(0) = \boldsymbol{0}$ and gain matrix $\boldsymbol{L} = 10\mathbb{I}$, the time history of velocity estimates is shown in Figure 3.5. To stress the observer, we also include noisy measurements of $\boldsymbol{y}$ and $\boldsymbol{u}$. Specifically, suppose

$$\begin{aligned} \boldsymbol{y}_q &= \boldsymbol{q} + \boldsymbol{w}_q & \boldsymbol{u}_\omega &= \boldsymbol{\omega} + \boldsymbol{w}_\omega \\ \boldsymbol{y}_{R_{\mathrm{IB}}} &= \boldsymbol{R}_{\mathrm{IB}} \exp(\boldsymbol{S}(\boldsymbol{w}_{R_{\mathrm{IB}}})) & \boldsymbol{u}_a &= \boldsymbol{a} + \boldsymbol{w}_a \end{aligned}$$

where $\boldsymbol{w}_q$, $\boldsymbol{w}_{R_{\mathrm{IB}}}$, $\boldsymbol{w}_\omega$, and $\boldsymbol{w}_a$ are zero-mean, Gaussian, continuous-time, "white noise" with power spectral densities $5 \times 10^{-4}\mathbb{I}\ \frac{\mathrm{m}^2}{\mathrm{Hz}}$, $10^{-7}\mathbb{I}\ \frac{1}{\mathrm{Hz}}$, $10^{-5}\mathbb{I}\ \frac{(\mathrm{rad/s})^2}{\mathrm{Hz}}$, and $2 \times 10^{-2}\mathbb{I}\ \frac{(\mathrm{m/s^2})^2}{\mathrm{Hz}}$, respectively. Figure 3.6 shows the velocity estimates when $\boldsymbol{y}$ and $\boldsymbol{u}$ are corrupted by a realization of these random processes. The results shown in Figure 3.6 are indicative of the observer's inherent robustness to disturbances, as expected from the fact that the undisturbed invariant error system is globally exponentially stable.

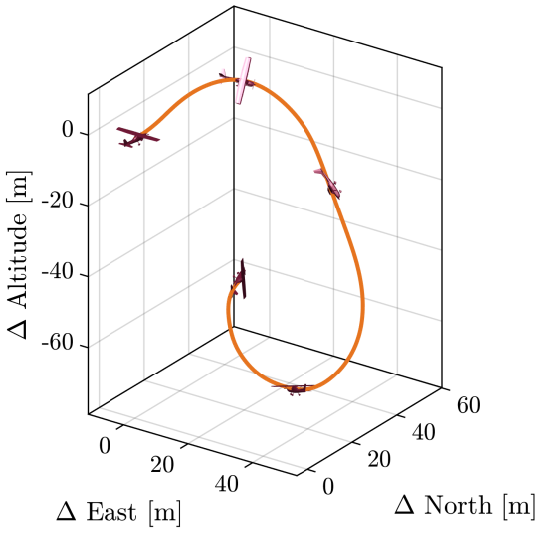

Figure 3.4: Maneuvering aircraft

Remark 3.2. *Proving stochastic stability for this example is beyond the scope of this dissertation since the noisy rotation matrix measurements multiply noisy position and angular velocity measurements. Therefore, the error dynamics would not be a stochastic differential equation as defined in Chapter 2, but rather something more general.*

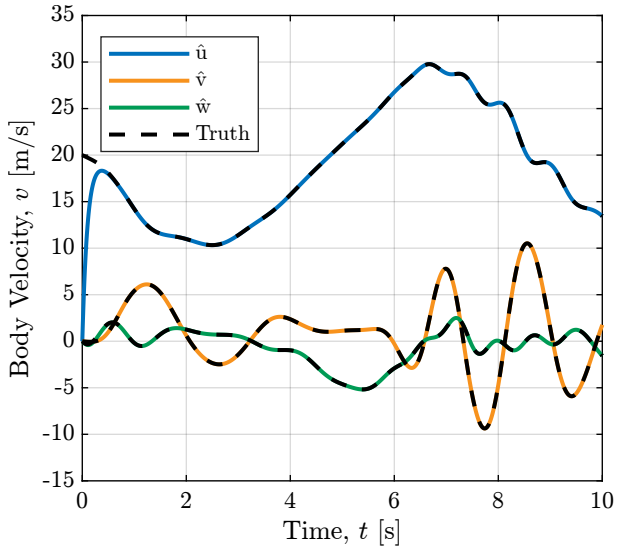

Figure 3.5: Velocity estimates

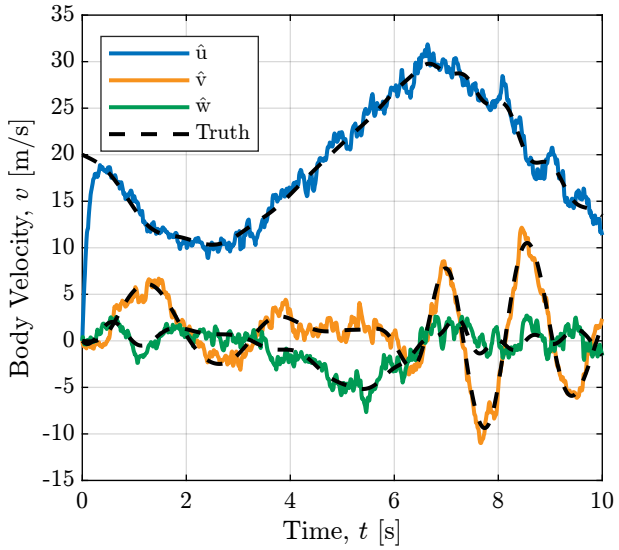

Figure 3.6: Velocity estimates with noisy measurements and inputs

This rigid-body velocity estimation example highlights the key advantage of a symmetry-preserving reduced-order observer; exploiting the system's symmetry simplifies the state-estimation error dynamics. In particular, Theorem 3.2 states that stability analysis of the invariant error system can be equivalently conducted under any transformation on the system as defined by the transformation group. The key result that enables this simplification is that the observer map $\boldsymbol{\beta}$ commutes with the transformation group — a property that arises from the equivariance of the moving frame. While not shown here, the application of this model-free approach (that is, no aerodynamic model) to flight in wind yields a linear error

system that is not stabilizable. Therefore, the extension of this example to wind estimation requires the use of an aerodynamic model instead of using accelerometer measurements.

Chapter 4

Nonlinear Flight Dynamic Modeling for Multirotor Aircraft

The nonlinear observer presented in Chapter 3 constitutes a method for obtaining provably accurate state estimates across the entire state space. These guarantees, however, are only as good as the system model. For aircraft, this means an aerodynamic model must be accurate across the full range of operating conditions in order to reap the benefits of a nonlinear observer. Much progress has been made in large-domain fixed-wing modeling; however, established methods for formulating and identifying large-domain multirotor flight dynamic models are lacking. To address these gaps, the following two chapters detail multirotor modeling and system identification methodologies that are applicable to general maneuvering flight.

This chapter is based on reference [74]. The results presented here (especially Section 4.4) are fruits of collaboration with Dr. Benjamin Simmons, Jared Cooper, and Dr. Craig Woolsey.

4.1 Introduction

Flight dynamic models for aircraft are often required for control, estimation, simulation, and design. It can be useful to formulate such a model as a low-dimensional system of ordinary differential equations to allow for direct use in control and estimation algorithms as well as efficient simulation and design optimization [71], [77], [138]. In particular, we aim to obtain a large-domain flight dynamic model for use in the model-based wind estimation schemes detailed in Chapters 6–8. Higher-fidelity models based on computational or wind tunnel data are not practical in such applications. Hence, this chapter details the development of nonlinear, quasi-steady flight dynamic models for multirotor aircraft that strike a balance between complexity and accuracy so that they may be identified from flight data and readily employed for model-based control and estimator design.

In general, there is no standard structure for compact, finite-dimensional models for full-envelope multirotor aircraft flight, though efforts have been made for fixed-wing aircraft [60], [113], [135]. Large-domain modeling for multirotor aircraft is especially challenging due to complex inflow conditions [127], unsteady effects [105], and aerodynamic interactions [19]. Therefore, typical approaches to multirotor modeling for the purposes of control and estimation involve identifying linear state space models in the time domain or low-order transfer

functions in the frequency domain [3], [37], [78], [119], [120], [152]. While these approaches enable a multitude of control and estimation approaches, incorporating an aerodynamic model that is more accurate over a broader envelope can yield stronger guarantees on safety and performance.

Approaches to expand the range of flight conditions for which a model accurately describes multirotor motion include stitched linear models [54], linear force and moment models for the otherwise nonlinear system [134], nonlinear aerodynamic models for a reduced number of degrees-of-freedom by assuming symmetry [15], and polynomial-based regressor determination using stepwise regression [142]. These models are valid across a wider range of flight conditions than linear flight dynamic models; however, broader applicability may still be obtained through physics-based modeling. Such an approach often begins with the aerodynamics of a single rotor, superposing these effects for multiple rotors to obtain a final model structure [14], [27], [37]. A model that is valid within a larger domain, accurately capturing nonlinear dynamic and aerodynamic phenomena, may be required for applications of interest. For example, the recent growth in urban air mobility has spawned novel vertical takeoff and landing vehicle designs, motivating physics-based, analytical models such as the one detailed by Nguyen and Webb [118]. While these models describe the complex phenomena driving the vehicle motion, they require a high-dimensional system representation, making identification and control difficult. Thus, there remains a middle ground to be explored — one in which a physics-based, nonlinear, quasi-steady flight dynamic model can be identified from flight data.

Accordingly, this chapter presents a nonlinear, quasi-steady multirotor aerodynamic model that is accurate over a wider range of flight conditions than typical control-oriented models, yet simpler to identify and use for model-based control and estimation than models that interpolate extensive archives of experimental or computational data. Similar to Fay [43], the approach presented here begins with the force and moment generated by a single rotor in forward flight, derived using blade-element theory and momentum theory. Using this result, unknown constants are lumped together to obtain force and moment expressions for a single rotor, which are then incorporated into the force and moment acting on the multirotor aircraft. The resulting nonlinear model is broadly applicable and is in a form amenable to identification from experimental data. Recognizing that simpler models may still be useful in some applications, a set of reasonable assumptions are presented to simplify the model structure and make the parameter identification problem even easier.

To evaluate the effectiveness of the postulated multirotor model structure, a simulation study was conducted using a high-fidelity multirotor aerodynamic model derived from wind tunnel data [68]. A statistically designed test matrix was developed to facilitate accurate identification of the model terms in each model structure [106], [117]. The models are assessed using prediction error metrics and comparisons of the model predictions to the known simulation database, which reveals the advantages and limitations of each modeling approach. Through these results, the relative importance of model terms was evaluated across a large domain of interest.

The remainder of this chapter is based on Hopwood *et al.* [74] and is organized as follows. Section 4.2 derives lumped-parameter expressions for the aerodynamic force and moment acting on a single rotor in forward flight using blade-element and momentum theory. The result is used in Section 4.3 to formulate the total force and moment for a rotating and translating multirotor aircraft. Section 4.4 describes the simulation study, followed by modeling results presented in Section 4.5.

4.2 Rotor Aerodynamics

In this chapter, we aim to model the aerodynamic force $\boldsymbol{F}$ and moment $\boldsymbol{M}$ acting on a multirotor aircraft. That is, a model is formulated for $\boldsymbol{F}$ and $\boldsymbol{M}$ in the rigid body equations of motion (2.14) in a way that captures the propulsion physics accurately enough to support effective model-based design of nonlinear control and estimation schemes, but simply enough to allow straightforward model parameter estimation. We aim to derive a model for the aerodynamic force and moment as a function of the vehicle's states, where the propulsors are assumed to be fixed-pitch, rigid rotors for simplicity. The aerodynamics of these rotors serve as the building block that will define the aerodynamic force and moment acting on the multirotor aircraft.

Consider an N_b-blade rotor of radius R rotating about its spin axis at the rate Ω $\frac{\text{rad}}{\text{s}}$ that is also steadily translating through still air with velocity $\boldsymbol{v}$ and airspeed $V = \|\boldsymbol{v}\|$.

Assumption 4.1. *The blade-element loads are steady, depending only on the the translational velocity of the rotor hub and the rotor rotational speed.*

In other words, the effect of rotor angular velocity orthogonal to the shaft on the blade element angle-of-attack is neglected. The farther the rotor hubs lie from the aircraft's CG, the less the vehicle's angular velocity influences blade element loads relative to its translational velocity. Consequently, Assumption 4.1 is well justified for many multirotor vehicles. Note, however, that the vehicle's angular velocity $\boldsymbol{\omega}$ is not entirely ignored; as detailed in Section 4.3, it will be used to compute the rotor hub's local translational velocity, thereby yielding a quasi-steady aerodynamic model.

To simplify the discussion of rotor aerodynamics, we assume for the time being that the "aircraft" comprises a single rotor located at the origin of the body frame with the rotor spin axis aligned with $\boldsymbol{b}_3$. Referring to Figure 4.1, let orthonormal vectors $\{\boldsymbol{r}_1, \boldsymbol{r}_2, \boldsymbol{r}_3\}$ define a reference frame centered at the rotor hub such that

a) $\boldsymbol{r}_3 = -\boldsymbol{b}_3$;

b) if $\|\boldsymbol{v}\| > 0$, then $\boldsymbol{v}$ lies in the $\boldsymbol{r}_1$-$\boldsymbol{r}_3$ plane such that $\boldsymbol{r}_1^\mathsf{T}\boldsymbol{v} > 0$;

c) if $\|\boldsymbol{v}\| = 0$, then $\boldsymbol{r}_1 = \boldsymbol{b}_1$;

d) $\boldsymbol{r}_2$ completes a right-handed frame.

The rotor frame is defined similar to the wind frame for fixed-wing aircraft in the sense that the frame axes are defined by the air-relative velocity vector. The rotor frame is related to the body frame by the transformation[1]

$$\boldsymbol{R}_{\mathrm{BR}} = \begin{bmatrix} \cos\beta_f & -\sin\beta_f & 0 \\ -\sin\beta_f & -\cos\beta_f & 0 \\ 0 & 0 & 1 \end{bmatrix} \tag{4.1}$$

where β_f is the angle from $\boldsymbol{r}_1$ to $\boldsymbol{b}_1$, measured about the $\boldsymbol{r}_3$ axis. In the rotor frame, the velocity of the rotor hub is $\tilde{\boldsymbol{v}} = [v_x \;\; 0 \;\; v_z]^{\mathsf{T}}$, where v_z is the *rotor ascent speed* and v_x is the *rotor-plane airspeed*. Referring to Figure 4.1, for a non-rotating body frame ($\boldsymbol{\omega} = \boldsymbol{0}$), the rotation matrix $\boldsymbol{R}_{\mathrm{BR}}$ defines the relations

$$\begin{bmatrix} u \\ v \\ w \end{bmatrix} = \boldsymbol{R}_{\mathrm{BR}}\tilde{\boldsymbol{v}} = \begin{bmatrix} v_x \cos\beta_f \\ -v_x \sin\beta_f \\ -v_z \end{bmatrix} \tag{4.2}$$

and

$$\begin{bmatrix} v_x \\ 0 \\ v_z \end{bmatrix} = \boldsymbol{R}_{\mathrm{BR}}^{\mathsf{T}}\boldsymbol{v} = \begin{bmatrix} u\cos\beta_f - v\sin\beta_f \\ -u\sin\beta_f - v\cos\beta_f \\ -w \end{bmatrix} \tag{4.3}$$

By the definition of the rotor frame, v_x also satisfies

$$v_x = \sqrt{u^2 + v^2} \geq 0 \tag{4.4}$$

Figure 4.1 depicts the relationship between the body and rotor frames along with the respective components of the velocity vector, $\boldsymbol{v}$, in this special case where we have assumed the rotor hub coincides with the aircraft CG. In Figure 4.1, $\boldsymbol{v}$ is depicted with $u < 0$, $v > 0$, and $w < 0$. Also note in this case that $v_z > 0$ and $\beta_f > 0$.

The non-dimensional *horizontal advance ratio* is

$$\mu_x = \frac{v_x}{\Omega R} \tag{4.5}$$

In a similar manner, the *total inflow ratio* is

$$\lambda = \frac{\nu + v_z}{\Omega R} \tag{4.6}$$

where ν is the induced rotor inflow velocity (positive in the $\boldsymbol{b}_3$ direction). For the purpose of rotor force and moment derivation, consider the following assumption on the rotor aerodynamics.

[1]Note that $\boldsymbol{R}_{\mathrm{BR}}$ is not a proper rotation matrix.

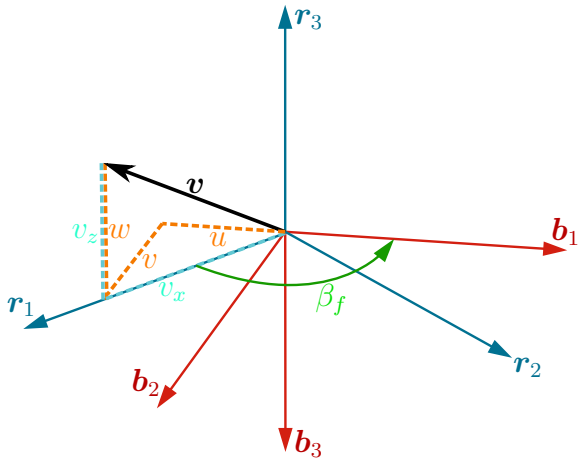

Figure 4.1: Rotor frame geometry

Assumption 4.2. *The rotor blades*

a) *are rigid (no flapping);*

b) *do not stall;*

c) *have linear twist:* $\theta(\mathfrak{r}) = \theta_0 + \theta_{\text{tw}}\mathfrak{r}$*, where* $\mathfrak{r}$ *is the non-dimensional radial station along the blade measured from the hub;*

d) *do not interact with the wake of upstream blades.*

Consider the thrust T, hub force H, side force S, rolling moment $\mathcal{R}$, pitching moment $\mathcal{P}$, and torque $\mathcal{Q}$ on the isolated rotor shown in Figure 4.2. Due to Assumptions 4.2a and 4.2d, the rotor-frame side force, S, and pitching moment, $\mathcal{P}$, are zero [83, Ch. 5].

As detailed by Johnson [83, Chs. 4 and 5], the rotor loads can be obtained by integrating the force and moment acting on an infinitesimal element of the rotor blade. It is convenient to express these quantities as the non-dimensional coefficients,

$$\begin{aligned} C_H &= \frac{H}{\rho\pi R^4\Omega^2} \quad C_T = \frac{T}{\rho\pi R^4\Omega^2} \\ C_{\mathcal{R}} &= \frac{\mathcal{R}}{\rho\pi R^5\Omega^2} \quad C_{\mathcal{Q}} = \frac{\mathcal{Q}}{\rho\pi R^5\Omega^2} \end{aligned} \tag{4.7}$$

where ρ is the air density. Denote the constant lift curve slope of a blade element as a and its mean drag coefficient as $\bar{c}_d$ (computed at $\mathfrak{r} = \sqrt{2}/2$). The rotor force and moment

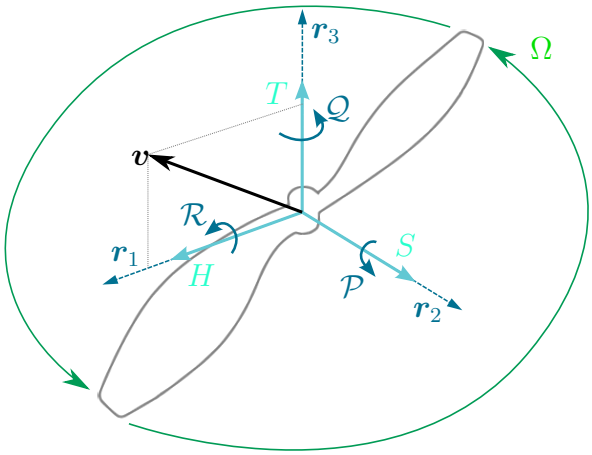

Figure 4.2: Isolated rotor force and moment

coefficients are given as

$$C_H = -\frac{N_\mathrm{b}\bar{c}a}{2\pi R}\left[\frac{1}{2a}\bar{c}_d\mu_x + \left(\frac{\theta_0}{2} + \frac{\theta_\mathrm{tw}}{4}\right)\lambda\mu_x\right] \tag{4.8a}$$

$$C_T = \frac{N_\mathrm{b}\bar{c}a}{2\pi R}\left[\frac{\theta_0}{3}\left(1 + \frac{3}{2}\mu_x^2\right) + \frac{\theta_\mathrm{tw}}{4}\left(1 + \mu_x^2\right) - \frac{\lambda}{2}\right] \tag{4.8b}$$

$$C_\mathcal{R} = -\frac{N_\mathrm{b}\bar{c}a}{2\pi R}\left[\frac{\theta_0}{3} + \frac{\theta_\mathrm{tw}}{4} - \frac{\lambda}{4}\right]\mu_x \tag{4.8c}$$

$$C_\mathcal{Q} = -\frac{N_\mathrm{b}\bar{c}a}{2\pi R}\left[\frac{\bar{c}_d}{4a}\left(1 + \mu_x^2\right) + \left(\frac{\theta_0}{3} + \frac{\theta_\mathrm{tw}}{4} - \frac{\lambda}{2}\right)\lambda\right] \tag{4.8d}$$

These coefficients are similarly derived by Fay [43] and Cooper *et al.* [36] as applied to multirotor vehicles.

An expression is still needed for the inflow ratio λ. From momentum theory [95, Ch. 2], the inflow velocity in hover is

$$\nu_0 = \sqrt{\frac{mg}{2\rho A_\mathrm{r}}} \tag{4.9}$$

where A_r is the total rotor disk area of the aircraft. However, we are interested in the more general forward flight condition where the steady, uniform inflow velocity is implicitly defined by

$$\nu = \frac{\nu_0^2}{\sqrt{v_x^2 + (\nu + v_z)^2}} \tag{4.10}$$

To simplify the dependence on v_x and v_z, we choose to linearly approximate the curvy surface defined by Eq. (4.10) with a plane in the ν-v_x-v_z space.

Assumption 4.3. *The rotor inflow velocity is steady and uniform, given by*

$$\nu = \nu_0 - C_{\nu_x} v_x - C_{\nu_z} v_z \tag{4.11}$$

where ν_0 is the hover inflow velocity given by Eq. (4.9).

Since the aim is to develop a model that is identifiable from experimental data, the values for the positive constants C_{ν_x} and C_{ν_z} will be implicitly chosen to best fit the selected data. An example of this fit for the small quadrotor considered by Foster and Hartman [44] is illustrated in Figure 4.3, where the curvy surface defined by Eq. (4.10) is approximated by the plane defined by Eq. (4.11).

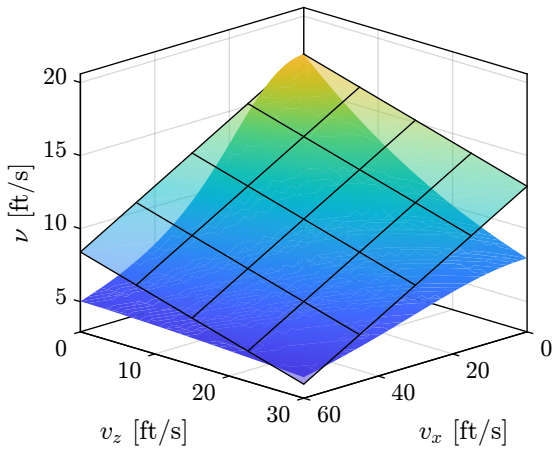

Figure 4.3: Steady inflow model (4.10) and the linear approximation (4.11)

Defining the *hover inflow ratio* $\mu_0 = \frac{\nu_0}{\Omega R}$ and *vertical advance ratio* $\mu_z = \frac{v_z}{\Omega R}$, the total inflow ratio λ becomes

$$\lambda = \mu_0 - C_{\nu_x}\mu_x - (C_{\nu_z} - 1)\mu_z \tag{4.12}$$

Let $C_\sigma = \frac{N_\mathrm{b}\bar{c}a}{2\pi R}$, $C_{\theta_1} = \frac{\theta_0}{3} + \frac{\theta_\mathrm{tw}}{4}$, and $C_{\theta_2} = \frac{\theta_0}{2} + \frac{\theta_\mathrm{tw}}{4}$ for compactness. The rotor coefficients in Eq. (4.8) are expanded using Eq. (4.12) to obtain the non-dimensional rotor force coefficients,

$$C_H = \underbrace{-\frac{1}{2a}C_\sigma \bar{c}_d}_{C_{H_{\mu_x}}}\mu_x - \underbrace{C_\sigma C_{\theta_2}}_{C_{H_{\mu_0,\mu_x}}}\mu_x\mu_0 + \underbrace{C_\sigma C_{\theta_2} C_{\nu_x}}_{C_{H_{\mu_x^2}}}\mu_x^2 + \underbrace{C_\sigma C_{\theta_2}(C_{\nu_z} - 1)}_{C_{H_{\mu_x,\mu_z}}}\mu_x\mu_z \tag{4.13a}$$

$$C_T = \underbrace{C_\sigma C_{\theta_1}}_{C_{T_0}} - \underbrace{\frac{1}{2}C_\sigma}_{C_{T_{\mu_0}}}\mu_0 + \underbrace{\frac{1}{2}C_\sigma C_{\nu_x}}_{C_{T_{\mu_x}}}\mu_x + \underbrace{C_\sigma C_{\theta_2}}_{C_{T_{\mu_x^2}}}\mu_x^2 + \underbrace{\frac{1}{2}C_\sigma(C_{\nu_z} - 1)}_{C_{T_{\mu_z}}}\mu_z \tag{4.13b}$$

and moment coefficients,

$$C_\mathcal{R} = \underbrace{-C_\sigma C_{\theta_1}}_{C_{R_{\mu_x}}}\mu_x + \underbrace{\frac{1}{4}C_\sigma}_{C_{R_{\mu_0,\mu_x}}}\mu_x\mu_0 - \underbrace{\frac{1}{4}C_\sigma C_{\nu_x}}_{C_{R_{\mu_x^2}}}\mu_x^2 - \underbrace{\frac{1}{4}C_\sigma(C_{\nu_z} - 1)}_{C_{R_{\mu_x,\mu_z}}}\mu_x\mu_z \tag{4.13c}$$

$$C_{\mathcal{Q}} = \underbrace{-\frac{1}{4a}C_\sigma \bar{c}_d}_{C_{Q_0}} \underbrace{- C_\sigma C_{\theta_1}}_{C_{Q_{\mu_0}}} \mu_0 + \underbrace{C_\sigma C_{\theta_1} C_{\nu_x}}_{C_{Q_{\mu_x}}} \mu_x + \underbrace{C_\sigma C_{\theta_1}(C_{\nu_z} - 1)}_{C_{Q_{\mu_z}}} \mu_z$$
$$+ \underbrace{\frac{1}{2}C_\sigma}_{C_{Q_{\mu_0^2}}} \mu_0^2 - \underbrace{C_\sigma\left(\frac{\bar{c}_d}{4a} - \frac{C_{\nu_x}^2}{2}\right)}_{C_{Q_{\mu_x^2}}} \mu_x^2 + \underbrace{\frac{1}{2}C_\sigma(C_{\nu_z} - 1)^2}_{C_{Q_{\mu_z^2}}} \mu_z^2 - \underbrace{C_\sigma C_{\nu_x}}_{C_{Q_{\mu_0,\mu_x}}} \mu_0\mu_x$$
$$- \underbrace{C_\sigma(C_{\nu_z} - 1)}_{C_{Q_{\mu_0,\mu_z}}} \mu_0\mu_z + \underbrace{C_\sigma C_{\nu_x}(C_{\nu_z} - 1)}_{C_{Q_{\mu_x,\mu_z}}} \mu_x\mu_z \quad (4.13d)$$

Because the ultimate aim is to identify a flight dynamic model from experimental data, constant parameters in Eq. (4.13) are lumped together to define a new set of parameters which will appear in the final multirotor model. Notice Eq. (4.13) comprises second-order polynomials of the advance ratios μ_x, μ_z, and μ_0. Hence, we refer to the quadratic terms (e.g., $C_{H_{\mu_x^2}}\mu_x^2$) in the model as *second-order effects*.

Remark 4.1. *The lumped rotor aerodynamic parameters in Eq. (4.13) are non-dimensional.*

The rotor aerodynamic analysis presented here provides a physically motivated model structure, but specific coefficient values will be determined from data for the complete aircraft, not from computations of the expressions above. Although the set of five base parameters $\{C_\sigma, C_{\nu_x}, C_{\nu_z}, C_{\theta_1}, C_{\theta_2}\}$ could be used in the final model structure, we choose to decouple these interdependent parameters (e.g., $C_{T_0} \neq C_{R_{\mu_x}}$) to better capture unmodeled effects and potential violations of Assumption 4.2.

For the steadily translating rotor depicted in Figure 4.2, the isolated body-frame rotor force $\boldsymbol{F}_{\mathrm{r}} = [X_{\mathrm{r}} \;\; Y_{\mathrm{r}} \;\; Z_{\mathrm{r}}]^{\mathsf{T}}$ and moment $\boldsymbol{M}_{\mathrm{r}} = [\mathcal{L}_{\mathrm{r}} \;\; \mathcal{M}_{\mathrm{r}} \;\; \mathcal{N}_{\mathrm{r}}]^{\mathsf{T}}$ applied to the rotor hub satisfy

$$\begin{bmatrix} X_{\mathrm{r}} \\ Y_{\mathrm{r}} \\ Z_{\mathrm{r}} \end{bmatrix} = \begin{bmatrix} H\cos\beta_f \\ -H\sin\beta_f \\ -T \end{bmatrix} \quad \text{and} \quad \begin{bmatrix} \mathcal{L}_{\mathrm{r}} \\ \mathcal{M}_{\mathrm{r}} \\ \mathcal{N}_{\mathrm{r}} \end{bmatrix} = \begin{bmatrix} \mathcal{R}\cos\beta_f \\ -\mathcal{R}\sin\beta_f \\ -\mathcal{Q} \end{bmatrix} \quad (4.14)$$

Using the re-dimensionalized lumped-parameter expressions (4.13) along with the velocity

component relation in Eq. (4.2), we have the isolated rotor model

$$X_\mathrm{r} = \rho\pi R^2 \left(-C_{H_{\mu_x}} R\Omega u - C_{H_{\mu_0,\mu_x}} \nu_0 u + C_{H_{\mu_x^2}} v_x u - C_{H_{\mu_x,\mu_z}} uw\right) \tag{4.15a}$$

$$Y_\mathrm{r} = \rho\pi R^2 \left(-C_{H_{\mu_x}} R\Omega v - C_{H_{\mu_0,\mu_x}} \nu_0 v + C_{H_{\mu_x^2}} v_x v - C_{H_{\mu_x,\mu_z}} vw\right) \tag{4.15b}$$

$$Z_\mathrm{r} = \rho\pi R^2 \left(-C_{T_0} R^2\Omega^2 + C_{T_{\mu_0}} R\Omega\nu_0 - C_{T_{\mu_x}} R\Omega v_x + C_{T_{\mu_z}} R\Omega w - C_{T_{\mu_x^2}} v_x^2\right) \tag{4.15c}$$

$$\mathcal{L}_\mathrm{r} = \rho\pi R^3 \left(-C_{R_{\mu_x}} R\Omega u + C_{R_{\mu_0,\mu_x}} \nu_0 u - C_{R_{\mu_x^2}} v_x u + C_{R_{\mu_x,\mu_z}} uw\right) \tag{4.15d}$$

$$\mathcal{M}_\mathrm{r} = \rho\pi R^3 \left(-C_{R_{\mu_x}} R\Omega v + C_{R_{\mu_0,\mu_x}} \nu_0 v - C_{R_{\mu_x^2}} v_x v + C_{R_{\mu_x,\mu_z}} vw\right) \tag{4.15e}$$

$$\begin{aligned}\mathcal{N}_\mathrm{r} = \rho\pi R^3 \Big(&C_{Q_0} R^2\Omega^2 + C_{Q_{\mu_0}} R\Omega\nu_0 - C_{Q_{\mu_x}} R\Omega v_x + C_{Q_{\mu_z}} R\Omega w - C_{Q_{\mu_0^2}} \nu_0^2 \\ &- C_{Q_{\mu_x^2}} v_x^2 - C_{Q_{\mu_z^2}} w^2 + C_{Q_{\mu_0,\mu_x}} \nu_0 v_x - C_{Q_{\mu_0,\mu_z}} \nu_0 w + C_{Q_{\mu_x,\mu_z}} v_x w\Big)\end{aligned} \tag{4.15f}$$

Equation (4.15) gives the components of the force and moment vectors, expressed in the body frame, applied to the hub of an isolated rotor that is steadily translating in still air. This model is adopted for the rotor aerodynamics of the multirotor aircraft considered in Section 4.3, where we consider the effects of multiple rotors displaced from a translating and rotating body frame.

4.3 Multirotor Forces and Moments

The rotor aerodynamic force and moment described in Eq. (4.15) are incomplete representations of the actual force and moment applied to the airframe. Here, we consider a number of other factors that influence a given rotor's effect on vehicle motion.

4.3.1 Motor Dynamics

Consider a motor fixed in space that is attached to the rotor depicted in Figure 4.2. While there are many approaches to the electric propulsion of multirotor aircraft, we consider the common assumption (also adopted by Cunningham and Hubbard [37] and Khan and Nahon [87], for example) that the system comprising the motor and electronic speed controller (ESC) is well-described by the DC motor model

$$L_\mathrm{m} \frac{\mathrm{d}i_\mathrm{m}}{\mathrm{d}t} + R_\mathrm{m} i_\mathrm{m} + k_\mathrm{v}\Omega = v_\mathrm{m} \tag{4.16a}$$

$$J_z \frac{\mathrm{d}\Omega}{\mathrm{d}t} = \mathcal{Q}_\mathrm{m} + \mathcal{Q} \tag{4.16b}$$

where L_m is the armature inductance, i_m is the armature current, R_m is the armature resistance, k_v is the back electro-magnetic force constant (often called the velocity constant), v_m is the voltage supplied to the motor, J_z is the moment of inertia of the motor and rotor

rigid body about the $\boldsymbol{r}_3$ axis, $\mathcal{Q}_\mathrm{m}$ is the torque applied to the rotor about its spin axis by the motor mounted to the airframe (a function of i_m and Ω), and $\mathcal{Q}$ is the aerodynamic torque acting on the rotor about its spin axis. The motor model in Eq. (4.16) may be simplified through use of the torque constant, k_t, which is a proportional constant relating $\mathcal{Q}_\mathrm{m}$ to i_m. Furthermore, the motor/ESC electrical dynamics evolve on a much faster time scale than the mechanical motor speed dynamics so that the steady-state solution to Eq. (4.16a) may be used to obtain

$$J_z\dot{\Omega} = -\frac{k_\mathrm{t}k_\mathrm{v}}{R_\mathrm{m}}\Omega + \frac{k_\mathrm{t}}{R_\mathrm{m}}v_\mathrm{m} + \mathcal{Q} \tag{4.17}$$

as corroborated by Cunningham and Hubbard [37].

Like Smeur *et al.* [138], we recognize that the motor dynamics influence the rigid body in three dimensions. Consider the ith motor located at the point $\boldsymbol{p}_i = [x_i \;\; y_i \;\; z_i]^\mathsf{T}$ in the body frame. Let $\boldsymbol{\Omega}_i = [0 \;\; 0 \;\; \sigma_i\Omega_i]^\mathsf{T}$ be its angular velocity vector with respect to the body frame, expressed in the body frame, where $\sigma_i \in \{-1, +1\}$ represents the rotor rotation direction according to the right-hand rule in the body frame. Assuming the motor inertia J_z is much smaller than the rigid-body moment of inertia about the $\boldsymbol{b}_3$ axis and that the magnitude of the yaw rate is much less than the motor speed,

$$\boldsymbol{J}\dot{\boldsymbol{\Omega}}_i = \boldsymbol{J}\boldsymbol{\Omega}_i \times \boldsymbol{\omega} - \boldsymbol{M}_{\mathrm{m},i} + \boldsymbol{M}_{\mathrm{r},i} \tag{4.18}$$

where $\boldsymbol{J} = \mathbf{diag}(J_x, J_y, J_z)$ is the moment of inertia matrix of the motor/rotor rigid body, $\boldsymbol{M}_{\mathrm{m},i}$ is the moment applied to the airframe (hence the sign reversal compared to Eq. (4.16b)), and

$$\boldsymbol{M}_{\mathrm{r},i} = -\sigma_i \begin{bmatrix} \mathcal{L}_{\mathrm{r},i} \\ \mathcal{M}_{\mathrm{r},i} \\ \mathcal{N}_{\mathrm{r},i} \end{bmatrix} \tag{4.19}$$

is the aerodynamic moment on the ith rotor expressed in the body frame. Equation (4.18) constitutes one dynamical equation for the rotor spin rate — the third component of $\boldsymbol{\Omega}_i$ — and two algebraic equations for the moments exerted by the motor on the airframe about the non-spin axes — the first and second components of $\boldsymbol{M}_{\mathrm{m},i}$. Here, as opposed to the isolated rotor moment components in Eq. (4.15), the rotor aerodynamic moments are evaluated at the velocities of the rotor hubs, $\boldsymbol{v}_i$, accounting for the body angular velocity $\boldsymbol{\omega}$. Like Bannwarth *et al.* [15], we assume knowledge of $\dot{\boldsymbol{\Omega}}_i$ so that an expression for $\boldsymbol{M}_{\mathrm{m},i}$ in terms of motor parameters and/or electrical states is not needed. Instead, we rearrange and simplify Eq. (4.18) to obtain the moment applied to the airframe by a single rotor,

$$\boldsymbol{M}_{\mathrm{m},i} = \boldsymbol{M}_{\mathrm{r},i} - \sigma_i J_z \begin{bmatrix} q\Omega_i \\ -p\Omega_i \\ \dot{\Omega}_i \end{bmatrix} \tag{4.20}$$

Equation (4.20) shows the relationship between the rotor aerodynamic moments derived in Section 4.2 and the moment applied to the rigid body by a single rotor. The terms $J_z q\Omega_i$ and $J_z p\Omega_i$ are the gyroscopic effects of the motor/rotor, and $J_z\dot{\Omega}_i$ is net motor torque. The

transmission of rotor aerodynamic forces is much simpler than that of the moments. The aerodynamic force of the ith rotor applied to the airframe at the base of the motor is

$$\boldsymbol{F}_{\mathrm{m},i} = \boldsymbol{F}_{\mathrm{r},i} \tag{4.21}$$

whose components are given by Eq. (4.15) evaluated using the local rotor velocity, $\boldsymbol{v}_i$. Equations (4.21) and (4.20) define the force and moment, respectively, applied by the ith motor to the rigid airframe at its point of attachment.

4.3.2 Multirotor Aerodynamics

With an understanding of how forces and moments are transmitted to the airframe from Section 4.3.1, and the individual rotor forces and moments developed in Section 4.2, we can derive expressions for the total force and moment on a multirotor aircraft. Let the total force and moment applied to the airframe be $\boldsymbol{F} = [F_x \;\; F_y \;\; F_z]^\mathsf{T}$ and $\boldsymbol{M} = [M_x \;\; M_y \;\; M_z]^\mathsf{T}$, respectively. Consider a multirotor aircraft whose configuration is defined by the following assumptions.

Assumption 4.4.

a) *The number of rotors, $N_\mathrm{r} \geq 4$, is even.*

b) *The rotors counter-rotate in an alternating fashion (i.e., neighboring rotors spin in opposite directions).*

c) *The rotor configuration is symmetric about the $\boldsymbol{b}_1$ and $\boldsymbol{b}_2$ axes.*

d) *The rotor arms have equal length, ℓ, and are arranged with equal interior angles, $2\pi/N_\mathrm{r}$.*

e) *The rotors are uncanted (coplanar) and located at the same height, $h = -z_i$, above the center of gravity.*

As an example, a quadrotor in a symmetric "X" configuration as pictured in Figure 4.4 satisfies Assumption 4.4. As it will be important for the final model, we define three classes of configurations that satisfy Assumption 4.4.

Definition 4.1.

a) *A* **quadrotor$_+$** *satisfies Assumption 4.4 with $N_\mathrm{r} = 4$ and $(x_i, y_i) = (0, \ell)$ for some $i \in \{1, 2, 3, 4\}$.*

b) *A* **quadrotor$_\times$** *satisfies Assumption 4.4 with $N_\mathrm{r} = 4$ and $(x_i, y_i) = (\ell\frac{\sqrt{2}}{2}, \ell\frac{\sqrt{2}}{2})$ for some $i \in \{1, 2, 3, 4\}$.*

c) *A* **multirotor$_{\geq 6}$** *satisfies Assumption 4.4 for $N_\mathrm{r} \geq 6$.*

Remark 4.2. *Although the following derivation considers the configuration in Assumption 4.4, the same approach may be used for any other configuration of interest.*

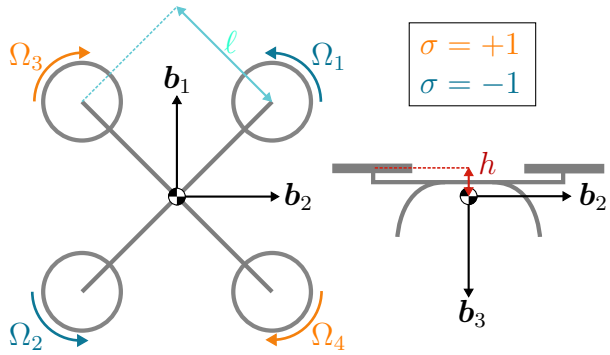

Figure 4.4: Quadrotor geometry

To this point, we have not mentioned airframe-specific (rotor-independent) forces and moments. The form of such a drag model is non-standard due to the varied and complex geometry of multirotor aircraft. Thus, experimentally-derived [35], [114] and/or simplified-geometry models [18], [30] are considered. We assume the following.

Assumption 4.5. *The airframe-specific aerodynamic force and moment are well-approximated by empirically-derived expressions that depend on body-frame translational and angular velocity.*

In reality, the flow induced by the rotors interacts with the airframe as well as among the rotors themselves. However, since these interaction effects are difficult to model [19], we make the following assumption.

Assumption 4.6. *The force and moment due to rotor-airframe and rotor-rotor interaction is lumped into the airframe and rotor forces and moments.*

As a consequence of Assumption 4.6, any rotor aerodynamic interactions will be expressed in the model as either a decrease in thrust or an increase in rotor and airframe drag (in the steady state, at least). Any unsteady effects of aerodynamic interactions are not captured by the model.

Because the motors are assumed to be rigidly attached to the aircraft, the body frame force, $\boldsymbol{F}$, is equal to the total rotor aerodynamic force, $\boldsymbol{F}_\mathrm{r} = [X_\mathrm{r} \quad Y_\mathrm{r} \quad Z_\mathrm{r}]^\mathsf{T}$, plus the airframe aerodynamic force, $\boldsymbol{F}_\mathrm{a} = [X_\mathrm{a} \quad Y_\mathrm{a} \quad Z_\mathrm{a}]^\mathsf{T}$. Here, $\boldsymbol{F}_\mathrm{r}$ and $\boldsymbol{M}_\mathrm{r}$ denote the total rotor-derived force and moment vectors applied to the aircraft as opposed to the isolated rotor force/moment components considered in Eq. (4.15). Thus, we have

$$\boldsymbol{F} = \boldsymbol{F}_\mathrm{r} + \boldsymbol{F}_\mathrm{a} = \sum_{i=1}^{N_\mathrm{r}} \boldsymbol{F}_{\mathrm{r},i} + \boldsymbol{F}_\mathrm{a} = \sum_{i=1}^{N_\mathrm{r}} \boldsymbol{F}_{\mathrm{m},i} + \boldsymbol{F}_\mathrm{a} \tag{4.22}$$

As shown in Section 4.3.1, however, $\boldsymbol{M}$ is not simply equal to the airframe aerodynamic

moment, $\boldsymbol{M}_{\mathrm{a}} \coloneqq [\mathcal{L}_{\mathrm{a}} \;\; \mathcal{M}_{\mathrm{a}} \;\; \mathcal{N}_{\mathrm{a}}]^{\mathsf{T}}$, plus the total rotor aerodynamic moment,

$$\boldsymbol{M}_{\mathrm{r}} = \sum_{i=1}^{N_{\mathrm{r}}} (\boldsymbol{M}_{\mathrm{r},i} + \boldsymbol{p}_i \times \boldsymbol{F}_{\mathrm{r},i}) =: \begin{bmatrix} \mathcal{L}_{\mathrm{r}} \\ \mathcal{M}_{\mathrm{r}} \\ \mathcal{N}_{\mathrm{r}} \end{bmatrix} \tag{4.23}$$

Instead, referring to Eqs. (4.20) and (4.21),

$$\boldsymbol{M} = \sum_{i=1}^{N_{\mathrm{r}}} (\boldsymbol{M}_{\mathrm{m},i} + \boldsymbol{p}_i \times \boldsymbol{F}_{\mathrm{m},i}) + \boldsymbol{M}_{\mathrm{a}} \tag{4.24}$$

Alternatively, the total applied moment in Eq. (4.24) can be written using the total aerodynamic moment in Eq. (4.23) as

$$\boldsymbol{M} = \boldsymbol{M}_{\mathrm{r}} + \boldsymbol{M}_{\mathrm{a}} - J_z \sum_{i=1}^{N_{\mathrm{r}}} \sigma_i \begin{bmatrix} q\Omega_i \\ -p\Omega_i \\ \dot{\Omega}_i \end{bmatrix} \tag{4.25}$$

Furthermore, we must determine for each rotor the contribution of vehicle angular velocity to the rotor aerodynamic force and moment. These forces and moments are defined in the body frame whose origin does not coincide with the rotor hubs. Recalling from Assumption 4.4 that the rotors are not canted, i.e., the $\boldsymbol{r}_1$-$\boldsymbol{r}_2$ plane is parallel to the $\boldsymbol{b}_1$-$\boldsymbol{b}_2$ plane, the local velocity of the ith rotor in the body frame is

$$\boldsymbol{v}_i = \boldsymbol{v} + \boldsymbol{\omega} \times \boldsymbol{p}_i \tag{4.26}$$

Incorporating this correction yields a complicated model structure, making parameter estimation from flight data difficult. To obtain a more compact and identifiable form, we make the following assumption.

Assumption 4.7. *When computing the local velocity for each rotor, the vehicle yaw rate, r, and the vertical moment arm, h, can be neglected.*

Assumption 4.7 reflects the expectation that the primary contribution of the vehicle angular velocity to the rotor forces and moments is the resulting change in inflow velocity. Following Assumption 4.7, we approximate the local velocity of the ith rotor as

$$\boldsymbol{v}_i \approx \boldsymbol{v} + \begin{bmatrix} p \\ q \\ 0 \end{bmatrix} \times \begin{bmatrix} x_i \\ y_i \\ 0 \end{bmatrix} = \begin{bmatrix} u \\ v \\ w + py_i - qx_i \end{bmatrix} \tag{4.27}$$

Given the local rotor velocity approximation in Eq. (4.27), the next step is to express the total force and moment in a form that simplifies control, analysis, and the design of excitation signals for system identification. Rather than using individual rotor speeds as inputs, which

can be cumbersome and less interpretable, we define a more compact representation using *virtual actuators*, which are defined by the *motor mixing* formula

$$\underbrace{\begin{bmatrix}\delta^2 t\\ \delta^2 a\\ \delta^2 e\\ \delta^2 r\end{bmatrix}}_{\boldsymbol{\delta}^2} \coloneqq \mathbf{M_{ix}} \underbrace{\begin{bmatrix}\Omega_1^2\\ \Omega_2^2\\ \vdots\\ \Omega_{N_\mathrm{r}}^2\end{bmatrix}}_{\boldsymbol{\Omega}^2} \tag{4.28}$$

where $\mathbf{M_{ix}}$ is determined by the geometry of the aircraft as follows:

$$\mathbf{M_{ix}} = \begin{bmatrix}1/N_\mathrm{r} & 1/N_\mathrm{r} & \cdots & 1/N_\mathrm{r}\\ -y_1 & -y_2 & \cdots & -y_{N_\mathrm{r}}\\ x_1 & x_2 & \cdots & x_{N_\mathrm{r}}\\ -\sigma_1 & -\sigma_2 & \cdots & -\sigma_{N_\mathrm{r}}\end{bmatrix} \tag{4.29}$$

To capture first-order rotor speed terms, we also define

$$\underbrace{\begin{bmatrix}\delta t\\ \delta a\\ \delta e\\ \delta r\end{bmatrix}}_{\boldsymbol{\delta}} \coloneqq \mathbf{M_{ix}} \underbrace{\begin{bmatrix}\Omega_1\\ \Omega_2\\ \vdots\\ \Omega_{N_\mathrm{r}}\end{bmatrix}}_{\boldsymbol{\Omega}} \tag{4.30}$$

In Eqs. (4.28) and (4.30), $\boldsymbol{\delta}^2$ and $\boldsymbol{\delta}$ serve as virtual actuators, providing a more compact representation of control inputs; $\boldsymbol{\Omega}^2$ and $\boldsymbol{\Omega}$ are the column vectors of squared and positive motor speeds, respectively. Specifically, δa, δe, δr, and δt represent virtual aileron, elevator, rudder, and thrust inputs. However, it is important to note that $\boldsymbol{\delta}^2$ and $\boldsymbol{\delta}$ are not independently controlled.

Finally, the body frame forces and moments are obtained using Eqs. (4.22) and (4.25), where $\boldsymbol{F}_{\mathrm{r},i}$ and $\boldsymbol{M}_{\mathrm{r},i}$ are evaluated at $\boldsymbol{v}_i$ as defined in Eq. (4.27) and rotor speeds are replaced using the virtual actuator definitions in Eqs. (4.28) and (4.30). As a result, we obtain the following model.

Model 1. *The force and moment components for a multirotor aircraft satisfying Assumption 4.4 are*

$$F_x = \rho\pi R^2 N_\mathrm{r} u \left(-C_{H_{\mu_x}} R\delta t - C_{H_{\mu_0,\mu_x}}\nu_0 + C_{H_{\mu_x^2}} v_x - C_{H_{\mu_x,\mu_z}} w\right) + X_\mathrm{a} \tag{4.31a}$$

$$F_y = \rho\pi R^2 N_\mathrm{r} v \left(-C_{H_{\mu_x}} R\delta t - C_{H_{\mu_0,\mu_x}}\nu_0 + C_{H_{\mu_x^2}} v_x - C_{H_{\mu_x,\mu_z}} w\right) + Y_\mathrm{a} \tag{4.31b}$$

$$\begin{aligned} F_z = \rho\pi R^2\Big(&- C_{T_0} R^2 N_\mathrm{r}\delta^2 t + C_{T_{\mu_0}} R N_\mathrm{r}\nu_0\delta t - C_{T_{\mu_x}} R N_\mathrm{r} v_x\delta t \\ &+ C_{T_{\mu_z}} R(N_\mathrm{r} w\delta t - \Delta\nu_Z) - C_{T_{\mu_x^2}} N_\mathrm{r} v_x^2\Big) + Z_\mathrm{a} \end{aligned} \tag{4.31c}$$

$$\begin{aligned} M_x = \rho\pi R^2\Big(&- C_{R_{\mu_x}} R^2 u\delta r + C_{T_0} R^2\delta^2 a - C_{T_{\mu_0}} R\nu_0\delta a + C_{T_{\mu_x}} R v_x\delta a \\ &- C_{T_{\mu_z}} R\Big(w\delta a - \Delta\nu_\mathcal{L}\Big) - C_{H_{\mu_x}} R N_\mathrm{r} hv\delta t - C_{H_{\mu_0,\mu_x}} N_\mathrm{r} hv\nu_0 \\ &+ C_{H_{\mu_x^2}} N_\mathrm{r} hv v_x - C_{H_{\mu_x,\mu_z}} N_\mathrm{r} hvw\Big) + \mathcal{L}_\mathrm{a} + J_z q\delta r \end{aligned} \tag{4.31d}$$

$$\begin{aligned} M_y = \rho\pi R^2\Big(&- C_{R_{\mu_x}} R^2 v\delta r + C_{T_0} R^2\delta^2 e - C_{T_{\mu_0}} R\nu_0\delta e + C_{T_{\mu_x}} R v_x\delta e \\ &- C_{T_{\mu_z}} R\Big(w\delta e - \Delta\nu_\mathcal{M}\Big) + C_{H_{\mu_x}} R N_\mathrm{r} hu\delta t + C_{H_{\mu_0,\mu_x}} N_\mathrm{r} hu\nu_0 \\ &- C_{H_{\mu_x^2}} N_\mathrm{r} hu v_x + C_{H_{\mu_x,\mu_z}} N_\mathrm{r} huw\Big) + \mathcal{M}_\mathrm{a} - J_z p\delta r \end{aligned} \tag{4.31e}$$

$$\begin{aligned} M_z = \rho\pi R^2\Big(&C_{Q_0} R^3\delta^2 r + C_{Q_{\mu_0}} R^2\nu_0\delta r - C_{Q_{\mu_x}} R^2 v_x\delta r \\ &+ C_{Q_{\mu_z}} R^2\Big(w\delta r - \Delta\nu_\mathcal{N}\Big) - C_{Q_{\mu_z^2}} R\Delta\nu_\mathcal{N}^2 - C_{H_{\mu_x}} R(u\delta a + v\delta e) \\ &+ \frac{1}{2} C_{H_{\mu_x,\mu_z}} N_\mathrm{r}\ell^2(up + vq)\Big) + \mathcal{N}_\mathrm{a} + J_z\dot{\delta r} \end{aligned} \tag{4.31f}$$

where $\Delta\nu_Z = p\delta a + q\delta e$ *and*

$$\Delta\nu_\mathcal{L} = \begin{cases} \frac{1}{2}\ell^2 p(N_\mathrm{r}\delta t + \delta r) & \text{quadrotor}_+ \\ \frac{1}{2}\ell^2(N_\mathrm{r} p\delta t + q\delta r) & \text{quadrotor}_\times \\ \frac{1}{2}\ell^2 N_\mathrm{r} p\delta t & \text{multirotor}_{\geq 6} \end{cases} \quad \Delta\nu_\mathcal{M} = \begin{cases} \frac{1}{2}\ell^2 q(N_\mathrm{r}\delta t - \delta r) & \text{quadrotor}_+ \\ \frac{1}{2}\ell^2(N_\mathrm{r} q\delta t + p\delta r) & \text{quadrotor}_\times \\ \frac{1}{2}\ell^2 N_\mathrm{r} q\delta t & \text{multirotor}_{\geq 6} \end{cases}$$

$$\Delta\nu_\mathcal{N} = \begin{cases} p\delta a - q\delta e & \text{quadrotor}_+ \\ p\delta e + q\delta a & \text{quadrotor}_\times \\ 0 & \text{multirotor}_{\geq 6} \end{cases} \quad \Delta\nu_\mathcal{N}^2 = \begin{cases} \frac{1}{2} N_\mathrm{r}\ell^2(p^2 - q^2) & \text{quadrotor}_+ \\ N_\mathrm{r}\ell^2 pq & \text{quadrotor}_\times \\ 0 & \text{multirotor}_{\geq 6} \end{cases}$$

A detailed derivation of Model 1 is given in Appendix A.1. Note the configuration-dependent terms, $\Delta\nu_{(\cdot)}$, stem from the effect of angular velocity on the change in total rotor inflow.

Remark 4.3. *The terms in Model 1 that do not explicitly depend on rotor speed retain implicit dependence through the induced inflow velocity model in Eq. (4.11). By choosing a linear inflow model, we have replaced the physically meaningful structure of Eq. (4.10) with an experimentally determined approximation (4.11). The constant parameters* $C_{H_{\mu_0,\mu_x}}$, $C_{H_{\mu_x^2}}$, $C_{H_{\mu_x,\mu_z}}$, *and* $C_{Q_{\mu_z^2}}$ *implicitly depend on the aggregate rotor speed data used to identify their values. The only exception is* $C_{T_{\mu_x^2}}$ *term, which does not arise from the inflow model.*

This proposed model has several benefits when applied to control and estimation applications. Mainly, this model structure is valid over a large range of velocities. For steady flight in any direction, barring descending flight into a vortex ring state, there are few approximations made in progressing from the initial blade element theory to the final model. This model is also valid for large roll rate and pitch rate perturbations from translating flight because the local rotor velocity is incorporated directly. Furthermore, the use of virtual actuators instead of rotor speeds not only generalizes the model to any configuration satisfying Assumption 4.4, but also reveals an intuitive understanding of non-trivial effects such as $C_{H_{\mu_x}} R(u\delta a + v\delta e)$ in the yawing moment equation, M_z. This term captures the yawing moment due to differential drag under virtual aileron and elevator commands; it is similar to adverse/proverse yaw for a fixed-wing aircraft.

However, Model 1 ignores effects that might be important in some applications. First, the angular velocity of the aircraft is not considered in the blade-element forces and moments. In applications where the vehicle is rapidly rotating (e.g., upset recovery from tumbling motion), the incorporation angular velocity in the blade-element loads may be beneficial. Second, unsteady effects such as blade flapping and inflow dynamics are neglected. While the linear approximation (4.11) is not a bad approximation of the steady inflow condition, unsteady inflow effects may be important to model when controlling and/or estimating motion at fast time scales.

4.3.3 Incorporation of Motor Dynamics

When used for state and/or disturbance estimation, the virtual actuators can be treated as inputs or may be estimated as states. In control applications, however, one must acknowledge that the virtual actuators $\boldsymbol{\delta}$ and $\boldsymbol{\delta}^2$ are not independently controlled. To resolve this issue, $\boldsymbol{\delta}$ and $\boldsymbol{\delta}^2$ may be included in a motor model, such as Eq. (4.17), whose input corresponds to physically realizable motor commands. In vector form, where $\boldsymbol{\mathcal{Q}} = [\mathcal{Q}_1 \cdots \mathcal{Q}_{N_\mathrm{r}}]^\mathsf{T}$ and $\boldsymbol{v}_\mathrm{m} = [v_{\mathrm{m},1} \cdots v_{\mathrm{m},N_\mathrm{r}}]^\mathsf{T}$, Eq. (4.17) becomes

$$J_z \dot{\boldsymbol{\Omega}} = -\frac{k_\mathrm{t} k_\mathrm{v}}{R_\mathrm{m}} \boldsymbol{\Omega} + \frac{k_\mathrm{t}}{R_\mathrm{m}} \boldsymbol{v}_\mathrm{m} + \boldsymbol{\mathcal{Q}} \tag{4.32}$$

Referring to Eqs. (4.16b)–(4.17),

$$\boldsymbol{\mathcal{Q}}_\mathrm{m} = -\frac{k_\mathrm{t} k_\mathrm{v}}{R_\mathrm{m}} \boldsymbol{\Omega} + \frac{k_\mathrm{t}}{R_\mathrm{m}} \boldsymbol{v}_\mathrm{m}$$

is the vector comprising the applied motor torques. Pre-multiplying both sides of Eq. (4.32) by $\mathbf{M_{ix}}$ and defining the actuator control input

$$\boldsymbol{u}_\delta \coloneqq \frac{1}{k_\mathrm{v}}\mathbf{M_{ix}}\boldsymbol{v}_\mathrm{m} \tag{4.33}$$

we obtain

$$J_z\dot{\boldsymbol{\delta}} = -\frac{k_\mathrm{t}k_\mathrm{v}}{R_\mathrm{m}}\boldsymbol{\delta} + \frac{k_\mathrm{t}k_\mathrm{v}}{R_\mathrm{m}}\boldsymbol{u}_\delta + \mathbf{M_{ix}}\boldsymbol{\mathcal{Q}} \tag{4.34}$$

Unlike in the derivation of the yawing moment equation (4.31f), the second-order rotor torque coefficients, such as $C_{Q_{\mu_x^2}}$ and $C_{Q_{\mu_0,\mu_x}}$, do not completely vanish from the term $\mathbf{M_{ix}}\boldsymbol{\mathcal{Q}}$ in Eq. (4.34). This introduces complexity into the model, with many terms that have negligible influence. To simplify the model, we neglect these second-order torque coefficients (as defined in Eq.(4.13d)) to yield

$$\begin{aligned} J_z\dot{\boldsymbol{\delta}} = &-\frac{k_\mathrm{t}k_\mathrm{v}}{R_\mathrm{m}}\boldsymbol{\delta} + \frac{k_\mathrm{t}k_\mathrm{v}}{R_\mathrm{m}}\boldsymbol{u}_\delta \\ &+ \rho\pi R^3\left(C_{Q_0}R^2\boldsymbol{\delta}^2 + C_{Q_{\mu_0}}R\nu_0\boldsymbol{\delta} + C_{Q_{\mu_x}}Rv_x\boldsymbol{\delta} - C_{Q_{\mu_z}}R\left(w\boldsymbol{\delta} - \boldsymbol{\Delta}\right)\right) \end{aligned} \tag{4.35}$$

where $\boldsymbol{\Delta} = [\Delta\nu_z/N_\mathrm{r} \quad \Delta\nu_\mathcal{L} \quad \Delta\nu_\mathcal{M} \quad \Delta\nu_\mathcal{N}]^\mathsf{T}$.

Remark 4.4. *It is important to note that these second-order coefficients do vanish in the virtual rudder dynamics (the final component of Eq. (4.34)). As a result, the simplified actuator dynamics*(4.35) *remain consistent with the yawing moment equation* (4.31f).

With the rotor aerodynamic torques incorporated into the actuator dynamics, we can construct the rigid-body yawing moment, M_z, by substituting the applied motor torque $\boldsymbol{\mathcal{Q}}_\mathrm{m}$ into Eq. (4.24) to obtain

$$M_z = \frac{k_\mathrm{t}k_\mathrm{v}}{R_\mathrm{m}}\left(\delta r - u_{\delta r}\right) + \rho\pi R^2\left(-C_{H_{\mu_x}}R(u\delta a + v\delta e) + \frac{1}{2}C_{H_{\mu_x,\mu_z}}N_\mathrm{r}\ell^2(up + vq)\right) + \mathcal{N}_\mathrm{a} \tag{4.36}$$

From this analysis, we see that the incorporation of a motor model changes where rotor aerodynamic torques $\mathcal{Q}_i$ enter the flight dynamic model. Instead of directly affecting the rigid-body moment M_z, they enter in the actuator dynamics.

4.3.4 Nonlinear Model Simplifications

For some applications, Model 1 may still be too complicated to experimentally identify and apply in control and estimator design. Here, we consider two optional assumptions, each of which progressively simplifies the model structure with the aim of simplifying the model identification process. One possible simplification of Model 1 is to neglect the change in induced inflow velocity due to changes in vehicle velocity.

Assumption 4.8 (Optional)**.** *The induced inflow velocity is constant and equal to the hover inflow velocity ν_0 given by Eq. (4.9).*

Under Assumption 4.8, Model 1 simplifies as follows.

Model 2. *The force and moment components for a multirotor aircraft additionally satisfying Assumption 4.8 are*

$$F_x = \rho\pi R^2 N_\mathrm{r} u\left(-C_{H_{\mu_x}} R\delta t - C_{H_{\mu_0,\mu_x}}\nu_0 - C_{H_{\mu_x,\mu_z}} w\right) + X_\mathrm{a} \tag{4.37a}$$

$$F_y = \rho\pi R^2 N_\mathrm{r} v\Big(-C_{H_{\mu_x}} R\delta t - C_{H_{\mu_0,\mu_x}}\nu_0 - C_{H_{\mu_x,\mu_z}} w\Big) + Y_\mathrm{a} \tag{4.37b}$$

$$\begin{aligned} F_z = \rho\pi R^2\Big(&-C_{T_0} R^2 N_\mathrm{r}\delta^2 t + C_{T_{\mu_0}} R N_\mathrm{r}\nu_0\delta t \\ &+ C_{T_{\mu_z}} R(N_\mathrm{r} w\delta t - \Delta\nu_Z) - C_{T_{\mu_x^2}} N_\mathrm{r} v_x^2\Big) + Z_\mathrm{a} \end{aligned} \tag{4.37c}$$

$$\begin{aligned} M_x = \rho\pi R^2\Big(&-C_{R_{\mu_x}} R^2 u\delta r + C_{T_0} R^2\delta^2 a - C_{T_{\mu_0}} R\nu_0\delta a - C_{T_{\mu_z}} R\Big(w\delta a - \Delta\nu_\mathcal{L}\Big) \\ &- C_{H_{\mu_x}} R N_\mathrm{r} hv\delta t - C_{H_{\mu_0,\mu_x}} N_\mathrm{r} hv\nu_0 - C_{H_{\mu_x,\mu_z}} N_\mathrm{r} hvw\Big) + \mathcal{L}_\mathrm{a} + J_z q\delta r \end{aligned} \tag{4.37d}$$

$$\begin{aligned} M_y = \rho\pi R^2\Big(&-C_{R_{\mu_x}} R^2 v\delta r + C_{T_0} R^2\delta^2 e - C_{T_{\mu_0}} R\nu_0\delta e - C_{T_{\mu_z}} R\Big(w\delta e - \Delta\nu_\mathcal{M}\Big) \\ &+ C_{H_{\mu_x}} R N_\mathrm{r} hu\delta t + C_{H_{\mu_0,\mu_x}} N_\mathrm{r} hu\nu_0 + C_{H_{\mu_x,\mu_z}} N_\mathrm{r} huw\Big) + \mathcal{M}_\mathrm{a} - J_z p\delta r \end{aligned} \tag{4.37e}$$

$$\begin{aligned} M_z = \rho\pi R^2\Big(&C_{Q_0} R^3\delta^2 r + C_{Q_{\mu_0}} R^2\nu_0\delta r + C_{Q_{\mu_z}} R^2\Big(w\delta r - \Delta\nu_\mathcal{N}\Big) - C_{Q_{\mu_z^2}} R\Delta\nu_\mathcal{N}^2 \\ &- C_{H_{\mu_x}} R(u\delta a + v\delta e) + \frac{1}{2} C_{H_{\mu_x,\mu_z}} N_\mathrm{r}\ell^2(up + vq)\Big) + \mathcal{N}_\mathrm{a} + J_z\dot{\delta r} \end{aligned} \tag{4.37f}$$

By assuming the inflow velocity to be the same as in hover, we have lessened the model's utility at high speeds. However, the model structure that remains now smoothly depends on the vehicle velocity, allowing for more flexibility in control law and estimator design. More specifically, Assumption 4.8 eliminates terms in Model 1 that depend linearly on rotor-plane airspeed, v_x, whose derivative does not exist at $\boldsymbol{v} = \mathbf{0}$. The quadratic term $C_{T_{\mu_x^2}} N_\mathrm{r} v_x^2$ remains in the F_z equation, however, as it does not arise from the assumed inflow model. Practically, this term can be interpreted as an "airspeed-dependent bias" to the thrust model.

Depending on the airframe design, it may be unnecessary to separately model rotor and airframe effects. For many vehicles, the airframe-specific force and moment are small compared to the rotor-based force and moment. Thus, it is often sufficient to lump these terms together to further simplify the Model 2.

Assumption 4.9 (Optional)**.** *Airframe aerodynamics can be lumped into the rotor aerodynamics.*

Model 3. *The force and moment components for a multirotor aircraft additionally satisfying Assumption 4.9 are obtained by setting X_a, Y_a, Z_a, $\mathcal{L}_\mathrm{a}$, $\mathcal{M}_\mathrm{a}$, $\mathcal{N}_\mathrm{a}$ to zero in Model 2.*

Model 3 may also be obtained by way of a second-order Taylor series approximation of Model 2 about hover. For some nonlinear control and estimation applications, especially where a Lyapunov stability approach is used [86, Ch. 3], this quadratic structure makes the control and stability problem more tractable.

4.3.5 Linear Flight Dynamic Models

For some applications, a linear, time-invariant flight dynamic model is sufficient for operation about some steady motion. Such a model may be obtained by linearizing the equations of motion about this nominal flight condition. Taking this approach for Model 1 reveals a physically principled structure of the linear system that can be identified from flight data.

Consider the nonlinear dynamics of the aircraft given by Eq. (2.15), where $\boldsymbol{\eta}$ is the aircraft configuration and $\boldsymbol{\nu}$ is its generalized velocity. For Model 1, the generalized force $\mathscr{F}$ comprising the applied force and moment has the general dependence

$$\mathscr{F}(\boldsymbol{\nu}, \boldsymbol{\Omega}, \dot{\boldsymbol{\Omega}}) = \begin{bmatrix} \boldsymbol{F}(\boldsymbol{\nu}, \boldsymbol{\Omega}) \\ \boldsymbol{M}(\boldsymbol{\nu}, \boldsymbol{\Omega}, \dot{\boldsymbol{\Omega}}) \end{bmatrix} \tag{4.38}$$

In Model 1, $\boldsymbol{F}$ and $\boldsymbol{M}$ are implicitly functions of $\boldsymbol{\Omega}$ through the definition of the virtual actuators. Specifically, $\boldsymbol{\Omega} = \mathbf{M}_{\mathbf{ix}}^{\dagger}\boldsymbol{\delta}$, where $(\cdot)^\dagger$ is the Moore-Penrose pseudoinverse.[2]

Consider small perturbations about some equilibrium flight condition defined by $\boldsymbol{\nu} = \boldsymbol{\nu}_0$ and $\boldsymbol{\Omega} = \boldsymbol{\Omega}_0$. The generalized velocity and rotor speed perturbations from this condition are denoted $\Delta\boldsymbol{\nu} = \boldsymbol{\nu} - \boldsymbol{\nu}_0$ and $\Delta\boldsymbol{\Omega} = \boldsymbol{\Omega} - \boldsymbol{\Omega}_0$, respectively. Note the equilibrium condition implies $\dot{\boldsymbol{\Omega}}_0 = \mathbf{0}$. If we assume δr changes sufficiently slowly, we can neglect the $\dot{\delta r}$ term in M_z and obtain a linear system through a first-order Taylor series approximation of Eq. (2.15). Letting the evaluation of partial derivatives at the equilibrium condition be denoted $\partial(\cdot)/\partial(\cdot)|_\mathrm{eq}$ and defining the state vector $\boldsymbol{x} = [\boldsymbol{\eta}^\mathsf{T} \;\; \boldsymbol{\nu}^\mathsf{T}]^\mathsf{T}$, we have

$$\underbrace{\begin{bmatrix} \Delta\dot{\boldsymbol{\eta}} \\ \Delta\dot{\boldsymbol{\nu}} \end{bmatrix}}_{\Delta\dot{\boldsymbol{x}}} = \Bigg(\underbrace{\begin{bmatrix} \frac{\partial \boldsymbol{f}_\eta}{\partial \boldsymbol{\eta}} & \frac{\partial \boldsymbol{f}_\eta}{\partial \boldsymbol{\nu}} \\ \frac{\partial \boldsymbol{f}_\nu}{\partial \boldsymbol{\eta}} & \frac{\partial \boldsymbol{f}_\nu}{\partial \boldsymbol{\nu}} \end{bmatrix}\Bigg|_\mathrm{eq}}_{\boldsymbol{A}_0} + \underbrace{\begin{bmatrix} \mathbf{0} & \mathbf{0} \\ \mathbf{0} & \mathscr{M}^{-1} \frac{\partial \mathscr{F}}{\partial \boldsymbol{\nu}}\big|_\mathrm{eq} \end{bmatrix}}_{\boldsymbol{A}_\mathrm{a}} \Bigg) \underbrace{\begin{bmatrix} \Delta\boldsymbol{\eta} \\ \Delta\boldsymbol{\nu} \end{bmatrix}}_{\Delta\boldsymbol{x}} + \underbrace{\begin{bmatrix} \mathbf{0} \\ \mathscr{M}^{-1} \frac{\partial \mathscr{F}}{\partial \boldsymbol{\Omega}}\big|_\mathrm{eq} \end{bmatrix}}_{\boldsymbol{B}_\Omega} \Delta\boldsymbol{\Omega} \tag{4.39}$$

More compactly,

$$\Delta\dot{\boldsymbol{x}} = \underbrace{\left(\boldsymbol{A}_0 + \boldsymbol{A}_\mathrm{a}\right)}_{\boldsymbol{A}} \Delta\boldsymbol{x} + \boldsymbol{B}_\Omega \Delta\boldsymbol{\Omega} \tag{4.40}$$

Now, the virtual actuator definition may be used again to obtain

$$\Delta\dot{\boldsymbol{x}} = \boldsymbol{A}\Delta\boldsymbol{x} + \boldsymbol{B}\Delta\boldsymbol{\delta} \tag{4.41}$$

[2] An analytical expression for $\mathbf{M}_{\mathbf{ix}}^{\dagger}$ is given in Eq. (A.5).

where $\boldsymbol{B} = \boldsymbol{B}_\Omega \mathbf{M}_{\mathbf{ix}}^\dagger$.

The linear, time-invariant system (4.41) may be used for model-based estimation and control applications where the aircraft motion remains close to the equilibrium state and the motor dynamics evolve on a significantly faster time scale than the rigid body dynamics while virtual rudder command changes remain slow. In scenarios where this assumption cannot be made, a linearization of Eqs. (4.35) and (4.36) can be used to include motor dynamics in the linear model to avoid the necessity of assuming $\dot{\delta r} = 0$. Redefining the applied force/moment vector, $\mathscr{F}$, as specified in Eq. (4.38) by incorporating M_z from the motor model (4.36), we subsequently adjust $\boldsymbol{A}$ and $\boldsymbol{B}$ in Eq. (4.41). As a result, the linearized dynamics of the augmented state vector, $\boldsymbol{\xi} = \begin{bmatrix}\boldsymbol{x}^\mathsf{T} & \boldsymbol{\delta}^\mathsf{T}\end{bmatrix}^\mathsf{T}$, are

$$\underbrace{\begin{bmatrix}\Delta\dot{\boldsymbol{x}} \\ \hdashline \Delta\dot{\boldsymbol{\delta}}\end{bmatrix}}_{\Delta\dot{\boldsymbol{\xi}}} = \underbrace{\left[\begin{array}{cc} \boldsymbol{A} & \boldsymbol{B} \\ \hdashline -\frac{1}{J_z}\mathbf{M}_{\mathbf{ix}} \left.\frac{\partial \boldsymbol{\mathcal{Q}}}{\partial \boldsymbol{x}}\right|_{\text{eq}} & -\frac{k_\text{t}k_\text{v}}{J_z R_\text{m}}\mathbb{I} - \frac{1}{J_z}\mathbf{M}_{\mathbf{ix}} \left.\frac{\partial \boldsymbol{\mathcal{Q}}}{\partial \boldsymbol{\Omega}}\right|_{\text{eq}} \mathbf{M}_{\mathbf{ix}}^\dagger \end{array}\right]}_{\boldsymbol{A}_\xi} \underbrace{\begin{bmatrix}\Delta\boldsymbol{x} \\ \hdashline \Delta\boldsymbol{\delta}\end{bmatrix}}_{\Delta\boldsymbol{\xi}} + \underbrace{\begin{bmatrix}\mathbf{0}_{9\times 4} \\ \hdashline -\frac{k_\text{t}k_\text{v}}{R_\text{m}}\boldsymbol{I}^{-1}\boldsymbol{e}_3 \\ \hdashline \frac{k_\text{t}k_\text{v}}{J_z R_\text{m}}\mathbb{I}\end{bmatrix}}_{\boldsymbol{B}_\xi} \Delta\boldsymbol{u}_\delta \tag{4.42}$$

where $\boldsymbol{e}_3 = [0\ 0\ 1]^\mathsf{T}$ and $\mathbf{0}_{9\times 4}$ is an 9×4 matrix of zeros.

Given an equilibrium condition, the two linear systems (4.41) and (4.42) each reveal a particular structure that is informed by the underlying theory. A major benefit of the preceding analysis is to provide an analytical framework for understanding the implications of model simplifications in control and estimator design.

Most commonly considered is the hover condition defined by $\boldsymbol{\nu}_0 = \mathbf{0}$ and $\boldsymbol{\Omega}_0 = \Omega_0 \mathbf{1}$, where $\mathbf{1}$ is a vector of ones. The Jacobian of the force and moment vectors defined in Model 1 with respect to translational velocity is singular at the origin, however, because the derivative of the rotor plane airspeed $v_x = \sqrt{u^2 + v^2}$ is undefined at zero. One remediation is to make the hyperbolic approximation $v_x \approx \sqrt{u^2 + v^2 + \varepsilon}$ for some sufficiently small value of the non-negative parameter ε. Computing the terms in Eqs. (4.39) and (4.42) respectively for the hover condition and taking the limit as $\varepsilon \to 0$, we obtain the following two linear flight dynamics models about hover.

Model 4. *Treating virtual actuators as inputs, a linear flight dynamic model about hover is given by Eqs. (4.39)–(4.41). The Jacobian matrices of the aerodynamic force/moment vector are*

$$\left.\frac{\partial \mathscr{F}}{\partial \boldsymbol{\nu}}\right|_{\text{eq}} = -\rho\pi R^3 N_\text{r} \Omega_0 \begin{bmatrix} \alpha_H & 0 & 0 & 0 & 0 & 0 \\ 0 & \alpha_H & 0 & 0 & 0 & 0 \\ 0 & 0 & C_{T_{\mu_z}} & 0 & 0 & 0 \\ 0 & h\alpha_H & 0 & C_{T_{\mu_z}}\ell^2/2 & 0 & 0 \\ -h\alpha_H & 0 & 0 & 0 & C_{T_{\mu_z}}\ell^2/2 & 0 \\ 0 & 0 & 0 & 0 & 0 & 0 \end{bmatrix} \tag{4.43a}$$

and

$$\left.\frac{\partial \mathscr{F}}{\partial \boldsymbol{\Omega}}\right|_{\text{eq}} \mathbf{M}_{\mathbf{ix}}^{\dagger} = \rho\pi R^3 \begin{bmatrix} 0 & 0 & 0 & 0 \\ 0 & 0 & 0 & 0 \\ \beta_t & 0 & 0 & 0 \\ 0 & \beta_{a,e} & 0 & 0 \\ 0 & 0 & \beta_{a,e} & 0 \\ 0 & 0 & 0 & \beta_r \end{bmatrix} \tag{4.43b}$$

where

$$\begin{aligned} \alpha_H &= C_{H_{\mu_0,\mu_x}} \mu_0 + C_{H_{\mu_x}} \\ \beta_t &= -2C_{T_0} R N_{\text{r}} \Omega_0 + C_{T_{\mu_0}} N_{\text{r}} \nu_0 \\ \beta_{a,e} &= C_{T_0} R N_{\text{r}} \Omega_0 / 2 - C_{T_{\mu_0}} \nu_0 \\ \beta_r &= -C_{Q_0} R^2 N_{\text{r}} \Omega_0 / 2 - C_{Q_{\mu_0}} R \nu_0 \end{aligned}$$

Model 5. *Treating actuator commands as inputs, a linear flight dynamic model about hover is given by Eq. (4.42), where* $\left.\frac{\partial \mathscr{F}}{\partial \boldsymbol{\nu}}\right|_{\text{eq}}$ *and* $\left.\frac{\partial \mathscr{F}}{\partial \boldsymbol{\Omega}}\right|_{\text{eq}} \mathbf{M}_{\mathbf{ix}}^{\dagger}$ *are given in Eq. (4.43) with*

$$\beta_r = \frac{k_{\text{t}} k_{\text{v}}}{R_{\text{m}} \rho\pi R^3}$$

and

$$\mathbf{M}_{\mathbf{ix}} \left.\frac{\partial \boldsymbol{\mathcal{Q}}}{\partial \boldsymbol{\nu}}\right|_{\text{eq}} = \rho\pi R^4 \Omega_0 C_{Q_{\mu_z}} \begin{bmatrix} 0 & 0 & -1 & 0 & 0 & 0 \\ 0 & 0 & 0 & \frac{1}{2} N_{\text{r}} \ell^2 & 0 & 0 \\ 0 & 0 & 0 & 0 & \frac{1}{2} N_{\text{r}} \ell^2 & 0 \\ 0 & 0 & 0 & 0 & 0 & 0 \end{bmatrix} \tag{4.44a}$$

$$\mathbf{M}_{\mathbf{ix}} \left.\frac{\partial \boldsymbol{\mathcal{Q}}}{\partial \boldsymbol{\Omega}}\right|_{\text{eq}} \mathbf{M}_{\mathbf{ix}}^{\dagger} = \rho\pi R^4 (2C_{Q_0} \Omega_0 R + C_{Q_{\mu_0}} \nu_0) \mathbb{I} \tag{4.44b}$$

The two linear models 4 and 5 are similar in structure to previous approaches, such as the one by Cunningham and Hubbard [37], but explicitly connect the linear model parameters to the underlying blade element and momentum theory.

4.4 Multirotor Simulation Experiment

A simulation study was conducted using a high-fidelity multirotor simulation [68] as the "true" dynamics to investigate the utility of the proposed multirotor model. The simulated vehicle is a small, commercial off-the-shelf quadrotor with 14-inch fixed-pitch propellers. The rigid body forces and moments computed in the simulation were obtained from isolated rotor and airframe wind tunnel data [44]. Thus, one may directly query the simulation's aerodynamics database at given vehicle state and control values in a similar manner to wind

tunnel testing and computational aerodynamic prediction techniques. For this analysis, only Model 3 was considered, which was done for two reasons. First, the regressors of Model 1 were highly co-linear for the queried data, which made accurate parameter estimation problematic. Second, since the empirically-derived form of airframe aerodynamics can vary greatly among aircraft and flight regimes, we chose to identify and analyze only rotor-derived terms using data for which the airframe force and moment are set to zero.

The test matrix was designed using design of experiments (DOE) and response surface methodology (RSM) techniques [106], [117] to facilitate accurate identification of the terms included in the postulated multirotor model structure. The test factors directly specified in the experiment included body-frame translational velocity (u, v, w), angular velocity (p, q, r), and rotor speeds (Ω_1, Ω_2, Ω_3, Ω_4). Table 4.1 lists the model terms associated with the model structure where all constant parameters are combined into coefficients for each of these regressors to estimate model parameters using least-squares regression.

Table 4.1: Rotor aerodynamics regressors corresponding to Model 3 (configuration-specific terms are shown in parentheses)

Response	Postulated Regressors
X_r	u, uw, $u\Omega_k$
Y_r	v, vw, $v\Omega_k$
Z_r	Ω_k, $w\Omega_k$, $p\Omega_k$, $q\Omega_k$, u^2, v^2, Ω_k^2
$\mathcal{L}_\mathrm{r}$	v, vw, Ω_k, $u\Omega_k$, $v\Omega_k$, $w\Omega_k$, $p\Omega_k$, Ω_k^2, $(q\Omega_k)$
$\mathcal{M}_\mathrm{r}$	u, uw, Ω_k, $u\Omega_k$, $v\Omega_k$, $w\Omega_k$, $q\Omega_k$, Ω_k^2, $(p\Omega_k)$
$\mathcal{N}_\mathrm{r}$	Ω_k, $u\Omega_k$, $v\Omega_k$, $w\Omega_k$, up, vq, Ω_k^2, $(p\Omega_k, q\Omega_k, pq)$

A response surface experiment design was created using Design-Expert [139] to support estimation of all possible nonlinear and cross model terms up to third-order, which includes each of the terms present in Table 4.1. A cuboidal I-optimal response surface experiment design [6], [57], [106], [117] was used to specify sets of test points defined by values of $\boldsymbol{v}$, $\boldsymbol{\omega}$, and $\boldsymbol{\Omega}$ at which the multirotor simulation is queried. I-optimal response surface designs minimize the integrated prediction variance across the design space for a given model structure. The data used for modeling were collected in three test blocks, each with 300 test points to sequentially improve the design by augmenting the previous blocks, meaning that the design points from previous blocks are considered when creating subsequent blocks. A final fourth test block served as validation data withheld from the model identification process and the points were selected from a uniform distribution using a random number generator. A two-dimensional slice of the experiment design is shown in Figure 4.5, where each block is plotted sequentially (denoted by "$\leq$") to show how the design points progressively fill the design space.

The ranges of factor settings used to conduct the experiment are listed in Table 4.2. The u and v body velocity components as well as the angular velocity bounds were chosen to be

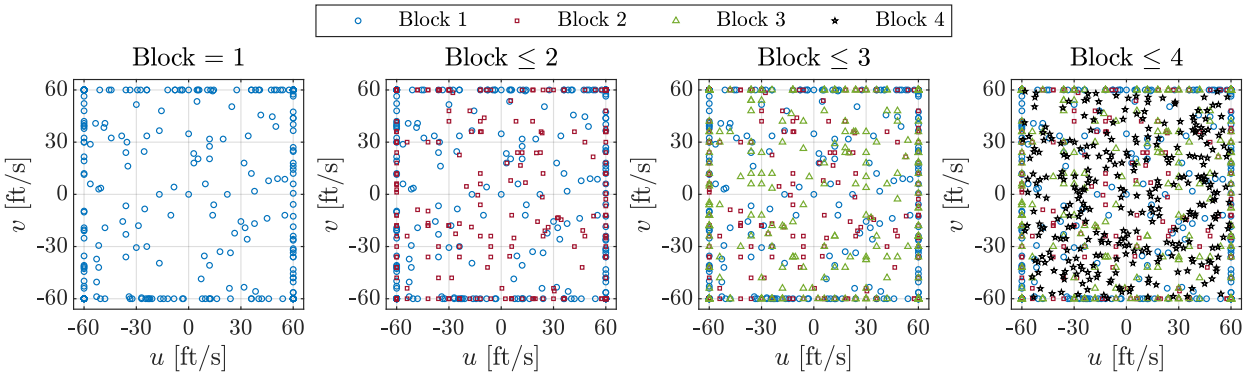

Figure 4.5: Two-dimensional slice of the multirotor simulation experiment design

Table 4.2: Test factor ranges for the multirotor simulation experiment

Factor(s)	Units	Minimum	Maximum
u, v	ft/s	-60	+60
w	ft/s	-60	+8.7
p, q, r	deg/s	-360	+360
$\Omega_1, \Omega_2, \Omega_3, \Omega_4$	rad/s	193	711

operationally representative for the vehicle size. The lower bound on vertical component w was chosen similarly, while the upper bound on w was chosen to be half the hover inflow velocity to avoid regions of flight susceptible to vortex ring state [154]. The bounds on the rotor speeds were chosen from the advance ratio limits of the wind tunnel data for the chosen body velocity limits.

4.5 Modeling Results

Using the queried simulation data from Blocks 1, 2, and 3 of the response surface experiment design, least squares parameter estimates were found for Model 3. A two step approach was used in which least squares regression was first performed independently for each force and moment component to characterize the "best case residuals" as well as the relative importance of terms in the model. Next, a multivariate multiple regression (MMR) approach was used to obtain weighted least-squares parameter estimates for the complete model. The identified model was validated against force and moment data from Block 4 of the response surface experiment design. Furthermore, the relative contributions of each term (regressor times parameter) in the final identified model were evaluated for increasing speeds of steady, forward flight.

4.5.1 Regressor Ordering and Initial Regression

First, the equation-error, ordinary least-squares approach was used to estimate the model parameters for each force and moment equation independently [113, Ch. 5], [80, Ch. 6]. The vector of N outputs for the ith force/moment equation is

$$\boldsymbol{y}_i = \boldsymbol{X}_i \boldsymbol{\theta}_i, \quad i = 1, \ldots, 6 \tag{4.45}$$

where $\boldsymbol{\theta}_i \in \mathbb{R}^{p_i}$ is the vector of unknown parameters that appear in the ith equation and $\boldsymbol{X}_i \in \mathbb{R}^{N \times p_i}$ is the matrix of model regressors. Let $\boldsymbol{z}_i$ be the vector of "measured" outputs from the simulation data for the ith force/moment component. While the outputs at the test points are obtained without error, the underlying wind tunnel data contains random errors which are transferred into $\boldsymbol{z}_i$ in a nonlinear manner. We also recognize there is deterministic residual error between $\boldsymbol{y}_i$ and $\boldsymbol{z}_i$ due to unmodeled aerodynamics. For these reasons, the least-squares solution is not necessarily a minimum mean squared error or maximum likelihood estimate in a statistical sense.

Because the justification for statistical interpretation of the regression results is weak (i.e., the assumptions of a partial F-test do not hold), the coefficient of determination,

$$\mathrm{R}^2 = \frac{\hat{\boldsymbol{y}}^\mathsf{T} \boldsymbol{z} - N\bar{z}^2}{\boldsymbol{z}^\mathsf{T} \boldsymbol{z} - N\bar{z}^2} = 1 - \frac{\mathrm{SS_R}}{\mathrm{SS_T}} \tag{4.46}$$

was used as the metric in a stepwise regression-like procedure to incrementally add all terms to the model in order of their contribution. Here, $\mathrm{SS_R}$ is the sum of squared residuals and $\mathrm{SS_T}$ is the total sum of squares. A stopping criterion is not considered as typically done in stepwise regression. The aim here is to order terms by their relative importance rather than determine a model structure. That is, all hypothesized terms are eventually included in the model.

Specifically, consider a linearly parameterized model with p regressors and let $\mathcal{C} = \{\boldsymbol{x}_1, \ldots, \boldsymbol{x}_p\}$, where $\boldsymbol{x}_j$ represents the jth column of the regressor matrix, $\boldsymbol{X}$. The *forward selection ordering algorithm* (FSOA), formally stated in Algorithm 1, begins by considering a model with only one regressor, where we denote $\mathcal{I}$ (initially the empty set, $\varnothing$) as the ordered set of regressors already added to the model. Linear regression is performed for the set of regressors $\mathcal{I} \cup \{\boldsymbol{x}_i\}$ for each $\boldsymbol{x}_i \in \mathcal{C}$. The coefficients of determination are computed for each of these identified models and denoted $\mathrm{R}^2(\mathcal{I} \cup \{\boldsymbol{x}_i\})$. The candidate regressor that yields the highest R^2 value, is then added to the end of $\mathcal{I}$ and removed from $\mathcal{C}$. This process is repeated until all p terms are included in the ordered set $\mathcal{I}$.

Algorithm 1: FSOA

Input: $\mathcal{C} = \{\boldsymbol{x}_1, \ldots, \boldsymbol{x}_p\}$
Output: $\mathcal{I}$
$\mathcal{I} \leftarrow \varnothing$
while $\mathcal{C} \neq \varnothing$ **do**
  $\boldsymbol{\xi} \leftarrow \underset{\boldsymbol{x} \in \mathcal{C}}{\arg\max}\ \mathrm{R}^2\left(\mathcal{I} \cup \{\boldsymbol{x}\}\right)$
  $\mathcal{I} \leftarrow \mathcal{I} \cup \{\boldsymbol{\xi}\}$
  $\mathcal{C} \leftarrow \mathcal{C} \setminus \{\boldsymbol{\xi}\}$
end

The FSOA results are given in Tables 4.3–4.6, where the boldface values indicate the term that yields the largest R^2 value. Note the R^2 values in Tables 4.3–4.6 may be negative, indicating the addition of that term produces a fit worse than a constant model. For each

Table 4.3: Model 3 X_r and Y_r regressors ordered by relative importance

	R^2 [%]		
Iter.	$C_{H_{\mu_x}}$	$C_{H_{\mu_0,\mu_x}}$	$C_{H_{\mu_x,\mu_z}}$
1	**97.4**	96.6	48.0
2	–	**98.7**	98.3
3	–	–	**99.2**

Table 4.4: Model 3 Z_r regressors ordered by relative importance

	R^2 [%]			
Iter.	C_{T_0}	$C_{T_{\mu_0}}$	$C_{T_{\mu_x^2}}$	$C_{T_{\mu_z}}$
1	**39.4**	31.3	−14.4	−177.3
2	–	39.7	40.1	**96.5**
3	–	96.7	**98.4**	–
4	–	**98.6**	–	–

of the models containing all regressors (the last rows of Tables 4.3–4.6), the coefficients of determination (R^2), normalized root mean squared errors (NRMSE),

$$\mathrm{NRMSE} = \frac{1}{\mathrm{range}(\boldsymbol{z})}\sqrt{\frac{1}{N}(\boldsymbol{z}-\hat{\boldsymbol{y}})^\mathsf{T}(\boldsymbol{z}-\hat{\boldsymbol{y}})} \tag{4.47}$$

and estimated model residual variances,

$$\hat{\sigma}^2 = \frac{1}{N-p}\sum_{k=1}^{N}(z(k)-\hat{y}(k))^2 \tag{4.48}$$

Table 4.5: Model 3 $\mathcal{L}_\mathrm{r}$ and $\mathcal{M}_\mathrm{r}$ regressors ordered by relative importance

	R^2 [%]						
Iter.	$C_{R_{\mu_x}}$	C_{T_0}	$C_{T_{\mu_0}}$	$C_{T_{\mu_z}}$	$C_{H_{\mu_x}}$	$C_{H_{\mu_0,\mu_x}}$	$C_{H_{\mu_x,\mu_z}}$
1	0.5	**83.6**	81.7	13.4	6.5	5.7	0.8
2	84.1	–	83.6	**90.4**	89.8	89.2	84.5
3	90.9	–	90.5	–	**96.4**	95.8	91.3
4	96.8	–	96.4	–	–	96.4	**96.9**
5	**97.3**	–	96.9	–	–	96.9	–
6	–	–	**97.4**	–	–	97.3	–
7	–	–	–	–	–	**97.4**	–

Table 4.6: Model 3 $\mathcal{N}_\mathrm{r}$ regressors ordered by relative importance

	R^2 [%]					
Iter.	C_{Q_0}	$C_{Q_{\mu_0}}$	$C_{Q_{\mu_z}}$	$C_{Q_{\mu_z^2}}$	$C_{H_{\mu_x}}$	$C_{H_{\mu_x,\mu_z}}$
1	**47.2**	45.8	19.8	0.0	27.8	0.2
2	–	47.2	47.2	47.2	**74.4**	47.5
3	–	74.5	74.4	74.5	–	**74.6**
4	–	**74.7**	74.7	74.7	–	–
5	–	–	74.7	**74.7**	–	–
6	–	–	**74.7**	–	–	–

Table 4.7: Model 3 Initial regression results

Component	R^2 [%]	$\hat{\sigma}^2$	NRMSE [%]
X_r	99.2	1.28×10^{-2}	2.50
Y_r	99.2	1.30×10^{-2}	2.43
Z_r	98.6	5.31×10^{-1}	2.29
$\mathcal{L}_\mathrm{r}$	97.4	1.97×10^{-1}	2.34
$\mathcal{M}_\mathrm{r}$	97.4	1.90×10^{-1}	2.15
$\mathcal{N}_\mathrm{r}$	74.7	2.79×10^{-2}	9.62

were computed. These three metrics are given in Table 4.7 for Model 3.

Using these results, we can relate each parameter in Model 3 to its definition in Eq. (4.13) to obtain insight into the predominant physical effects captured by the model. In the X_r and Y_r force components, the most influential model terms are $C_{H_{\mu_x}}\{u, v\}\delta t$, which come from the rotor blade drag coefficient. For example,

$$C_{H_{\mu_x}} u\delta t = \frac{1}{2a} C_\sigma \bar{c}_d u \frac{1}{N_\mathrm{r}} \sum_{i=1}^{N_\mathrm{r}} \Omega_i \tag{4.49}$$

where $C_{H_{\mu_x}} = \frac{1}{2a} C_\sigma \bar{c}_d$ from Eq. (4.13) and $\delta t = \frac{1}{N_\mathrm{r}} \sum_{i=1}^{N_\mathrm{r}} \Omega_i$ from Eq. (4.30). The remaining terms stem from the inflow velocity effects. In the Z_r force equation, the dominant term is $C_{T_0}\delta^2 t$, which comes from the sum of blade-element lift due to rotor speed. This is often the only effect included in control applications. However, we see the subsequent addition of term containing $C_{T_{\mu_z}}$ greatly increases the R^2 value, indicating its overall importance. In the rolling and pitching moment equations, the most important terms are $C_{T_0}\delta^2\{a, e\}$, which come from the difference in lift due to the difference in rotor speeds (similar to $C_{T_0}\delta^2 t$ in Z_r). Finally, the most significant term in the yawing moment is $C_{Q_0}\delta^2 r$, which models the rotor profile drag due to the difference in rotor speeds [83, Sec. 5-3]. The second most influential term is $C_{H_{\mu_x}}(u\delta a + v\delta e)$, which models the yawing moment due to differential rotor blade drag under virtual aileron and elevator commands (previously mentioned in Section 4.3.2). In the yawing moment, the addition of the final three terms does not appreciably increase the R^2 value. While blade element theory indicates the presence of these terms, their importance is low for the given simulation data. Overall, these results and this approach, in general, help to inform the model selection process for a given application. It is important to note that the magnitude of the yawing moment data was an order of magnitude smaller than the other moments, thus leading to a lower signal-to-noise ratio.

4.5.2 Multivariate Multiple Regression and Validation

Recognizing that parameters are shared among axes, the estimates in Section 4.5.1 are not obtained using all possible data. For example, the parameter $C_{H_{\mu_x}}$ appears in all but the F_z equation, but is estimated five separate times. One approach for reconciling the five distinct estimates of this single parameter is to compute a weighted average of these estimates by the inverse of their variance [158, Ch. 4]:

$$\hat{\theta}_i = \frac{\sum_{j=1}^{p_i} \beta_{ij} \hat{\theta}_{ij}}{\sum_{j=1}^{p_i} \beta_{ij}} \tag{4.50}$$

where $\beta_{ij} = 1/\sigma_{ij}^2$. The variance of the weighted parameter estimate is then $\sigma_i^2 = 1/\sum_{j=1}^{p_i} \beta_{ij}$. However, Eq. (4.50) assumes correct parameter variances, which is hard to justify in this deterministic interpretation of the least squares solution. Another approach is to include data from all force and moment components to simultaneously estimate these parameters, which has three main benefits. First, the independent models for each axis may be overfit – especially the rotor aerodynamic moments. This alternative approach greatly reduces the total number of parameters to be identified. Second, all data are used to estimate the set of parameters. For example, $C_{H_{\mu_x}}$ can be estimated using five times as many measurements. Third, as will be detailed shortly, the residuals of the initial deterministic regression in Section 4.5.1 can justify a statistical interpretation of the final parameter estimates.

Considering all force and moment components, the output of the kth test point, $\boldsymbol{y}(k) = [y_1(k) \ \cdots \ y_6(k)]^\mathsf{T} \in \mathbb{R}^6$, is

$$\boldsymbol{y}(k) = \boldsymbol{H}(\boldsymbol{v}(k), \boldsymbol{\omega}(k), \boldsymbol{\Omega}(k))\boldsymbol{\theta} \tag{4.51}$$

where $\boldsymbol{\theta} \in \mathbb{R}^{n_\theta}$ is the vector of proposed parameters and $\boldsymbol{H} : \mathbb{R}^3 \times \mathbb{R}^3 \times \mathbb{R}^{N_\mathrm{r}} \to \mathbb{R}^{6 \times n_\theta}$ is the regressor function for the model. The "measured" output of this model is

$$\boldsymbol{z}(k) = \boldsymbol{y}(k) + \boldsymbol{w}(k) \tag{4.52}$$

where each $\boldsymbol{w}(k)$ is assumed to be independently sampled from a Gaussian distribution. Let $\tilde{\boldsymbol{w}}(k) = \hat{\boldsymbol{y}}(k) - \boldsymbol{z}(k)$ where $\hat{\boldsymbol{y}}(k) = [\hat{y}_1(k) \ \cdots \ \hat{y}_6(k)]^\mathsf{T}$ was computed through the initial regression in Section 4.5.1. The mean and covariance of $\boldsymbol{w}(k)$ are then respectively approximated by

$$\bar{\boldsymbol{w}} = \mathrm{E}\left\{\boldsymbol{w}(k)\right\} \approx \frac{1}{N} \sum_{j=1}^{N} \tilde{\boldsymbol{w}}(j) \approx \boldsymbol{0} \tag{4.53a}$$

$$\boldsymbol{R} = \mathrm{E}\left\{[\boldsymbol{w}(k) - \bar{\boldsymbol{w}}][\boldsymbol{w}(k) - \bar{\boldsymbol{w}}]^\mathsf{T}\right\} \approx \frac{1}{N-1} \sum_{j=1}^{N} \tilde{\boldsymbol{w}}(j)\tilde{\boldsymbol{w}}^\mathsf{T}(j) \tag{4.53b}$$

The diagonal elements of $\boldsymbol{R}$ are given in Table 4.7 as $\hat{\sigma}^2$. The validity of the Gaussian assumption is qualitatively evaluated in Figures 4.6 and 4.7 by fitting a Gaussian probability density function to the histogram of residual data and plotting the inverse cumulative distribution function (ICDF), $\Phi^{-1}(P(k))$, against the ordered model residuals. The model residuals appear to follow the shape of a normal distribution (shown as the red line in Figure 4.6), and the ordered residuals are mostly linear with respect to the ICDF. The least "Gaussian" residuals appear in the Z_r data, where very positive residuals occur with higher probability than a Gaussian distribution would predict. However, Figure 4.7 shows a straight line is formed by residuals closer to zero, which are more influential in the validity of statistical conclusions [113, Ch. 5]. Altogether, these results indicate normality of the residuals is a reasonable assumption.

With the measurement model determined and random measurement errors characterized, statistical estimates of the model parameters were obtained using multivariate multiple regression (MMR) [80, Ch. 6]. Let

$$\boldsymbol{\mathcal{Z}} = \begin{bmatrix} \boldsymbol{z}(1) \\ \boldsymbol{z}(2) \\ \vdots \\ \boldsymbol{z}(N) \end{bmatrix} \qquad \boldsymbol{\mathcal{H}} = \begin{bmatrix} \boldsymbol{H}(\boldsymbol{v}(1), \boldsymbol{\omega}(1), \boldsymbol{\Omega}(1)) \\ \boldsymbol{H}(\boldsymbol{v}(2), \boldsymbol{\omega}(2), \boldsymbol{\Omega}(2)) \\ \vdots \\ \boldsymbol{H}(\boldsymbol{v}(N), \boldsymbol{\omega}(N), \boldsymbol{\Omega}(N)) \end{bmatrix} \qquad \boldsymbol{\mathcal{W}} = \begin{bmatrix} \boldsymbol{w}(1) \\ \boldsymbol{w}(2) \\ \vdots \\ \boldsymbol{w}(N) \end{bmatrix} \tag{4.54}$$

The stacked vector of model outputs is given by $\boldsymbol{\mathcal{Z}} = \boldsymbol{\mathcal{H}}\boldsymbol{\theta} + \boldsymbol{\mathcal{W}}$, and the covariance matrix for $\boldsymbol{\mathcal{W}}$ is $\boldsymbol{\mathcal{R}} = \boldsymbol{R} \otimes \mathbb{I}_N$, where $\otimes$ is the Kronecker product and $\mathbb{I}_N$ is the $N \times N$ identity matrix. Then, the parameter estimates are given by the weighted least squares solution

$$\hat{\boldsymbol{\theta}} = (\boldsymbol{\mathcal{H}}^\mathsf{T}\boldsymbol{\mathcal{R}}^{-1}\boldsymbol{\mathcal{H}})^{-1}\boldsymbol{\mathcal{H}}^\mathsf{T}\boldsymbol{\mathcal{R}}^{-1}\boldsymbol{\mathcal{Z}} \tag{4.55}$$

and the output of the kth test point is $\hat{\boldsymbol{y}}(k) = \boldsymbol{H}(\boldsymbol{v}(k), \boldsymbol{\omega}(k), \boldsymbol{\Omega}(k))\hat{\boldsymbol{\theta}}$. Because each $\boldsymbol{w}(k)$ was assumed to be independently sampled from a Gaussian distribution, these parameter

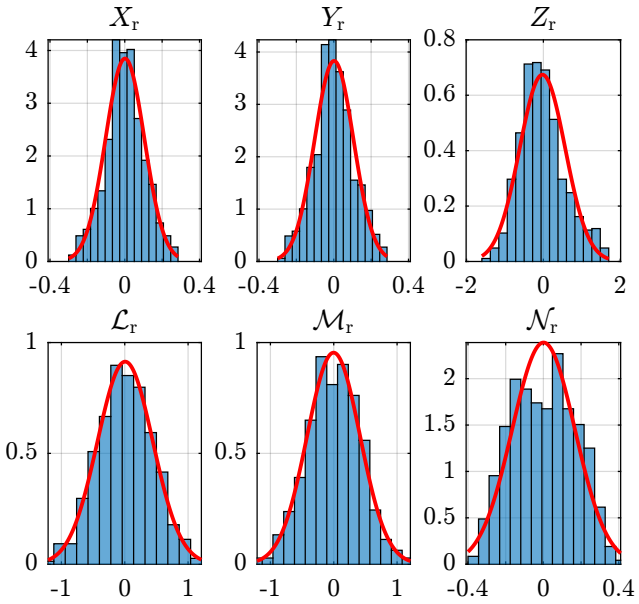

Figure 4.6: Probability density of residuals for Model 3

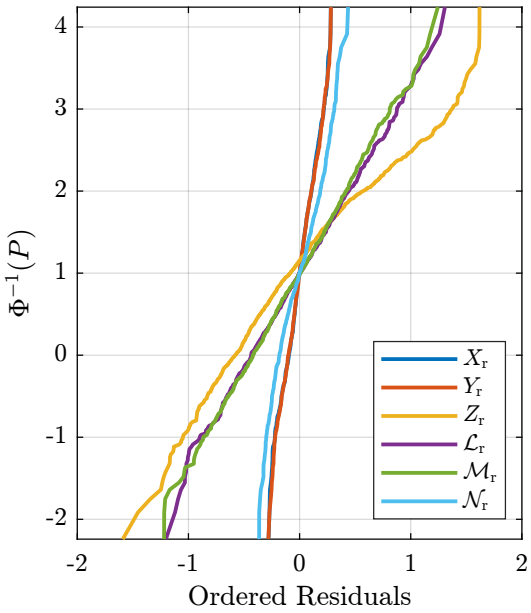

Figure 4.7: Normality of residuals for Model 3

estimates are both minimum mean square error (MMSE) and maximum likelihood (ML) estimates [16, Ch. 2].

The statistical significance of each of the identified parameters is evaluated using the t-

statistic,

$$t_{0_j} = \frac{\hat{\theta}_j}{\sigma(\hat{\theta}_j)} \tag{4.56}$$

where $\sigma(\hat{\theta}_j)$ is the estimated standard deviation of the $\hat{\theta}_j$. The null hypothesis, $H_0 : \hat{\theta}_j = 0$, is rejected with a significance level of α if $|t_{0_j}| > t(\alpha/2, N-n_\theta)$, and the alternate hypothesis, $H_1 : \hat{\theta}_j \neq 0$, is accepted. Here, $t(\alpha/2, N - n_\theta)$ is the sample of a one-tail t-distribution with confidence $\alpha/2$ and $N - n_\theta$ degrees of freedom. Alternatively, the P-value can be used to give the probability of the null hypothesis, H_0. In other words, it is the smallest significance level that results in the rejection of H_0 [106, pg. 40]. It is given by

$$\mathrm{P}\left\{H_0\right\} = 2\left(1 - F_t\left(|t_{0_j}|, N - n_\theta\right)\right) \tag{4.57}$$

where $F_t\left(|t_{0_j}|, N - n_\theta\right)$ is the cumulative distribution function of the $N - n_\theta$ degree-of-freedom one-tail t-distribution evaluated at $|t_{0_j}|$. If $\mathrm{P}\left\{H_0\right\} < \alpha$, then H_0 is rejected and θ_j is statistically different from zero.

The MMR results are tabulated in Table 4.8, where $\mathrm{R}^2_{\mathrm{MMR}}$ and $\mathrm{NRMSE}_{\mathrm{MMR}}$ are the coefficient of determination and normalized root mean square error for the weighted least squares solution, respectively. Another useful measure of model fit included in Table 4.8 is Theil's inequality coefficient (TIC),

$$\mathrm{TIC}_i = \frac{\sqrt{\frac{1}{N}(\hat{\boldsymbol{y}}_i - \boldsymbol{z}_i)^\mathsf{T}(\hat{\boldsymbol{y}}_i - \boldsymbol{z}_i)}}{\sqrt{\frac{1}{N}\hat{\boldsymbol{y}}_i^\mathsf{T}\hat{\boldsymbol{y}}_i} + \sqrt{\frac{1}{N}\boldsymbol{z}_i^\mathsf{T}\boldsymbol{z}_i}} \tag{4.58}$$

which is normalized between zero and one with zero indicating perfect fit [80, Ch. 11]. The parameter estimates computed using Eq. (4.55) are given in Table 4.9 along with their standard deviation, t-statistic, and P-value (given to double precision). It can be seen that most parameter standard deviations are at least an order of magnitude less than their estimates. The notable exceptions are $C_{Q_{\mu_0}}$, $C_{Q_{\mu_z}}$, and $C_{Q_{\mu_z^2}}$. This is also seen in their t-statistics and P-values. While blade element theory indicates the presence of these terms, their statistical significance is low for the given simulation data. This result indicates these terms are not statistically significant using the available data. However, additional data or sampling approaches may reveal their significance to the yawing moment. Note that the variance-weighted estimates using Eq. (4.50) resulted in generally similar results to the MMR approach except for $C_{T_{\mu_0}}$ which had a 45% smaller mean but the same standard deviation. It is hypothesized that overfit in the initial regression of the rolling and pitching moments caused this discrepancy.

Finally, the identified models were validated against the force and moment data from Block 4 of the response surface experiment design. The validation metrics are given in Table 4.10. It can be seen that the axes that validate most poorly as compared to the model fit are the rolling and pitching moments. Due to the moment arm effects of rotor drag forces,

Table 4.8: Model 3 MMR results

Component	NRMSE [%]	TIC
X_r	2.55	0.046
Y_r	2.48	0.046
Z_r	2.31	0.035
$\mathcal{L}_\mathrm{r}$	3.77	0.133
$\mathcal{M}_\mathrm{r}$	3.55	0.135
$\mathcal{N}_\mathrm{r}$	9.64	0.272
$\mathrm{R}^2_{\mathrm{MMR}} = 98.4\%,\ \mathrm{NRMSE}_{\mathrm{MMR}} = 1.85\%$		

Table 4.9: Model 3 MMR parameter estimates

Parameter	Estimate	Std. Dev.	$\lvert t_0 \rvert$	P-value
$C_{H_{\mu_x}}$	6.38×10^{-3}	1.08×10^{-4}	59.10	0.00
$C_{H_{\mu_0,\mu_x}}$	6.65×10^{-2}	1.68×10^{-3}	39.59	3.59×10^{-301}
$C_{H_{\mu_x,\mu_z}}$	-1.05×10^{-2}	3.16×10^{-4}	33.14	2.22×10^{-219}
C_{T_0}	1.48×10^{-2}	1.44×10^{-4}	102.65	0.00
$C_{T_{\mu_0}}$	3.29×10^{-2}	3.53×10^{-3}	9.33	1.57×10^{-20}
$C_{T_{\mu_x^2}}$	4.57×10^{-2}	1.50×10^{-3}	30.51	1.09×10^{-188}
$C_{T_{\mu_z}}$	-7.05×10^{-2}	3.85×10^{-4}	182.94	0.00
$C_{R_{\mu_x}}$	1.14×10^{-2}	8.22×10^{-4}	13.88	4.57×10^{-43}
C_{Q_0}	1.31×10^{-3}	2.59×10^{-4}	5.08	3.91×10^{-7}
$C_{Q_{\mu_0}}$	-5.12×10^{-3}	7.70×10^{-3}	0.67	5.06×10^{-1}
$C_{Q_{\mu_z}}$	-3.49×10^{-4}	7.74×10^{-4}	0.45	6.51×10^{-1}
$C_{Q_{\mu_z^2}}$	6.22×10^{-2}	1.06×10^{-1}	0.59	5.57×10^{-1}

these model structures contain the highest number of terms and thus are susceptible to overfit. This observation along with the FSOA results of Section 4.5.1 indicate that system identification efforts may benefit from the removal of terms such as $C_{H_{\mu_0,\mu_x}}$ and $C_{T_{\mu_0}}$ from the rolling and pitching moments, which did not increase the coefficient of determination by any appreciable amount.

4.5.3 Steady Flight Analysis

The regressor importance analysis in Section 4.5.1 is based on the the ensemble of data across a broad range of conditions. For motion in the neighborhood of some nominal flight condition, however, the relative importance of regressors may differ. For this reason, we also consider the relative contributions of model terms (regressors times parameters) throughout increasing speeds of forward flight.

Using the high-fidelity simulation environment described by Foster and Hartman [44], the

Table 4.10: Model 3 validation metrics

Component	$\hat{\sigma}^2$	NRMSE [%]	TIC
X_r	1.04×10^{-2}	2.26	0.046
Y_r	9.50×10^{-3}	2.00	0.045
Z_r	3.97×10^{-1}	2.84	0.042
$\mathcal{L}_\mathrm{r}$	2.86×10^{-1}	5.14	0.158
$\mathcal{M}_\mathrm{r}$	2.76×10^{-1}	4.68	0.148
$\mathcal{N}_\mathrm{r}$	1.75×10^{-2}	9.52	0.291

family of equilibrium constant altitude, forward flight conditions was numerically determined for airspeeds ranging from zero to 60 ft/s. Next, the normalized contributions of model terms across these forward flight conditions were evaluated. For the ith force/moment component, let the jth term be denoted $y_{ij} = h_{ij}\theta_j$, where h_{ij} is the i,j-element of the regressor matrix $\boldsymbol{H}$ in Eq. (4.51). Since these steady motions are characterized by zero applied moment and side-force, we qualitatively evaluate the normalized contributions of modeled terms $\hat{X}_{\mathrm{r},j}$ and $\hat{Z}_{\mathrm{r},j}$ in the X_r and Z_r forces as shown in Figures 4.8a and 4.8b, respectively.

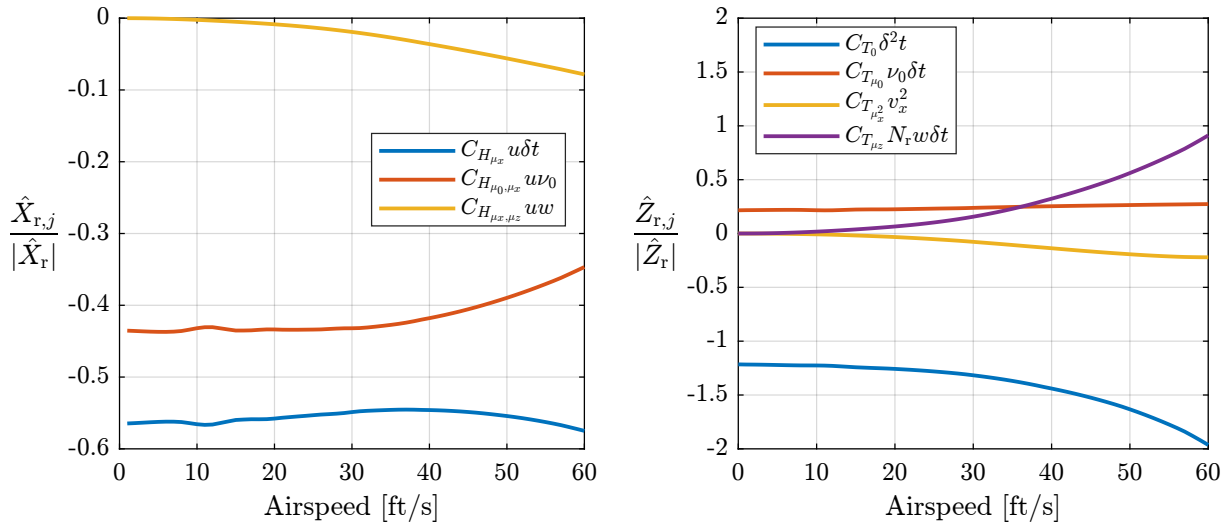

(a) X_r model term contributions

(b) Z_r model term contributions

Figure 4.8: Model term contributions in forward flight

For the X_r force component, the most important term across all forward flight conditions is $C_{H_{\mu x}} u\delta t$, which is in agreement with the FSOA results. Additionally, we see that as airspeed increases, the importance of the term $C_{H_{\mu_x,\mu_z}} uw$ increases. This result should be kept in mind for control and estimation applications involving flight at high speeds. The Z_r force component tells a more interesting story. Again, the most important term, $C_{T_0}\delta^2 t$, agrees with the FSOA results. However, the magnitude of $C_{T_{\mu_z}}(N_\mathrm{r} w\delta t - \Delta\nu_Z)$ (one of the least

important terms at low speeds) rapidly increases with airspeed. The intersection of curves in Figure 4.8b represents forward speeds at which the relative importance of terms changes.

Chapter 5

Robust Control for System Identification of Unstable Aircraft

5.1 Introduction

Large domain flight dynamic models, such as those derived in Chapter 4, are often required for estimation and control design. In contrast with numerical or wind tunnel data, flight data is preferred because it captures the true, full-scale dynamics of the aircraft under real-world operating conditions. However, accurately estimating model parameters from flight data is a non-trivial task. For fixed-wing aircraft, the use of orthogonal phase-optimized multisine excitation signals (*multisines* for short) and multivariate orthogonal function (MOF) modeling have been successfully used to obtain global flight data and model structures, respectively [60], [107]. Note that in this context, the term *global* refers to the feasible flight envelope as opposed to the full mathematical state space. The use of multisines and MOF modeling works very well for statically stable aircraft that can be excited in an open-loop manner, that is, without feedback stabilization. For unstable aircraft such as multirotor air vehicles, on the other hand, a nominal trajectory must be stabilized before actuator excitation can be applied. Therefore, an iterative approach is generally used, with each iteration involving data collection, model identification, control law design, and robustness analysis [149]. Part of the difficulty in this process stems from the fact that a stabilizing control law tends to introduce correlation, suppress dynamics of interest, and amplify artificial dynamics [80, Ch. 9]. More importantly, it is possible that input excitation signals used for model identification may drive the system outside the region of attraction of the locally stable reference motion. This chapter details a methodology for obtaining uncorrelated large-domain excitation data while guaranteeing stability.

Identification of unstable aircraft can be done using either open-loop or closed-loop flight data. The former approach is only feasible, however, over time horizons that are short relative to the growth of the fastest unstable mode. This means global excitation data cannot be obtained in a continuous experiment. Having continuous, large-domain experimental data simplifies data collection and supports time-domain model identification methods such as output-error, filter-error, and Kalman filtering methods [80], [113]. To alleviate the practical issues associated with open-loop excitation, experimental data for unstable aircraft is typically obtained under stabilizing closed-loop control. Since we are interested in flight dynamic models for control and estimation purposes, we desire an open-loop model from

closed-loop flight data. This is often done for linear model identification of multirotor aircraft [37]. However, in applications where the model must be applicable over a large domain, a nonlinear model must be identified [36]. In this chapter, we aim to concurrently design a controller and an excitation signal that allow for larger amplitude excitation suitable for identifying large-domain nonlinear models. Larger excitations provide better signal-to-noise ratio (SNR), which is important in identifying flight dynamic models for small UAS [137]. These observations further motivate the need to develop safe methods of performing large-amplitude identification maneuvers for unstable UAS.

While we focus on the multirotor, the methods presented here apply to unstable fixed-wing configurations as well as vertical takeoff and landing (VTOL) aircraft, including hybrid aircraft that transition between rotor-borne and wing-borne flight regimes. The approach we present involves two data collection phases of the system identification process as opposed to the traditional approach of incremental flight envelope expansions. First, linear time invariant (LTI) models are identified about a set of specific flight conditions, which are determined using a hypothesized model structure for the aerodynamic force and moment. The identified models define an uncertain linear parameter-varying (LPV) system. Next, input excitation signals and a reference trajectory are concurrently designed along with a robust LPV control law that places a sub-optimal H_∞ norm bound on the map from input excitation to perturbation from this reference. Finally, this control law is used in the second phase of data collection in which the UAS is capable of fully-automated flights that span the desired flight domain in an efficient and safe manner for obtaining informative, uncorrelated data for nonlinear model identification.

The rest of this chapter, which is based on reference [76], is organized as follows. Section 5.2 introduces the small quadrotor aircraft used to demonstrate the proposed methodology and presents the assumptions required to formulate the rigid-body aircraft dynamics (2.15) as a polytopic LPV system. The initial model identification process is detailed in Section 5.3, which involves the first phase of data collection in the proposed methodology. Section 5.4 covers the development of excitation and reference signals along with the formulation of the H_∞ performance measure. The robust control design and closed-loop analysis is presented in Section 5.5. Finally, Section 5.6 presents simulation results for the automated system identification flight experiment — the second and final phase of flight data collection.

5.2 LPV Flight Dynamic Modeling

5.2.1 General System of Consideration

The proposed modeling methodology begins with the postulation of a nonlinear flight dynamic model for the aircraft of interest. Here, we consider the rigid-body aircraft dynamics (2.15) with an Euler angle parameterization for the attitude rotation matrix. Specifically,

$$\boldsymbol{R}_{\mathrm{IB}} = e^{\boldsymbol{S}(\boldsymbol{e}_3\psi)} e^{\boldsymbol{S}(\boldsymbol{e}_2\theta)} e^{\boldsymbol{S}(\boldsymbol{e}_1\phi)} \tag{5.1}$$

where ϕ, θ, and ψ are the roll, pitch, and yaw angles of the aircraft, respectively, and $\boldsymbol{e}_1 = [1\ 0\ 0]^\mathsf{T}$, etc. With $\boldsymbol{\Theta} = [\phi\ \theta\ \psi]^\mathsf{T}$, the rotational kinematics (2.9) become

$$\dot{\boldsymbol{\Theta}} = \underbrace{\begin{bmatrix} 1 & \sin\phi\tan\theta & \cos\phi\tan\theta \\ 0 & \cos\phi & -\sin\phi \\ 0 & \sin\phi\sec\theta & \cos\phi\sec\theta \end{bmatrix}}_{\boldsymbol{L}_{\mathrm{IB}}} \underbrace{\begin{bmatrix} p \\ q \\ r \end{bmatrix}}_{\boldsymbol{\omega}} \tag{5.2}$$

Considering a quasi-steady aerodynamic model, the generalized force $\mathscr{F}$ is a function of the generalized velocity $\boldsymbol{\nu}$, the m aircraft control inputs composing $\boldsymbol{\delta}$, and a parameter vector $\boldsymbol{\vartheta}$ which we ultimately aim to estimate. Considering a smooth model, we can (in a non-unique manner) always write

$$\mathscr{F}(\boldsymbol{\nu}, \boldsymbol{\delta}; \boldsymbol{\vartheta}) = \mathscr{A}(\boldsymbol{\rho}(\boldsymbol{\nu}), \boldsymbol{\delta}; \boldsymbol{\vartheta})\boldsymbol{\nu} + \mathscr{B}(\boldsymbol{\delta}; \boldsymbol{\vartheta}) \tag{5.3}$$

where $\mathscr{A}(\boldsymbol{\rho}(\boldsymbol{\nu}), \boldsymbol{\delta}; \boldsymbol{\vartheta}) \in \mathbb{R}^{6\times 6}$ and $\mathscr{B}(\boldsymbol{\delta}; \boldsymbol{\vartheta}) \in \mathbb{R}^6$. The matrix $\mathscr{A}$ contains functions $\boldsymbol{\rho}$ of the generalized velocity $\boldsymbol{\nu}$ that describe the model's *dominant nonlinearities*. As an example, the longitudinal aerodynamics of a fixed-wing aircraft depend on the angle-of-attack, $\alpha = \tan^{-1}(w/u) = \rho(\boldsymbol{\nu})$, which appears as the dominant nonlinearity (e.g., α and α^2 are important regressor functions).

To simplify control synthesis, we aim to formulate the nonlinear dynamics as a *quasi*-LPV system that is affine in $\boldsymbol{\rho}$, which we take to be a scheduling parameter (recognizing that $\boldsymbol{\rho}$ is, in fact, a function of the system state). To this end, let

$$\bar{\mathscr{F}}(\boldsymbol{\rho}, \boldsymbol{\nu}, \boldsymbol{\delta}; \boldsymbol{\vartheta}) = \mathscr{A}(\boldsymbol{\rho}, \boldsymbol{\delta}; \boldsymbol{\vartheta})\boldsymbol{\nu} + \mathscr{B}(\boldsymbol{\delta}; \boldsymbol{\vartheta}) \tag{5.4}$$

We then consider $\boldsymbol{\rho}(t) = \boldsymbol{\rho}(\boldsymbol{\nu}(t))$ to be a known, exogenous signal so that a first-order Taylor series approximation of $\bar{\mathscr{F}}$ with respect to its second and third arguments about $(\boldsymbol{\nu}_0, \boldsymbol{\delta}_0)$ reads

$$\bar{\mathscr{F}}(\boldsymbol{\rho}, \boldsymbol{\nu}, \boldsymbol{\delta}; \boldsymbol{\vartheta}) \approx \bar{\mathscr{F}}(\boldsymbol{\rho}, \boldsymbol{\nu}_0, \boldsymbol{\delta}_0; \boldsymbol{\vartheta}) + \partial_2\bar{\mathscr{F}}(\boldsymbol{\rho}, \boldsymbol{\nu}_0, \boldsymbol{\delta}_0; \boldsymbol{\vartheta})(\boldsymbol{\nu} - \boldsymbol{\nu}_0) + \partial_3\bar{\mathscr{F}}(\boldsymbol{\rho}, \boldsymbol{\nu}_0, \boldsymbol{\delta}_0; \boldsymbol{\vartheta})(\boldsymbol{\delta} - \boldsymbol{\delta}_0) \tag{5.5}$$

where $\partial_j\bar{\mathscr{F}}(\cdot)$ is the Jacobian of $\bar{\mathscr{F}}$ with respect to its jth argument, evaluated at $(\cdot)$. Define

$$\boldsymbol{\mathcal{A}}(\boldsymbol{\rho}; \boldsymbol{\vartheta}) \coloneqq \partial_2\bar{\mathscr{F}}(\boldsymbol{\rho}, \boldsymbol{\nu}_0(\boldsymbol{\rho}), \boldsymbol{\delta}_0(\boldsymbol{\rho}); \boldsymbol{\vartheta}) \quad \text{and} \quad \boldsymbol{\mathcal{B}}(\boldsymbol{\rho}; \boldsymbol{\vartheta}) \coloneqq \partial_3\bar{\mathscr{F}}(\boldsymbol{\rho}, \boldsymbol{\nu}_0(\boldsymbol{\rho}), \boldsymbol{\delta}_0(\boldsymbol{\rho}); \boldsymbol{\vartheta}) \tag{5.6}$$

where we have implicitly assumed the equilibrium generalized velocity $\boldsymbol{\nu}_0$ and actuator values $\boldsymbol{\delta}_0$ can be expressed as functions of the model's dominant nonlinearities $\boldsymbol{\rho}$. Consider the following assumption.

Assumption 5.1. *The matrix functions $\boldsymbol{\mathcal{A}}$ and $\boldsymbol{\mathcal{B}}$ are affine in $\boldsymbol{\rho}$.*

It is important to realize nonlinearities exist in the system besides in the aerodynamics. Therefore, we assume the aircraft's steady-state roll and pitch angles remain small such that their equilibrium values vary affinely in the model's dominant nonlinearities, $\boldsymbol{\rho}$.

Assumption 5.2. *All equilibrium values of ϕ_0 and θ_0 in a prescribed domain of interest affinely depend on $\boldsymbol{\rho}$.*

Referring to Eq. (2.15), Assumption 5.2 is important in ensuring that Jacobians of the drift vector field $\boldsymbol{f} = (\boldsymbol{f}_\eta, \boldsymbol{f}_\nu)$ affinely depend on $\boldsymbol{\rho}$. Since there is no position or heading angle tracking objective for system identification, consider the reduced configuration vector $\boldsymbol{\eta}_r = [\phi \ \theta]^\mathsf{T}$ and let $\boldsymbol{f}_{\eta_r}(\boldsymbol{\eta}_r, \boldsymbol{\nu})$ be defined by the first two rows of Eq. (5.2). We then have the Jacobians

$$\begin{aligned} \boldsymbol{A}_{\eta_r,\eta_r}(\boldsymbol{\rho}) &\coloneqq \partial_1 \boldsymbol{f}_{\eta_r}(\boldsymbol{\eta}_{r,0}(\boldsymbol{\rho}), \boldsymbol{\nu}_0(\boldsymbol{\rho})), \quad & \boldsymbol{A}_{\eta_r,\nu}(\boldsymbol{\rho}) &\coloneqq \partial_2 \boldsymbol{f}_{\eta_r}(\boldsymbol{\eta}_{r,0}(\boldsymbol{\rho}), \boldsymbol{\nu}_0(\boldsymbol{\rho})) \\ \boldsymbol{A}_{\nu,\eta_r}(\boldsymbol{\rho}) &\coloneqq \partial_1 \boldsymbol{f}_{\nu}(\boldsymbol{\eta}_0(\boldsymbol{\rho}), \boldsymbol{\nu}_0(\boldsymbol{\rho})), \quad & \boldsymbol{A}_{\nu,\nu}(\boldsymbol{\rho}) &\coloneqq \partial_2 \boldsymbol{f}_{\nu}(\boldsymbol{\eta}_0(\boldsymbol{\rho}), \boldsymbol{\nu}_0(\boldsymbol{\rho})) \end{aligned} \tag{5.7}$$

Assumption 5.3. *The roll and pitch angles remain sufficiently small such $\boldsymbol{A}_{\eta_r,\eta_r}$, $\boldsymbol{A}_{\eta_r,\nu}$, $\boldsymbol{A}_{\nu,\eta_r}$, and $\boldsymbol{A}_{\nu,\nu}$ are affine.*

Assumptions 5.2 and 5.3 effectively define an implicit relationship between roll/pitch angles and $\boldsymbol{\rho}$ such that the nonlinearities in $\boldsymbol{R}_{\mathrm{IB}}$ and $\boldsymbol{L}_{\mathrm{IB}}$ are replaced by linear dependence on ϕ and θ (the small angle assumption) which in turn depend linearly on $\boldsymbol{\rho}$.

5.2.2 Multirotor LPV Modeling

Recall the original goal of obtaining large-domain excitation data for multirotor aircraft such as the quadrotor UAV shown in Figure 5.1. This aircraft will be used throughout the

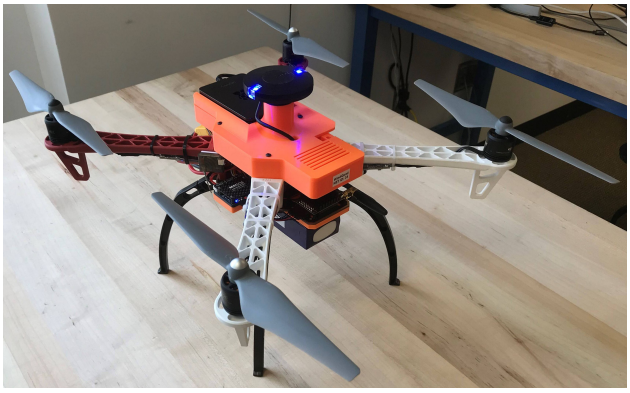

Figure 5.1: Small quadrotor UAV

remainder of this Chapter to demonstrate the proposed methodology. It was built using a DJI FlameWheel 450 frame and instrumented with a Cubepilot CubeOrange flight computer running PX4 firmware. An onboard Raspberry Pi co-computer was included for control law and excitation implementation over MAVROS. The quadrotor was instrumented with CAN electronic speed controllers (ESCs) capable of rotor speed measurements as well as a real-time kinematics (RTK) capable GNSS receiver. The instrumentation, co-computer setup, and data processing for this aircraft followed the methods detailed in references [62], [136].

Since we are considering only smooth models, suppose Model 3 defines the generalized force $\mathscr{F}$. Since the aim here is control, however, the yawing moment is written in terms of the actuator dynamics (4.35) like in Eq. (4.36). The parameters which we ultimately want to identify are $\boldsymbol{\vartheta} = [C_{(\cdot)}]$. Comparing Model 3 with Eq. (5.3), we see the state variables that capture the model's nonlinearities are the components of body velocity $\boldsymbol{v} = \boldsymbol{\rho}(\boldsymbol{\nu})$. Therefore, we choose to design a velocity reference signal $\boldsymbol{v}_\mathrm{d}$ that effectively covers the desired flight envelope along. Under Assumption 5.1, the matrices $\boldsymbol{\mathcal{A}}$ and $\boldsymbol{\mathcal{B}}$ have an affine dependence on $\boldsymbol{v}_\mathrm{d} = [u_\mathrm{d}\ v_\mathrm{d}\ w_\mathrm{d}]^\mathsf{T}$:

$$\boldsymbol{\mathcal{A}} = \boldsymbol{\mathcal{A}}_0 + \boldsymbol{\mathcal{A}}_u u_\mathrm{d} + \boldsymbol{\mathcal{A}}_v v_\mathrm{d} + \boldsymbol{\mathcal{A}}_w w_\mathrm{d} \tag{5.8a}$$

$$\boldsymbol{\mathcal{B}} = \boldsymbol{\mathcal{B}}_0 + \boldsymbol{\mathcal{B}}_u u_\mathrm{d} + \boldsymbol{\mathcal{B}}_v v_\mathrm{d} + \boldsymbol{\mathcal{B}}_w w_\mathrm{d} \tag{5.8b}$$

where the elements of the matrices $\boldsymbol{\mathcal{A}}_{(\cdot)}$ and $\boldsymbol{\mathcal{B}}_{(\cdot)}$ that are functions of the unknown parameter vector, $\boldsymbol{\vartheta}$, are given in Appendix A.2.

Since the control input is the virtual actuator input $\boldsymbol{u}_\delta$, one would need to augment the rigid body dynamics with the actuator dynamics (4.35). Then with the same motivation as Assumption 5.3, one would assume the linearization of these nonlinear actuator dynamics about steady, translating flight conditions defined by $(\boldsymbol{v}_0, \boldsymbol{\delta}_0)$ depend affinely on $\boldsymbol{v}_0$. However, the vehicle depicted in Figure 5.1 is equipped with motor speed controllers that regulate motor speeds. Therefore, we assume the first-order, linear actuator model

$$\dot{\boldsymbol{\delta}} = -\frac{1}{\tau}(\boldsymbol{\delta} - \boldsymbol{u}) \tag{5.9}$$

where $\boldsymbol{u}$ is the commanded virtual actuator vector and τ is an uncertain time constant (appended to the parameter vector $\boldsymbol{\vartheta}$).

An LPV flight dynamic model can now be formulated. Consider the state vector $\boldsymbol{x} = [\boldsymbol{\eta}_r^\mathsf{T}\ \ \boldsymbol{\nu}^\mathsf{T}\ \ \boldsymbol{\delta}^\mathsf{T}]^\mathsf{T} = [\phi\ \ \theta\ \ \boldsymbol{v}^\mathsf{T}\ \boldsymbol{\omega}^\mathsf{T}\ \ \boldsymbol{\delta}^\mathsf{T}]^\mathsf{T}$ with perturbation

$$\Delta\boldsymbol{x} = \begin{bmatrix} \Delta\phi \\ \Delta\theta \\ \Delta\boldsymbol{v} \\ \Delta\boldsymbol{\omega} \\ \Delta\boldsymbol{\delta} \end{bmatrix} = \begin{bmatrix} \phi - \phi_0(\boldsymbol{v}_\mathrm{d}) \\ \theta - \theta_0(\boldsymbol{v}_\mathrm{d}) \\ \boldsymbol{v} - \boldsymbol{v}_\mathrm{d} \\ \boldsymbol{\omega} \\ \boldsymbol{\delta} - \boldsymbol{\delta}_0(\boldsymbol{v}_\mathrm{d}) \end{bmatrix} \tag{5.10}$$

Also, let

$$\Delta\boldsymbol{u} = \boldsymbol{u} - \boldsymbol{\delta}_0(\boldsymbol{v}_\mathrm{d}) \tag{5.11}$$

be the small-perturbation control input. Then, an LPV model of the system is written as

$$\begin{bmatrix} \Delta\dot{\boldsymbol{\eta}}_r \\ \Delta\dot{\boldsymbol{\nu}} \\ \Delta\dot{\boldsymbol{\delta}} \end{bmatrix} = \underbrace{\begin{bmatrix} \boldsymbol{A}_{\eta_r,\eta_r} & \boldsymbol{A}_{\eta_r,\nu} & \boldsymbol{0} \\ \boldsymbol{A}_{\nu,\eta_r} & \boldsymbol{A}_{\nu,\nu} + \mathscr{M}^{-1}\boldsymbol{\mathcal{A}} & \mathscr{M}^{-1}\boldsymbol{\mathcal{B}} \\ \boldsymbol{0} & \boldsymbol{0} & -\frac{1}{\tau}\mathbb{I} \end{bmatrix}}_{\boldsymbol{A}} \begin{bmatrix} \Delta\boldsymbol{\eta}_r \\ \Delta\boldsymbol{\nu} \\ \Delta\boldsymbol{\delta} \end{bmatrix} + \underbrace{\begin{bmatrix} \boldsymbol{0} \\ \mathscr{M}^{-1}\boldsymbol{\mathcal{B}}_\mathrm{cmd} \\ \frac{1}{\tau}\mathbb{I} \end{bmatrix}}_{\boldsymbol{B}} \Delta\boldsymbol{u} \tag{5.12}$$

where

$$\boldsymbol{\mathcal{B}}_{\text{cmd}} = \begin{bmatrix} \mathbf{0} & \mathbf{0} & \mathbf{0} & \mathbf{0} \\ \mathbf{0} & \mathbf{0} & \mathbf{0} & \frac{J_z}{\tau}\boldsymbol{e}_3 \end{bmatrix}$$

More compactly, we have

$$\Delta\dot{\boldsymbol{x}} = \boldsymbol{A}(\boldsymbol{v}_{\text{d}};\boldsymbol{\theta})\Delta\boldsymbol{x} + \boldsymbol{B}(\boldsymbol{\theta})\Delta\boldsymbol{u} \tag{5.13}$$

where $\boldsymbol{\theta}$ is the vector of unknown elements of the constant matrices that define the affine LPV system in Eq. (5.12).

5.2.3 Performance-Based Polytopic LPV Model

Since we are simultaneously stabilizing a reference trajectory and exciting the aircraft dynamics about it, we decompose the input vector, $\boldsymbol{u}$, into two parts — a control input $\boldsymbol{u}_{\text{c}}$ and a normalized excitation input $\boldsymbol{u}_{\text{e}}$. In general, we write

$$\boldsymbol{u} = \boldsymbol{u}_{\text{c}} + \boldsymbol{R}\boldsymbol{u}_{\text{e}} \tag{5.14}$$

for some constant invertible scaling matrix $\boldsymbol{R}$ that defines the effective excitation input $\tilde{\boldsymbol{u}}_{\text{e}} = \boldsymbol{R}\boldsymbol{u}_{\text{e}}$. Referring to Eq. (5.11), the decomposition (5.14) also reads

$$\Delta\boldsymbol{u} = \underbrace{\boldsymbol{u}_{\text{c}} - \boldsymbol{\delta}_0(\boldsymbol{v}_{\text{d}})}_{\Delta\boldsymbol{u}_{\text{c}}} + \boldsymbol{R}\boldsymbol{u}_{\text{e}} \tag{5.15}$$

We also define a performance output that represents some scaled value of the perturbation from the desired velocity reference:

$$\boldsymbol{z} = \boldsymbol{Q}^{-1}(\boldsymbol{v} - \boldsymbol{v}_{\text{d}}) = \boldsymbol{Q}^{-1}\Delta\boldsymbol{v} \tag{5.16}$$

for some constant invertible matrix $\boldsymbol{Q}$. Thus, the LPV system (5.13) is now written as

$$\Delta\dot{\boldsymbol{x}} = \boldsymbol{A}(\boldsymbol{v}_{\text{d}};\boldsymbol{\theta})\Delta\boldsymbol{x} + \boldsymbol{B}_{\text{c}}(\boldsymbol{\theta})\Delta\boldsymbol{u}_{\text{c}} + \boldsymbol{B}_{\text{e}}(\boldsymbol{\theta})\boldsymbol{u}_{\text{e}} \tag{5.17a}$$

$$\boldsymbol{z} = \boldsymbol{C}\Delta\boldsymbol{x} \tag{5.17b}$$

where $\boldsymbol{B}_{\text{c}} = \boldsymbol{B}$, $\boldsymbol{B}_{\text{e}} = \boldsymbol{B}\boldsymbol{R}$, and the output matrix $\boldsymbol{C}$ is constructed using Eq. (5.16).

Since every affine description can be written as a polytopic one,[1] we express the LPV system (5.17) as polytopic in the scheduling variable $\boldsymbol{v}_{\text{d}}$. Let

$$\boldsymbol{v}_{\text{d}} \in [\boldsymbol{v}_{\min}, \boldsymbol{v}_{\max}] =: \mathbb{P}_{v_{\text{d}}} \tag{5.18}$$

[1] See reference [51] and the references therein.

Then we can write the system (5.17) as the convex combination

$$\begin{aligned}\boldsymbol{\Lambda}(\boldsymbol{v}_{\mathrm{d}},\boldsymbol{\theta}) &:= \begin{bmatrix}\boldsymbol{A}(\boldsymbol{v}_{\mathrm{d}},\boldsymbol{\theta}) & \boldsymbol{B}_{\mathrm{c}}(\boldsymbol{\theta}) & \boldsymbol{B}_{\mathrm{e}}(\boldsymbol{\theta})\\ \boldsymbol{C} & \boldsymbol{0} & \boldsymbol{0}\end{bmatrix}\\ &= \sum_{i=1}^{N}\alpha_i(\boldsymbol{v}_{\mathrm{d}})\begin{bmatrix}\boldsymbol{A}_i(\boldsymbol{\theta}) & \boldsymbol{B}_{\mathrm{c}}(\boldsymbol{\theta}) & \boldsymbol{B}_{\mathrm{e}}(\boldsymbol{\theta})\\ \boldsymbol{C} & \boldsymbol{0} & \boldsymbol{0}\end{bmatrix}\\ &=: \sum_{i=1}^{N}\alpha_i(\boldsymbol{v}_{\mathrm{d}})\boldsymbol{\Lambda}_i(\boldsymbol{\theta})\end{aligned} \tag{5.19}$$

where

$$\sum_{i=1}^{N}\alpha_i(\boldsymbol{v}_{\mathrm{d}}) = 1$$

This equation defines a polytope with $N = 2^3$ vertices given by the corners of the box constraint in Eq. (5.18), where each vertex system, $\boldsymbol{\Lambda}_i(\boldsymbol{\theta})$ is uncertain for

$$\boldsymbol{\theta} \in [\boldsymbol{\theta}_{\min},\boldsymbol{\theta}_{\max}] =: \mathbb{P}_{\theta} \tag{5.20}$$

Thus for each $i \in \{1,\ldots,N\}$, we have

$$\boldsymbol{\Lambda}_i(\boldsymbol{\theta}) = \sum_{j=1}^{M_i}\beta_i^j(\boldsymbol{\theta})\begin{bmatrix}\boldsymbol{A}_i^j & \boldsymbol{B}_{\mathrm{c}}^j & \boldsymbol{B}_{\mathrm{e}}^j\\ \boldsymbol{C} & \boldsymbol{0} & \boldsymbol{0}\end{bmatrix} =: \sum_{j=1}^{M_i}\beta_i^j(\boldsymbol{\theta})\boldsymbol{\Lambda}_i^j, \qquad \sum_{j=1}^{M_i}\beta_i^j(\boldsymbol{\theta}) = 1 \tag{5.21}$$

Therefore, in order to design a control law, we need only identify small perturbation linear models for each ith vertex of the polytopic LPV system. The uncertainty polytope vertices are then defined using the parameter confidence intervals found in the parameter estimation process. The resulting description of the system is a nested polytope, as depicted in Figure 5.2 for two scheduling parameters ρ_1 and ρ_2. In this figure, each point in the scheduling parameter space contained within the blue polytope defines an uncertain LTI system. The true LTI system at that parameter value is defined at some point in the orange polytope, which lies in the uncertain parameter space (axes not shown).

5.3 Vertex Model Identification

In order to proceed with identification of the polytopic LPV model (5.19), we assume there exists a set of baseline control laws that locally stabilize the set of steady flight conditions defined by the vertices of the polytope, $\mathbb{P}_{v_{\mathrm{d}}}$. This is often a model-free control law such as proportional-integral-derivative (PID) control. Using this control law, flight test data is collected at the vertices of $\mathbb{P}_{v_{\mathrm{d}}}$. In this initial model identification process, the parametric uncertainty is also accurately characterized, yielding the polytopic uncertain LPV model (5.21).

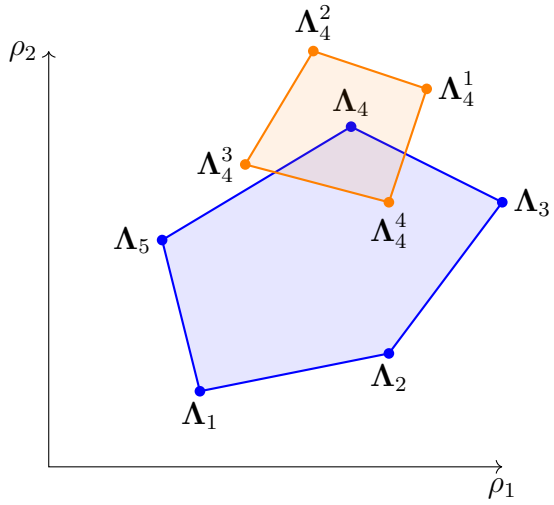

Figure 5.2: Nested polytopic description

For each LPV vertex system, we identify the elements of each matrix $\boldsymbol{A}_i$ that depend on unknown aerodynamic parameters, $C_{(\cdot)}$, from flight data. The actuator time constant τ, however, was identified separately. For UAV shown in Figure 5.1, the motor time constant is $\tau = 0.082 \pm 0.002$ seconds. Each of the vertex LTI models was identified using the equation-error "gray-box" identification process detailed in Appendix A.3. This method solves the parameter estimation problem using ordinary least-squares for the unknown elements of each $\boldsymbol{A}_i$.

Due to hardware implementation restrictions, the quadrotor LTI dynamics were excited using body velocity and yaw rate reference commands. This was mainly due to the inability to command "broken-loop" excitation signals from the co-computer over MAVROS. Although the use of velocity commands is not ideal because the resulting actuator states may be correlated, this choice of excitation makes initial model identification easier, and was found to be sufficient. The reference command excitation signal was a 4-axis, 30 second multisine signal with uniform power spectral density in the frequency range from 0.2 to 2 Hz, generated using SIDPAC software [111]. The multisine body velocity reference components were superimposed over constant body velocity commands corresponding to the vertices of the LPV polytope described in Section 5.2.

For this example, the maximum and minimum velocities were chosen to be +5 m/s and −5 m/s, respectively, in all components. For the flight test data collection, the constant body velocity reference was commanded for 10 seconds prior to excitation to allow for experimental determination of the equilibrium flight condition, $(\boldsymbol{x}_0(\boldsymbol{v}_\mathrm{d}), \boldsymbol{u}_0(\boldsymbol{v}_\mathrm{d}))$. Because the baseline controller performance is limited, the equilibrium condition from flight data does not perfectly align with the commanded velocity, as shown in Table 5.1. Note, in particular, that for vertices corresponding to descending flight, the magnitude of the actual downward velocity (w_0) is much smaller than the commanded value.

Table 5.1: Flight Data Vertex Equilibria

Vertex [m/s]	u_0 [m/s]	v_0 [m/s]	w_0 [m/s]	ϕ_0 [deg]	θ_0 [deg]	$\delta_{t,0}$ [rad/s]	$\delta_{a,0}$ [rad/s]	$\delta_{e,0}$ [rad/s]	$\delta_{r,0}$ [rad/s]
$[-5 \ -5 \ -5]^\mathsf{T}$	−4.99	−5.04	−4.20	−10.87	9.28	691.4	−36.7	29.0	310.5
$[+5 \ -5 \ -5]^\mathsf{T}$	4.95	−5.04	−4.17	−10.44	−8.05	685.0	−34.1	−1.5	39.2
$[-5 \ +5 \ -5]^\mathsf{T}$	−5.01	5.03	−3.95	8.55	8.11	689.0	−2.8	25.3	34.9
$[+5 \ +5 \ -5]^\mathsf{T}$	5.03	5.01	−4.00	8.04	−8.98	679.5	−5.8	−4.0	305.4
$[-5 \ -5 \ +5]^\mathsf{T}$	−4.83	−4.68	2.88	−5.00	3.17	554.9	−45.0	28.0	367.6
$[+5 \ -5 \ +5]^\mathsf{T}$	4.73	−4.61	2.72	−5.14	−4.08	521.8	−34.6	−18.3	158.9
$[-5 \ +5 \ +5]^\mathsf{T}$	−4.85	4.75	3.00	3.80	3.00	546.9	14.0	23.4	−9.8
$[+5 \ +5 \ +5]^\mathsf{T}$	4.64	4.73	2.86	3.85	−4.83	525.8	3.49	−15.8	298.1

Equation error least squares parameter estimation was conducted for each axis of each vertex system using this flight data. The coefficient of determination is tabulated for these results in Table 5.2. The model fit is poor for flight conditions where the quadrotor is descending through its rotor wake. We note, however, that poor results are perfectly acceptable for the proposed use, provided the parametric *uncertainty* is well characterized for the robust LPV controller.

Table 5.2: LTI Equation Error Coefficient of Determination, R^2 [%]

	LTI State Equation Axis					
Nominal Vertex	$\dot{u}$	$\dot{v}$	$\dot{w}$	$\dot{p}$	$\dot{q}$	$\dot{r}$
$[-5 \ -5 \ -5]^\mathsf{T}$	30.1	39.3	81.2	83.2	88.9	95.5
$[+5 \ -5 \ -5]^\mathsf{T}$	39.8	29.9	86.4	84.0	91.4	94.1
$[-5 \ +5 \ -5]^\mathsf{T}$	40.4	38.1	78.8	76.8	84.5	95.4
$[+5 \ +5 \ -5]^\mathsf{T}$	38.6	33.2	69.7	80.0	85.0	94.6
$[-5 \ -5 \ +5]^\mathsf{T}$	9.4	15.7	97.8	80.2	75.2	95.0
$[+5 \ -5 \ +5]^\mathsf{T}$	19.8	12.6	98.9	75.4	85.1	96.6
$[-5 \ +5 \ +5]^\mathsf{T}$	10.7	18.3	96.5	80.3	85.3	93.7
$[+5 \ +5 \ +5]^\mathsf{T}$	17.4	14.3	97.6	79.0	83.3	95.9

The identified LTI models along with the estimated parameter variances were used to define the uncertain LPV model described by Eq. (5.17). This model was then validated against an independent maneuver generated with a 4-axis multisine about the hover condition. From this maneuver, the time derivative of the state vector from flight data, $\dot{\boldsymbol{x}}_\mathrm{f}$, was obtained along with the modeled state derivative from Eq. (5.17), $\dot{\boldsymbol{x}}_\mathrm{m}$. The validation time history of K samples is shown in Figure 5.3. Let $\dot{\boldsymbol{x}}_{\mathrm{m},i}$ and $\dot{\boldsymbol{x}}_{\mathrm{f},i}$ be the $K \times 1$ column vectors containing the time history of the respective time derivatives for the ith state. Theil's inequality

coefficient (TIC),

$$\text{TIC} = \frac{\sqrt{\frac{1}{K}(\dot{\boldsymbol{x}}_{\text{m},i} - \dot{\boldsymbol{x}}_{\text{f},i})^{\mathsf{T}}(\dot{\boldsymbol{x}}_{\text{m},i} - \dot{\boldsymbol{x}}_{\text{f},i})}}{\sqrt{\frac{1}{K}\dot{\boldsymbol{x}}_{\text{m},i}^{\mathsf{T}}\dot{\boldsymbol{x}}_{\text{m},i}} + \sqrt{\frac{1}{K}\dot{\boldsymbol{x}}_{\text{f},i}^{\mathsf{T}}\dot{\boldsymbol{x}}_{\text{f},i}}} \tag{5.22}$$

and normalized root-mean squared error (NRMSE),

$$\text{NRMSE} = \frac{1}{\text{range}(\dot{\boldsymbol{x}}_{\text{f},i})}\sqrt{\frac{1}{K}(\dot{\boldsymbol{x}}_{\text{m},i} - \dot{\boldsymbol{x}}_{\text{f},i})^{\mathsf{T}}(\dot{\boldsymbol{x}}_{\text{m},i} - \dot{\boldsymbol{x}}_{\text{f},i})} \tag{5.23}$$

were then computed and are given in Table 5.3. The model validates well with small values of TIC and NRMSE, especially in the translational dynamics. There is a slight bias apparent in the rotational dynamics, causing larger values of TIC and NRMSE.

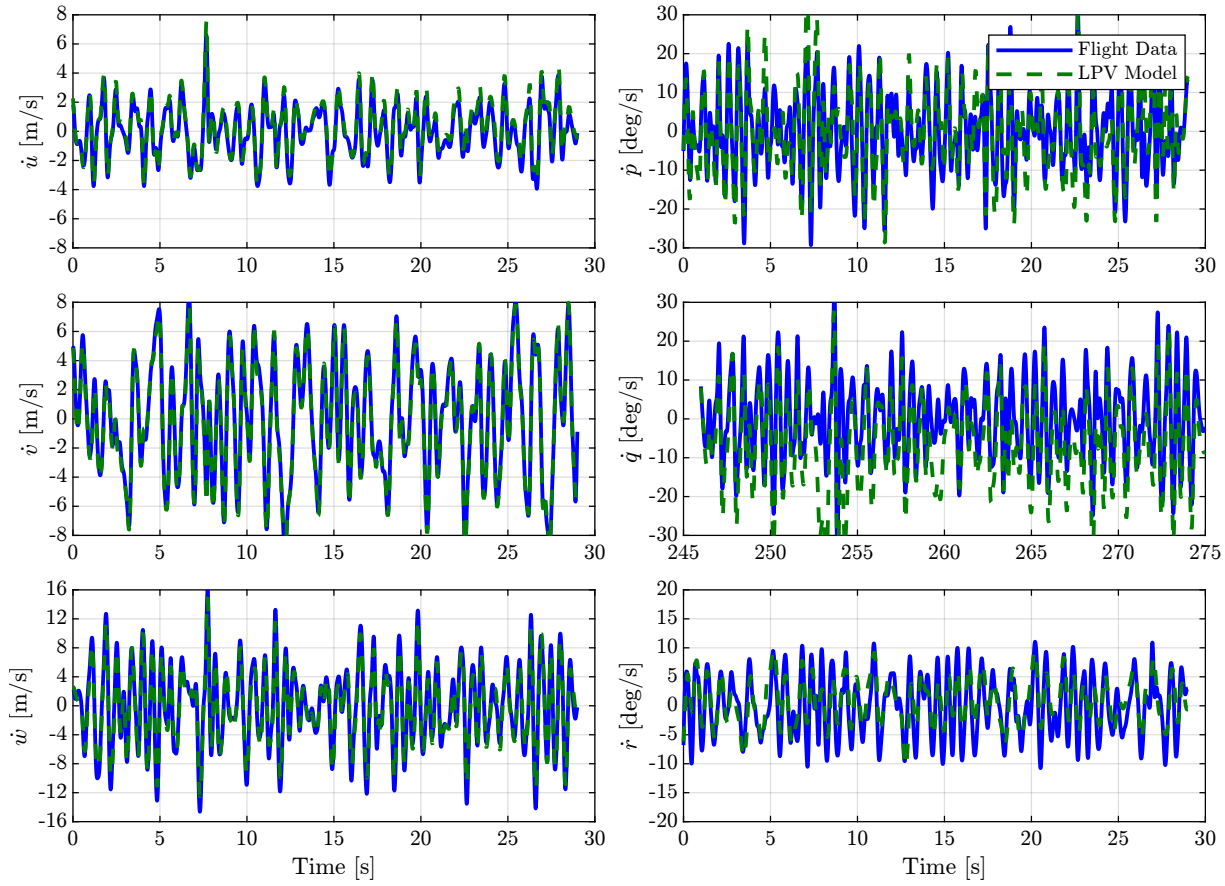

Figure 5.3: LPV model independent validation

Table 5.3: LPV model validation metrics

Equation	$\dot{u}$	$\dot{v}$	$\dot{w}$	$\dot{p}$	$\dot{q}$	$\dot{r}$
TIC	0.110	0.049	0.104	0.274	0.355	0.352
NRMSE	0.036	0.021	0.035	0.094	0.119	0.148

5.4 Signal Design

With the polytopic LPV model identified and parametric uncertainty characterized, we can design the input signals to be used in the nonlinear model identification experiments. The two signals that need to be designed are the body velocity reference, $\boldsymbol{v}_{\mathrm{d}}(t)$, that covers the desired domain and the superposed command signal $\boldsymbol{u}_{\mathrm{e}}$ that is intended to excite the vehicle dynamics about the reference motion. Since body velocity is an explanatory variable which appears in regressor functions that also depend nonlinearly on actuator states, $\boldsymbol{\delta}$, we want to ensure the $\boldsymbol{v}_{\mathrm{d}}$ and $\boldsymbol{u}_{\mathrm{e}}$ are uncorrelated. An efficient way to accomplish this task is to design multisine signals for $\boldsymbol{v}_{\mathrm{d}}$ and $\boldsymbol{u}_{\mathrm{e}}$ concurrently such that they are orthogonal and phase-optimized [112]. Inspired by Simmons *et al.* [135], we select the frequency range of the velocity reference to be sufficiently low in the interval $[0.01, 0.5]$ Hz, while the motor excitation signals are higher-frequency, in the interval $(0.5, 5]$ Hz. The upper limit on the excitation frequency was chosen based on recommendations from Ivler *et al.* [78], but slightly lower due to concerns about damaging the ESCs.[2] Using SIDPAC's `mkmsswp.m` function, these signals were generated and are shown in Figure 5.4, normalized to unit amplitude, with their spectral content given in Figure 5.5. The correlation coefficients and plots of this signal are displayed in Figure 5.6, showing good coverage of the velocity space in the $\boldsymbol{v}_{\mathrm{d}}$ signals and proper decorrelation overall.

Since the excitation input of T seconds is known, we can now make an informed choice of the performance output weighting $\boldsymbol{Q}$ and excitation input weighting $\boldsymbol{R}$. While in typical H_∞ control approaches the exogenous input is unknown, that is not the case here; we have direct knowledge of the "disturbance" that is perturbing the vehicle motion from equilibrium flight. We select tunable excitation input magnitudes Δ_t, Δ_a, Δ_e, and Δ_r. The $\boldsymbol{R}$ matrix is chosen such that the normalized excitation input $\boldsymbol{u}_{\mathrm{e}}$, defined to have unit energy

$$\sqrt{\int_0^T \boldsymbol{u}_{\mathrm{e}}^{\mathsf{T}}(t)\boldsymbol{u}_{\mathrm{e}}(t)\mathrm{d}t} = 1 \tag{5.24}$$

results in the effective excitation inputs having magnitudes Δ_t, Δ_a, Δ_e, and Δ_r. Thus, $\boldsymbol{R}$ is defined as

$$\boldsymbol{R} = \sqrt{\frac{n_u T}{2}}\,\mathbf{diag}(\Delta_t, \Delta_a, \Delta_e, \Delta_r) \tag{5.25}$$

[2] Another approach for determining the appropriate frequency range is to analyze the vehicle's response to frequency sweep data in each of the virtual actuators.

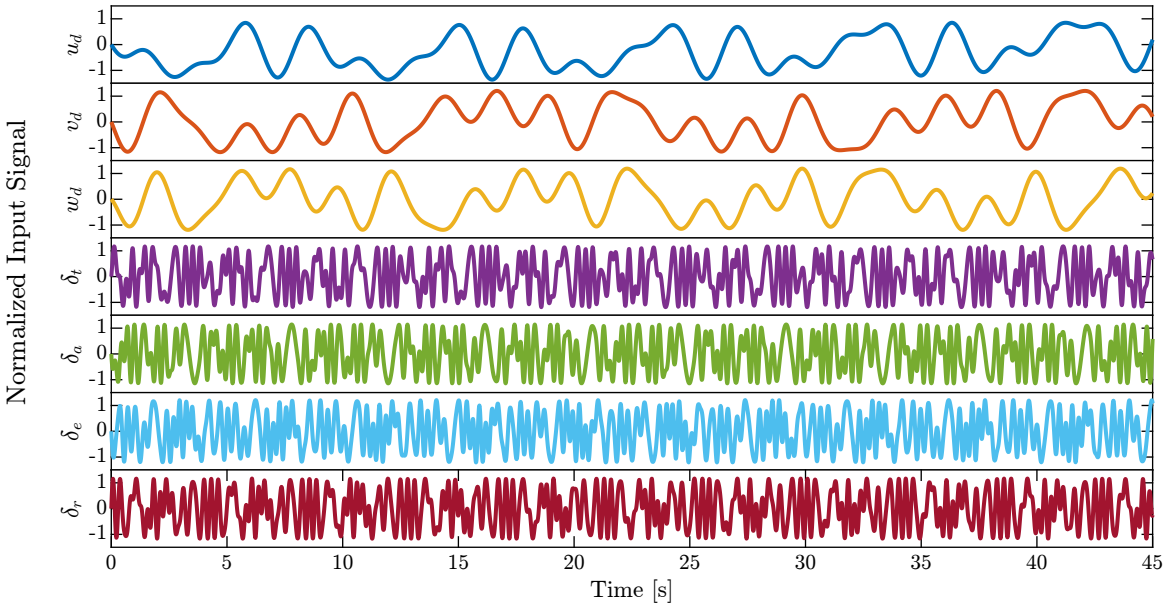

Figure 5.4: Velocity reference and motor excitation multisine signal

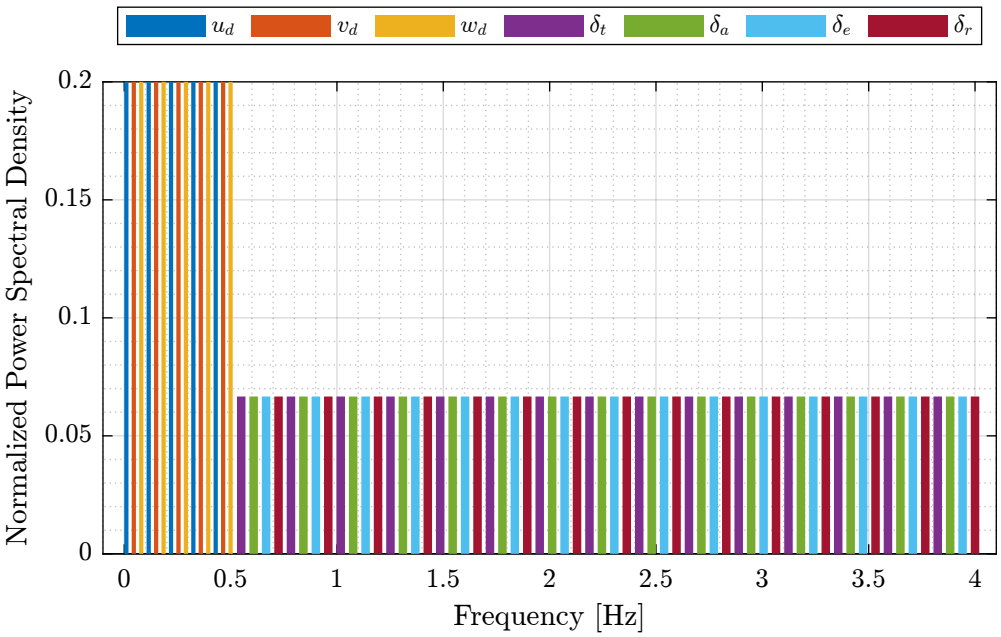

Figure 5.5: Velocity reference and motor excitation multisine spectra

where $n_u = 4$. Similarly, we define maximum body velocity perturbations Δ_u, Δ_v, and Δ_w. The performance output, $\boldsymbol{z} = \boldsymbol{Q}^{-1}\Delta\boldsymbol{v}$, is then scaled such that the worst-case velocity perturbations corresponding to step changes of Δ_u, Δ_v, and Δ_w will generate a performance

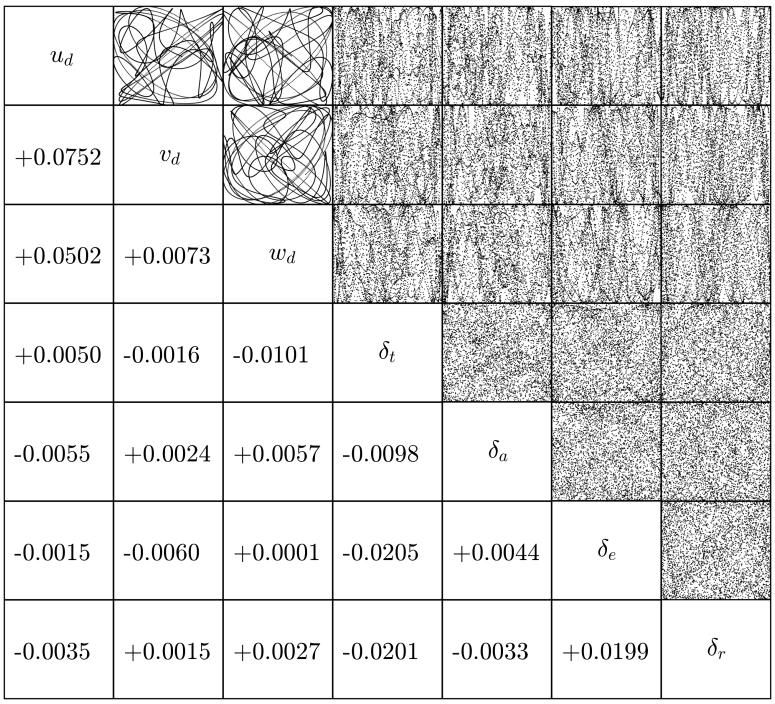

Figure 5.6: Velocity reference and motor excitation multisine correlation

output that also has unit energy. Therefore, $\boldsymbol{Q}$ is chosen to be

$$\boldsymbol{Q} = \sqrt{n_z T}\,\mathbf{diag}(\Delta_u, \Delta_v, \Delta_w) \tag{5.26}$$

where $n_z = 3$. Note the factor of $1/\sqrt{2}$ that appears in $\boldsymbol{R}$ is not present in $\boldsymbol{Q}$ due to the asymmetry of the worst-case step perturbations mentioned above. This normalization provides a clear control objective of ensuring that the worst case energy gain from the normalized excitation input, $\boldsymbol{u}_{\mathrm{e}}$, to the normalized performance output, $\boldsymbol{z}$, is no greater than one. This performance objective is formalized as follows.

Recall a signal $\boldsymbol{\xi}$ is said to be an element of the vector space L_2 if its L_2 norm is finite, meaning

$$\|\boldsymbol{\xi}\|_{L_2} = \sqrt{\int_0^\infty \boldsymbol{\xi}^{\mathsf{T}}(t)\boldsymbol{\xi}(t)\mathrm{d}t} < \infty$$

We are interested in prescribing the worst-case L_2-gain from $\boldsymbol{u}_{\mathrm{e}} \in L_2$ to $\boldsymbol{z} \in L_2$ for all uncertain parameter values, $\boldsymbol{\theta} \in \mathbb{P}_\theta$. Thus, the design goal is stated as

$$\sup_{\boldsymbol{\theta}\in\mathbb{P}_\theta} \|\boldsymbol{u}_{\mathrm{e}} \mapsto \boldsymbol{z}\|_\infty = \sup_{\mathbf{0}\neq\boldsymbol{u}_{\mathrm{e}}\in L_2,\, \boldsymbol{\theta}\in\mathbb{P}_\theta} \frac{\|\boldsymbol{z}\|_{L_2}}{\|\boldsymbol{u}_{\mathrm{e}}\|_{L_2}} = 1 \tag{5.27}$$

Remark 5.1. *The control objective stated above for system excitation is contrast with the typical robust control problem where the aim is to* suppress *disturbances. Here, we wish to create sufficiently rich "disturbances" and to only* bound *their effect on the vehicle response.*

5.5 Robust LPV Control Law Design

For the control law synthesis, we consider the polytopic uncertain LPV system (5.21) without the position and yaw states since they are ignorable coordinates. For this system, a static state feedback control law that satisfies Eq. (5.27) can readily be obtained. Adapting Theorem 2 by Rotondo *et al.* [129] to the system in Eq. (5.17) for the case with no pole placement constraints or H_2 norm objectives, we have the following Lemma.

Lemma 5.1 (Theorem 2 by Rotondo *et al.* [129])**.** *Consider the polytopic linear, parameter-varying system with polytopic uncertainty in Eq. (5.17). Given a constant $\gamma > 0$, if there exist symmetric positive definite matrices $\boldsymbol{X}_i^j$, matrices $\boldsymbol{S}_i$, and a matrix $\boldsymbol{H}$ for all $i \in \{1, \cdots, N\}$ and $j \in \{1, \cdots, M_i\}$ such that*

$$\begin{bmatrix} \boldsymbol{U}_i^j + \boldsymbol{U}_i^{j\mathsf{T}} & -\boldsymbol{X}_i^j + \boldsymbol{H}^\mathsf{T} - \boldsymbol{U}_i^j & \boldsymbol{B}_\mathrm{e}^j & \boldsymbol{H}^\mathsf{T}\boldsymbol{C}^\mathsf{T} \\ -\boldsymbol{X}_i^j + \boldsymbol{H} - \boldsymbol{U}_i^{j\mathsf{T}} & -(\boldsymbol{H} + \boldsymbol{H}^\mathsf{T}) & \boldsymbol{0} & -\boldsymbol{H}^\mathsf{T}\boldsymbol{C}^\mathsf{T} \\ \boldsymbol{B}_\mathrm{e}^{j\mathsf{T}} & \boldsymbol{0} & -\mathbb{I} & \boldsymbol{0} \\ \boldsymbol{C}\boldsymbol{H} & -\boldsymbol{C}\boldsymbol{H} & \boldsymbol{0} & -\gamma^2\mathbb{I} \end{bmatrix} \prec \boldsymbol{0} \tag{5.28}$$

where

$$\boldsymbol{U}_i^j = \boldsymbol{A}_i^j\boldsymbol{H} + \boldsymbol{B}_\mathrm{c}^j\boldsymbol{S}_i$$

then the static state feedback

$$\Delta\boldsymbol{u}_\mathrm{c} = \boldsymbol{K}(\boldsymbol{v}_\mathrm{d})\Delta\boldsymbol{x}, \qquad \boldsymbol{K}(\boldsymbol{v}_\mathrm{d}) = \sum_{i=1}^{N} \alpha_i(\boldsymbol{v}_\mathrm{d})\boldsymbol{K}_i, \qquad \boldsymbol{K}_i = \boldsymbol{S}_i\boldsymbol{H}^{-1} \tag{5.29}$$

renders the H_∞ norm of the closed-system less than γ for all $\boldsymbol{v}_\mathrm{d} \in \mathbb{P}_{v_\mathrm{d}}$ and all $\boldsymbol{\theta} \in \mathbb{P}_\theta$.

Using this lemma, we can choose $\gamma = 1$ yielding a convex feasibility problem that can be solved using a linear matrix inequity (LMI) solver. If the problem is not feasible, then there are three remediations, all of which may be used. First, the input magnitudes Δ_t, Δ_a, Δ_e and Δ_r can be reduced. Second, the allowed output magnitudes Δ_u, Δ_v, and Δ_w can be increased. Third, the uncertainty in the identified LTI models can be reduced through refined model identification.

For the quadrotor model identified in Section 5.3, we chose the tuning parameters

$$\begin{aligned} \Delta_t = \Delta_a = \Delta_e = \Delta_r = 0.1 \\ \Delta_u = \Delta_v = \Delta_w = 5 \end{aligned} \tag{5.30}$$

The convex feasibility problem in Lemma 5.1 was solved using CVX [58], [59] in MATLAB with the Mosek solver [7]. The total number of scalar optimization variables was 332,920 with 45,768 constraints, and the total computation time[3] was 52 seconds using default precision. The final result is eight feedback gain matrices that are used to compute $\boldsymbol{K}(\boldsymbol{v}_\mathrm{d})$ from Eq. (5.29). In implementation, the equilibrium state and input vectors are similarly computed as convex combinations of the vertex equilibria.

[3]Performed on a laptop with an Intel Core i7-1185G7 and 16GB DDR4-3200 memory

5.6 Simulation

The synthesized robust LPV control law was simulated with the identified LPV model. First, the uncertain parameters were evaluated at their nominal values, $\boldsymbol{\theta}_0$, and the following closed-loop system was simulated in MATLAB using `ode45`:

$$\dot{\boldsymbol{x}} = \boldsymbol{A}(\boldsymbol{v}_\mathrm{d}, \boldsymbol{\theta}_0)(\boldsymbol{x} - \boldsymbol{x}_0) + \boldsymbol{B}_\mathrm{c}(\boldsymbol{\theta}_0)(\boldsymbol{u}_\mathrm{c} - \boldsymbol{u}_0) + \boldsymbol{B}_\mathrm{e}(\boldsymbol{\theta}_0)\kappa\boldsymbol{u}_\mathrm{e} + \dot{\boldsymbol{x}}_0 \tag{5.31}$$

for some constant $\kappa > 0$. Note the designed input magnitudes of Δ_t, Δ_a, Δ_e and Δ_r need not be used, as they are just used to normalize the performance objective. If their L_2 norm is doubled, for instance, then the worst-case L_2 norm of the velocity perturbation is simply doubled as well. The important result is that we prescribe this gain. For this demonstration, however, the excitation multiplier κ was set to unity. The equilibrium state derivative, $\dot{\boldsymbol{x}}_0$, in Eq. (5.31) was computed with

$$\dot{\boldsymbol{x}}_0 = \frac{\partial \boldsymbol{x}_0(\boldsymbol{v}_\mathrm{d})}{\partial \boldsymbol{v}_\mathrm{d}} \frac{\mathrm{d}\boldsymbol{v}_\mathrm{d}}{\mathrm{d}t} \tag{5.32}$$

In Figure 5.7, the body velocity reference is plotted in black dashed lines along with the actual body velocity in solid lines, where the time history shows sufficient tracking of the velocity reference command. The perturbation from the reference was also computed and is

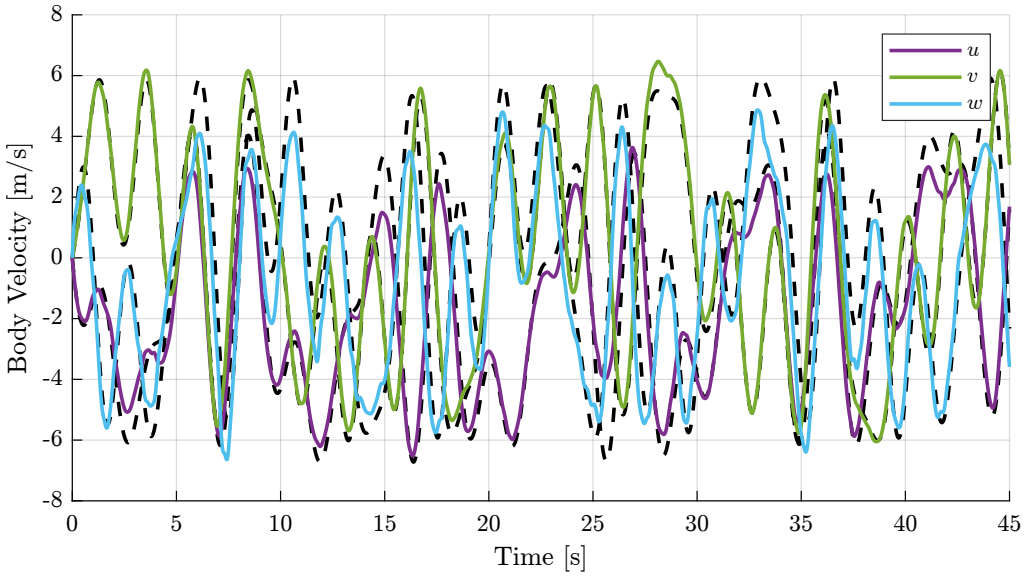

Figure 5.7: Nominal model simulation body velocity and reference

displayed in Figure 5.8. Here, the perturbations remain below an acceptable threshold and qualitatively indicate good information content.

For each axis of Model 3, the correlation coefficients of the regressors were computed and are shown in Figure 5.9. We see good decorrelation of most regressors, indicating that we should

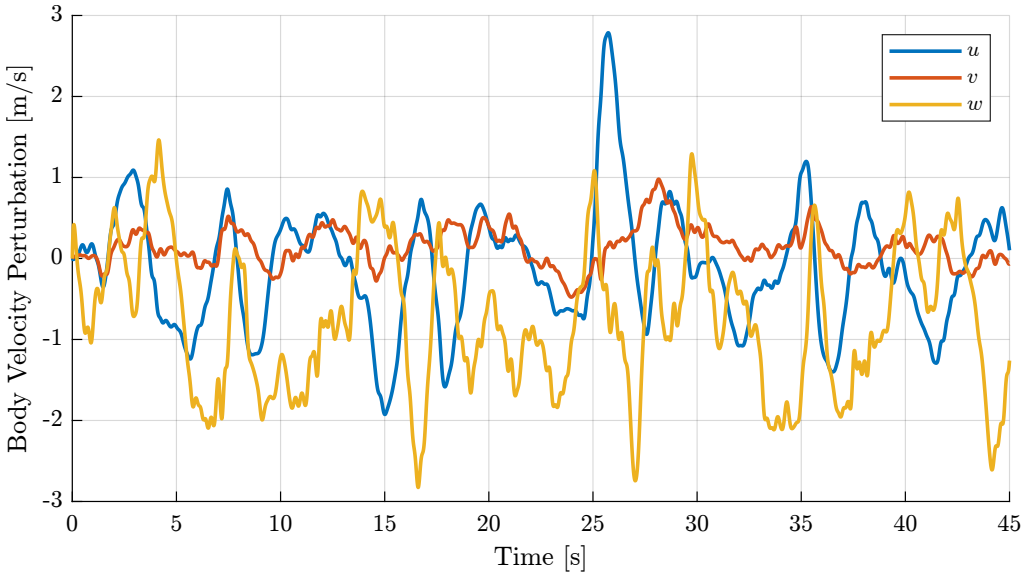

Figure 5.8: Nominal model simulation body velocity perturbation

be able accurately identify the aerodynamic parameters in Model 3 (assuming a sufficiently high signal-to-noise ratio, etc.). The regressors that show extremely high correlation among each other are those that depend on $\boldsymbol{\delta}$. This is expected since the magnitude of excitation was small. To further decorrelate these regressors, one would either select a greater $\kappa > 1$ or increase the maximum velocity components in the vertex model identification.

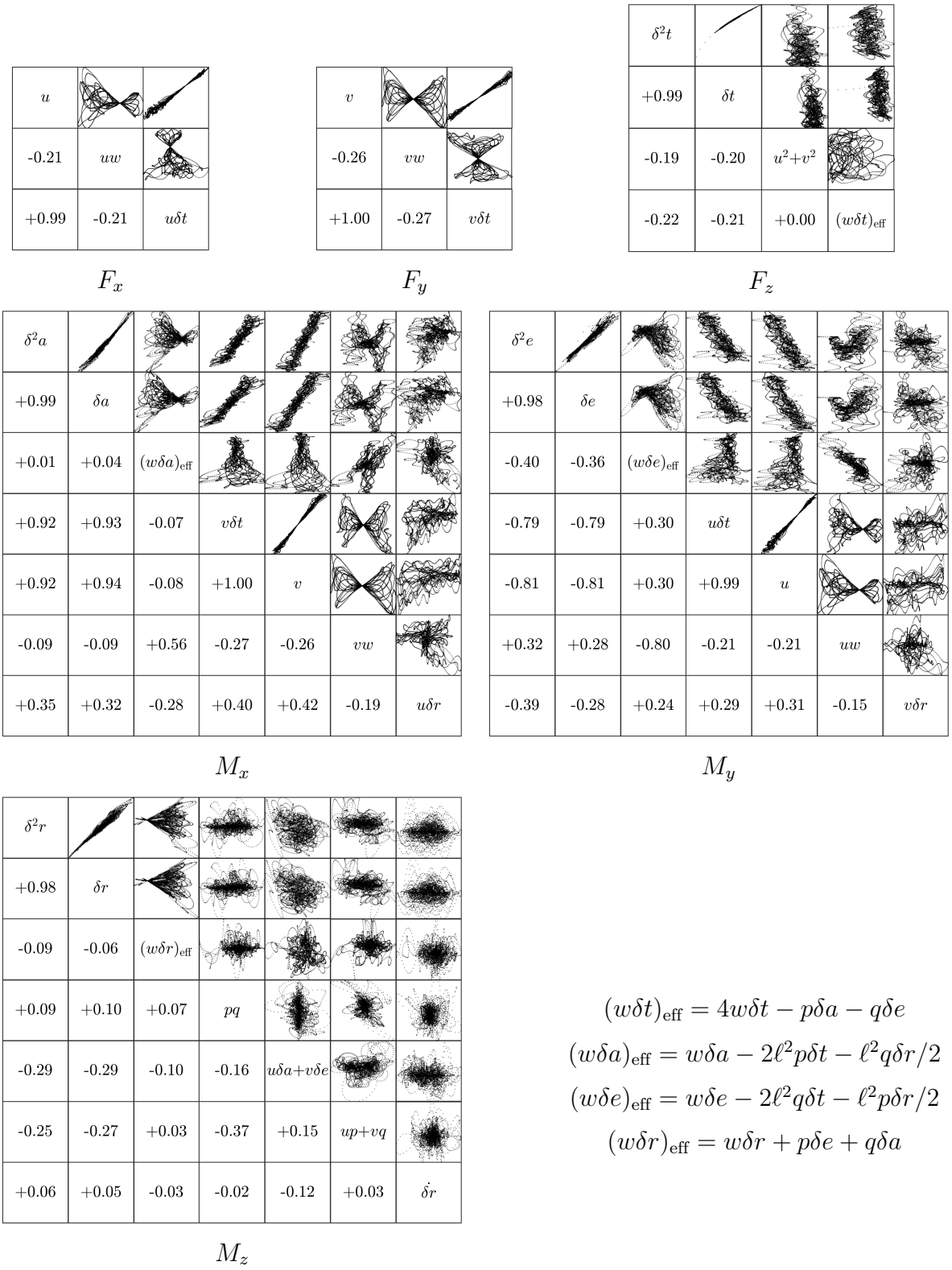

$$(w\delta t)_{\text{eff}} = 4w\delta t - p\delta a - q\delta e$$
$$(w\delta a)_{\text{eff}} = w\delta a - 2\ell^2 p\delta t - \ell^2 q\delta r/2$$
$$(w\delta e)_{\text{eff}} = w\delta e - 2\ell^2 q\delta t - \ell^2 p\delta r/2$$
$$(w\delta r)_{\text{eff}} = w\delta r + p\delta e + q\delta a$$

Figure 5.9: Nonlinear model regressor correlation

Chapter 6

Model-Based Wind Estimation

6.1 Introduction

As mentioned in Chapter 1, wind estimation enables scientists and engineers to solve crucial problems across disciplines. When sensors such as air data probes or anemometers are able to be used, direct approaches such as that by Lee *et al.* [93] can very accurately estimate the wind and aircraft's air-relative velocity. Of particular interest are approaches that do not require specialized sensors such as anemometers or air data probes to measure wind and air-relative velocity. The motion of the aircraft in response to external disturbances can be used to continuously estimate the wind at the aircraft's location. Minimal instrumentation requirements make aircraft-based wind estimation at low altitudes viable for a variety of aircraft sizes (e.g., small UAVs up to large commercial airplanes) and types (e.g., fixed-wing, multirotor, and VTOL).

The development of model-based indirect wind estimation algorithms has brought finer temporal resolution and greater accuracy to wind velocity estimates. For fixed-wing aircraft, Lie and Gebre-Egziabher [96] developed a synthetic air data system using model-based estimation techniques. This approach improved accuracy and robustness to noise over wind triangle-based approaches such as Langelaan *et al.* [91] that use static estimation. Tian *et al.* [145] provides a thorough review of fixed-wing wind estimation techniques. More recent approaches to fixed-wing wind estimation include Halefom *et al.* [67] which uses an unsteady aerodynamic model, as well as Gahan *et al.* [50], which uses an H_∞ filter to account for arbitrary finite-energy turbulence. The H_∞ filtering approach was also extended in Gahan *et al.* [48], [49] to account for parametric uncertainty using generalized Polynomial Chaos (gPC).

For multirotor aircraft, González-Rocha *et al.* [56] refined and generalized earlier model-based approaches such as Xiang *et al.* [156] and Pappu *et al.* [124]. More recent multirotor wind estimation efforts that use nonlinear aerodynamic models include Perozzi *et al.* [126] and Chen and Bai [31]. Another approach to multirotor wind estimation by Azid *et al.* [13] uses unknown input estimation techniques and treats the wind velocity as an unknown input to the system. Other approaches such as those by Asignacion *et al.* [11] and Yu *et al.* [159] use a disturbance observer to infer the wind velocity. Another noteworthy approach is Chen *et al.* [32] which uses the invariant extended Kalman filter — a locally stable, statistically informed version of a symmetry-preserving observer.

This chapter introduces key concepts and tools that enable the application of symmetry-

preserving reduced-order observer theory (Chapter 3) in combination with nonlinear flight dynamics and system identification (Chapter 4) to the problem of wind estimation for maneuvering aircraft (Chapters 7 and 8). First, Section 6.2 discusses the wind field in which aircraft fly and how it is experienced by the aircraft. Next, Section 6.3 extends the rigid-body aircraft equations of motion in Section 2.4 to flight in turbulent wind. The stochastic model that results can then be used as the process model in an estimator such as the extended Kalman filter or a deterministic observer such as the symmetry-preserving reduced-order observer presented in Chapter 3. Finally, Section 6.4 discusses the reconstruction of wind velocity using specialized instrumentation to validate the wind estimation techniques presented in Chapters 7 and 8.

6.2 Wind Models

In general and independent of the aircraft's motion, wind is a time-varying vector field, $\boldsymbol{W} : \mathbb{R}^3 \times \mathbb{R} \to \mathbb{R}^3$, defined in the inertial frame. Let the instantaneous wind vector as experienced by the aircraft be defined as

$$\boldsymbol{w}(t) = \boldsymbol{W}(\boldsymbol{q}(t), t) \tag{6.1}$$

The *apparent wind* $\boldsymbol{w}$ is defined by evaluating the wind field $\boldsymbol{W}$ at the aircraft's position $\boldsymbol{q}$ at time t as if the aircraft were absent. Using the chain rule, the time derivative of $\boldsymbol{w}$ is

$$\frac{\mathrm{d}\boldsymbol{w}}{\mathrm{d}t} = \frac{\partial \boldsymbol{W}}{\partial t}(\boldsymbol{q}, t) + \nabla \boldsymbol{W}(\boldsymbol{q}, t)\frac{\mathrm{d}\boldsymbol{q}}{\mathrm{d}t} \tag{6.2}$$

Note that we have arrived at Eq. (6.2) under the implicit assumption that the vehicle does not affect the flow field in which it is immersed. When the aircraft's velocity through a wind field is significantly faster than the time rate of change of the eddies (such as for fixed-wing aircraft), we can make a *frozen turbulence* assumption [40], meaning $\frac{\partial \boldsymbol{W}}{\partial t}(\boldsymbol{q}, t) = \boldsymbol{0}$. Therefore, Eq. (6.2) becomes

$$\dot{\boldsymbol{w}} = \nabla \boldsymbol{W}(\boldsymbol{q})\dot{\boldsymbol{q}} \tag{6.3}$$

Conversely, if the aircraft is not moving, the eddies are being convected over the aircraft by the bulk flow. Therefore, $\dot{\boldsymbol{w}}$ would instead become

$$\dot{\boldsymbol{w}} = \frac{\partial \boldsymbol{W}(t)}{\partial t} \tag{6.4}$$

where $\frac{\partial \boldsymbol{W}}{\partial t}$ is the time rate of change of wind velocity at the aircraft's position due to the convected eddies.

The above models for the apparent wind treat the aircraft as a single point in the wind field. However, the gradient of the wind field on the scale of the aircraft also influences its motion. Independent of the vehicle's geometry, the *body-frame wind field gradient* for the aircraft's current pose ($\boldsymbol{q}$ and $\boldsymbol{R}_{\mathrm{IB}}$ at time t) is

$$\boldsymbol{\Phi}_W(\boldsymbol{q}, \boldsymbol{R}_{\mathrm{IB}}, t) \coloneqq \boldsymbol{R}_{\mathrm{IB}}^{\mathsf{T}} \nabla \boldsymbol{W}(\boldsymbol{q}, t) \boldsymbol{R}_{\mathrm{IB}} \tag{6.5}$$

Following the approach of Frost and Bowles [45], the body-frame gradient of the wind field can be decomposed into its symmetric and skew-symmetric parts,

$$\boldsymbol{\Phi}_W = \frac{1}{2}(\boldsymbol{\Phi}_W + \boldsymbol{\Phi}_W^\mathsf{T}) + \frac{1}{2}(\boldsymbol{\Phi}_W - \boldsymbol{\Phi}_W^\mathsf{T}) \tag{6.6}$$

The skew-symmetric part $\frac{1}{2}(\boldsymbol{\Phi}_W - \boldsymbol{\Phi}_W^\mathsf{T})$ defines the *angular velocity of the wind* in the body frame. As a vector-valued map,

$$\boldsymbol{\omega}_W = \frac{1}{2}\boldsymbol{S}^{-1}(\boldsymbol{\Phi}_W - \boldsymbol{\Phi}_W^\mathsf{T}) \tag{6.7}$$

While $\boldsymbol{\omega}_W$ is in fact a vector field assigning a body-frame wind angular velocity to each time t and aircraft configuration $(\boldsymbol{q}, \boldsymbol{R}_{\text{IB}})$, each aircraft will "experience" a different gradient based on its geometry. Consider an arbitrary point $\boldsymbol{r} = [x\ y\ z]^\mathsf{T}$ defined relative to the CG in the body frame. At an instant in time,

$$\boldsymbol{W}_b(\boldsymbol{r}) = \begin{bmatrix} u_W(x,y,z) \\ v_W(x,y,z) \\ w_W(x,y,z) \end{bmatrix} \coloneqq \boldsymbol{R}_{\text{IB}}^\mathsf{T}(t)\boldsymbol{W}(\boldsymbol{R}_{\text{IB}}^\mathsf{T}(t)\boldsymbol{q}(t) + \boldsymbol{r}, t) \tag{6.8}$$

is the *body-frame wind field*. In the case of traditional fixed-wing aircraft, for example, Etkin [41] argues the only non-negligible gradients of the body-frame wind field $\boldsymbol{W}_b$ are

$$p_w \coloneqq \frac{\partial w_W}{\partial y}, \quad q_w \coloneqq -\frac{\partial w_W}{\partial x}, \quad \text{and} \quad r_w \coloneqq \frac{\partial v_W}{\partial x} \tag{6.9}$$

reflecting an assumption that

a) the body-longitudinal component of wind, u_W, is constant/uniform over the entire aircraft,

b) the body-lateral component of wind, v_W, varies only along the aircraft's length, and

c) the body-vertical component of wind, w_W, varies only along the aircraft's length and span.

The vector $\boldsymbol{\omega}_w = [p_w\ q_w\ r_w]^\mathsf{T}$ as defined by Eq. (6.9) is called the *apparent angular velocity of the wind*. Therefore, a fixed-wing aircraft experiences the *apparent body-frame wind gradient*

$$\boldsymbol{\Phi}_w \coloneqq \begin{bmatrix} 0 & 0 & 0 \\ r_w & 0 & 0 \\ -q_w & p_w & 0 \end{bmatrix} \tag{6.10}$$

For other types of aircraft, $\boldsymbol{\Phi}_w$ may take on a different structure, and $\boldsymbol{\omega}_w$ will be defined accordingly. In general, the relationship between the body-frame wind field gradient $\boldsymbol{\omega}_W$ and the apparent body frame wind gradient $\boldsymbol{\omega}_w$ depends on the aircraft's geometry and aerodynamics.

Incorporation of the aircraft dynamics (2.14) into a model-based wind estimation scheme requires the postulation of a model for the apparent wind dynamics (6.2). In general, we cannot practically formulate a deterministic model that accurately describes the dynamics of the apparent wind $\boldsymbol{w}$ and the wind gradient $\boldsymbol{\Phi}_W$. The best we can do in a deterministic setting is assume the wind field $\boldsymbol{W}$ is uniform and constant. In this case, the apparent wind is constant (i.e., $\dot{\boldsymbol{w}} = \boldsymbol{0}$) and the gradient terms vanish (i.e., $\boldsymbol{\Phi}_W \equiv \boldsymbol{0} \implies \boldsymbol{\omega}_{\mathrm{r}} \equiv \boldsymbol{\omega}$). Even though the wind is assumed to be constant, this model does not preclude a wind estimation scheme from estimating variations in the apparent wind velocity $\boldsymbol{w}$.

In the stochastic setting, however, much effort has been spent in characterizing the statistics of the apparent wind. Dryden and von Kármán turbulence models have been used for decades and constitute a standard approach across flight mechanics disciplines [148]. These models aim to characterize the frequency content of the body-frame wind fluctuations $\delta\boldsymbol{w}_b$ and the body-frame apparent angular velocity $\boldsymbol{\omega}_w$. The fluctuations $\delta\boldsymbol{w}_b$ satisfy a Reynolds decomposition,

$$\boldsymbol{w} = \bar{\boldsymbol{w}} + \boldsymbol{R}_{\mathrm{IB}}\delta\boldsymbol{w}_b \tag{6.11}$$

where $\bar{\boldsymbol{w}}$ is the deterministic bulk flow, assumed to be constant on the time scales of motion considered. With a state space realization, Dryden and approximations of von Kármán turbulence models act as noise shaping filters and take the general form

$$\dot{\boldsymbol{x}}_w = \boldsymbol{A}_w\boldsymbol{x}_w + \boldsymbol{B}_w\boldsymbol{\xi}_w \tag{6.12a}$$
$$\delta\boldsymbol{w}_b = \boldsymbol{C}_{\delta w_b}\boldsymbol{x}_w \tag{6.12b}$$
$$\boldsymbol{\omega}_w = \boldsymbol{C}_{\omega_w}\boldsymbol{x}_w \tag{6.12c}$$

where $\boldsymbol{\xi}_w$ is 6-dimensional continuous-time white noise with unit variance. As discussed in Chapter 2, $\boldsymbol{\xi}_w$ is the distributional derivative of the standard Wiener process.

6.3 Wind Estimation Process Models

The wind model (6.12) may now be incorporated with the aircraft dynamics (2.14) to form the process model used in a wind estimation scheme. Under a quasi-steady assumption, the aerodynamic force $\boldsymbol{F}$ and moment $\boldsymbol{M}$ have the general dependence

$$\boldsymbol{F} = \boldsymbol{F}(\boldsymbol{v}_{\mathrm{r}}, \boldsymbol{\omega}_{\mathrm{r}}, \boldsymbol{\delta})$$
$$\boldsymbol{M} = \boldsymbol{M}(\boldsymbol{v}_{\mathrm{r}}, \boldsymbol{\omega}_{\mathrm{r}}, \boldsymbol{\delta})$$

where $\boldsymbol{\delta}$ comprises the aircraft control inputs (e.g., control surface deflections and propeller speeds) and

$$\boldsymbol{v}_{\mathrm{r}} = \boldsymbol{v} - \boldsymbol{R}_{\mathrm{IB}}^{\mathsf{T}}\boldsymbol{w} \tag{6.13}$$
$$\boldsymbol{\omega}_{\mathrm{r}} = \boldsymbol{\omega} - \boldsymbol{\omega}_w \tag{6.14}$$

Equation (6.13) is known as the *wind triangle*. In model-based wind estimation it is advantageous to include $\boldsymbol{v}_{\mathrm{r}}$ as a state variable instead of $\boldsymbol{v}$ since the apparent wind then appears in the translational kinematics [56].

Taking the time derivative of wind triangle (6.13), we have

$$\begin{aligned}
\dot{\boldsymbol{v}}_{\mathrm{r}} &= \dot{\boldsymbol{v}} - \dot{\boldsymbol{R}}_{\mathrm{IB}}^{\mathsf{T}}\boldsymbol{w} - \boldsymbol{R}_{\mathrm{IB}}^{\mathsf{T}}\dot{\boldsymbol{w}} \\
&= \boldsymbol{v} \times \boldsymbol{\omega} + \boldsymbol{R}_{\mathrm{IB}}^{\mathsf{T}}\boldsymbol{g} + \frac{1}{m}\boldsymbol{F}(\boldsymbol{v}_{\mathrm{r}}, \boldsymbol{\omega}_{\mathrm{r}}, \boldsymbol{\delta}) + \boldsymbol{S}(\boldsymbol{\omega})\boldsymbol{R}_{\mathrm{IB}}^{\mathsf{T}}\boldsymbol{w} - \boldsymbol{R}_{\mathrm{IB}}^{\mathsf{T}}\dot{\boldsymbol{w}} \\
&= \boldsymbol{v} \times \boldsymbol{\omega} + \boldsymbol{R}_{\mathrm{IB}}^{\mathsf{T}}\boldsymbol{g} + \frac{1}{m}\boldsymbol{F}(\boldsymbol{v}_{\mathrm{r}}, \boldsymbol{\omega}_{\mathrm{r}}, \boldsymbol{\delta}) - (\boldsymbol{R}_{\mathrm{IB}}^{\mathsf{T}}\boldsymbol{w}) \times \boldsymbol{\omega} - \boldsymbol{R}_{\mathrm{IB}}^{\mathsf{T}}\dot{\boldsymbol{w}} \\
&= (\boldsymbol{v} - \boldsymbol{R}_{\mathrm{IB}}^{\mathsf{T}}\boldsymbol{w}) \times \boldsymbol{\omega} + \boldsymbol{R}_{\mathrm{IB}}^{\mathsf{T}}\boldsymbol{g} + \frac{1}{m}\boldsymbol{F}(\boldsymbol{v}_{\mathrm{r}}, \boldsymbol{\omega}_{\mathrm{r}}, \boldsymbol{\delta}) - \boldsymbol{R}_{\mathrm{IB}}^{\mathsf{T}}\dot{\boldsymbol{w}}
\end{aligned}$$

Again, making use of the wind triangle yields

$$\dot{\boldsymbol{v}}_{\mathrm{r}} = \boldsymbol{v}_{\mathrm{r}} \times \boldsymbol{\omega} + \boldsymbol{R}_{\mathrm{IB}}^{\mathsf{T}}\boldsymbol{g} + \frac{1}{m}\boldsymbol{F}(\boldsymbol{v}_{\mathrm{r}}, \boldsymbol{\omega}_{\mathrm{r}}, \boldsymbol{\delta}) - \boldsymbol{R}_{\mathrm{IB}}^{\mathsf{T}}\dot{\boldsymbol{w}} \tag{6.15}$$

Similarly for the air-relative angular velocity, the time derivative of Eq. (6.14) is

$$\dot{\boldsymbol{\omega}}_{\mathrm{r}} = \boldsymbol{I}^{-1}\big((\boldsymbol{I}\boldsymbol{\omega}_{\mathrm{r}} + \boldsymbol{I}\boldsymbol{\omega}_{w}) \times (\boldsymbol{\omega}_{\mathrm{r}} + \boldsymbol{\omega}_{w}) + \boldsymbol{M}(\boldsymbol{v}_{\mathrm{r}}, \boldsymbol{\omega}_{\mathrm{r}}, \boldsymbol{\delta})\big) - \dot{\boldsymbol{\omega}}_{w} \tag{6.16}$$

Altogether, aircraft motion in a non-uniform, time-varying wind field satisfies

$$\dot{\boldsymbol{q}} = \boldsymbol{R}_{\mathrm{IB}}\boldsymbol{v}_{\mathrm{r}} + \boldsymbol{w} \tag{6.17a}$$

$$\dot{\boldsymbol{R}}_{\mathrm{IB}} = \boldsymbol{R}_{\mathrm{IB}}\boldsymbol{S}(\boldsymbol{\omega}_{\mathrm{r}} + \boldsymbol{\omega}_{w}) \tag{6.17b}$$

$$\dot{\boldsymbol{v}}_{\mathrm{r}} = \boldsymbol{v}_{\mathrm{r}} \times (\boldsymbol{\omega}_{\mathrm{r}} + \boldsymbol{\omega}_{w}) + \boldsymbol{R}_{\mathrm{IB}}^{\mathsf{T}}\boldsymbol{g} + \frac{1}{m}\boldsymbol{F}(\boldsymbol{v}_{\mathrm{r}}, \boldsymbol{\omega}_{\mathrm{r}}, \boldsymbol{\delta}) - \boldsymbol{R}_{\mathrm{IB}}^{\mathsf{T}}\dot{\boldsymbol{w}} \tag{6.17c}$$

$$\dot{\boldsymbol{\omega}}_{\mathrm{r}} = \boldsymbol{I}^{-1}\big((\boldsymbol{I}\boldsymbol{\omega}_{\mathrm{r}} + \boldsymbol{I}\boldsymbol{\omega}_{w}) \times (\boldsymbol{\omega}_{\mathrm{r}} + \boldsymbol{\omega}_{w}) + \boldsymbol{M}(\boldsymbol{v}_{\mathrm{r}}, \boldsymbol{\omega}_{\mathrm{r}}, \boldsymbol{\delta})\big) - \dot{\boldsymbol{\omega}}_{w} \tag{6.17d}$$

where $\dot{\boldsymbol{w}}$ and $\dot{\boldsymbol{\omega}}_{w}$ satisfy Eqs. (6.11)–(6.12).

Before incorporating Eq. (6.17) into a model-based wind estimation scheme, it is critical to recognize the force and moment models $\boldsymbol{F}(\boldsymbol{v}_{\mathrm{r}}, \boldsymbol{\omega}_{\mathrm{r}}, \boldsymbol{\delta})$ and $\boldsymbol{M}(\boldsymbol{v}_{\mathrm{r}}, \boldsymbol{\omega}_{\mathrm{r}}, \boldsymbol{\delta})$ are imperfect. That is, the true force and moment differ from the modeled force and moment due to both parametric error and unmodeled dynamics. As explained by Morelli and Klein [113, Ch. 5], principled experiment design and model structure determination should yield independently distributed model residuals. However, restricting ourselves to quasi-steady models implies the residuals

$$\begin{aligned}
\delta\boldsymbol{F} &\coloneqq \boldsymbol{F}_{\mathrm{true}} - \boldsymbol{F}(\boldsymbol{v}_{\mathrm{r}}, \boldsymbol{\omega}_{\mathrm{r}}, \boldsymbol{\delta}) \\
\delta\boldsymbol{M} &\coloneqq \boldsymbol{M}_{\mathrm{true}} - \boldsymbol{M}(\boldsymbol{v}_{\mathrm{r}}, \boldsymbol{\omega}_{\mathrm{r}}, \boldsymbol{\delta})
\end{aligned} \tag{6.18}$$

will not exactly resemble white noise, but may exhibit additional frequency content associated with unsteady aerodynamic modes. With experimentally-obtained data for $\delta\boldsymbol{F}$ and

$\delta \boldsymbol{M}$, one can thus design a shaping filter

$$\dot{\boldsymbol{x}}_a = \boldsymbol{A}_a \boldsymbol{x}_a + \boldsymbol{B}_a \boldsymbol{\xi}_a \tag{6.19}$$
$$\delta \boldsymbol{F} = \boldsymbol{C}_{\delta F} \boldsymbol{x}_a \tag{6.20}$$
$$\delta \boldsymbol{M} = \boldsymbol{C}_{\delta M} \boldsymbol{x}_a \tag{6.21}$$

where $\boldsymbol{\xi}_a$ is 6-dimensional continuous-time white noise with unit variance.

Finally, the shaping filters for both the wind (Eq. (6.12a)) and aerodynamic modeling error (Eq. (6.19)) are incorporated into the air-relative aircraft equations of motion (6.17) with the appropriate substitutions to form the process model

$$\dot{\boldsymbol{q}} = \boldsymbol{R}_{\mathrm{IB}} \boldsymbol{v}_{\mathrm{r}} + \boldsymbol{w} \tag{6.22a}$$
$$\dot{\boldsymbol{R}}_{\mathrm{IB}} = \boldsymbol{R}_{\mathrm{IB}} \boldsymbol{S}(\boldsymbol{\omega}_{\mathrm{r}} + \boldsymbol{C}_{\omega_w} \boldsymbol{x}_w) \tag{6.22b}$$
$$\dot{\boldsymbol{v}}_{\mathrm{r}} = \boldsymbol{v}_{\mathrm{r}} \times (\boldsymbol{\omega}_{\mathrm{r}} + \boldsymbol{C}_{\omega_w} \boldsymbol{x}_w) + \boldsymbol{R}_{\mathrm{IB}}^{\mathsf{T}} \boldsymbol{g} + \frac{1}{m} \boldsymbol{F}(\boldsymbol{v}_{\mathrm{r}}, \boldsymbol{\omega}_{\mathrm{r}}, \boldsymbol{\delta}) + \frac{1}{m} \boldsymbol{C}_{\delta F} \boldsymbol{x}_a - \boldsymbol{R}_{\mathrm{IB}}^{\mathsf{T}} \dot{\boldsymbol{w}} \tag{6.22c}$$
$$\dot{\boldsymbol{\omega}}_{\mathrm{r}} = \boldsymbol{I}^{-1} \big((\boldsymbol{I} \boldsymbol{\omega}_{\mathrm{r}} + \boldsymbol{I} \boldsymbol{C}_{\omega_w} \boldsymbol{x}_w) \times (\boldsymbol{\omega}_{\mathrm{r}} + \boldsymbol{C}_{\omega_w} \boldsymbol{x}_w) + \boldsymbol{M}(\boldsymbol{v}_{\mathrm{r}}, \boldsymbol{\omega}_{\mathrm{r}}, \boldsymbol{\delta}) \big) + \boldsymbol{I}^{-1} \boldsymbol{C}_{\delta M} \boldsymbol{x}_a - \boldsymbol{C}_{\omega_w} (\boldsymbol{A}_w \boldsymbol{x}_w + \boldsymbol{B}_w \boldsymbol{\xi}_w) \tag{6.22d}$$
$$\dot{\boldsymbol{x}}_w = \boldsymbol{A}_w \boldsymbol{x}_w + \boldsymbol{B}_w \boldsymbol{\xi}_w \tag{6.22e}$$
$$\dot{\boldsymbol{x}}_a = \boldsymbol{A}_a \boldsymbol{x}_a + \boldsymbol{B}_a \boldsymbol{\xi}_a \tag{6.22f}$$

While the techniques presented in this chapter are applicable to process model (6.22), we choose to simplify the discussion and comparison among approaches by assuming the following.

Assumption 6.1.

i) *The angular velocity of the wind $\boldsymbol{\omega}_w$ is zero.*

ii) *The apparent wind $\boldsymbol{w}$ is Brownian motion.*

iii) *The aerodynamic force and moment modeling error are Gaussian, white noise.*

Accordingly, consider a 9-dimensional Wiener process $\boldsymbol{W} = (\boldsymbol{W}^w, \boldsymbol{W}^M, \boldsymbol{W}^F)$ defined on a probability space $(\Omega, \mathcal{F}, \mathbb{P})$ such that

$$\mathrm{d}\boldsymbol{w}(t) = \boldsymbol{\sigma}_w(t) \mathrm{d}\boldsymbol{W}_t^w, \quad \boldsymbol{I}^{-1} \delta \boldsymbol{M} \mathrm{d}t = \boldsymbol{\sigma}_M(t) \mathrm{d}\boldsymbol{W}_t^M, \quad \text{and} \quad \frac{1}{m} \delta \boldsymbol{F} \mathrm{d}t = \boldsymbol{\sigma}_F(t) \mathrm{d}\boldsymbol{W}_t^F \tag{6.23}$$

Let $\boldsymbol{\sigma} = \mathbf{diag}(\boldsymbol{\sigma}_w, \boldsymbol{\sigma}_M, \boldsymbol{\sigma}_F) \in \mathbb{R}^{9 \times 9}$. The matrix $\boldsymbol{\sigma}\boldsymbol{\sigma}^{\mathsf{T}}$ is the infinitesimal covariance of the scaled Wiener process $\boldsymbol{\sigma}\boldsymbol{W}$. From another perspective, it is the power spectral density of the continuous-time white noise $\boldsymbol{\sigma}\dot{\boldsymbol{W}}$, where $\dot{\boldsymbol{W}}$ is the distributional derivative of $\boldsymbol{w}$ (see Section 2.6).

Under Assumption 6.1, Eq. (6.22) is now written as the stochastic differential equation

$$\mathrm{d}\boldsymbol{q} = \big(\boldsymbol{R}_{\mathrm{IB}}\boldsymbol{v}_{\mathrm{r}} + \boldsymbol{w}\big)\mathrm{d}t \tag{6.24a}$$
$$\mathrm{d}\boldsymbol{R}_{\mathrm{IB}} = \big(\boldsymbol{R}_{\mathrm{IB}}\boldsymbol{S}(\boldsymbol{\omega})\big)\mathrm{d}t \tag{6.24b}$$
$$\mathrm{d}\boldsymbol{v}_{\mathrm{r}} = \big(\boldsymbol{v}_{\mathrm{r}} \times \boldsymbol{\omega} + \boldsymbol{R}_{\mathrm{IB}}^{\mathsf{T}}\boldsymbol{g} + \tfrac{1}{m}\boldsymbol{F}(\boldsymbol{v}_{\mathrm{r}}, \boldsymbol{\omega}, \boldsymbol{\delta})\big)\mathrm{d}t + \boldsymbol{\sigma}_F \mathrm{d}\boldsymbol{W}^F - \boldsymbol{R}_{\mathrm{IB}}^{\mathsf{T}}\boldsymbol{\sigma}_w \mathrm{d}\boldsymbol{W}^w \tag{6.24c}$$
$$\mathrm{d}\boldsymbol{\omega} = \boldsymbol{I}^{-1}\big(\boldsymbol{I}\boldsymbol{\omega} \times \boldsymbol{\omega} + \boldsymbol{M}(\boldsymbol{v}_{\mathrm{r}}, \boldsymbol{\omega}, \boldsymbol{\delta})\big)\mathrm{d}t + \boldsymbol{\sigma}_M \mathrm{d}\boldsymbol{W}^M \tag{6.24d}$$
$$\mathrm{d}\boldsymbol{w} = \boldsymbol{\sigma}_w \mathrm{d}\boldsymbol{W}^w \tag{6.24e}$$

Here, the rotational kinematics $\mathrm{d}\boldsymbol{R}_{\mathrm{IB}}$ can just be interpreted as shorthand for an ordinary integral since no noise appears. We have not introduced the required machinery to describe statistics of trajectories $\boldsymbol{R}_{\mathrm{IB}}(t)$; however, such a technical distinction does not matter since the the wind estimation problem does not require the probabilistic characterization of $\boldsymbol{R}_{\mathrm{IB}}(t)$.

Remark 6.1. *Although not considered in this dissertation, there are several competing perspectives on how to describe stochastic dynamics on non-Euclidean manifolds. The most straightforward approach is to consider an alternative to the Itô integral — the* Stratonovich integral *— which obeys the chain rule of normal calculus. However, the result is no longer non-anticipating; that is, the nice statistical properties of the Itô integral go away. Sticking with the Itô integral, the approach of Gliklikh [52] and others (e.g., Belopolskaya and Dalecky [21]) defines* sections *(a generalization of vector fields) of* Itô bundles *(a generalization of the tangent bundle). The more modern approach of Armstrong and Brigo [9] involves* jet bundles *and describes SDEs using 2-jets. Analogous to a coordinate-free second-order Taylor series expansion, fields of these 2-jets define infinitesimal quadratic curves at each point on the manifold, describing the stochastic evolution of the state. Yet another approach by Emery [39] is using* diffusors *(second-order tangent vectors) and the* Schwartz morphism *— a special extension of the tangent map for second-order tangent spaces.*

6.4 Wind Reconstruction

As part of the development process for wind estimation techniques, it can be instrumental to have a truth source for comparison. For applications where the mean wind velocity is of interest, a stationary anemometer or remote sensing solution (e.g., Doppler LiDAR) is sufficient. The model-based wind estimation techniques presented in this dissertation, however, aim to also accurately estimate the wind fluctuations. In this case, an *in situ* measurement must be used to validate the wind estimates. For multirotor aircraft, sonic anemometers are often placed on a mast sufficiently high above the rotors [123]. For fixed-wing aircraft, air data units (ADUs) are instead used to reconstruct the wind velocity. A vaned air data unit was designed and manufactured to validate the wind estimation approaches in this dissertation. Depending on the aircraft, it was either mounted out the nose (Figure 6.1a) or out each wingtip (Figure 6.1b). Each ADU consists of two 3D-printed vanes attached to 12-bit (4,096-position) PWM magnetic rotary encoders that are sampled at a rate of 200 Hz by a microcontroller. The vane angles are transmitted to the autopilot over the CAN bus using a

(a) MTD air data unit

(b) eSPAARO air data unit

Figure 6.1: Vaned air data unit mounting locations

custom PX4 driver. The tip of the ADU is a 3D-printed Kiel probe connected to a DLVR-10 differential pressure sensor, also communicating with the autopilot over the CAN bus, with the sensor sampled at 50 Hz.

Let V, α, and β_f be the airspeed, angle-of-attack, and flank angle, respectively, reported by the ADU. First, the angle-of-attack and flank angle data were low-pass filtered with a cutoff frequency of 10 Hz to filter out any structural dynamics of the wing. Next, the autopilot's inertial velocity estimates $\boldsymbol{v}_{\text{i}}$ (average standard deviation of $[0.01 \;\; 0.01 \;\; 0.005]^{\mathsf{T}}$ m/s), attitude estimates (average attitude estimate standard deviation of $[0.004 \;\; 0.004 \;\; 0.013]^{\mathsf{T}} \in \mathsf{T}_{\hat{\boldsymbol{R}}_{\text{IB}}}\mathsf{SO}(3)$), and angular velocity measurements from the calibrated gyroscope (noise and bias removed) were used to reconstruct the apparent wind velocity as

$$\boldsymbol{w} = \boldsymbol{v}_{\text{i}} - \boldsymbol{R}_{\text{IB}} \left(\boldsymbol{v}_{\text{ADU}} - \boldsymbol{\omega} \times \boldsymbol{r}_{\text{ADU}} \right) \tag{6.25}$$

where

$$\boldsymbol{v}_{\text{ADU}} = \boldsymbol{R}_{\text{BW}}(\alpha, \beta) \boldsymbol{e}_1 V$$

is the air-relative velocity at the geometric center of the two ADU vanes, whose position in the body frame is denoted $\boldsymbol{r}_{\text{ADU}}$. The rotation matrix $\boldsymbol{R}_{\text{BW}}(\alpha, \beta) = e^{-\boldsymbol{S}(\boldsymbol{e}_2)\alpha} e^{\boldsymbol{S}(\boldsymbol{e}_3)\beta}$, which maps free vectors from the wind frame to the body frame, is parameterized by the measured angle-of-attack α and the sideslip angle

$$\beta = \tan^{-1}(\tan(\beta_f) \cos(\alpha))$$

The accuracy of the reconstructed wind velocity can be characterized by propagating measurement uncertainties through Eq. (6.25) as done by Halefom *et al.* [67].

Chapter 7

Symmetry-Preserving Reduced-Order Wind Observers

7.1 Introduction

As described in Chapter 6, typical approaches to model-based wind estimation produce estimates of not only wind and air-relative velocity, but also known signals such as position, attitude, and angular velocity. In many cases, there is no practical use in re-estimating this measured part of the aircraft's state using *full-order* observers and estimators. Instead, *reduced-order* observers are of great interest in which only the unmeasured part of the state is estimated. This approach can decrease computational complexity and simplify the observer design process. As demonstrated in Section 3.6, aircraft dynamics possess symmetries. In particular, they are invariant under rotations and translations (e.g., the standard orientation of the body frame with respect to the physical airframe corresponds to just one of many valid coordinate representations). Motivated by these observations, we now apply the symmetry-preserving, reduced-order observer theory of Chapter 3 to estimate wind velocity for maneuvering aircraft. This chapter is largely based on references [77] and [71].

7.2 A Symmetry-Preserving Reduced-Order Wind Observer

7.2.1 Problem Setting

In this section, we consider the deterministic aircraft dynamics in wind; that is, the noise terms in Eq. (6.24) are neglected. To simplify the observer gain selection, we also make the following assumption on the aircraft's aerodynamics.

Assumption 7.1. *The aerodynamic force and moment satisfy*

$$\boldsymbol{F} = \boldsymbol{F}_0 + \boldsymbol{F}_v \boldsymbol{v}_{\mathrm{r}} + \boldsymbol{F}_\omega \boldsymbol{\omega} \tag{7.1}$$

$$\boldsymbol{M} = \boldsymbol{M}_0 + \boldsymbol{M}_v \boldsymbol{v}_{\mathrm{r}} + \boldsymbol{M}_\omega \boldsymbol{\omega} \tag{7.2}$$

where $\boldsymbol{F}_{(\cdot)}$ and $\boldsymbol{M}_{(\cdot)}$ are known "inputs" that vary with the aircraft state and control.

Equations (7.1)–(7.2) reflect a linearization of force and moment nonlinearities comprising

the unknown air-relative velocity $\boldsymbol{v}_{\mathrm{r}}$. Practical considerations and consequences of Assumption 7.1 are discussed in Section 7.6.3.

Altogether, the aircraft equations of motion used in the design of a symmetry-preserving reduced-order wind observer are

$$\dot{\boldsymbol{q}} = \boldsymbol{R}_{\mathrm{IB}}\boldsymbol{v}_{\mathrm{r}} + \boldsymbol{w} \tag{7.3a}$$

$$\dot{\boldsymbol{R}}_{\mathrm{IB}} = \boldsymbol{R}_{\mathrm{IB}}\boldsymbol{S}(\boldsymbol{\omega}) \tag{7.3b}$$

$$\dot{\boldsymbol{\omega}} = \boldsymbol{I}^{-1}\left(\boldsymbol{I}\boldsymbol{\omega}\times\boldsymbol{\omega} + \boldsymbol{M}_0 + \boldsymbol{M}_v\boldsymbol{v}_{\mathrm{r}} + \boldsymbol{M}_\omega\boldsymbol{\omega}\right) \tag{7.3c}$$

$$\dot{\boldsymbol{v}}_{\mathrm{r}} = \boldsymbol{v}_{\mathrm{r}}\times\boldsymbol{\omega} + \boldsymbol{R}_{\mathrm{IB}}^{\mathsf{T}}\boldsymbol{g} + \frac{1}{m}\left(\boldsymbol{F}_0 + \boldsymbol{F}_v\boldsymbol{v}_{\mathrm{r}} + \boldsymbol{F}_\omega\boldsymbol{\omega}\right) \tag{7.3d}$$

$$\dot{\boldsymbol{w}} = \boldsymbol{0} \tag{7.3e}$$

It is often the case that aircraft are instrumented with an accelerometer, gyroscope, magnetometer, and inertial positioning system (i.e. vision-based or GNSS) such that position, attitude, and angular velocity measurements can be readily obtained with negligible noise from a low-level estimation algorithm. Therefore, we make the following assumption.

Assumption 7.2. *The aircraft's position $\boldsymbol{q}$, attitude $\boldsymbol{R}_{\mathrm{IB}}$, and angular velocity $\boldsymbol{\omega}$ are obtained without error.*

Thus, we take $\boldsymbol{y} = (\boldsymbol{q}, \boldsymbol{R}_{\mathrm{IB}}, \boldsymbol{\omega}) \in \mathcal{Y} = \mathsf{SE}(3)\times\mathbb{R}^3$ to be the measured part of the state and $\boldsymbol{x} = (\boldsymbol{v}_{\mathrm{r}}, \boldsymbol{w}) \in \mathcal{X} = \mathbb{R}^n$ to be the unmeasured part. Here, the dimension of $\mathcal{Y}$ is $p = 9$ ($\mathsf{SE}(3)$ is a 6-dimensional smooth manifold), and the dimension of $\mathcal{X}$ is $n = 6$. The total state space of the system is the $(n+p=15)$-dimensional manifold $\mathcal{X}\times\mathcal{Y}$. As described in Chapter 3, the input $\boldsymbol{u}$ for the purpose of observer design is not necessarily flight control inputs as in the vector $\boldsymbol{\delta}$ above; rather it is a collection of known quantities on which a particular transformation group acts. In this case, it is composed of all quantities, other than the system state, that are expressed in either $\mathcal{F}_{\mathrm{B}}$ or $\mathcal{F}_{\mathrm{I}}$. That is, $\boldsymbol{u} = (\boldsymbol{g}, \boldsymbol{I}, \boldsymbol{M}_0, \boldsymbol{M}_v, \boldsymbol{M}_\omega, \boldsymbol{F}_0, \boldsymbol{F}_v, \boldsymbol{F}_\omega) \in \mathcal{U}$. With these definitions, the aircraft dynamics (7.3) are in the form of Eq. (3.1), where the vector field $(\boldsymbol{f}, \boldsymbol{h})$ in Eq. (3.1) is appropriately constructed from the right-hand side of Eq. (7.3).

Remark 7.1. *Note that inertial velocity measurements from GNSS are not included in the measured part of the state, $\boldsymbol{y}$. For the state variables considered here, position data is better suited for obtaining a stable observer. As discussed in Section 7.3.3, however, inertial velocity measurements are still useful in practical implementation for approximating continuous-time position data between GNSS samples. It remains to be explored whether other combinations of state variables may benefit from including inertial velocity in $\boldsymbol{y}$ rather than position.*

7.2.2 $\mathsf{SO}(3)$-Invariance of the Aircraft Dynamics in Wind

First, we aim to find a transformation group $\{\boldsymbol{\varphi}_g, \boldsymbol{\varrho}_g, \boldsymbol{\psi}_g\}_{g\in G}$ under which the system (7.3) is invariant. Here, $\boldsymbol{\varphi}_g$ acts on the unmeasured part of state, $\boldsymbol{\varrho}_g$ acts on the measured part,

and $\boldsymbol{\psi}_g$ acts on the input. As described in Section 2.4, the configuration of the rigid-body aircraft is a point on $\mathsf{SE}(3)$, the special Euclidean group of 3-dimensional translations and rotations. Therefore, $\mathsf{SE}(3)$ is a natural choice of Lie group G for which a transformation group is defined (as done by Chen *et al.* [32]). However, since position does not explicitly appear on the right-hand side of Eq. (7.3), choosing $G = \mathsf{SO}(3)$ to define the transformation group is sufficient for the construction of a reduced-order observer.

Furthermore, we recognize the aircraft dynamics are invariant under not just a single transformation group, but rather a family of transformation groups. The two most natural choices from this family are given as follows.

Proposition 7.1. *The aircraft dynamics* (7.3) *are* $\mathsf{SO}(3)$*-invariant under the transformation groups*

$$\begin{aligned}
\boldsymbol{\varphi}_g(\boldsymbol{x}) &= \begin{pmatrix} \boldsymbol{v}_{\mathrm{r}} \\ \boldsymbol{R}_g \boldsymbol{w} \end{pmatrix} =: \begin{pmatrix} \boldsymbol{\varphi}_g^{v_{\mathrm{r}}}(\boldsymbol{x}) \\ \boldsymbol{\varphi}_g^{w}(\boldsymbol{x}) \end{pmatrix} \\
\boldsymbol{\varrho}_g(\boldsymbol{y}) &= \begin{pmatrix} \boldsymbol{R}_g \boldsymbol{q} \\ \boldsymbol{R}_g \boldsymbol{R}_{\mathrm{IB}} \\ \boldsymbol{\omega} \end{pmatrix} =: \begin{pmatrix} \boldsymbol{\varrho}_g^{q}(\boldsymbol{y}) \\ \boldsymbol{\varrho}_g^{R_{\mathrm{IB}}}(\boldsymbol{y}) \\ \boldsymbol{\varrho}_g^{\omega}(\boldsymbol{y}) \end{pmatrix}
\end{aligned} \qquad \boldsymbol{\psi}_g(\boldsymbol{u}) = \begin{pmatrix} \boldsymbol{R}_g \boldsymbol{g} \\ \boldsymbol{I} \\ \boldsymbol{M}_0 \\ \boldsymbol{M}_v \\ \boldsymbol{M}_\omega \\ \boldsymbol{F}_0 \\ \boldsymbol{F}_v \\ \boldsymbol{F}_\omega \end{pmatrix} =: \begin{pmatrix} \boldsymbol{\psi}_g^{g}(\boldsymbol{u}) \\ \boldsymbol{\psi}_g^{I}(\boldsymbol{u}) \\ \boldsymbol{\psi}_g^{M_0}(\boldsymbol{u}) \\ \boldsymbol{\psi}_g^{M_v}(\boldsymbol{u}) \\ \boldsymbol{\psi}_g^{M_\omega}(\boldsymbol{u}) \\ \boldsymbol{\psi}_g^{F_0}(\boldsymbol{u}) \\ \boldsymbol{\psi}_g^{F_v}(\boldsymbol{u}) \\ \boldsymbol{\psi}_g^{F_\omega}(\boldsymbol{u}) \end{pmatrix} \tag{7.4.I}$$

and

$$\begin{aligned}
\boldsymbol{\varphi}_g(\boldsymbol{x}) &= \begin{pmatrix} \boldsymbol{R}_g \boldsymbol{v}_{\mathrm{r}} \\ \boldsymbol{w} \end{pmatrix} =: \begin{pmatrix} \boldsymbol{\varphi}_g^{v_{\mathrm{r}}}(\boldsymbol{x}) \\ \boldsymbol{\varphi}_g^{w}(\boldsymbol{x}) \end{pmatrix} \\
\boldsymbol{\varrho}_g(\boldsymbol{y}) &= \begin{pmatrix} \boldsymbol{q} \\ \boldsymbol{R}_{\mathrm{IB}} \boldsymbol{R}_g^{\mathsf{T}} \\ \boldsymbol{R}_g \boldsymbol{\omega} \end{pmatrix} =: \begin{pmatrix} \boldsymbol{\varrho}_g^{q}(\boldsymbol{y}) \\ \boldsymbol{\varrho}_g^{R_{\mathrm{IB}}}(\boldsymbol{y}) \\ \boldsymbol{\varrho}_g^{\omega}(\boldsymbol{y}) \end{pmatrix}
\end{aligned} \qquad \boldsymbol{\psi}_g(\boldsymbol{u}) = \begin{pmatrix} \boldsymbol{g} \\ \boldsymbol{R}_g \boldsymbol{I} \boldsymbol{R}_g^{\mathsf{T}} \\ \boldsymbol{R}_g \boldsymbol{M}_0 \\ \boldsymbol{R}_g \boldsymbol{M}_v \boldsymbol{R}_g^{\mathsf{T}} \\ \boldsymbol{R}_g \boldsymbol{M}_\omega \boldsymbol{R}_g^{\mathsf{T}} \\ \boldsymbol{R}_g \boldsymbol{F}_0 \\ \boldsymbol{R}_g \boldsymbol{F}_v \boldsymbol{R}_g^{\mathsf{T}} \\ \boldsymbol{R}_g \boldsymbol{F}_\omega \boldsymbol{R}_g^{\mathsf{T}} \end{pmatrix} =: \begin{pmatrix} \boldsymbol{\psi}_g^{g}(\boldsymbol{u}) \\ \boldsymbol{\psi}_g^{I}(\boldsymbol{u}) \\ \boldsymbol{\psi}_g^{M_0}(\boldsymbol{u}) \\ \boldsymbol{\psi}_g^{M_v}(\boldsymbol{u}) \\ \boldsymbol{\psi}_g^{M_\omega}(\boldsymbol{u}) \\ \boldsymbol{\psi}_g^{F_0}(\boldsymbol{u}) \\ \boldsymbol{\psi}_g^{F_v}(\boldsymbol{u}) \\ \boldsymbol{\psi}_g^{F_\omega}(\boldsymbol{u}) \end{pmatrix} \tag{7.4.B}$$

where $g = \boldsymbol{R}_g \in \mathsf{SO}(3)$.

Both transformation groups characterize the rotational symmetry of the aircraft dynamics. Since the transformation group defined by Eq. (7.4.I) consists of rotations of inertial frame quantities, we call it the *inertial transformation group*. This transformation group reflects the fact that the orientation of the inertial frame is arbitrary. Conversely, Eq. (7.4.B) consists of rotations of body frame quantities and is thus called the *body transformation group*. Its definition recognizes that the orientation of the body frame is also arbitrary as long as parameters (e.g., aerodynamic force and moment parameters) are appropriately expressed in the rotated coordinate frame. When appropriate, we will append equation numbers with "I" or "B" when they apply to transformation groups (7.4.I) or (7.4.B), respectively.

Proof of Proposition 7.1. First, note that the tangent maps of the transformation groups (7.4.I) and (7.4.B) at $(\boldsymbol{x}, \boldsymbol{y}, \boldsymbol{u})$ applied to $\boldsymbol{f}(\boldsymbol{x}, \boldsymbol{y}, \boldsymbol{u})$ and $\boldsymbol{h}(\boldsymbol{x}, \boldsymbol{y}, \boldsymbol{u})$ respectively satisfy

$$\mathrm{T}_{\boldsymbol{x}}\boldsymbol{\varphi}_g\big(\boldsymbol{f}(\boldsymbol{x}, \boldsymbol{y}, \boldsymbol{u})\big) = \begin{pmatrix} \boldsymbol{f}_{v_\mathrm{r}}(\boldsymbol{x}, \boldsymbol{u}) \\ \boldsymbol{R}_g \boldsymbol{f}_w(\boldsymbol{x}, \boldsymbol{u}) \end{pmatrix} \quad \text{and} \quad \mathrm{T}_{\boldsymbol{y}}\boldsymbol{\varrho}_g\big(\boldsymbol{h}(\boldsymbol{x}, \boldsymbol{y}, \boldsymbol{u})\big) = \begin{pmatrix} \boldsymbol{R}_g \boldsymbol{f}_q(\boldsymbol{x}, \boldsymbol{u}) \\ \boldsymbol{R}_g \boldsymbol{f}_{R_\mathrm{IB}}(\boldsymbol{x}, \boldsymbol{u}) \\ \boldsymbol{f}_\omega(\boldsymbol{x}, \boldsymbol{u}) \end{pmatrix} \tag{7.5.I}$$

$$\mathrm{T}_{\boldsymbol{x}}\boldsymbol{\varphi}_g\big(\boldsymbol{f}(\boldsymbol{x}, \boldsymbol{y}, \boldsymbol{u})\big) = \begin{pmatrix} \boldsymbol{R}_g \boldsymbol{f}_{v_\mathrm{r}}(\boldsymbol{x}, \boldsymbol{u}) \\ \boldsymbol{f}_w(\boldsymbol{x}, \boldsymbol{u}) \end{pmatrix} \quad \text{and} \quad \mathrm{T}_{\boldsymbol{y}}\boldsymbol{\varrho}_g\big(\boldsymbol{h}(\boldsymbol{x}, \boldsymbol{y}, \boldsymbol{u})\big) = \begin{pmatrix} \boldsymbol{f}_q(\boldsymbol{x}, \boldsymbol{u}) \\ \boldsymbol{f}_{R_\mathrm{IB}}(\boldsymbol{x}, \boldsymbol{u}) \boldsymbol{R}_g^\mathsf{T} \\ \boldsymbol{R}_g \boldsymbol{f}_\omega(\boldsymbol{x}, \boldsymbol{u}) \end{pmatrix} \tag{7.5.B}$$

We must show that the expressions above are equal to the evaluation of $\boldsymbol{f}$ and $\boldsymbol{h}$ at the transformed point $(\boldsymbol{\varphi}_g(\boldsymbol{x}), \boldsymbol{\varrho}_g(\boldsymbol{u}), \boldsymbol{\psi}_g(\boldsymbol{u}))$. Starting with the relative velocity dynamics, we have

$$\begin{aligned} \boldsymbol{f}_{v_\mathrm{r}}(\boldsymbol{\varphi}_g(\boldsymbol{x}), \boldsymbol{\varrho}_g(\boldsymbol{y}), \boldsymbol{\psi}_g(\boldsymbol{u})) &= \boldsymbol{v}_\mathrm{r} \times \boldsymbol{\omega} + \boldsymbol{R}_\mathrm{IB}^\mathsf{T} \boldsymbol{R}_g^\mathsf{T} \boldsymbol{R}_g \boldsymbol{g} + \frac{1}{m}\left(\boldsymbol{F}_0 + \boldsymbol{F}_v \boldsymbol{v}_\mathrm{r} + \boldsymbol{F}_\omega \boldsymbol{\omega}\right) \\ &= \boldsymbol{f}_{v_\mathrm{r}}(\boldsymbol{x}, \boldsymbol{y}, \boldsymbol{u}) \end{aligned} \tag{7.6.I}$$

$$\begin{aligned} \boldsymbol{f}_{v_\mathrm{r}}(\boldsymbol{\varphi}_g(\boldsymbol{x}), \boldsymbol{\varrho}_g(\boldsymbol{y}), \boldsymbol{\psi}_g(\boldsymbol{u})) &= \boldsymbol{R}_g \boldsymbol{v}_\mathrm{r} \times \boldsymbol{R}_g \boldsymbol{\omega} + \boldsymbol{R}_g \boldsymbol{R}_\mathrm{IB}^\mathsf{T} \boldsymbol{g} \\ &\quad + \frac{1}{m}\left(\boldsymbol{R}_g \boldsymbol{F}_0 + \boldsymbol{R}_g \boldsymbol{F}_v \boldsymbol{R}_g^\mathsf{T} \boldsymbol{R}_g \boldsymbol{v}_\mathrm{r} + \boldsymbol{R}_g \boldsymbol{F}_\omega \boldsymbol{R}_g^\mathsf{T} \boldsymbol{R}_g \boldsymbol{\omega}\right) \\ &= \boldsymbol{R}_g \left(\boldsymbol{v}_\mathrm{r} \times \boldsymbol{\omega} + \boldsymbol{R}_\mathrm{IB}^\mathsf{T} \boldsymbol{g} + \tfrac{1}{m}\left(\boldsymbol{F}_0 + \boldsymbol{F}_v \boldsymbol{v}_\mathrm{r} + \boldsymbol{F}_\omega \boldsymbol{\omega}\right)\right) \\ &= \boldsymbol{R}_g \boldsymbol{f}_{v_\mathrm{r}}(\boldsymbol{x}, \boldsymbol{y}, \boldsymbol{u}) \end{aligned} \tag{7.6.B}$$

The invariance of the apparent wind velocity dynamics $\dot{\boldsymbol{w}} = \boldsymbol{0}$ is trivially satisfied. For the position kinematics, we write

$$\boldsymbol{f}_q(\boldsymbol{\varphi}_g(\boldsymbol{x}), \boldsymbol{\varrho}_g(\boldsymbol{y}), \boldsymbol{\psi}_g(\boldsymbol{u})) = \boldsymbol{R}_g \boldsymbol{R}_\mathrm{IB} \boldsymbol{v}_\mathrm{r} + \boldsymbol{R}_g \boldsymbol{w} = \boldsymbol{R}_g \boldsymbol{f}_q(\boldsymbol{x}, \boldsymbol{y}, \boldsymbol{u}) \tag{7.7.I}$$

$$\boldsymbol{f}_q(\boldsymbol{\varphi}_g(\boldsymbol{x}), \boldsymbol{\varrho}_g(\boldsymbol{y}), \boldsymbol{\psi}_g(\boldsymbol{u})) = \boldsymbol{R}_\mathrm{IB} \boldsymbol{R}_g^\mathsf{T} \boldsymbol{R}_g \boldsymbol{v}_\mathrm{r} + \boldsymbol{w} = \boldsymbol{f}_q(\boldsymbol{x}, \boldsymbol{y}, \boldsymbol{u}) \tag{7.7.B}$$

The attitude kinematics at the transformed point satisfy

$$\boldsymbol{f}_{R_\mathrm{IB}}(\boldsymbol{\varphi}_g(\boldsymbol{x}), \boldsymbol{\varrho}_g(\boldsymbol{y}), \boldsymbol{\psi}_g(\boldsymbol{u})) = \boldsymbol{R}_g \boldsymbol{R}_\mathrm{IB} \boldsymbol{S}(\boldsymbol{\omega}) = \boldsymbol{R}_g \boldsymbol{f}_{R_\mathrm{IB}}(\boldsymbol{x}, \boldsymbol{y}, \boldsymbol{u}) \tag{7.8.I}$$

$$\begin{aligned} \boldsymbol{f}_{R_\mathrm{IB}}(\boldsymbol{\varphi}_g(\boldsymbol{x}), \boldsymbol{\varrho}_g(\boldsymbol{y}), \boldsymbol{\psi}_g(\boldsymbol{u})) &= \boldsymbol{R}_\mathrm{IB} \boldsymbol{R}_g^\mathsf{T} \boldsymbol{S}(\boldsymbol{R}_g \boldsymbol{\omega}) \\ &= \boldsymbol{R}_\mathrm{IB} \boldsymbol{R}_g^\mathsf{T} \boldsymbol{R}_g \boldsymbol{S}(\boldsymbol{\omega}) \boldsymbol{R}_g^\mathsf{T} \\ &= \boldsymbol{f}_{R_\mathrm{IB}}(\boldsymbol{x}, \boldsymbol{y}, \boldsymbol{u}) \boldsymbol{R}_g^\mathsf{T} \end{aligned} \tag{7.8.B}$$

In the second line of Eq. (7.8.B), we have used the property that $\boldsymbol{S}(\boldsymbol{R}\boldsymbol{\omega}) = \boldsymbol{R}\boldsymbol{S}(\boldsymbol{\omega})\boldsymbol{R}^\mathsf{T}$ for any $\boldsymbol{R} \in \mathsf{SO}(3)$ and $\boldsymbol{\omega} \in \mathbb{R}^3$. Finally, the angular velocity dynamics are invariant since

$$\boldsymbol{f}_\omega(\boldsymbol{\varphi}_g(\boldsymbol{x}), \boldsymbol{\varrho}_g(\boldsymbol{y}), \boldsymbol{\psi}_g(\boldsymbol{u})) = \boldsymbol{I}^{-1}\left(\boldsymbol{I}\boldsymbol{\omega} \times \boldsymbol{\omega} + \boldsymbol{M}_0 + \boldsymbol{M}_v \boldsymbol{v}_\mathrm{r} + \boldsymbol{M}_\omega \boldsymbol{\omega}\right) = \boldsymbol{f}_\omega(\boldsymbol{x}, \boldsymbol{y}, \boldsymbol{u}) \tag{7.9.I}$$

$$\begin{aligned}\boldsymbol{f}_\omega(\boldsymbol{\varphi}_g(\boldsymbol{x}),\boldsymbol{\varrho}_g(\boldsymbol{y}),\boldsymbol{\psi}_g(\boldsymbol{u})) &= \left(\boldsymbol{R}_g\boldsymbol{I}\boldsymbol{R}_g^\mathsf{T}\right)^{-1}\left(\boldsymbol{R}_g\boldsymbol{I}\boldsymbol{R}_g^\mathsf{T}\boldsymbol{R}_g\boldsymbol{\omega}\times\boldsymbol{R}_g\boldsymbol{\omega}\right.\\ &\qquad\left.+\boldsymbol{R}_g\boldsymbol{M}_0+\boldsymbol{R}_g\boldsymbol{M}_v\boldsymbol{R}_g^\mathsf{T}\boldsymbol{R}_g\boldsymbol{v}_\mathrm{r}+\boldsymbol{R}_g\boldsymbol{M}_\omega\boldsymbol{R}_g^\mathsf{T}\boldsymbol{R}_g\boldsymbol{\omega}\right)\\ &= \boldsymbol{R}_g\boldsymbol{I}^{-1}\left(-\boldsymbol{S}(\boldsymbol{\omega})\boldsymbol{I}\boldsymbol{\omega}+\boldsymbol{M}_0+\boldsymbol{M}_v\boldsymbol{v}_\mathrm{r}+\boldsymbol{M}_\omega\boldsymbol{\omega}\right)\\ &= \boldsymbol{R}_g\boldsymbol{f}_\omega(\boldsymbol{x},\boldsymbol{y},\boldsymbol{u})\end{aligned} \tag{7.9.B}$$

Therefore, the transformed tangent vectors in Eq. (7.5) satisfy the statement (2.5) of G-invariance. □

7.2.3 Invariant Pre-Observer

Recall the design of a symmetry-preserving reduced-order observer requires the assumption that the moving frame depends only on the measured part of the transformation group, $\boldsymbol{\varrho}_g(\boldsymbol{y})$. Since the measured attitude state space of the system is G itself, the moving frame $\gamma:\mathcal{Y}\to G$ is naturally defined by the element of $G=\mathsf{SO}(3)$ whose action on the rotational configuration yields the identity element, $e=\mathbb{I}$. Therefore, the normalization equation (3.8) is written for the two transformation groups as

$$\boldsymbol{R}_h\boldsymbol{R}_\mathrm{IB}=\mathbb{I} \tag{7.10.I}$$
$$\boldsymbol{R}_\mathrm{IB}\boldsymbol{R}_h^\mathsf{T}=\mathbb{I} \tag{7.10.B}$$

which implies

$$h=\gamma(\boldsymbol{y})=\boldsymbol{R}_\mathrm{IB}^\mathsf{T} \tag{7.11.I}$$
$$h=\gamma(\boldsymbol{y})=\boldsymbol{R}_\mathrm{IB} \tag{7.11.B}$$

are the group elements that define moving frames with the equivariance property (2.4). The moving frame will be used to construct an invariant mapping from the measured states to estimates of the unmeasured states, which is then used to define the form of the symmetry-preserving reduced-order observer and obtain sufficient conditions for its stability.

Recalling the discussion in Chapter 3, the key to preserving symmetries in the pre-observer (3.9) is the observer map $\boldsymbol{\beta}$, which commutes with the transformation group. From Lemma 3.1, we have

$$\boldsymbol{\beta}(\boldsymbol{y})=\boldsymbol{\varphi}_{\gamma(\boldsymbol{y})^{-1}}\Big(\boldsymbol{\ell}\big(\boldsymbol{\varrho}_{\gamma(\boldsymbol{y})}(\boldsymbol{y})\big)\Big) \tag{3.13}$$

where $\boldsymbol{\ell}:\mathcal{Y}\to\mathcal{X}$ is a smooth map. Inspecting the form for $\boldsymbol{\beta}$ in Eq. (3.13), we notice that $\boldsymbol{\varrho}^{R_\mathrm{IB}}_{\gamma(\boldsymbol{y})}(\boldsymbol{y})=\mathbb{I}$. Therefore, we need only consider $\boldsymbol{\ell}:\mathcal{Y}\setminus\mathsf{SO}(3)\to\mathcal{X}$. Let

$$\boldsymbol{\ell}(\boldsymbol{y})=\underbrace{\begin{bmatrix}\boldsymbol{L}^q_{v_\mathrm{r}} & \boldsymbol{L}^\omega_{v_\mathrm{r}}\\ \boldsymbol{L}^q_w & \boldsymbol{L}^\omega_w\end{bmatrix}}_{\boldsymbol{L}}\begin{bmatrix}\boldsymbol{q}\\ \boldsymbol{\omega}\end{bmatrix} \tag{7.12}$$

where $\boldsymbol{L}$ is the *observer gain matrix* which we allow to vary with time. With this choice of the gain map $\boldsymbol{\ell}$, the observer map (3.13) becomes

$$\boldsymbol{\beta}(\boldsymbol{y}) = \begin{bmatrix} \boldsymbol{L}^q_{v_\mathrm{r}} \boldsymbol{R}^\mathsf{T}_\mathrm{IB} \boldsymbol{q} + \boldsymbol{L}^\omega_{v_\mathrm{r}} \boldsymbol{\omega} \\ \boldsymbol{R}_\mathrm{IB} \boldsymbol{L}^q_w \boldsymbol{R}^\mathsf{T}_\mathrm{IB} \boldsymbol{q} + \boldsymbol{R}_\mathrm{IB} \boldsymbol{L}^\omega_w \boldsymbol{\omega} \end{bmatrix} \tag{7.13.I}$$

$$\boldsymbol{\beta}(\boldsymbol{y}) = \begin{bmatrix} \boldsymbol{R}^\mathsf{T}_\mathrm{IB} \boldsymbol{L}^q_{v_\mathrm{r}} \boldsymbol{q} + \boldsymbol{R}^\mathsf{T}_\mathrm{IB} \boldsymbol{L}^\omega_{v_\mathrm{r}} \boldsymbol{R}_\mathrm{IB} \boldsymbol{\omega} \\ \boldsymbol{L}^q_w \boldsymbol{q} + \boldsymbol{L}^\omega_w \boldsymbol{R}_\mathrm{IB} \boldsymbol{\omega} \end{bmatrix} \tag{7.13.B}$$

Next, Theorem 3.1 is used to obtain an expression for $\boldsymbol{\alpha}$ that yields a G-invariant pre-observer. For the aircraft in wind, we write the components of $\boldsymbol{\alpha}$ as

$$\begin{aligned} \boldsymbol{\alpha}_{v_\mathrm{r}}(\boldsymbol{z}, \boldsymbol{y}, \boldsymbol{u}) = \hat{\boldsymbol{v}}_\mathrm{r} \times \boldsymbol{\omega} + \boldsymbol{R}^\mathsf{T}_\mathrm{IB} \boldsymbol{g} + \frac{1}{m} (\boldsymbol{F}_0 + \boldsymbol{F}_v \hat{\boldsymbol{v}}_\mathrm{r} + \boldsymbol{F}_\omega \boldsymbol{\omega}) - \boldsymbol{L}^q_{v_\mathrm{r}} \boldsymbol{R}^\mathsf{T}_\mathrm{IB} (\boldsymbol{R}_\mathrm{IB} \hat{\boldsymbol{v}}_\mathrm{r} + \hat{\boldsymbol{w}}) \\ - \boldsymbol{L}^\omega_{v_\mathrm{r}} \boldsymbol{I}^{-1} (\boldsymbol{I}\boldsymbol{\omega} \times \boldsymbol{\omega} + \boldsymbol{M}_0 + \boldsymbol{M}_v \hat{\boldsymbol{v}}_\mathrm{r} + \boldsymbol{M}_\omega \boldsymbol{\omega}) \\ + \boldsymbol{L}^q_{v_\mathrm{r}} \boldsymbol{S}(\boldsymbol{\omega}) \boldsymbol{R}^\mathsf{T}_\mathrm{IB} \boldsymbol{q} - \dot{\boldsymbol{L}}^q_{v_\mathrm{r}} \boldsymbol{R}^\mathsf{T}_\mathrm{IB} \boldsymbol{q} - \dot{\boldsymbol{L}}^\omega_{v_\mathrm{r}} \boldsymbol{\omega} \end{aligned} \tag{7.14a.I}$$

$$\begin{aligned} \boldsymbol{\alpha}_w(\boldsymbol{z}, \boldsymbol{y}, \boldsymbol{u}) = -\boldsymbol{R}_\mathrm{IB} \boldsymbol{L}^q_w \boldsymbol{R}^\mathsf{T}_\mathrm{IB} (\boldsymbol{R}_\mathrm{IB} \hat{\boldsymbol{v}}_\mathrm{r} + \hat{\boldsymbol{w}}) - \boldsymbol{R}_\mathrm{IB} \boldsymbol{S}(\boldsymbol{\omega}) \boldsymbol{L}^\omega_w \boldsymbol{\omega} \\ - \boldsymbol{R}_\mathrm{IB} \boldsymbol{L}^\omega_w \boldsymbol{I}^{-1} (\boldsymbol{I}\boldsymbol{\omega} \times \boldsymbol{\omega} + \boldsymbol{M}_0 + \boldsymbol{M}_v \hat{\boldsymbol{v}}_\mathrm{r} + \boldsymbol{M}_\omega \boldsymbol{\omega}) \\ - \boldsymbol{R}_\mathrm{IB} (\boldsymbol{S}(\boldsymbol{\omega}) \boldsymbol{L}^q_w - \boldsymbol{L}^q_w \boldsymbol{S}(\boldsymbol{\omega})) \boldsymbol{R}^\mathsf{T}_\mathrm{IB} \boldsymbol{q} - \boldsymbol{R}_\mathrm{IB} \dot{\boldsymbol{L}}^q_w \boldsymbol{R}^\mathsf{T}_\mathrm{IB} \boldsymbol{q} - \boldsymbol{R}_\mathrm{IB} \dot{\boldsymbol{L}}^\omega_w \boldsymbol{\omega} \end{aligned} \tag{7.14b.I}$$

and

$$\begin{aligned} \boldsymbol{\alpha}_{v_\mathrm{r}}(\boldsymbol{z}, \boldsymbol{y}, \boldsymbol{u}) = \hat{\boldsymbol{v}}_\mathrm{r} \times \boldsymbol{\omega} + \boldsymbol{R}^\mathsf{T}_\mathrm{IB} \boldsymbol{g} + \frac{1}{m} (\boldsymbol{F}_0 + \boldsymbol{F}_v \hat{\boldsymbol{v}}_\mathrm{r} + \boldsymbol{F}_\omega \boldsymbol{\omega}) - \boldsymbol{R}^\mathsf{T}_\mathrm{IB} \boldsymbol{L}^q_{v_\mathrm{r}} (\boldsymbol{R}_\mathrm{IB} \hat{\boldsymbol{v}}_\mathrm{r} + \hat{\boldsymbol{w}}) \\ - \boldsymbol{R}^\mathsf{T}_\mathrm{IB} \boldsymbol{L}^\omega_{v_\mathrm{r}} \boldsymbol{R}_\mathrm{IB} \boldsymbol{I}^{-1} (\boldsymbol{I}\boldsymbol{\omega} \times \boldsymbol{\omega} + \boldsymbol{M}_0 + \boldsymbol{M}_v \hat{\boldsymbol{v}}_\mathrm{r} + \boldsymbol{M}_\omega \boldsymbol{\omega}) + \boldsymbol{S}(\boldsymbol{\omega}) \boldsymbol{R}^\mathsf{T}_\mathrm{IB} \boldsymbol{L}^q_{v_\mathrm{r}} \boldsymbol{q} \\ + \boldsymbol{S}(\boldsymbol{\omega}) \boldsymbol{R}^\mathsf{T}_\mathrm{IB} \boldsymbol{L}^\omega_{v_\mathrm{r}} \boldsymbol{R}_\mathrm{IB} \boldsymbol{\omega} - \boldsymbol{R}^\mathsf{T}_\mathrm{IB} \dot{\boldsymbol{L}}^q_{v_\mathrm{r}} \boldsymbol{q} - \boldsymbol{R}^\mathsf{T}_\mathrm{IB} \dot{\boldsymbol{L}}^\omega_{v_\mathrm{r}} \boldsymbol{R}_\mathrm{IB} \boldsymbol{\omega} \end{aligned} \tag{7.14a.B}$$

$$\begin{aligned} \boldsymbol{\alpha}_w(\boldsymbol{z}, \boldsymbol{y}, \boldsymbol{u}) = -\boldsymbol{L}^q_w (\boldsymbol{R}_\mathrm{IB} \hat{\boldsymbol{v}}_\mathrm{r} + \hat{\boldsymbol{w}}) - \boldsymbol{L}^\omega_w \boldsymbol{R}_\mathrm{IB} \boldsymbol{I}^{-1} (\boldsymbol{I}\boldsymbol{\omega} \times \boldsymbol{\omega} + \boldsymbol{M}_0 + \boldsymbol{M}_v \hat{\boldsymbol{v}}_\mathrm{r} + \boldsymbol{M}_\omega \boldsymbol{\omega}) \\ - \dot{\boldsymbol{L}}^q_w \boldsymbol{q} - \dot{\boldsymbol{L}}^\omega_w \boldsymbol{R}_\mathrm{IB} \boldsymbol{\omega} \end{aligned} \tag{7.14b.B}$$

for transformation groups (7.4.I) and (7.4.B), respectively, where

$$\begin{aligned} \hat{\boldsymbol{v}}_\mathrm{r} &= \boldsymbol{z}_{v_\mathrm{r}} + \boldsymbol{L}^q_{v_\mathrm{r}} \boldsymbol{R}^\mathsf{T}_\mathrm{IB} \boldsymbol{q} + \boldsymbol{L}^\omega_{v_\mathrm{r}} \boldsymbol{\omega} \\ \hat{\boldsymbol{w}} &= \boldsymbol{z}_w + \boldsymbol{R}_\mathrm{IB} \boldsymbol{L}^q_w \boldsymbol{R}^\mathsf{T}_\mathrm{IB} \boldsymbol{q} + \boldsymbol{R}_\mathrm{IB} \boldsymbol{L}^\omega_w \boldsymbol{\omega} \end{aligned} \tag{7.15.I}$$

$$\begin{aligned} \hat{\boldsymbol{v}}_\mathrm{r} &= \boldsymbol{z}_{v_\mathrm{r}} + \boldsymbol{R}^\mathsf{T}_\mathrm{IB} \boldsymbol{L}^q_{v_\mathrm{r}} \boldsymbol{q} + \boldsymbol{R}^\mathsf{T}_\mathrm{IB} \boldsymbol{L}^\omega_{v_\mathrm{r}} \boldsymbol{R}_\mathrm{IB} \boldsymbol{\omega} \\ \hat{\boldsymbol{w}} &= \boldsymbol{z}_w + \boldsymbol{L}^q_w \boldsymbol{q} + \boldsymbol{L}^\omega_w \boldsymbol{R}_\mathrm{IB} \boldsymbol{\omega} \end{aligned} \tag{7.15.B}$$

7.2.4 Invariant Observer

We now aim to choose the gain matrix $\boldsymbol{L}$ such that the pre-observer given by Eqs. (7.14)–(7.15) is a G-invariant reduced-order *observer*. That is, we seek sufficient conditions for which the zero-error manifold $\mathcal{Z}$ defined in Eq. (3.12) is asymptotically attractive. Given by Eq. (3.19), the invariant error coordinates are

$$\begin{aligned}\boldsymbol{\eta}_{v_{\mathrm{r}}} &= \boldsymbol{z}_{v_{\mathrm{r}}} + \boldsymbol{L}^{q}_{v_{\mathrm{r}}}\boldsymbol{R}_{\mathrm{IB}}^{\mathsf{T}}\boldsymbol{q} + \boldsymbol{L}^{\omega}_{v_{\mathrm{r}}}\boldsymbol{\omega} - \boldsymbol{v}_{\mathrm{r}} \\ \boldsymbol{\eta}_{w} &= \boldsymbol{R}_{\mathrm{IB}}^{\mathsf{T}}\boldsymbol{z}_{w} + \boldsymbol{L}^{q}_{w}\boldsymbol{R}_{\mathrm{IB}}^{\mathsf{T}}\boldsymbol{q} + \boldsymbol{L}^{\omega}_{w}\boldsymbol{\omega} - \boldsymbol{R}_{\mathrm{IB}}^{\mathsf{T}}\boldsymbol{w}\end{aligned} \tag{7.16.I}$$

$$\begin{aligned}\boldsymbol{\eta}_{v_{\mathrm{r}}} &= \boldsymbol{R}_{\mathrm{IB}}\boldsymbol{z}_{v_{\mathrm{r}}} + \boldsymbol{L}^{q}_{v_{\mathrm{r}}}\boldsymbol{q} + \boldsymbol{L}^{\omega}_{v_{\mathrm{r}}}\boldsymbol{R}_{\mathrm{IB}}\boldsymbol{\omega} - \boldsymbol{R}_{\mathrm{IB}}\boldsymbol{v}_{\mathrm{r}} \\ \boldsymbol{\eta}_{w} &= \boldsymbol{z}_{w} + \boldsymbol{L}^{q}_{w}\boldsymbol{q} + \boldsymbol{L}^{\omega}_{w}\boldsymbol{R}_{\mathrm{IB}}\boldsymbol{\omega} - \boldsymbol{w}\end{aligned} \tag{7.16.B}$$

Theorem 3.2 states sufficient conditions for Eqs. (7.14)–(7.15) to be a symmetry-preserving reduced-order observer; that is, $\hat{\boldsymbol{x}} \to \boldsymbol{x}$ as $t \to \infty$. To apply Theorem 3.2, we expand and simplify Eq. (3.21) using the invariant error coordinates (7.16) to obtain the invariant error system

$$\begin{aligned}\dot{\boldsymbol{\eta}}_{v_{\mathrm{r}}} &= -\boldsymbol{S}(\boldsymbol{\omega})\boldsymbol{\eta}_{v_{\mathrm{r}}} + \frac{1}{m}\boldsymbol{F}_{v}\boldsymbol{\eta}_{v_{\mathrm{r}}} - \boldsymbol{L}^{q}_{v_{\mathrm{r}}}\left(\boldsymbol{\eta}_{v_{\mathrm{r}}} + \boldsymbol{\eta}_{w}\right) - \boldsymbol{L}^{\omega}_{v_{\mathrm{r}}}\boldsymbol{I}^{-1}\boldsymbol{M}_{v}\boldsymbol{\eta}_{v_{\mathrm{r}}} \\ \dot{\boldsymbol{\eta}}_{w} &= -\boldsymbol{L}^{q}_{w}\left(\boldsymbol{\eta}_{v_{\mathrm{r}}} + \boldsymbol{\eta}_{w}\right) - \boldsymbol{L}^{\omega}_{w}\boldsymbol{I}^{-1}\boldsymbol{M}_{v}\boldsymbol{\eta}_{v_{\mathrm{r}}} - \boldsymbol{S}(\boldsymbol{\omega})\boldsymbol{\eta}_{w}\end{aligned} \tag{7.17.I}$$

$$\begin{aligned}\dot{\boldsymbol{\eta}}_{v_{\mathrm{r}}} &= \frac{1}{m}\boldsymbol{R}_{\mathrm{IB}}\boldsymbol{F}_{v}\boldsymbol{R}_{\mathrm{IB}}^{\mathsf{T}}\boldsymbol{\eta}_{v_{\mathrm{r}}} - \boldsymbol{L}^{q}_{v_{\mathrm{r}}}\left(\boldsymbol{\eta}_{v_{\mathrm{r}}} + \boldsymbol{\eta}_{w}\right) - \boldsymbol{L}^{\omega}_{v_{\mathrm{r}}}\boldsymbol{R}_{\mathrm{IB}}\boldsymbol{I}^{-1}\boldsymbol{M}_{v}\boldsymbol{R}_{\mathrm{IB}}^{\mathsf{T}}\boldsymbol{\eta}_{v_{\mathrm{r}}} \\ \dot{\boldsymbol{\eta}}_{w} &= -\boldsymbol{L}^{q}_{w}\left(\boldsymbol{\eta}_{v_{\mathrm{r}}} + \boldsymbol{\eta}_{w}\right) - \boldsymbol{L}^{\omega}_{w}\boldsymbol{R}_{\mathrm{IB}}\boldsymbol{I}^{-1}\boldsymbol{M}_{v}\boldsymbol{R}_{\mathrm{IB}}^{\mathsf{T}}\boldsymbol{\eta}_{v_{\mathrm{r}}}\end{aligned} \tag{7.17.B}$$

Notice that for the body transformation group, the transformed input signal appears as $\boldsymbol{R}_{\mathrm{IB}}\boldsymbol{F}_{v}\boldsymbol{R}_{\mathrm{IB}}^{\mathsf{T}} = \boldsymbol{U}_{F_v}$ and $\boldsymbol{R}_{\mathrm{IB}}\boldsymbol{I}^{-1}\boldsymbol{M}_{v}\boldsymbol{R}_{\mathrm{IB}}^{\mathsf{T}} = \boldsymbol{U}_{I}\boldsymbol{U}_{M_v}$. Also, the time derivative of the observer gain matrix does not appear in the invariant error dynamics, allowing for flexibility in its selection.

We now aim to choose the gain matrix $\boldsymbol{L}$ to render the origin $\boldsymbol{\eta} = \boldsymbol{0}$ asymptotically stable. Equation (7.17) can be viewed as a linear, time-varying (LTV) system since $\boldsymbol{Y} = \boldsymbol{\varrho}_{\gamma(\boldsymbol{y})}(\boldsymbol{y})$ and $\boldsymbol{U} = \boldsymbol{\psi}_{\gamma(\boldsymbol{y})}(\boldsymbol{u})$ are known signals. Therefore, the stabilization of the invariant error system is reduced to LTV observer design for the fictitious system

$$\begin{aligned}\dot{\boldsymbol{\xi}} &= \boldsymbol{A}(t)\boldsymbol{\xi} \\ \boldsymbol{\zeta} &= \boldsymbol{C}(t)\boldsymbol{\xi}\end{aligned} \tag{7.18}$$

where

$$\boldsymbol{A}(t) = \begin{bmatrix}-\boldsymbol{S}(\boldsymbol{\omega}(t)) + \boldsymbol{F}_{v}(t)/m & \boldsymbol{0} \\ \boldsymbol{0} & -\boldsymbol{S}(\boldsymbol{\omega}(t))\end{bmatrix}, \qquad \boldsymbol{C}(t) = \begin{bmatrix}\mathbb{I} & \mathbb{I} \\ \boldsymbol{I}^{-1}\boldsymbol{M}_{v}(t) & \boldsymbol{0}\end{bmatrix} \tag{7.19.I}$$

$$\boldsymbol{A}(t) = \begin{bmatrix}\boldsymbol{R}_{\mathrm{IB}}(t)\boldsymbol{F}_{v}(t)\boldsymbol{R}_{\mathrm{IB}}^{\mathsf{T}}(t)/m & \boldsymbol{0} \\ \boldsymbol{0} & \boldsymbol{0}\end{bmatrix}, \qquad \boldsymbol{C}(t) = \begin{bmatrix}\mathbb{I} & \mathbb{I} \\ \boldsymbol{R}_{\mathrm{IB}}(t)\boldsymbol{I}^{-1}\boldsymbol{M}_{v}(t)\boldsymbol{R}_{\mathrm{IB}}^{\mathsf{T}}(t) & \boldsymbol{0}\end{bmatrix} \tag{7.19.B}$$

Using $\boldsymbol{L}(t)$ as the linear observer gain matrix for the system (7.18), the closed-loop error dynamics

$$\dot{\boldsymbol{\eta}} = (\boldsymbol{A}(t) - \boldsymbol{L}(t)\boldsymbol{C}(t))\,\boldsymbol{\eta} \tag{7.20}$$

are exactly the invariant error system (7.17). Therefore, one must simply choose positive definite matrices $\boldsymbol{Q}$ and $\boldsymbol{R}$, propagate the differential Riccati equation

$$\dot{\boldsymbol{P}}(t) = \boldsymbol{A}(t)\boldsymbol{P}(t) + \boldsymbol{P}(t)\boldsymbol{A}^{\mathsf{T}}(t) - \boldsymbol{P}(t)\boldsymbol{C}^{\mathsf{T}}(t)\boldsymbol{R}^{-1}\boldsymbol{C}(t)\boldsymbol{P}(t) + \boldsymbol{Q} \tag{7.21}$$

and let

$$\boldsymbol{L}(t) = \boldsymbol{P}(t)\boldsymbol{C}^{\mathsf{T}}(t)\boldsymbol{R}^{-1} \tag{7.22}$$

The preceding discussion (and results by Anderson and Moore [5, Ch. 8]) proves the following result.

Theorem 7.1. *If the pair $(\boldsymbol{A}(t), \boldsymbol{C}(t))$ is observable, then the $\mathsf{SO}(3)$-invariant pre-observer (3.9)–(3.10) with $\boldsymbol{\alpha}$ given by Eq. (7.14) and $\boldsymbol{L}(t)$ satisfying Eq. (7.22) is an exponentially stable $\mathsf{SO}(3)$-invariant observer for the aircraft in wind given by Eq. (7.3).*

Remark 7.2. *The observability of $(\boldsymbol{A}(t), \boldsymbol{C}(t))$ is not overly restrictive. Most nonlinear aerodynamic models for both fixed-wing and multirotor aircraft satisfy this observability requirement. For example, constructing $\boldsymbol{F}_v$ and $\boldsymbol{M}_v$ from Model 3 or the large-domain fixed-wing model given by Grauer and Morelli [60], both yield observability.*

7.3 Demonstration of Theoretical Guarantees and Robustness

The symmetry-preserving reduced-order wind observer was implemented on simulated flight data for the small quadrotor UAV considered in Chapter 4. In particular, we used Model 3 to ensure smoothness of $\boldsymbol{F}$ and $\boldsymbol{M}$ so that the decomposition in Assumption (7.1) is well-defined.

7.3.1 A Note on Tuning

The tuning parameters $\boldsymbol{Q}$ and $\boldsymbol{R}$ can be selected in a number of ways, albeit less intuitively than a linear quadratic regulator or a Kalman-Bucy filter since the state and output of the LTV system (7.18) do not hold similar physical meaning. In this work, we chose to select $\boldsymbol{Q}$ and $\boldsymbol{R}$ using an inverse optimality approach. Let $\boldsymbol{A}_0$ and $\boldsymbol{C}_0$ be the constant matrices defined by evaluating Eq. (7.19) at hover (or any other nominal flight condition). Then, choose a gain matrix $\boldsymbol{L}_{\text{pp}}$ to place the poles of the LTI nominal error system $\dot{\boldsymbol{\eta}} = (\boldsymbol{A}_0 - \boldsymbol{L}_{\text{pp}}\boldsymbol{C}_0)\boldsymbol{\eta}$ at some desired location. We chose to place the poles in a first-order low-pass Butterworth configuration with a cutoff frequency of 4 rad/s. Let $\boldsymbol{L}_0 = \boldsymbol{P}_0\boldsymbol{C}_0^{\mathsf{T}}\boldsymbol{R}^{-1}$ where $\boldsymbol{P}_0$ satisfies the algebraic Riccati equation $\boldsymbol{A}_0\boldsymbol{P}_0 + \boldsymbol{P}_0\boldsymbol{A}_0^{\mathsf{T}} - \boldsymbol{P}_0\boldsymbol{C}_0^{\mathsf{T}}\boldsymbol{R}^{-1}\boldsymbol{C}_0\boldsymbol{P}_0 + \boldsymbol{Q} = \boldsymbol{0}$. Using a constrained

optimization solver, the inverse optimality problem is solved by numerically finding $\boldsymbol{Q}$ and $\boldsymbol{R}$ that minimize the cost function

$$J = \frac{1}{2}\,\mathrm{Tr}\left[(\boldsymbol{L}_0 - \boldsymbol{L}_{\mathrm{pp}})^{\mathsf{T}}(\boldsymbol{L}_0 - \boldsymbol{L}_{\mathrm{pp}})\right] \tag{7.23}$$

while constraining $\boldsymbol{Q}$ and $\boldsymbol{R}$ to be positive definite and norm bounded (e.g., $\|\boldsymbol{Q}\| \leq 100$ and $\|\boldsymbol{R}\| \leq 100$). This tuning approach was found to yield favorable results across many simulation scenarios. All results in this section were obtained using

$$\boldsymbol{Q} = \begin{bmatrix} 90.8 & 0 & 0 & 0 & 0 & 0 \\ 0 & 90.8 & 0 & 0 & 0 & 0 \\ 0 & 0 & 36.4 & 0 & 0 & -23.8 \\ 0 & 0 & 0 & 90.8 & 0 & 0 \\ 0 & 0 & 0 & 0 & 90.8 & 0 \\ 0 & 0 & -23.8 & 0 & 0 & 80.4 \end{bmatrix}, \quad \boldsymbol{R} = \begin{bmatrix} 11.4 & 0 & 0 & 0 & -2.0 & 0 \\ 0 & 11.4 & 0 & -2.1 & 0 & 0 \\ 0 & 0 & 7.0 & 0 & 0 & 0 \\ 0 & -2.1 & 0 & 0.8 & 0 & 0 \\ -2.0 & 0 & 0 & 0 & 0.7 & 0 \\ 0 & 0 & 0 & 0 & 0 & 50.3 \end{bmatrix} \tag{7.24}$$

7.3.2 Demonstration of Theoretical Guarantees

The symmetry-preserving reduced-order wind observers detailed in this section were first implemented in simulation with all assumptions satisfied in order to demonstrate the theoretical convergence guarantees. That is, the aerodynamic force and moment perfectly satisfy Assumption 7.1 and the wind is constant. For this ideal case, we decompose Model 3 according to Eq. (7.64) and evaluate the argument $\boldsymbol{v}_{\mathrm{r}}$ in $\boldsymbol{F}_0$, $\boldsymbol{F}_v$, etc. to a nominal value of zero. Note this only affects the few terms in the aerodynamic model that are nonlinear in air-relative velocity. The aircraft dynamics with the idealized aerodynamic model were simulated in a uniform wind field with components $W_{\mathrm{N}} = 10$ m/s, $W_{\mathrm{E}} = -10$ m/s, and $W_{\mathrm{D}} = 0$ m/s using MATLAB. To showcase the nonlinear stability guarantees and global nature of the observer, a large-amplitude multisine input excitation was injected on top of the feedback control signal (Figure 7.1a). The multisine was constructed with frequencies ranging from 0.01 to 1 Hz to effectively explore the state space as seen in Figure 7.1.

The observability condition of Theorem 7.1 was verified for the simulated trajectory. The LTV observability Gramian $\boldsymbol{G}_o(t_0, t_f)$ was numerically constructed backwards in time from $t_f = 20$ to $t_0 = 0$. As shown in Figure 7.2, the minimum eigenvalue of the observability Gramian is bounded away from zero backwards in time, implying observability of $(\boldsymbol{A}(t), \boldsymbol{C}(t))$ on the interval $[t_0, 20)$ for any $t_0 \geq 0$ [130, Ch. 9]. Due to the structure of $\boldsymbol{A}$ and $\boldsymbol{C}$, the minimum eigenvalue $\lambda_{\min}(\boldsymbol{G}_o)$ is the same for both transformation groups. Also shown in Figure 7.2 is the minimum eigenvalue of the observability Gramian for the nominal hover flight condition in zero wind, showing persistent maneuvering is not a requirement for this observer (as it is for some model-free approaches) — the reason being that the observer's stability holds uniformly in the measured states and inputs.

Next, the observers constructed using both the inertial and body transformation groups were numerically simulated. The resulting estimates of air-relative and wind velocity are shown

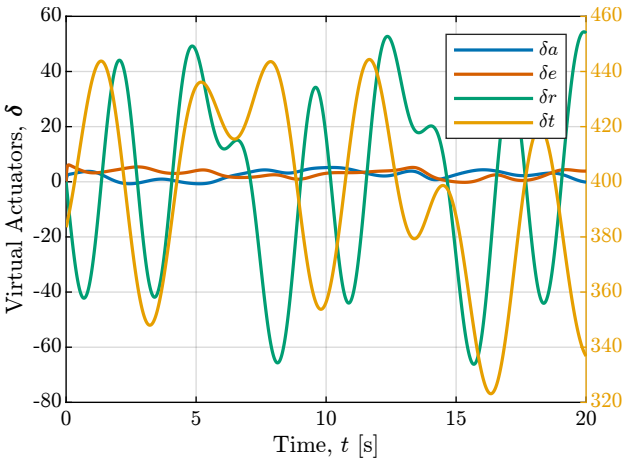

(a) Control inputs

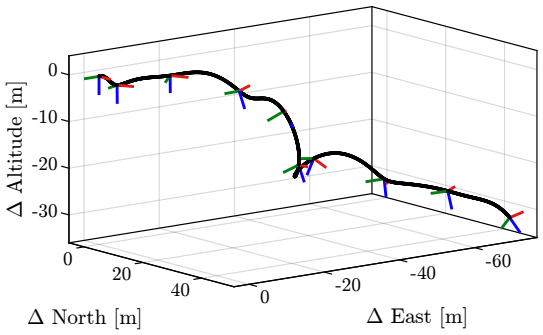

(b) Simulated trajectory

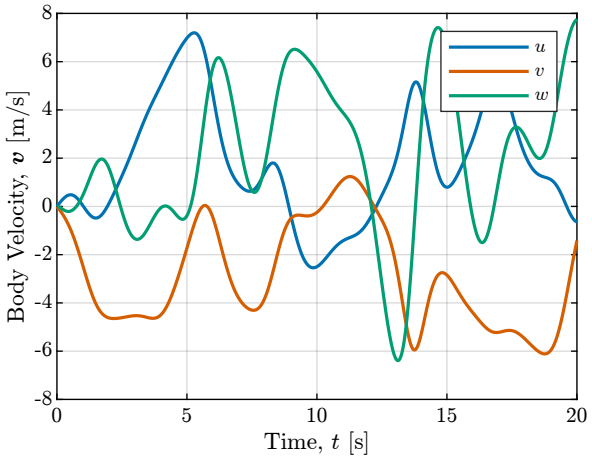

(c) Body velocity

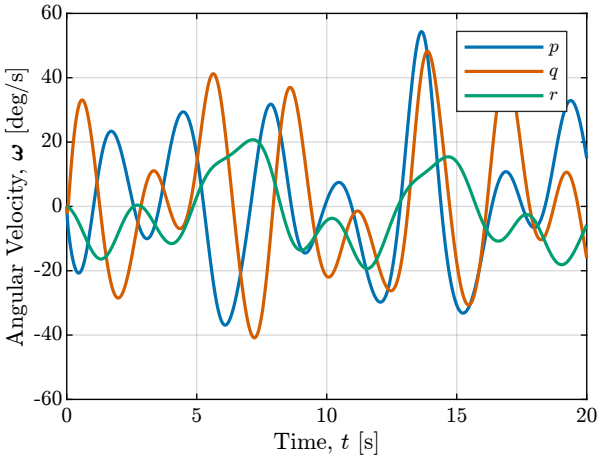

(d) Angular velocity

Figure 7.1: Ideal simulation in uniform wind

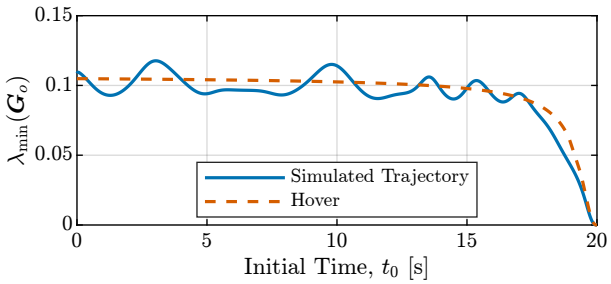

Figure 7.2: Minimum eigenvalue of the LTV observability Gramian on the interval $[t_0, 20]$

in Figures 7.3 and 7.4, respectively. These results demonstrate the guaranteed exponential convergence despite large variations in the aircraft state. Since all assumptions were satisfied, the observers designed using both transformation groups yielded nearly identical

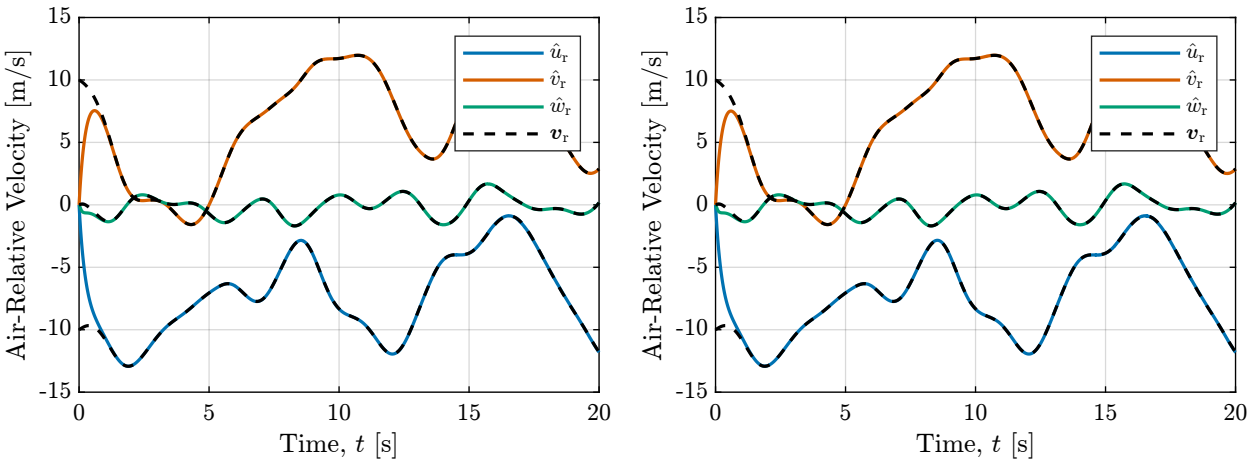

(a) Inertial transformation group (b) Body transformation group

Figure 7.3: Estimated air-relative velocity (ideal case)

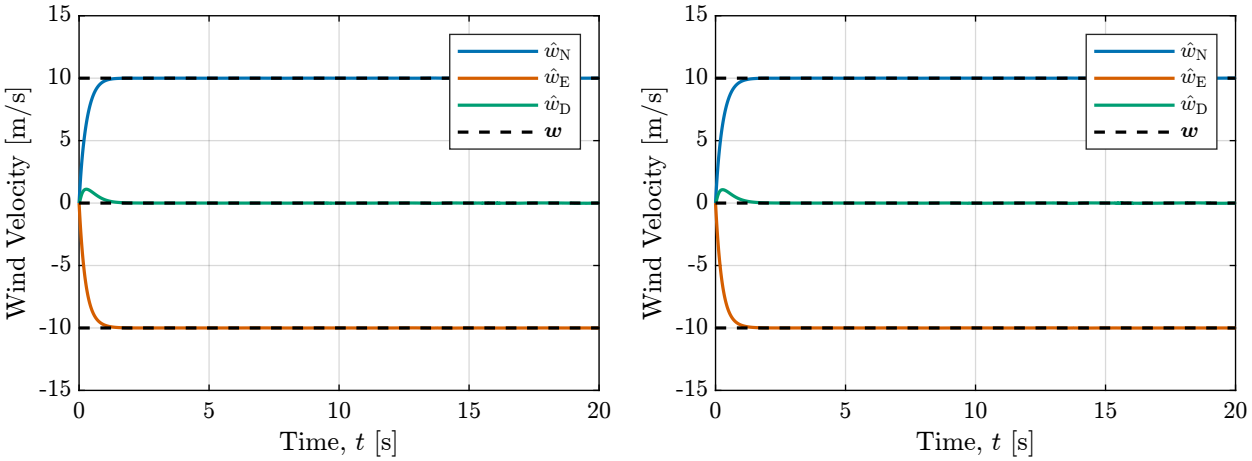

(a) Inertial transformation group (b) Body transformation group

Figure 7.4: Estimated wind velocity (ideal case)

results. This parity is expected since the same rotational symmetry of the dynamics is equivalently preserved — just from the viewpoint of different reference frames. The practical difference between using transformation groups (7.4.I) and (7.4.B) is the coordinate frame in which the observer mapping $\boldsymbol{\ell}$ is expressed.

7.3.3 Robustness Analysis

To explore the differences between transformation groups (7.4.I) and (7.4.B) and to stress the proposed observer, the aircraft was simulated in von Kármán turbulence using the full nonlinear aerodynamic model, violating the observer's assumptions. Additionally, Assumption 7.2

was violated by introducing measurement noise (the same realization for all simulations). Specifically, the measurements of $\boldsymbol{q}$, $\boldsymbol{R}_{\mathrm{IB}}$, and $\boldsymbol{\omega}$ respectively satisfied

$$\boldsymbol{y}_q = \boldsymbol{q} + \tilde{\boldsymbol{w}}_q, \quad \boldsymbol{y}_{R_{\mathrm{IB}}} = \boldsymbol{R}_{\mathrm{IB}} \exp(\boldsymbol{S}(\tilde{\boldsymbol{w}}_{R_{\mathrm{IB}}})), \quad \boldsymbol{y}_\omega = \boldsymbol{\omega} + \tilde{\boldsymbol{w}}_\omega \tag{7.25}$$

where $\tilde{\boldsymbol{w}}_q$, $\tilde{\boldsymbol{w}}_{R_{\mathrm{IB}}}$, and $\tilde{\boldsymbol{w}}_\omega$ are zero-mean, Gaussian, continuous-time, white noise with power spectral densities $2 \times 10^{-3}\mathbb{I}\ \frac{\mathrm{m}^2}{\mathrm{Hz}}$, $10^{-6}\mathbb{I}\ \frac{1}{\mathrm{Hz}}$, and $5 \times 10^{-6}\mathbb{I}\ \frac{(\mathrm{rad/s})^2}{\mathrm{Hz}}$, respectively. Since the transient performance and steady state accuracy of all components of air-relative and wind velocity estimates were similar, we only discuss the North component of wind velocity. The results for this scenario are shown in Figure 7.5a, were we see that measurement noise corrupts the resulting estimate but does not cause an unbounded response. For comparison, the same simulation scenario with measurement noise removed is shown in Figure 7.5b. Here, we see good tracking of the fluctuations in wind velocity — an important aim in this work. While proof of stability for this case is beyond the scope of this dissertation, the results shown are indicative of the observer's inherent robustness to disturbances, as expected from the fact that the undisturbed invariant error system is globally exponentially stable [86, Lemma 5.1].

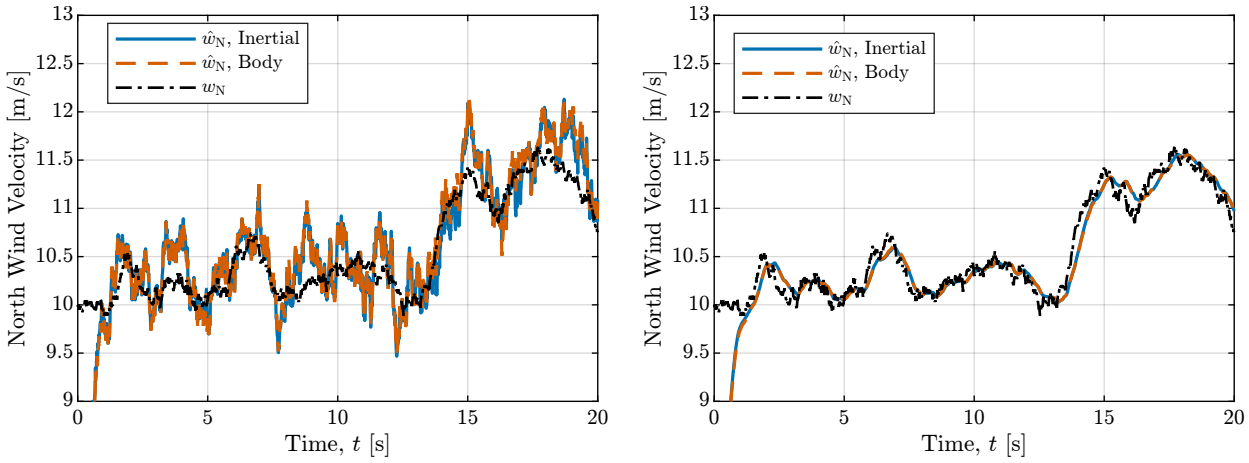

(a) With measurement noise

(b) No measurement noise

Figure 7.5: Estimated North wind velocity using full nonlinear aerodynamic model with von Kármán turbulence

One caveat about the proposed observer is that care must be taken in its numerical implementation. For example, it was found that the use of a fixed-step Runge-Kutta integration scheme necessitated small time steps (10^{-4} seconds). This issue may be alleviated by using adaptive step sizing as well as methods that leverage the Jacobian of the observer dynamics. A similar problem encountered in practical implementation is that position data is often available at a much lower rate than angular rate and attitude data. To investigate, a comparison among position data rates of 8 Hz, 20 Hz, and 50 Hz was conducted using the idealized simulation discussed in Section 7.3.2. The results for the North wind velocity estimate are

shown in Figure 7.6. In this case, the most recent position data was held constant between samples. As the sampling rate increases, we recover the continuous-time results. To improve performance for sampled data, predictions of position should be propagated between samples using GNSS velocity data. This is an inexpensive computation and is expected to greatly improve accuracy.

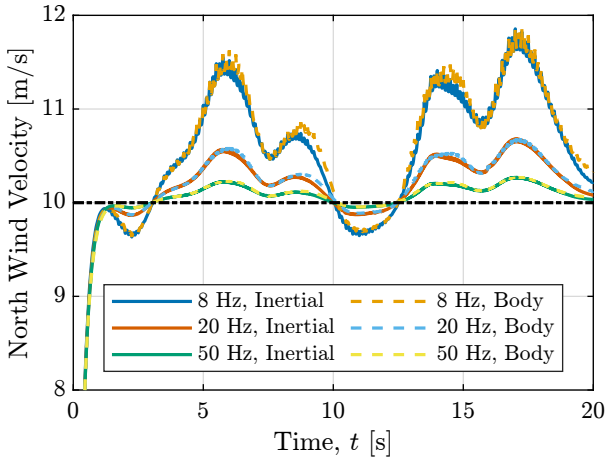

Figure 7.6: North wind velocity estimate using sampled position data

From these results, the benefit of using one transformation group over another is not apparent. To quantify the small difference between transformation groups, the state estimate root mean square error

$$\text{RMSE} = \left(\frac{1}{t_f - t_0} \int_{t_0}^{t_f} \|\hat{\boldsymbol{x}}(t) - \boldsymbol{x}(t)\|^2 \right)^{\frac{1}{2}} \tag{7.26}$$

was computed and is tabulated in Table 7.1. Across all the simulation scenarios considered,

Table 7.1: Simulated state estimate root mean square error in m/s

	Transformation Group	
Simulation Scenario	Inertial	Body
Ideal (Figure 7.4)	0.528	0.532
Von Kármán plus Noise (Figure 7.5a)	0.894	0.902
Von Kármán (Figure 7.5b)	0.774	0.779
8 Hz Position Data (Figure 7.6)	1.260	1.272
20 Hz Position Data (Figure 7.6)	0.881	0.889
50 Hz Position Data (Figure 7.6)	0.686	0.691

the inertial transformation group produced marginally more accurate estimates. This difference is more significant when applying the proposed observers to flight data, as explored in Section 7.6.

7.4 Stochastic Symmetry-Preserving Reduced-Order Wind Observer

The symmetry-preserving reduced-order wind observer (7.14)–(7.15) was derived ignoring all sources of noise in the aircraft dynamics. Now, we relax this assumption and extend the results of Section 7.2 to include process noise. That is, we consider the aircraft dynamics in turbulent wind described by the stochastic differential equation (6.24) and prove the origin of a stochastic error system is noise-to-state stable as defined in Section 2.8.

7.4.1 Stochastic Invariance of the Aircraft Dynamics in Turbulent Wind

Consider the same affine decomposition of the aerodynamics stated in Assumption 7.1, but additionally allow this decomposition to include the random modeling error (6.18) as stated in Assumption 6.1. Under these assumptions, Eqs. (6.24c) and (6.24d) become

$$\mathrm{d}\boldsymbol{v}_{\mathrm{r}} = \Big(\boldsymbol{v}_{\mathrm{r}} \times \boldsymbol{\omega} + \boldsymbol{R}_{\mathrm{IB}}^{\mathsf{T}}\boldsymbol{g} + \frac{1}{m}\big(\boldsymbol{F}_0 + \boldsymbol{F}_v\boldsymbol{v}_{\mathrm{r}} + \boldsymbol{F}_\omega\boldsymbol{\omega}\big)\Big)\mathrm{d}t + \boldsymbol{\sigma}_F\mathrm{d}\boldsymbol{W}_F - \boldsymbol{R}_{\mathrm{IB}}^{\mathsf{T}}\boldsymbol{\sigma}_w\mathrm{d}\boldsymbol{W}_w \tag{7.27a}$$

$$\mathrm{d}\boldsymbol{\omega} = \boldsymbol{I}^{-1}\big(\boldsymbol{I}\boldsymbol{\omega} \times \boldsymbol{\omega} + \boldsymbol{M}_0 + \boldsymbol{M}_v\boldsymbol{v}_{\mathrm{r}} + \boldsymbol{M}_\omega\boldsymbol{\omega}\big)\mathrm{d}t + \boldsymbol{\sigma}_M\mathrm{d}\boldsymbol{W}_M \tag{7.27b}$$

Like the deterministic case, we split the state into an unmeasured part $\boldsymbol{x}$ and a measured part $\boldsymbol{y}$ so that the SDE (6.24) is written as

$$\mathrm{d}\boldsymbol{x} = \boldsymbol{f}(\boldsymbol{x}, \boldsymbol{y}, \boldsymbol{u})\mathrm{d}t + \boldsymbol{G}_x(\boldsymbol{y})\boldsymbol{\sigma}\mathrm{d}\boldsymbol{W} \tag{7.28a}$$

$$\mathrm{d}\boldsymbol{y} = \boldsymbol{h}(\boldsymbol{x}, \boldsymbol{y}, \boldsymbol{u})\mathrm{d}t + \boldsymbol{G}_y\boldsymbol{\sigma}\mathrm{d}\boldsymbol{W} \tag{7.28b}$$

where $(\boldsymbol{f}, \boldsymbol{h})$ is the *drift vector field* and $(\boldsymbol{G}_x, \boldsymbol{G}_y)$ is the *diffusion matrix field*, both constructed from the right-hand side of Eq. (6.24) using Eq. (6.23). To avoid technical difficulties, we restrict the unmeasured part of the state $\boldsymbol{x}$ to be defined on all of $\mathbb{R}^n$, which is satisfied for $\boldsymbol{x} = (\boldsymbol{v}_{\mathrm{r}}, \boldsymbol{w})$. Also, note the slight abuse of notation "$\mathrm{d}\boldsymbol{y}$" in Eq. (7.28) where, although $\boldsymbol{y}$ lives on a smooth manifold, the noise in Eq. (6.24) enters only in the equations defined on Euclidean space. That is, the technicalities mentioned in Remark 6.1 can be ignored.

In order to design a symmetry-preserving observer for the aircraft in wind, we must determine what transformations of the aircraft state, input, and noise leave the SDE (7.28) invariant. Previously, this concept has only been applied to observer design for *ordinary* differential equations. As an extension of the work by Gaeta and Lunini [46], we propose the following definition of G-invariance for controlled SDEs, which builds off the concepts reviewed in Chapter 2.

Definition 7.1 (G-invariant SDE)**.** *Suppose a Lie group G acts on the SDE*

$$\mathrm{d}\boldsymbol{x} = \boldsymbol{f}(\boldsymbol{x}, \boldsymbol{u})\mathrm{d}t + \boldsymbol{G}(\boldsymbol{x}, \boldsymbol{u})\boldsymbol{\sigma}\mathrm{d}\boldsymbol{W} \tag{7.29}$$

via the stochastic transformation group

$$(g, \boldsymbol{x}, \boldsymbol{u}, \boldsymbol{W}) \in G \times \mathbb{R}^n \times \mathcal{U} \times \mathbb{R}^q \mapsto (\boldsymbol{\varphi}_g(\boldsymbol{x}), \boldsymbol{\psi}_g(\boldsymbol{u}), \boldsymbol{\varpi}_g(\boldsymbol{W})) \in \mathbb{R}^n \times \mathcal{U} \times \mathbb{R}^q$$

The SDE (7.29) *is called* G-invariant *if*

$$\mathrm{d}\boldsymbol{\varphi}_g(\boldsymbol{x}) = \boldsymbol{f}(\boldsymbol{\varphi}_g(\boldsymbol{x}), \boldsymbol{\psi}_g(\boldsymbol{u}))\mathrm{d}t + \boldsymbol{G}(\boldsymbol{\varphi}_g(\boldsymbol{x}), \boldsymbol{\psi}_g(\boldsymbol{u}))\mathrm{d}\boldsymbol{\varpi}_g(\boldsymbol{W}) \tag{7.30}$$

where $\mathrm{d}\boldsymbol{\varphi}_g$ *and* $\mathrm{d}\boldsymbol{\varpi}_g$ *are understood in the sense of Itô.*

Comparing with Definition 7.1, the condition (2.5) for G-invariance of deterministic systems may be written as $\mathrm{d}\boldsymbol{\varphi}_g(\boldsymbol{x})/\mathrm{d}t = \boldsymbol{f}(\boldsymbol{\varphi}_g(\boldsymbol{x}), \boldsymbol{\psi}_g(\boldsymbol{u}))$, which differs from Definition 7.1 in the same way that $\dot{\boldsymbol{x}} = \boldsymbol{f}(\boldsymbol{x}, \boldsymbol{u})$ differs from $\mathrm{d}\boldsymbol{x} = \boldsymbol{f}(\boldsymbol{x}, \boldsymbol{u})\mathrm{d}t + \boldsymbol{G}(\boldsymbol{x}, \boldsymbol{u})\boldsymbol{\sigma}\mathrm{d}\boldsymbol{W}$.

We aim to find a stochastic transformation group $\{\boldsymbol{\varphi}_g, \boldsymbol{\varrho}_g, \boldsymbol{\psi}_g, \boldsymbol{\varpi}_g\}_{g\in G}$ for the SDE (7.28), where $\boldsymbol{\varphi}_g$ acts on the unmeasured part of state, $\boldsymbol{\varrho}_g$ acts on the measured part, $\boldsymbol{\psi}_g$ acts on the input, and $\boldsymbol{\varpi}_g$ acts on the Wiener process $\boldsymbol{W}$. In fact, only a slight augmentation to the deterministic transformation groups (7.4.I) and (7.4.B) is required. In particular, we only need to add the appropriate transformations on the increments $\mathrm{d}\boldsymbol{W}_w$, $\mathrm{d}\boldsymbol{W}_M$, and $\mathrm{d}\boldsymbol{W}_F$. To simplify the discussion, we will only consider the inertial transformation group, whose stochastic extension is given as follows.

Proposition 7.2. *The stochastic aircraft dynamics represented by the SDE* (7.28) *are* $\mathsf{SO}(3)$*-invariant under the stochastic transformation group*

$$\begin{aligned}
\boldsymbol{\varphi}_g(\boldsymbol{x}) &= \begin{pmatrix} \boldsymbol{v}_{\mathrm{r}} \\ \boldsymbol{R}_g\boldsymbol{w} \end{pmatrix} =: \begin{pmatrix} \boldsymbol{\varphi}_g^{v_{\mathrm{r}}}(\boldsymbol{x}) \\ \boldsymbol{\varphi}_g^{w}(\boldsymbol{x}) \end{pmatrix}, \quad \boldsymbol{\varrho}_g(\boldsymbol{y}) = \begin{pmatrix} \boldsymbol{R}_g\boldsymbol{q} \\ \boldsymbol{R}_g\boldsymbol{R}_{\mathrm{IB}} \\ \boldsymbol{\omega} \end{pmatrix} =: \begin{pmatrix} \boldsymbol{\varrho}_g^{q}(\boldsymbol{y}) \\ \boldsymbol{\varrho}_g^{R_{\mathrm{IB}}}(\boldsymbol{y}) \\ \boldsymbol{\varrho}_g^{\omega}(\boldsymbol{y}) \end{pmatrix} \\
\boldsymbol{\psi}_g(\boldsymbol{u}) &= \boldsymbol{R}_g\boldsymbol{g}, \qquad \mathrm{d}\boldsymbol{\varpi}_g(\boldsymbol{\sigma}\boldsymbol{W}) = \begin{pmatrix} \boldsymbol{R}_g\boldsymbol{\sigma}_w\mathrm{d}\boldsymbol{W}_w \\ \boldsymbol{\sigma}_M\mathrm{d}\boldsymbol{W}_M \\ \boldsymbol{\sigma}_F\mathrm{d}\boldsymbol{W}_F \end{pmatrix} =: \begin{pmatrix} \mathrm{d}\boldsymbol{\varpi}_g^{w}(\boldsymbol{\sigma}\boldsymbol{W}) \\ \mathrm{d}\boldsymbol{\varpi}_g^{M}(\boldsymbol{\sigma}\boldsymbol{W}) \\ \mathrm{d}\boldsymbol{\varpi}_g^{F}(\boldsymbol{\sigma}\boldsymbol{W}) \end{pmatrix}
\end{aligned} \tag{7.31}$$

where $g = \boldsymbol{R}_g \in \mathsf{SO}(3)$.

The proof of Proposition 7.2 is omitted for brevity. It follows the proof of Proposition 7.1, but uses the Itô differential instead of the tangent map.

7.4.2 Stochastic Invariant Pre-Observer

Definition 3.1 can now be extended to the SDE (7.28). In fact, the general form of the observer is the same; it is the conditions on the dynamics of $\hat{\boldsymbol{x}}$ that differ.

Definition 7.2. *The dynamical system* (3.9) *with output* (3.10) *is a* stochastic G-invariant reduced-order pre-observer *for the system* (7.28) *if the SDE*

$$\mathrm{d}\hat{\boldsymbol{x}} = \boldsymbol{\alpha}(\hat{\boldsymbol{x}} - \boldsymbol{\beta}(\boldsymbol{y}), \boldsymbol{y}, \boldsymbol{u})\mathrm{d}t + \mathrm{d}\boldsymbol{\beta}(\boldsymbol{y}) \tag{7.32}$$

is G-invariant and the manifold

$$\mathcal{Z} = \{(\boldsymbol{z}, \boldsymbol{x}, \boldsymbol{y}) \in \mathbb{R}^n \times \mathbb{R}^n \times \mathcal{Y} \mid \boldsymbol{z} = \boldsymbol{x} - \boldsymbol{\beta}(\boldsymbol{y})\} \tag{7.33}$$

is positively invariant under the flow of the drift vector field $(\boldsymbol{f}, \boldsymbol{h})$.

Notice how this definition contrasts with Definition 3.1. Primarily, the dynamics of the (now stochastic) state estimate are G-invariant according to Definition 7.1. Also, the zero-error manifold $\mathcal{Z}$ needs to be positively invariant only under the deterministic part of the dynamics — the drift vector field. One might also call this property *weak positive invariance*.

For the design of a stochastic G-invariant wind observer, the moving frame $\gamma : \mathcal{Y} \to G$ and the observer map $\boldsymbol{\beta}$ are the same as the deterministic case. As an extension of Theorem 3.1 for the stochastic aircraft dynamics (6.24), consider the following proposition.

Theorem 7.2. *Let*

$$\boldsymbol{\alpha}(\boldsymbol{z}, \boldsymbol{y}, \boldsymbol{u}) = \boldsymbol{f}(\boldsymbol{z} + \boldsymbol{\beta}(\boldsymbol{y}), \boldsymbol{y}, \boldsymbol{u}) - \mathscr{L}\boldsymbol{\beta}(\boldsymbol{y})|_{\boldsymbol{x}=\boldsymbol{z}+\boldsymbol{\beta}(\boldsymbol{y})} \tag{7.34}$$

Then, the dynamical system

$$\dot{\boldsymbol{z}} = \boldsymbol{\alpha}(\boldsymbol{z}, \boldsymbol{y}, \boldsymbol{u}) \tag{3.9}$$

with output

$$\hat{\boldsymbol{x}} = \boldsymbol{z} + \boldsymbol{\beta}(\boldsymbol{y}) \tag{3.10}$$

is a stochastic G-invariant, reduced-order pre-observer for the SDE (7.28).

Proof. First, we recognize that $\boldsymbol{\alpha}$ as defined by Eq. (7.34) is the same as the deterministic case in Eq. (7.14). This is true because $\boldsymbol{\beta}$ is linear in the states for which noise enters the stochastic dynamics (6.24). Therefore, the Hessian in Itô's rule vanishes. Since the drift vector field of the SDE (6.24) is exactly the same as the vector field defining the deterministic dynamics (7.3), the zero-error manifold (7.33) is positively invariant by Theorem 3.1. □

The remaining task is to choose the time-varying gain matrix $\boldsymbol{L}$ so that we can make a probabilistic statement about the convergence of $\hat{\boldsymbol{x}}$ to $\boldsymbol{x}$.

7.4.3 Stochastic Invariant Observer

We now aim to choose the gain matrix $\boldsymbol{L}$ so that the stochastic pre-observer in Theorem 7.2 is a stochastic *observer*. That is, we seek sufficient conditions for which a probabilistic statement of stability can be made about the zero-error manifold $\mathcal{Z}$. Since the sources of noise in Eq. (6.24) do not vanish on $\mathcal{Z}$, we will develop conditions under which the origin of a stochastic invariant error system is noise-to-state stable.

Consider the same invariant error coordinates $\boldsymbol{\eta}$ as the deterministic case in Eq. (7.16). The application of Itô's lemma to $\boldsymbol{\eta}$ yields the *invariant error SDE*

$$\mathrm{d}\boldsymbol{\eta}_{v_\mathrm{r}} = \left(-\boldsymbol{S}(\boldsymbol{\omega})\boldsymbol{\eta}_{v_\mathrm{r}} + \tfrac{1}{m}\boldsymbol{F}_v\boldsymbol{\eta}_{v_\mathrm{r}} - \boldsymbol{L}^q_{v_\mathrm{r}}\left(\boldsymbol{\eta}_{v_\mathrm{r}} + \boldsymbol{\eta}_w\right) - \boldsymbol{L}^\omega_{v_\mathrm{r}}\boldsymbol{I}^{-1}\boldsymbol{M}_v\boldsymbol{\eta}_{v_\mathrm{r}}\right)\mathrm{d}t + \begin{bmatrix}\boldsymbol{R}_{\mathrm{IB}}^\mathsf{T} & \boldsymbol{L}^\omega_{v_\mathrm{r}} & -\mathbb{I}\end{bmatrix}\boldsymbol{\sigma}\mathrm{d}\boldsymbol{W} \tag{7.35a}$$

$$\mathrm{d}\boldsymbol{\eta}_w = \left(-\boldsymbol{L}^q_w\left(\boldsymbol{\eta}_{v_\mathrm{r}} + \boldsymbol{\eta}_w\right) - \boldsymbol{L}^\omega_w\boldsymbol{I}^{-1}\boldsymbol{M}_v\boldsymbol{\eta}_{v_\mathrm{r}} - \boldsymbol{S}(\boldsymbol{\omega})\boldsymbol{\eta}_w\right)\mathrm{d}t + \begin{bmatrix}-\boldsymbol{R}_{\mathrm{IB}}^\mathsf{T} & \boldsymbol{L}^\omega_w & \boldsymbol{0}\end{bmatrix}\boldsymbol{\sigma}\mathrm{d}\boldsymbol{W} \tag{7.35b}$$

which we may compactly write as

$$\mathrm{d}\boldsymbol{\eta} = \big(\boldsymbol{A}(t) - \boldsymbol{L}\boldsymbol{C}(t)\big)\boldsymbol{\eta}\,\mathrm{d}t + \big(\boldsymbol{B}(t) - \boldsymbol{L}\boldsymbol{D}\big)\boldsymbol{\sigma}\mathrm{d}\boldsymbol{W} \tag{7.36}$$

where

$$\begin{aligned}\boldsymbol{A}(t) &= \begin{bmatrix}-\boldsymbol{S}(\boldsymbol{\omega}(t)) + \boldsymbol{F}_v(t)/m & \boldsymbol{0}\\ \boldsymbol{0} & -\boldsymbol{S}(\boldsymbol{\omega}(t))\end{bmatrix} & \boldsymbol{C}(t) &= \begin{bmatrix}\mathbb{I} & \mathbb{I}\\ \boldsymbol{I}^{-1}\boldsymbol{M}_v(t) & \boldsymbol{0}\end{bmatrix}\\ \boldsymbol{B}(t) &= \begin{bmatrix}\boldsymbol{R}_{\mathrm{IB}}^\mathsf{T}(t) & \boldsymbol{0} & -\mathbb{I}\\ -\boldsymbol{R}_{\mathrm{IB}}^\mathsf{T}(t) & \boldsymbol{0} & \boldsymbol{0}\end{bmatrix} & \boldsymbol{D} &= \begin{bmatrix}\boldsymbol{0} & \boldsymbol{0} & \boldsymbol{0}\\ \boldsymbol{0} & -\mathbb{I} & \boldsymbol{0}\end{bmatrix}\end{aligned} \tag{7.37}$$

Since $\boldsymbol{y}$ is a known signal, the stabilization of the invariant error SDE (7.36) is reduced to LTV observer design for the fictitious linear input-output SDE

$$\begin{aligned}\mathrm{d}\boldsymbol{\xi} &= \boldsymbol{A}(t)\boldsymbol{\xi}\mathrm{d}t + \boldsymbol{B}(t)\boldsymbol{\sigma}\mathrm{d}\boldsymbol{W}\\ \mathrm{d}\boldsymbol{\zeta} &= \boldsymbol{C}(t)\boldsymbol{\xi}\mathrm{d}t + \boldsymbol{D}\boldsymbol{\sigma}\mathrm{d}\boldsymbol{W}\end{aligned} \tag{7.38}$$

where $\boldsymbol{\zeta}$ is the *observation process* whose derivative is the typical output considered in the linear filtering problem. The remarkable result here is that the solution to the gain design problem for the stochastic symmetry-preserving reduced-order wind observer is *almost* that of the standard Kalman-Bucy filter. The only barrier is that $\boldsymbol{D}$ has rows of zeros, meaning some of the outputs are noise-free. Since we are constrained to the closed loop error dynamics (7.36) and cannot consider more general formulations (e.g., taking derivatives of the noise-free output [115]), we consider a *blended approach* to tuning which does not necessarily produce the minimum variance estimate, but still will be shown to be noise-to-state stable. First, notice the structures of $\boldsymbol{B}$ and $\boldsymbol{D}$ imply that the components of $\mathrm{d}\boldsymbol{W}$ entering the $\mathrm{d}\boldsymbol{\xi}$ and $\mathrm{d}\boldsymbol{\zeta}$ equations are distinct; that is, the "process noise" and "measurement noise" in Eq. (7.38) are uncorrelated. Accordingly, let

$$\bar{\boldsymbol{B}} = \begin{bmatrix}\boldsymbol{R}_{\mathrm{IB}}^\mathsf{T} & -\mathbb{I}\\ -\boldsymbol{R}_{\mathrm{IB}}^\mathsf{T} & \boldsymbol{0}\end{bmatrix}, \qquad \bar{\boldsymbol{D}} = \begin{bmatrix}\boldsymbol{0}\\ -\mathbb{I}\end{bmatrix} \tag{7.39}$$

reflect the non-zero input channels of $\boldsymbol{B}$ and $\boldsymbol{D}$, respectively. To circumvent the rank deficiency of $\bar{\boldsymbol{D}}\bar{\boldsymbol{D}}^\mathsf{T}$, define

$$\bar{\boldsymbol{R}} = \begin{bmatrix}\bar{\boldsymbol{D}}\boldsymbol{\sigma}_M & \boldsymbol{\Gamma}\end{bmatrix}\begin{bmatrix}\bar{\boldsymbol{D}}\boldsymbol{\sigma}_M & \boldsymbol{\Gamma}\end{bmatrix}^\mathsf{T} \tag{7.40}$$

where $\boldsymbol{\Gamma} \in \mathbb{R}^{6\times 3}$ is a tuning parameter that ensures $\bar{\boldsymbol{R}}$ is invertible. The positive definite matrix $\bar{\boldsymbol{R}}$ can be thought of as the power spectral density of an augmented measurement noise vector in Eq. (7.38). For the process noise, we have

$$\bar{\boldsymbol{Q}} = \mathbf{diag}(\boldsymbol{\sigma}_w \boldsymbol{\sigma}_w^\mathsf{T}, \boldsymbol{\sigma}_F \boldsymbol{\sigma}_F^\mathsf{T}) \tag{7.41}$$

Since $\boldsymbol{A}(t)$ and $\boldsymbol{B}(t)$ are bounded, uniform observability of the pair $(\boldsymbol{A}(t), \boldsymbol{C}(t))$ is a sufficient condition [4] for the existence of a bounded solution $\boldsymbol{P}(t)$ to the differential Riccati equation

$$\dot{\boldsymbol{P}}(t) = \boldsymbol{A}(t)\boldsymbol{P}(t) + \boldsymbol{P}(t)\boldsymbol{A}(t)^\mathsf{T} - \boldsymbol{P}(t)\boldsymbol{C}(t)^\mathsf{T}\bar{\boldsymbol{R}}^{-1}\boldsymbol{C}(t)\boldsymbol{P}(t) + \bar{\boldsymbol{B}}(t)\bar{\boldsymbol{Q}}\bar{\boldsymbol{B}}(t)^\mathsf{T} \tag{7.42}$$

Assuming uniform observability (see Remark 7.2), the observer gain matrix is

$$\boldsymbol{L}(t) = \boldsymbol{P}(t)\boldsymbol{C}(t)^\mathsf{T}\bar{\boldsymbol{R}}^{-1} \tag{7.43}$$

Theorem 7.3. *If the pair $(\boldsymbol{A}(t), \boldsymbol{C}(t))$ is observable, then the $\mathsf{SO}(3)$-invariant pre-observer (3.9)–(3.10) with $\boldsymbol{\alpha}$ given by Eq. (7.34) and $\boldsymbol{L}(t)$ satisfying Eq. (7.43) is a noise-to-state stable $\mathsf{SO}(3)$-invariant observer for the aircraft in turbulent wind given by the SDE (6.24).*

Since the invariant error system (7.36) is a linear SDE, proving noise-to-state stability is straightforward.

Proof. Consider the Lyapunov function

$$V(\boldsymbol{\eta}, t) = \boldsymbol{\eta}^\mathsf{T}\boldsymbol{P}^{-1}(t)\boldsymbol{\eta} \tag{7.44}$$

where $\boldsymbol{P}(t)$ satisfies Eq. (7.42). Consider an arbitrary time interval $\mathbb{T} = [t_0, T)$ and let

$$k_1 = \inf_{t\in\mathbb{T}} \lambda_{\min}(\boldsymbol{P}^{-1}(t)), \qquad k_2 = \sup_{t\in\mathbb{T}} \lambda_{\max}(\boldsymbol{P}^{-1}(t)) \tag{7.45}$$

By the Rayleigh-Ritz inequality,

$$k_1\|\boldsymbol{\eta}\|^2 \leq V(\boldsymbol{\eta}, t) \leq k_2\|\boldsymbol{\eta}\|^2 \tag{7.46}$$

to satisfy Eq. (2.46). The infinitesimal generator applied to V yields

$$\begin{aligned}\mathscr{L}V = -\boldsymbol{\eta}^\mathsf{T}\Big(\boldsymbol{C}^\mathsf{T}(t)\bar{\boldsymbol{R}}^{-1}\boldsymbol{C}(t) + \boldsymbol{P}^{-1}(t)\bar{\boldsymbol{B}}(t)\bar{\boldsymbol{Q}}\bar{\boldsymbol{B}}^\mathsf{T}(t)\boldsymbol{P}^{-1}(t)\Big)\boldsymbol{\eta} \\ + \frac{1}{2}\operatorname{Tr}\Big(\boldsymbol{\sigma}^\mathsf{T}\big(\boldsymbol{B}(t) - \boldsymbol{L}\boldsymbol{D}\big)^\mathsf{T}\boldsymbol{P}^{-1}\big(\boldsymbol{B}(t) - \boldsymbol{L}\boldsymbol{D}\big)\boldsymbol{\sigma}\Big)\end{aligned} \tag{7.47}$$

Let

$$k_3 = \inf_{t\in\mathbb{T}} \lambda_{\min}\Big(\boldsymbol{C}^\mathsf{T}(t)\bar{\boldsymbol{R}}^{-1}\boldsymbol{C}(t) + \boldsymbol{P}^{-1}(t)\bar{\boldsymbol{B}}(t)\bar{\boldsymbol{Q}}\bar{\boldsymbol{B}}^\mathsf{T}(t)\boldsymbol{P}^{-1}(t)\Big) \tag{7.48}$$

$$k_4 = \sup_{t\in\mathbb{T}} \operatorname{Tr}\Big(\big(\boldsymbol{B}(t) - \boldsymbol{L}\boldsymbol{D}\big)^\mathsf{T}\boldsymbol{P}^{-1}(t)\big(\boldsymbol{B}(t) - \boldsymbol{L}\boldsymbol{D}\big)\Big) \tag{7.49}$$

By the definition and sub-multiplicative property of the Frobenius norm, it follows that

$$\mathscr{L}V \leq -k_3\|\boldsymbol{\eta}\|^2 + \frac{1}{2}k_4\|\boldsymbol{\sigma}\|_{\mathrm{F}}^2 \tag{7.50}$$

which satisfies Eq. (2.47). Recalling the positive integer p represents the order of a particular statistical moment of interest, the comparison functions in Eqs. (2.46)–(2.48) are

$$\alpha_1(a) = \begin{cases} k_1 a^2, & p=1 \\ k_1 a, & p=2 \end{cases}, \quad \alpha_2(a) = \begin{cases} k_2 a^2, & p=1 \\ k_2 a, & p=2 \end{cases}, \quad \alpha_3(a) = \frac{k_2}{k_3}a, \quad \rho(a) = \frac{1}{2}k_4 a^2 \tag{7.51}$$

which proves noise-to-state stability of the invariant error system (7.36). Furthermore, since α_1 is convex, the error system is both first and second moment noise-to-state stable. □

We can now state the probabilistic guarantees that come from the proof of Theorem 7.3. Because α_3 is linear, the class-$\mathcal{KL}$ function μ in Eqs. (2.49) and (2.51) is simply the exponential decay

$$\mu(a,\tau) = a\exp\left(-\frac{1}{2}\frac{k_3}{k_2}\tau\right) \tag{7.52}$$

Therefore, the invariant error system (7.36) is *exponentially* noise-to-state stable with guarantees that

$$\mathbb{P}\left\{\|\boldsymbol{\eta}(t)\| > \sqrt{\frac{2}{\epsilon}\frac{k_2}{k_1}}\|\boldsymbol{\eta}_0\|\sqrt{\exp\left(-\frac{1}{2}\frac{k_3}{k_2}t\right)} + \sqrt{\frac{2}{\epsilon}\frac{k_2k_4}{k_1k_3}}\|\boldsymbol{\sigma}\|_{\mathrm{F}}\right\} \leq \epsilon \tag{7.53a}$$

$$\mathbb{E}\left\{\|\boldsymbol{\eta}(t)\|\right\} \leq \sqrt{2\frac{k_2}{k_1}}\|\boldsymbol{\eta}_0\|\sqrt{\exp\left(-\frac{1}{2}\frac{k_3}{k_2}t\right)} + \sqrt{2\frac{k_2k_4}{k_1k_3}}\|\boldsymbol{\sigma}\|_{\mathrm{F}} \tag{7.53b}$$

$$\mathbb{P}\left\{\|\boldsymbol{\eta}(t)\|^2 > \frac{2}{\epsilon}\frac{k_2}{k_1}\|\boldsymbol{\eta}_0\|^2\exp\left(-\frac{1}{2}\frac{k_3}{k_2}t\right) + \frac{2}{\epsilon}\frac{k_2k_4}{k_1k_3}\|\boldsymbol{\sigma}\|_{\mathrm{F}}^2\right\} \leq \epsilon \tag{7.54a}$$

$$\mathbb{E}\left\{\|\boldsymbol{\eta}(t)\|^2\right\} \leq 2\frac{k_2}{k_1}\|\boldsymbol{\eta}_0\|^2\exp\left(-\frac{1}{2}\frac{k_3}{k_2}t\right) + 2\frac{k_2k_4}{k_1k_3}\|\boldsymbol{\sigma}\|_{\mathrm{F}}^2 \tag{7.54b}$$

The probabilistic convergence guarantees in Eqs. (7.53) and (7.54) can be extremely useful. Equations (7.53a) and (7.54a) may be used to provide confidence intervals on bounds of the exponential convergence. For example, one can conclude there is a 1% chance that $\|\boldsymbol{\eta}(t)\|$ ever exceeds

$$10\sqrt{2\frac{k_2}{k_1}}\|\boldsymbol{\eta}_0\|\sqrt{\exp\left(-\frac{1}{2}\frac{k_3}{k_2}t\right)} + 10\sqrt{2\frac{k_2k_4}{k_1k_3}}\|\boldsymbol{\sigma}\|_{\mathrm{F}}$$

From another perspective, one may wish to know bounds on the steady-state statistics of the invariant error. That is,

$$\mathbb{E}\left\{\|\boldsymbol{\eta}(\infty)\|\right\} \leq \sqrt{2\frac{k_2k_4}{k_1k_3}}\|\boldsymbol{\sigma}\|_{\mathrm{F}} \quad \text{and} \quad \mathbb{E}\left\{\|\boldsymbol{\eta}(\infty)\|^2\right\} \leq 2\frac{k_2k_4}{k_1k_3}\|\boldsymbol{\sigma}\|_{\mathrm{F}}^2$$

Alternative Tuning Approach

Altogether, the noise-to-state stability guarantees in Eqs. (7.53) and (7.54) are a principled quantification of wind estimation performance in the presence of both modeling error and turbulence. However, these bounds may be overly conservative, especially in scenarios where $k_1 \ll k_2$. An alternative approach is to consider $\bar{\boldsymbol{Q}}$ and $\bar{\boldsymbol{R}}$ as tuning parameters rather than noise power spectral densities. In this case, it is beneficial to choose $\bar{\boldsymbol{Q}}$ and $\bar{\boldsymbol{R}}$ to optimize the noise-to-state stability bounds. In contrast to the blended approach described earlier, we call this the *optimal bounds approach* to tuning the observer. Examining Eqs. (7.53) and (7.54), we let

$$J_{\text{init}} = \frac{k_2}{k_1}, \quad J_{\text{rate}} = \frac{k_2}{k_3}, \quad \text{and} \quad J_{\text{ss}} = \frac{k_4}{k_3} \tag{7.55}$$

which are proportional to the guaranteed initial error, inverse of the convergence rate, and steady-state error, respectively. This observation motivates choosing the penalty matrices in the design of the observer gain matrix to minimize the cost function

$$J = J_{\text{init}} + \kappa_1 J_{\text{rate}} + \kappa_2 J_{\text{ss}} \tag{7.56}$$

where κ_1 and κ_2 are non-negative weighting parameters. To simplify this optimization, let $\boldsymbol{A}_0$, $\boldsymbol{B}_0$, and $\boldsymbol{C}_0$ be the constant matrices defined by evaluating Eq. (7.37) at some nominal flight condition. Then, let $\boldsymbol{L}_0 = \boldsymbol{P}_0 \boldsymbol{C}_0^\mathsf{T} \bar{\boldsymbol{R}}^{-1}$ where $\boldsymbol{P}_0$ satisfies the algebraic Riccati equation $\boldsymbol{A}_0 \boldsymbol{P}_0 + \boldsymbol{P}_0 \boldsymbol{A}_0^\mathsf{T} - \boldsymbol{P}_0 \boldsymbol{C}_0^\mathsf{T} \bar{\boldsymbol{R}}^{-1} \boldsymbol{C}_0 \boldsymbol{P}_0 + \bar{\boldsymbol{B}}_0 \bar{\boldsymbol{Q}} \bar{\boldsymbol{B}}_0^\mathsf{T} = \boldsymbol{0}$. Using a constrained optimization solver, J can be minimized over $\bar{\boldsymbol{Q}}$ and $\bar{\boldsymbol{R}}$ while constraining $\bar{\boldsymbol{Q}}$ and $\bar{\boldsymbol{R}}$ to be positive definite and norm bounded (e.g., $\|\bar{\boldsymbol{Q}}\|_\text{F} \leq 100$ and $\|\bar{\boldsymbol{R}}\|_\text{F} \leq 100$).

7.5 Demonstration of Stochastic Stability Guarantees

Using the same quadrotor considered in Section 7.3, the stochastic aircraft dynamics (6.24) and observer were simulated using the Euler-Maruyama scheme outlined in Section 2.7. To demonstrate the probabilistic performance guarantees, the simulation was conducted with all assumptions satisfied. For all simulations, the components of $\boldsymbol{\sigma}$ were considered constant values of

$$\boldsymbol{\sigma}_w = 0.5\,\mathbb{I}, \quad \boldsymbol{\sigma}_M = \mathbf{diag}(2.30, 2.21, 5.83) \times 10^{-2}, \quad \boldsymbol{\sigma}_F = \mathbf{diag}(3.55, 3.55, 1.77) \times 10^{-2}$$

To showcase the nonlinear stability guarantees and global nature of the observer, the same large-amplitude multisine input excitation as Section 7.3 was injected on top of the feedback control signal.

7.5.1 Blended Approach to Tuning

First, the blended approach to tuning was considered in which fictitious measurement noise is assumed so that the reduced-order linear error dynamics coincide with that of a full-order

Kalman-Bucy filter. The free tuning parameter $\boldsymbol{\Gamma}$ was chosen as $\boldsymbol{\Gamma} = [\mathbb{I} \;\; \mathbf{0}]^\mathsf{T} \times 10^{-3}$. To evaluate the conservatism of the noise-to-state stability guarantees, 1000 simulations of the stochastic aircraft dynamics and observer with initial estimate $\hat{\boldsymbol{x}} = \mathbf{0}$ were conducted to numerically approximate the probability density of $\|\boldsymbol{\eta}(t)\|$. The result of these simulations is shown in Figure 7.7, where we see exponential convergence to a quasi-stationary[1] distribution within about one second. The computed mean $\mu(t) = \mathrm{E}\{\|\boldsymbol{\eta}(t)\|\}$ and standard

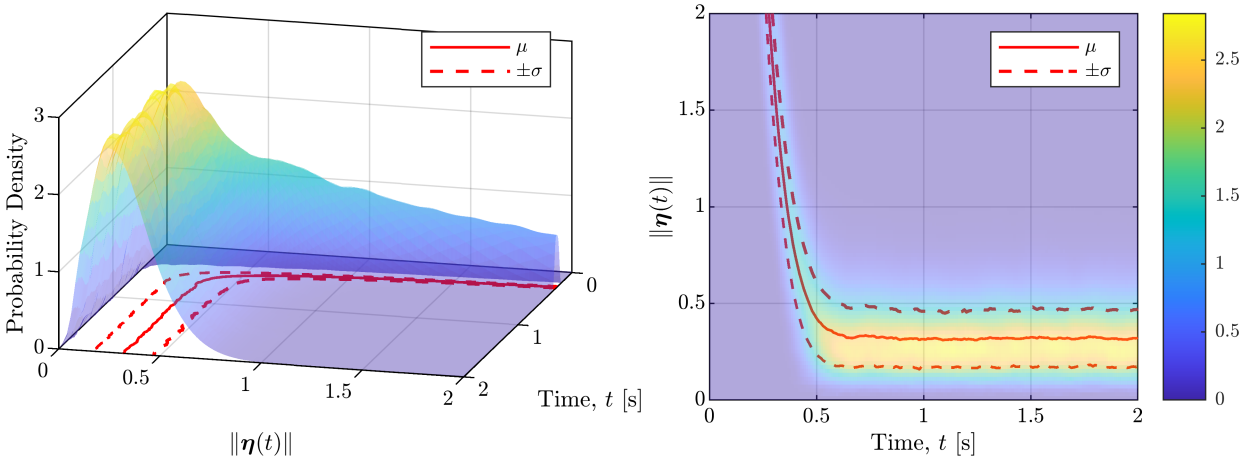

Figure 7.7: Probability density of the error $\|\boldsymbol{\eta}(t)\|$ using the blended tuning approach

deviation $\sigma(t) = \sqrt{\mathrm{E}\{(\|\boldsymbol{\eta}(t)\| - \mu(t))^2\}}$ are shown in red. For this tuning, the noise-to-state stability guarantees held across all simulations with

$$k_1 = 15.6, \quad k_2 = 5.9 \times 10^4, \quad k_3 = 240, \quad \text{and} \quad k_4 = 1.21 \times 10^5 \tag{7.57}$$

The corresponding bounds on the first and second moments of $\|\boldsymbol{\eta}(t)\|$ are shown in Figure 7.8 along with the moments computed from Monte-Carlo simulations. Clearly, these bounds are extremely conservative and thus not useful. Regardless, the representative time history in Figure 7.9 along with the Monte-Carlo results demonstrate the excellent performance of the observer even though the statistical guarantees are too conservative to support it.

7.5.2 Optimal Bounds Approach to Tuning

Next, we consider the alternative tuning approach in which the aim is to minimize a weighted sum of the guaranteed initial error, inverse of the convergence rate, and steady-state error. With $\kappa_1 = 10$ and $\kappa_2 = 1$, the cost function J given in Eq. (7.56) was minimized to yield $\bar{\boldsymbol{Q}}$ and $\bar{\boldsymbol{R}}$ as follows.

[1]Since the system (7.36) is time-varying, this distribution is not quite stationary; rather, it is modulated by the vehicle's attitude.

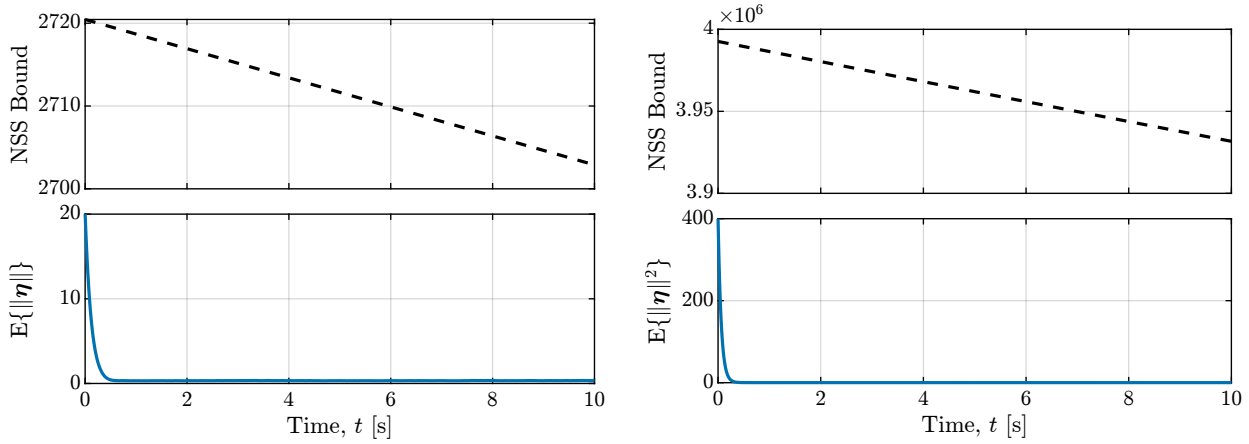

(a) First moment (b) Second Moment

Figure 7.8: First and second moment noise-to-state stability guarantees for the blended tuning approach

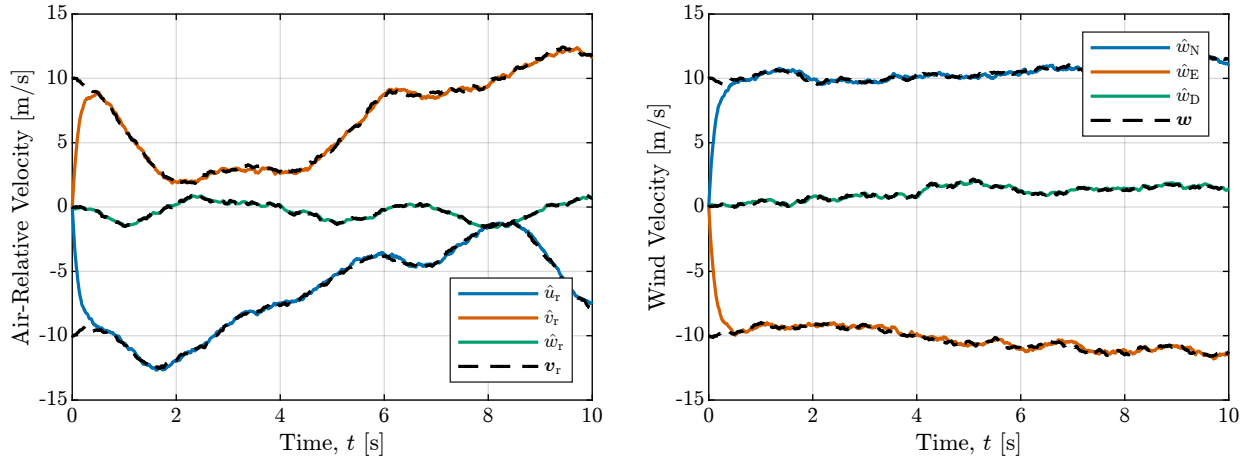

(a) Air-relative velocity (b) Wind velocity

Figure 7.9: Sample time history of state estimates using the blended tuning approach

$$\bar{\boldsymbol{Q}} = \begin{bmatrix} 13.60 & 0.65 & -0.28 & 22.98 & 1.76 & -0.71 \\ 0.65 & 15.71 & 0.75 & 1.90 & 29.06 & 0.45 \\ -0.28 & 0.75 & 18.86 & -0.24 & 1.27 & 15.66 \\ 22.98 & 1.90 & -0.24 & 46.92 & 4.82 & -1.51 \\ 1.76 & 29.06 & 1.27 & 4.82 & 63.07 & 0.68 \\ -0.71 & 0.45 & 15.66 & -1.51 & 0.68 & 91.99 \end{bmatrix}, \quad \bar{\boldsymbol{R}} = \begin{bmatrix} 16.79 & -2.15 & 0.02 & 0.44 & 3.17 & -0.02 \\ -2.15 & 8.91 & -0.18 & -1.78 & -0.39 & 0 \\ 0.02 & -0.18 & 4.08 & 0.04 & -0.01 & 0 \\ 0.44 & -1.78 & 0.04 & 1.06 & 0.08 & 0 \\ 3.17 & -0.39 & -0.01 & 0.08 & 1.25 & -0.01 \\ -0.02 & 0 & 0 & 0 & -0.01 & 52.79 \end{bmatrix}$$

Again, we perform 1000 simulations of the stochastic aircraft dynamics and observer to numerically approximate the probability density of $\|\boldsymbol{\eta}(t)\|$. These results are shown in Figure 7.10, where we see exponential convergence to a distribution distinct from Figure 7.7. Note the difference in scale between Figures 7.7 and 7.10. For this tuning approach, the

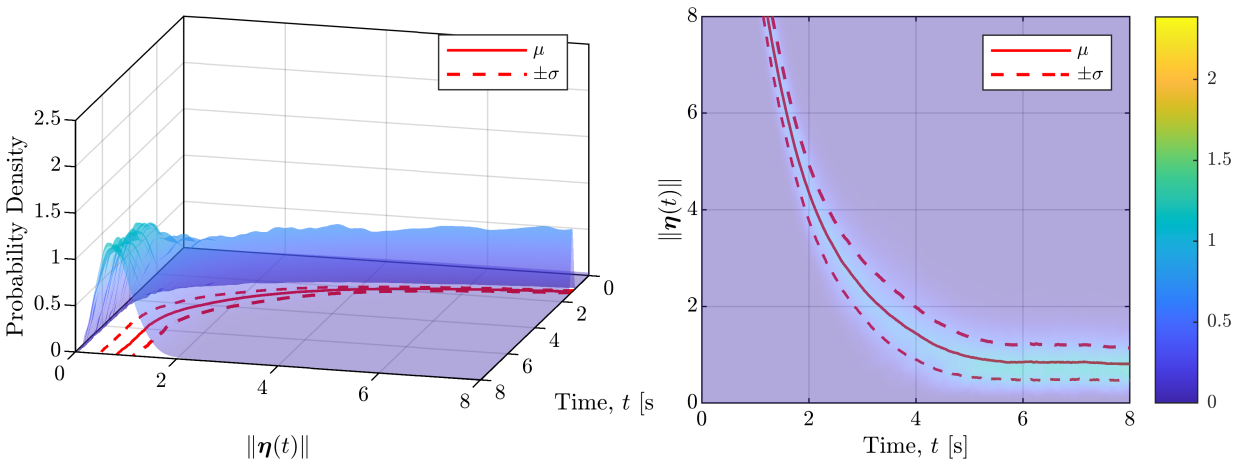

Figure 7.10: Probability density of the error $\|\boldsymbol{\eta}(t)\|$ using the optimal bounds tuning approach

noise-to-state stability guarantees held across all simulations with

$$k_1 = 0.06, \quad k_2 = 0.24, \quad k_3 = 0.14, \quad \text{and} \quad k_4 = 5.08 \tag{7.58}$$

The guarantees shown in Figure 7.11 are much less conservative than the previous tuning, but are still not a reflection of the Monte-Carlo results. Further, as seen in Figure 7.12,

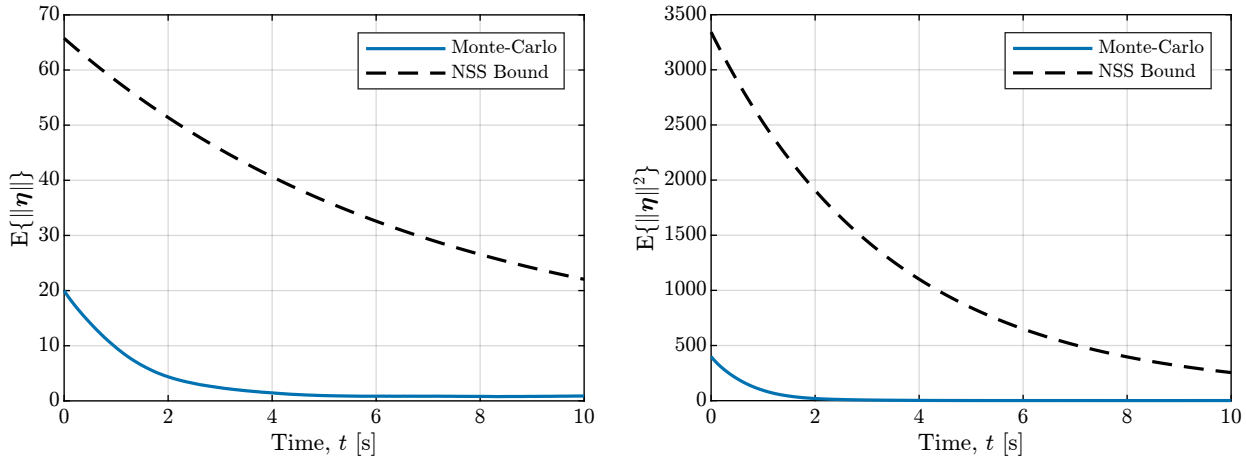

(a) First moment (b) Second Moment

Figure 7.11: First and second moment noise-to-state stability guarantees for the optimal bounds tuning approach

this tuning approach yields less conservative bounds at the expense of performance. The convergence of the first and second moments of the estimate error is slower than in Figure 7.7. Similarly, the computed steady-state mean and standard deviation are roughly twice as large.

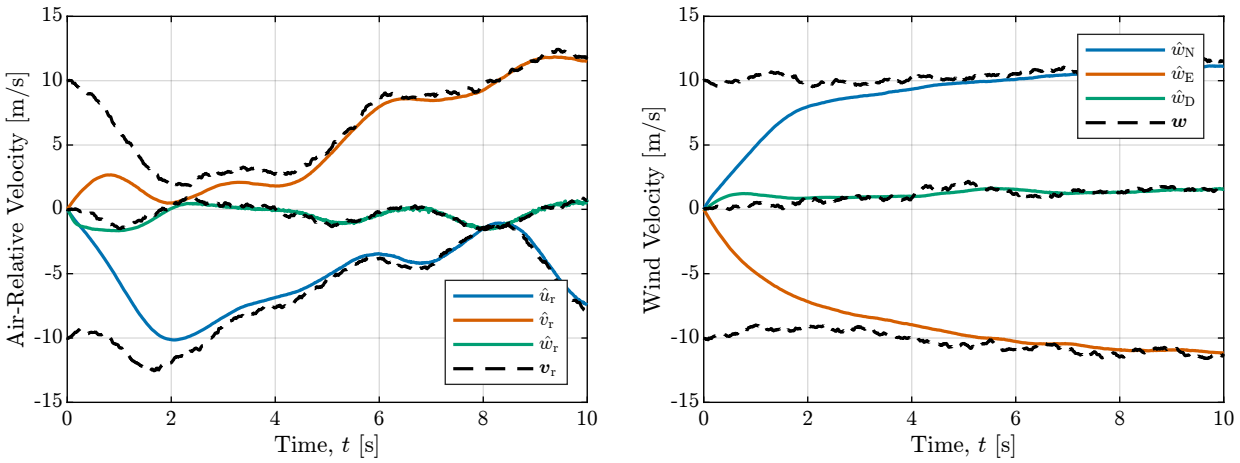

(a) Air-relative velocity

(b) Wind velocity

Figure 7.12: Sample time history of state estimates using the optimal bounds tuning approach

7.6 Fixed-Wing Flight Test Results

7.6.1 Research Aircraft

As a demonstration of robustness and practical utility, the proposed wind observer was implemented on flight data for the eSPAARO fixed-wing UAV shown in Figure 7.13. The

Figure 7.13: The eSPAARO research aircraft

eSPAARO is a 12 ft. wingspan, 45 lb. small UAS designed and built by Virginia Tech's

Nonlinear Systems Laboratory. The eSPAARO is an inverted V-tail design with a pusher propeller configuration. The aircraft control surfaces comprise two ruddervators and two ailerons. The eSPAARO is instrumented with a Cubepilot CubeBlue flight computer running PX4 firmware, along with a HERE4 RTK GNSS system. It is propelled by a 22×12 in. Advanced Precision Composites (APC) propeller mounted to a 500 W brushless motor. The propulsion system is electrically powered by a ten-cell lithium-ion battery; it's avionics and servos are redundantly powered by a separate three-cell lithium-ion polymer battery. More information about the general approach to instrumentation, flight test, and data processing can be found in references [61], [62], [133]. The eSPAARO's physical properties are listed in Table 7.2.

Table 7.2: eSPAARO properties

Property	Symbol	Value	Units
Mass	m	22.498	kg
Mean aerodynamic chord	c	0.5588	m
Wing span	b	3.6576	m
Wing planform area	S	2.0439	m^2
Roll moment of inertia	I_{xx}	8.7698	$\mathrm{kg}\cdot\mathrm{m}^2$
Pitch moment of inertia	I_{yy}	9.0390	$\mathrm{kg}\cdot\mathrm{m}^2$
Yaw moment of inertia	I_{zz}	12.563	$\mathrm{kg}\cdot\mathrm{m}^2$
x-z product of inertia	I_{xz}	0.6548	$\mathrm{kg}\cdot\mathrm{m}^2$
Other products of inertia	I_{xy}, I_{yz}	≈ 0	$\mathrm{kg}\cdot\mathrm{m}^2$

Two of the vaned air data units described in Section 6.4 were mounted to the eSPAARO's wingtips to aid in wind estimate validation. The ADUs were not used as part of the proposed wind observer; they were only used to validate wind estimates. Each ADU was used to reconstruct the apparent wind velocity according to Eq. (6.25). The true apparent wind $\boldsymbol{w}$ was then taken to be the average of the wind velocities reconstructed between the two ADUs.

7.6.2 System Identification

An aero-propulsive model for the eSPAARO was identified from flight data following the approach detailed by Simmons *et al.* [135]. Orthogonal phase-optimized multisine inputs [109], [110], [113] were used to simultaneously excite the aircraft's propulsion system and control surfaces to provide informative six degree-of-freedom motion data. Specifically, independent excitations were applied to the throttle, left ruddervator, right ruddervator, and linked ailerons. The frequency content of the control surface excitation was between 0.05 Hz and 1.875 Hz to effectively excite the modes of longitudinal and lateral-directional motion. The propulsion excitation signal's frequency content was between 0.050 Hz and 0.675 Hz due to the lower bandwidth of the propulsion system.

The aerodynamic force $\boldsymbol{F} = [X\ Y\ Z]^\mathsf{T}$ and moment $\boldsymbol{M} = [\mathcal{L}\ \mathcal{M}\ \mathcal{N}]^\mathsf{T}$ in the body frame is non-dimensionalized with

$$\begin{aligned} C_x &= \frac{X}{\bar{q}S}, \quad C_y = \frac{Y}{\bar{q}S}, \quad C_z = \frac{Z}{\bar{q}S} \\ C_l &= \frac{\mathcal{L}}{\bar{q}Sb}, \quad C_m = \frac{\mathcal{M}}{\bar{q}Sc}, \quad C_n = \frac{\mathcal{N}}{\bar{q}Sb} \end{aligned} \tag{7.59}$$

where $\bar{q}$ is dynamic pressure, S is the wing planform area, b is the wingspan, and c is the mean chord length. The candidate explanatory variables for the model were angle of attack α, angle of sideslip β, non-dimensional angular rates

$$\breve{p} = \frac{pb}{2V}, \quad \breve{q} = \frac{qc}{2V}, \quad \breve{r} = \frac{rb}{2V} \tag{7.60}$$

control surface deflections δv_L, δv_R, δa, centered inverse advance ratio

$$\mathcal{J}_c = \frac{\Omega D}{V} - \mathcal{J}_0 \tag{7.61}$$

and non-dimensional angle of attack rate $\breve{\dot{\alpha}} = \dot{\alpha}c/(2V)$. Here, δv_L and δv_R are the left and right ruddervator deflections, δa is the aileron deflection, Ω is the propeller speed, D is the propeller diameter, and $\mathcal{J}_0 = 15.7$ is the nominal inverse advance ratio. All angular quantities are expressed in radians.

An effective strategy used to efficiently and effectively develop model structures is a combination of multivariate orthogonal function (MOF) modeling [108], [113] and stepwise regression [113]. First, MOF modeling is executed for several separate flight maneuvers. The model structures developed from each flight maneuver are compared, and the model terms appearing in a majority of the maneuvers are retained in the model. As a final step, the MOF results are reviewed by an analyst using stepwise regression to assess whether to include or exclude fringe model terms. From flight data collected using the 4-input multisine excitation signal, it was found that the following model structure accurately predicted the vehicle's motion from the training data.

$$C_x = C_{x_\alpha}\alpha + C_{x_{\alpha^2}}\alpha^2 + C_{x_{\mathcal{J}_c}}\mathcal{J}_c + C_{x_{\mathcal{J}_c^2}}\mathcal{J}_c^2 + C_{x_0} \tag{7.62a}$$

$$C_y = C_{y_\beta}\beta + C_{y_r}\breve{r} + C_{y_{\delta v_\mathrm{L}}}\delta v_\mathrm{L} + C_{y_{\delta v_\mathrm{R}}}\delta v_\mathrm{R} + C_{y_0} \tag{7.62b}$$

$$C_z = C_{z_\alpha}\alpha + C_{z_q}\breve{q} + C_{z_{\dot{\alpha}}}\breve{\dot{\alpha}} + C_{z_0} \tag{7.62c}$$

$$C_l = C_{l_\beta}\beta + C_{l_p}\breve{p} + C_{l_r}\breve{r} + C_{l_{\delta a}}\delta a + C_{l_0} \tag{7.62d}$$

$$C_m = C_{m_\alpha}\alpha + C_{m_q}\breve{q} + C_{m_{\delta v_\mathrm{L}}}\delta v_\mathrm{L} + C_{m_{\delta v_\mathrm{R}}}\delta v_\mathrm{R} + C_{m_0} \tag{7.62e}$$

$$C_n = C_{n_\beta}\beta + C_{n_p}\breve{p} + C_{n_r}\breve{r} + C_{n_{\delta a}}\delta a + C_{n_{\delta v_\mathrm{L}}}\delta v_\mathrm{L} + C_{n_{\delta v_\mathrm{R}}}\delta v_\mathrm{R} + C_{n_0} \tag{7.62f}$$

Note that even though the inclusion of the non-dimensional angle of attack rate $\breve{\dot{\alpha}}$ improved the model fit, it was neglected in the wind observer implementation since it does not fit Eq. (7.64).

Following the equation error approach to system identification [113], the dependent variables C_x, C_y, C_z, C_l, C_m, and C_n were computed from flight data using filtered accelerometer and gyroscope data as described by Simmons [133] and Simmons *et al.* [136]. Equating these measurements to the model structure in Eq. (7.62), least squares regression was used to find the parameter estimates given in Table A.1, located in Appendix A.4. The model's valid domain, given in Table A.2, was defined to be the interval between the minimum and maximum explanatory values with outliers beyond 1.5 times the interquartile range removed (as typical of a box and whisker plot).

7.6.3 Practical Implementation

Since the nonlinear aerodynamic model in Eq. (7.62) does not precisely satisfy Assumption 7.1, the time-varying parameters $\boldsymbol{F}_{(\cdot)}$, $\boldsymbol{M}_{(\cdot)}$ must be constructed using the current estimate of the air-relative velocity $\boldsymbol{v}_{\mathrm{r}}$ — akin to linearizing about the best estimate in an extended Kalman filter. Using the force model as an example, we often consider smooth, nonlinear, quasi-steady aerodynamic models $\boldsymbol{F}(\boldsymbol{v}_{\mathrm{r}}, \boldsymbol{\omega}, \boldsymbol{\delta})$, where $\boldsymbol{\delta}$ is the vector of flight control inputs (e.g., throttle setting and control surface deflections). Performing a Taylor series expansion about $\hat{\boldsymbol{v}}_{\mathrm{r}}$, we have

$$\boldsymbol{F}(\boldsymbol{v}_{\mathrm{r}}, \boldsymbol{\omega}, \boldsymbol{\delta}) = \boldsymbol{F}(\hat{\boldsymbol{v}}_{\mathrm{r}}, \boldsymbol{\omega}, \boldsymbol{\delta}) + \underbrace{\left.\frac{\partial \boldsymbol{F}}{\partial \boldsymbol{v}_{\mathrm{r}}}\right|_{\boldsymbol{v}_{\mathrm{r}}=\hat{\boldsymbol{v}}_{\mathrm{r}}}}_{\boldsymbol{F}_v(\hat{\boldsymbol{v}}_{\mathrm{r}}, \boldsymbol{\omega}, \boldsymbol{\delta})} (\boldsymbol{v}_{\mathrm{r}} - \hat{\boldsymbol{v}}_{\mathrm{r}}) + \text{H.O.T.} \tag{7.63}$$

Noting that any smooth function $\boldsymbol{f}(\boldsymbol{x})$ may be written as $\boldsymbol{A}(\boldsymbol{x})\boldsymbol{x} + \boldsymbol{b}(\boldsymbol{x})$, one may write

$$\boldsymbol{F}(\hat{\boldsymbol{v}}_{\mathrm{r}}, \boldsymbol{\omega}, \boldsymbol{\delta}) = \boldsymbol{F}_{\omega}(\hat{\boldsymbol{v}}_{\mathrm{r}}, \boldsymbol{\omega}, \boldsymbol{\delta})\boldsymbol{\omega} + \bar{\boldsymbol{F}}_0(\hat{\boldsymbol{v}}_{\mathrm{r}}, \boldsymbol{\omega}, \boldsymbol{\delta})$$

Then, letting $\boldsymbol{F}_0(\hat{\boldsymbol{v}}_{\mathrm{r}}, \boldsymbol{\omega}, \boldsymbol{\delta}) = \bar{\boldsymbol{F}}_0(\hat{\boldsymbol{v}}_{\mathrm{r}}, \boldsymbol{\omega}, \boldsymbol{\delta}) - \boldsymbol{F}_v(\hat{\boldsymbol{v}}_{\mathrm{r}}, \boldsymbol{\omega}, \boldsymbol{\delta})\hat{\boldsymbol{v}}_{\mathrm{r}}$ yields

$$\boldsymbol{F}(\boldsymbol{v}_{\mathrm{r}}, \boldsymbol{\omega}, \boldsymbol{\delta}) = \boldsymbol{F}_0(\boldsymbol{v}_{\mathrm{r}}, \boldsymbol{\omega}, \boldsymbol{\delta}) + \boldsymbol{F}_v(\boldsymbol{v}_{\mathrm{r}}, \boldsymbol{\omega}, \boldsymbol{\delta})\boldsymbol{v}_{\mathrm{r}} + \boldsymbol{F}_{\omega}(\boldsymbol{v}_{\mathrm{r}}, \boldsymbol{\omega}, \boldsymbol{\delta})\boldsymbol{\omega} + \text{H.O.T.} \tag{7.64}$$

Assuming the estimate $\hat{\boldsymbol{v}}_{\mathrm{r}}$ is sufficiently close to $\boldsymbol{v}_{\mathrm{r}}$, the higher-order terms can be neglected so that "known" signals $\boldsymbol{F}_{(\cdot)}$ in Assumption 7.1 are obtained by setting

$$\begin{aligned}
\boldsymbol{F}_v(t) &= \left.\frac{\partial \boldsymbol{F}(\boldsymbol{v}_{\mathrm{r}}, \boldsymbol{\omega}(t), \boldsymbol{\delta}(t))}{\partial \boldsymbol{v}_{\mathrm{r}}}\right|_{\boldsymbol{v}_{\mathrm{r}}=\hat{\boldsymbol{v}}_{\mathrm{r}}(t)} \\
\boldsymbol{F}_{\omega}(t) &= \left.\frac{\partial \boldsymbol{F}(\hat{\boldsymbol{v}}_{\mathrm{r}}(t), \boldsymbol{\omega}, \boldsymbol{\delta}(t))}{\partial \boldsymbol{\omega}}\right|_{\boldsymbol{\omega}=\boldsymbol{\omega}(t)} \\
\boldsymbol{F}_0(t) &= \boldsymbol{F}(\hat{\boldsymbol{v}}_{\mathrm{r}}(t), \boldsymbol{\omega}(t), \boldsymbol{\delta}(t)) - \boldsymbol{F}_v(t)\hat{\boldsymbol{v}}_{\mathrm{r}} - \boldsymbol{F}_{\omega}(t)\boldsymbol{\omega}
\end{aligned} \tag{7.65}$$

The force model error incurred by assuming $\boldsymbol{v}_{\mathrm{r}} - \hat{\boldsymbol{v}}_{\mathrm{r}} \approx \boldsymbol{0}$ is captured by the higher-order terms in Eq. (7.64); it is

$$\delta\hat{\boldsymbol{F}} = \boldsymbol{F}(\boldsymbol{v}_{\mathrm{r}}, \boldsymbol{\omega}, \boldsymbol{\delta}) - \boldsymbol{F}(\hat{\boldsymbol{v}}_{\mathrm{r}}, \boldsymbol{\omega}, \boldsymbol{\delta}) \tag{7.66}$$

Furthermore, the quasi-steady force model $\boldsymbol{F}(\boldsymbol{v}_{\mathrm{r}}, \boldsymbol{\omega}, \boldsymbol{\delta})$ differs from the true force $\boldsymbol{F}_{\mathrm{true}}$ by unmodeled dynamics, parametric error, and wind gradients on the scale of the aircraft. Thus,

$$\Delta \boldsymbol{F} = \boldsymbol{F}_{\mathrm{true}} - \boldsymbol{F}(\hat{\boldsymbol{v}}_{\mathrm{r}}, \boldsymbol{\omega}, \boldsymbol{\delta}) \tag{7.67}$$

is the total force modeling error that perturbs the invariant error dynamics (7.36) — not just $\delta \boldsymbol{F} = \boldsymbol{F}_{\mathrm{true}} - \boldsymbol{F}(\boldsymbol{v}_{\mathrm{r}}, \boldsymbol{\omega}, \boldsymbol{\delta})$ appearing in Eq. (6.24). The decomposition defined by Eq. (7.65) and the total modeling error in Eq. (7.67) are similarly defined for the moment $\boldsymbol{M}$.

Now, the practitioner needs only to determine the power spectral densities $\boldsymbol{Q}_w = \boldsymbol{\sigma}_w \boldsymbol{\sigma}_w^{\mathsf{T}}$, $\boldsymbol{Q}_M = \boldsymbol{\sigma}_M \boldsymbol{\sigma}_M^{\mathsf{T}}$, and $\boldsymbol{Q}_F = \boldsymbol{\sigma}_F \boldsymbol{\sigma}_F^{\mathsf{T}}$ and select the tuning parameter $\boldsymbol{\Gamma}$. For the eSPARRO UAV described in Section 7.6.1, these parameters were chosen using historical flight data. To include flight in various directions with respect to the wind, the cloverleaf maneuver shown in Figure 7.14 was used to infer $\boldsymbol{Q}_w$, $\boldsymbol{Q}_M$, and $\boldsymbol{Q}_F$.

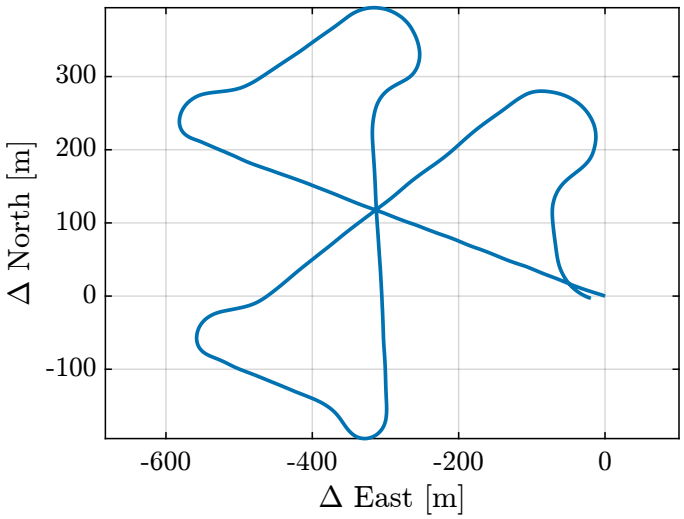

Figure 7.14: Cloverleaf maneuver used for tuning

The power spectral density of $\dot{\boldsymbol{w}}$ may be determined in two different ways. The first approach involves using some truth source, such as an air data unit, to take a numerical derivative of the reconstructed wind $\boldsymbol{w}$. The power spectral density of $\dot{\boldsymbol{w}}$ may be computed using `pwelch` in Matlab. Then, $\boldsymbol{Q}_w$ is taken to be the maximum value of this power spectral density over all frequencies; that is, the colored noise $\dot{\boldsymbol{w}}$ is bounded by white noise with constant power spectral density $\boldsymbol{Q}_w$. The second approach, which is used to produce the results in this chapter, begins by assuming the apparent wind is Brownian motion. Therefore, it should hold that

$$\operatorname{cov}\big(\boldsymbol{w}(t+\tau) - \boldsymbol{w}(t)\big) = \tau \boldsymbol{Q}_w \tag{7.68}$$

for any $\tau > 0$. Using the reconstructed wind, Eq. (7.68) can be used to compute $\boldsymbol{Q}_w$ for a variety of lag times τ. The final $\boldsymbol{Q}_w$ is then selected using its maximum value over all $\tau > 0$.

For the aircraft and altitudes considered here, $\boldsymbol{Q}_w$ was taken to be the diagonal matrix

$$\boldsymbol{Q}_w = \mathbf{diag}(0.96, 0.93, 1.38)\ \frac{(\mathrm{m/s})^2}{\mathrm{Hz}} \tag{7.69}$$

whose elements were selected from the results shown in Figure 7.15.

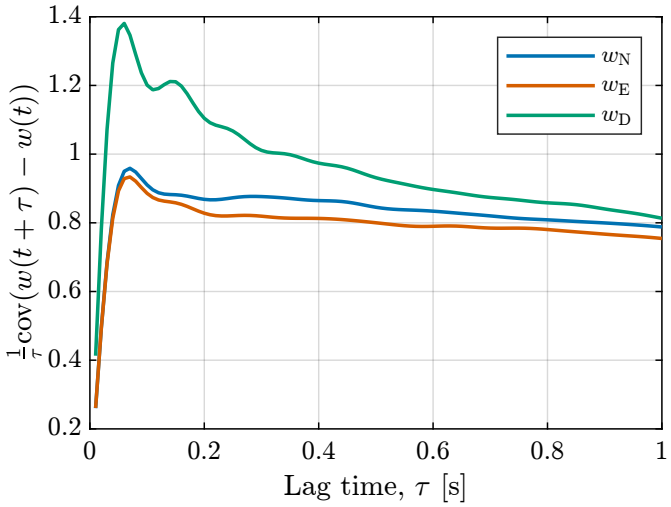

Figure 7.15: Selection of $\boldsymbol{Q}_w$ through a Brownian motion assumption

The power spectral densities of the force and moment modeling error signals $\Delta\boldsymbol{F}$ and $\Delta\boldsymbol{M}$ may be determined using a variety of methods. Here, we use the estimated aerodynamic model residual variance $\hat{\sigma}^2$ obtained through the system identification process for each force and moment component [113, Ch. 5]. Thus, $\hat{\sigma}^2$ can be used to construct the power spectral density of the nonlinear model error $\delta\boldsymbol{F} = \boldsymbol{F}_{\text{true}} - \boldsymbol{F}(\boldsymbol{v}_\mathrm{r}, \boldsymbol{\omega}, \boldsymbol{\delta})$, for instance. To accurately characterize the total modeling error $\Delta\boldsymbol{F}$, the additional perturbation $\delta\hat{\boldsymbol{F}}$ defined in Eq. (7.66) must also be quantified. We recognize, however, that the term $\Delta\hat{\boldsymbol{F}}$ is a vanishing perturbation; that is, $\delta\hat{\boldsymbol{F}} = \mathbf{0}$ when $\hat{\boldsymbol{v}}_\mathrm{r} = \boldsymbol{v}_\mathrm{r}$. Therefore, we choose to neglect $\delta\hat{\boldsymbol{F}}$ when selecting the power spectral density $\boldsymbol{Q}_F$ (and similarly for $\boldsymbol{Q}_M$). For the eSPAARO model given above,

$$\boldsymbol{Q}_F = \mathbf{diag}(7.6, 14.1, 108.0)\ \frac{\mathrm{N}^2}{\mathrm{Hz}} \tag{7.70}$$

$$\boldsymbol{Q}_M = \mathbf{diag}(37.7, 19.9, 11.3)\ \frac{(\mathrm{N}\cdot\mathrm{m})^2}{\mathrm{Hz}} \tag{7.71}$$

Finally, the tuning parameter $\boldsymbol{\Gamma}$ was chosen to be $\boldsymbol{\Gamma} = [\mathbb{I}\ \ \mathbf{0}]^\mathsf{T}$. This value was large enough to not cause over-amplification of measurement noise but still small enough not hinder the convergence rate of the observer.

Remark 7.3. *While $\delta\hat{\boldsymbol{F}}$ is neglected in the above selection of $\boldsymbol{Q}_F$ due to its vanishing behavior when $\hat{\boldsymbol{v}}_\mathrm{r} = \boldsymbol{v}_\mathrm{r}$, one could incorporate it to improve performance or strengthen stability*

guarantees. Let $\tilde{\boldsymbol{v}}_{\mathrm{r,max}}$ denote the maximum expected error in the air-relative velocity estimate — for instance, constrained to prevent stalling or overspeeding a fixed-wing aircraft. Then, using Monte-Carlo analysis over the model's valid domain (e.g., Table A.2), the power spectral density of $\delta\hat{\boldsymbol{F}}$ could be estimated and used to inform a more conservative choice of $\boldsymbol{Q}_F$.

7.6.4 Flight Test Experiment and Results

To demonstrate the observer's large region of attraction, the automated S-turn shown in Figure 7.16 was performed in moderate wind and turbulence levels for the vehicle's size. During the flight test experiment, the prevailing wind averaged 9.5 m/s from 285 degrees (West-Northwest) with gusts up to 12 m/s. The symmetry-preserving reduced-order wind

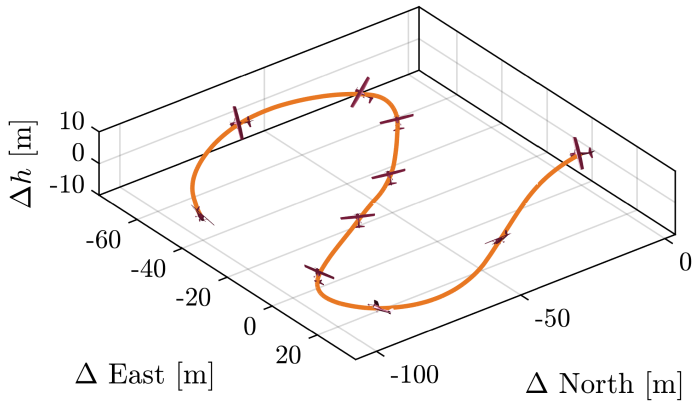

Figure 7.16: Automated S-turn trajectory (aircraft wingspan to scale)

observer was implemented on this flight data using both the inertial and body transformation groups. The initial unmeasured state estimates corresponded to straight-and-level flight at 20 m/s in zero wind. Specifically, $\hat{\boldsymbol{w}}(0) = \boldsymbol{0}$ and $\hat{\boldsymbol{v}}_{\mathrm{r}}(0) = [19.98 \quad 0 \quad 0.66]^{\mathsf{T}}$. The wind estimates are shown in Figure 7.17. For these results, the noise-to-state stability guarantees (7.53a) and (7.54a) hold with

$$k_1 = 0.253, \quad k_2 = 13.7, \quad k_3 = 0.166, \quad \text{and} \quad k_4 = 51.3 \tag{7.72}$$

Although these guarantees are less conservative than the quadrotor simulation results in Section 7.5, they are still quite conservative.

As seen in Figure 7.17, the observer's performance during the S-turn is similar between the two transformation groups. To further investigate, the wind observer was implemented on the cloverleaf maneuver used to determine $\boldsymbol{Q}_w$, $\boldsymbol{Q}_F$, and $\boldsymbol{Q}_M$. The estimates of north wind component are shown in Figure 7.18. Here, a key difference between the inertial and body transformation groups becomes apparent — especially around 46 seconds. The observer designed using the body transformation group is more robust to the modeling errors and measurement perturbations that occur in tight turns. The radius of curvature

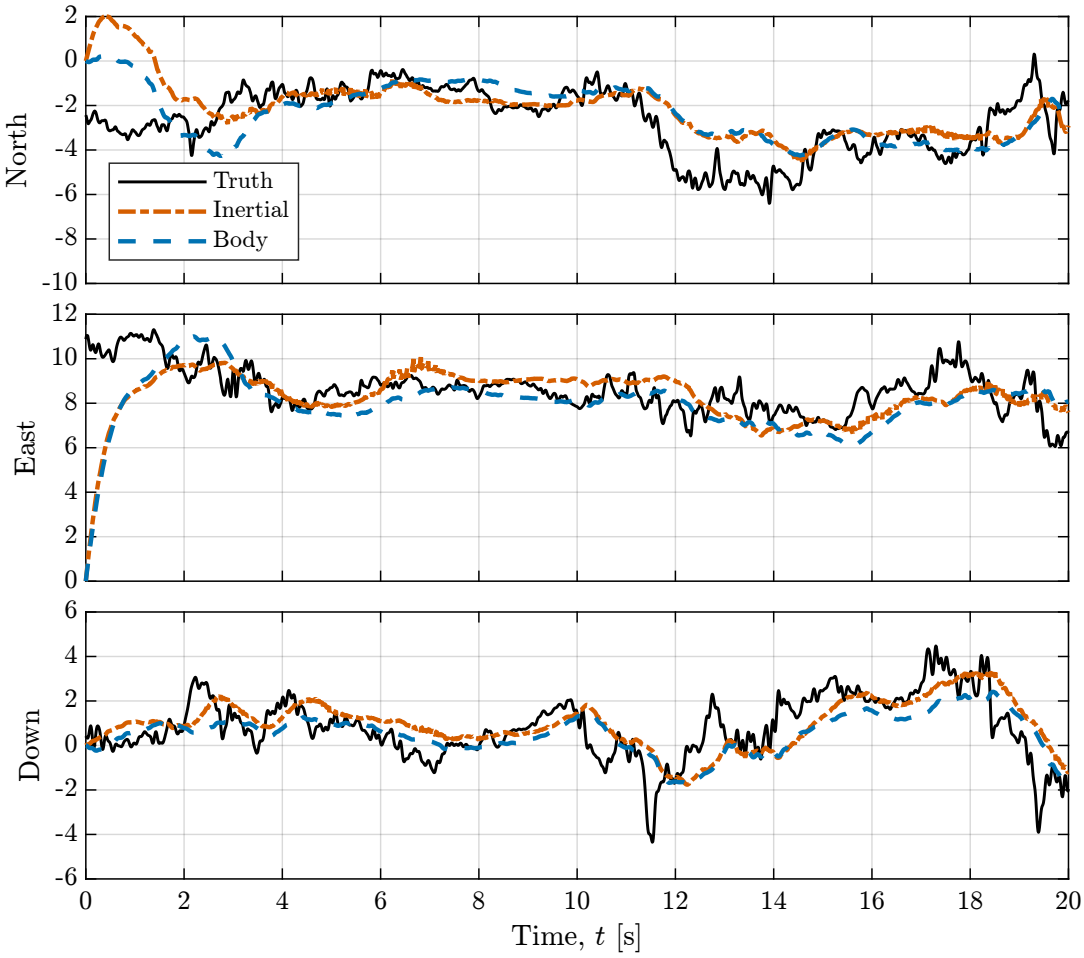

Figure 7.17: Comparison of north, east, and down wind velocity estimates in m/s between the inertial and body transformation groups

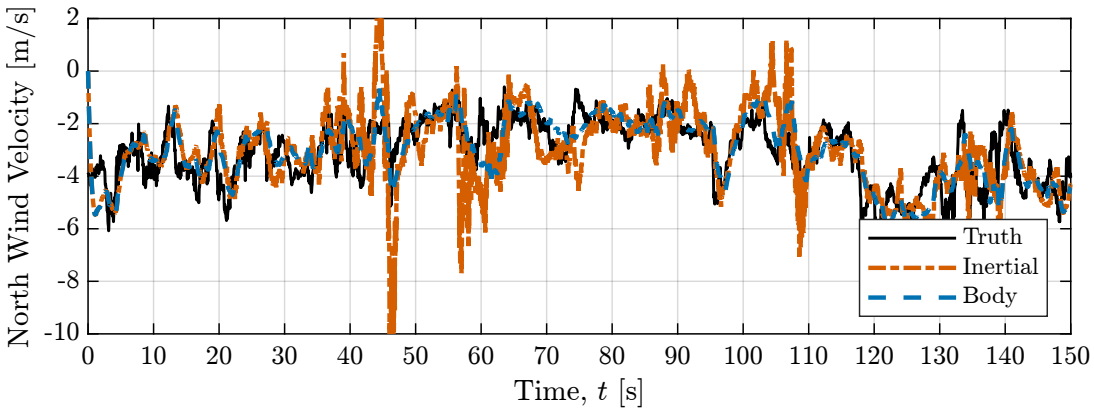

Figure 7.18: Comparison of north wind velocity estimates between the inertial and body transformation groups

for the turns in the cloverleaf maneuver was much smaller than the S-turn, thus resulting in aileron deflections and roll rates well beyond the model's valid domain given in Table A.2. To quantify the difference between the transformation groups, the root mean square error (7.26) was computed over the cloverleaf maneuver results. For the inertial transformation group, we have RMSE = 1.35 m/s, whereas the body transformation group yielded RMSE = 1.14 m/s.

The symmetry-preserving wind observer was also compared to a continuous-discrete extended Kalman filter (EKF) constituting a baseline full-order filtering approach. The EKF assumed the same process model (6.24) as the symmetry-preserving observer. Thus, the sources of process noise are the same between these two approaches. The same measurements were assumed (position, attitude, and angular velocity), except that discrete-time measurement noise was considered. The measurement noise covariances for position and attitude were taken to be the average state estimation error covariance reported by the autopilot's navigation solution. From the cloverleaf maneuver, we have

$$\boldsymbol{P}_q = \mathbf{diag}\left(0.027,\ 0.027,\ 0.039\right)\ \mathrm{m}^2$$
$$\boldsymbol{P}_{R_{\mathrm{IB}}} = \mathbf{diag}\left(1.54\times10^{-5},\ 1.54\times10^{-5},\ 1.66\times10^{-4}\right)$$

where $\boldsymbol{P}_{R_{\mathrm{IB}}}$ is the covariance of the attitude estimate error in $\mathsf{T}_{\hat{\boldsymbol{R}}_{\mathrm{IB}}}\mathsf{SO}(3)$. The angular velocity measurement noise was characterized by comparing raw to smoothed gyroscope data. The power spectral density of the gyro noise was computed in this way as

$$\boldsymbol{Q}_{\mathrm{gyro}} = \mathbf{diag}\left(2.18\times10^{-4},\ 1.05\times10^{-4},\ 4.01\times10^{-6}\right)\ \frac{(\mathrm{rad/s})^2}{\mathrm{Hz}}$$

Thus, the discrete-time measurement noise covariance for the EKF is

$$\boldsymbol{R} = \mathbf{diag}\left(\boldsymbol{P}_q, \boldsymbol{P}_{R_{\mathrm{IB}}}, \boldsymbol{Q}_{\mathrm{gyro}}/\Delta t\right) \tag{7.73}$$

where Δt is the time between measurements.

For the S-turn shown in Figure 7.16, the wind estimates using the EKF are shown in Figure 7.19 along with the symmetry-preserving observer synthesized using the inertial transformation group. Here, we see the performance of the EKF is comparable to the nonlinear

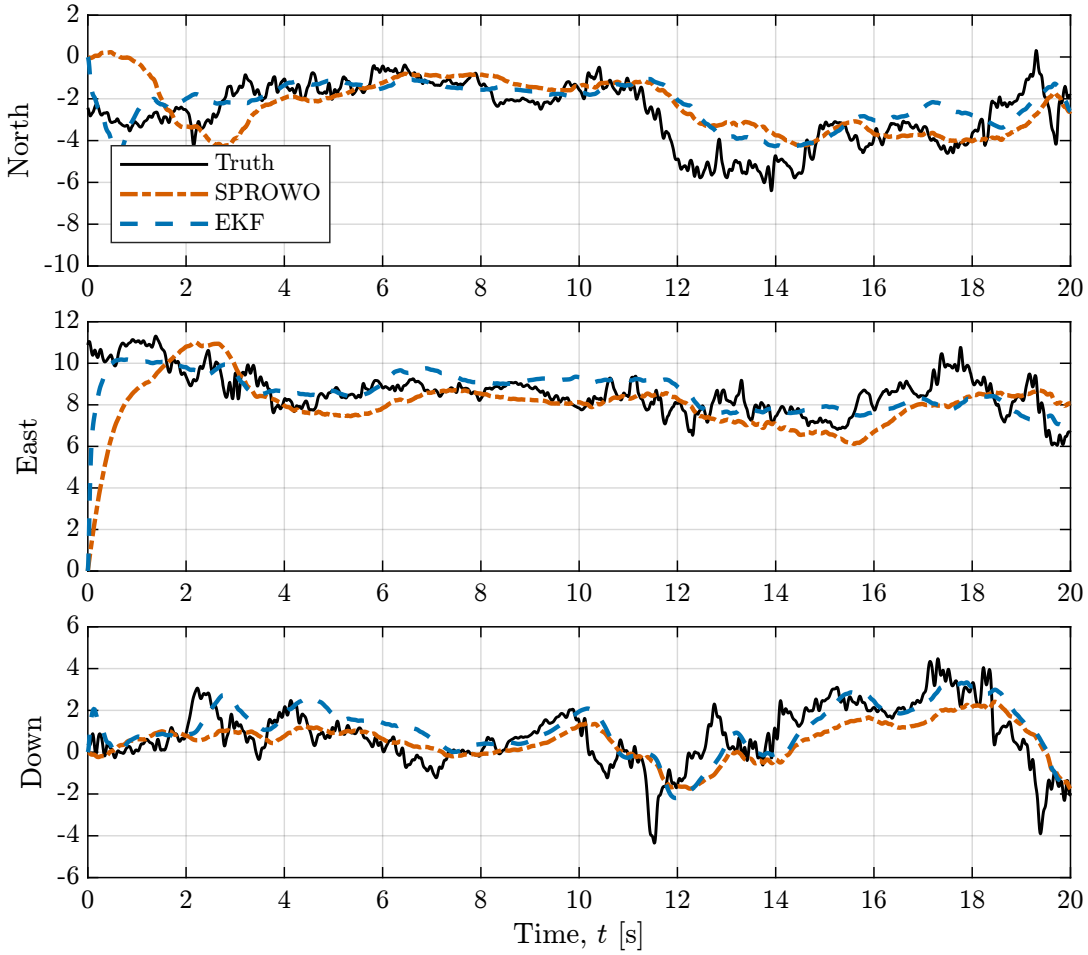

Figure 7.19: Comparison of the symmetry-preserving reduced-order wind observer (SPROWO) with a continuous-discrete extended Kalman filter (EKF) on the S-turn maneuver

observer with a root mean square error (7.26) of RMSE = 1.27 m/s. The two approaches differ in the initial transients, where we see faster "convergence" using the EKF. However, it is important to stress that the EKF's performance is not guaranteed like it is for the symmetry-preserving reduced-order observer. One potential way to combine the strengths of these two methods is use the exogenous Kalman filter (XKF) developed by Johansen and Fossen [82]. In this approach, the nonlinear dynamics are linearized about the state estimates obtained from the nonlinear observer, which are then used in a Kalman filter. The benefit here is that state estimation error covariances are obtained in addition to the stability guarantees enjoyed by the nonlinear observer.

Chapter 8

Passivity-Based Wind Estimation

8.1 Introduction

The primary disadvantage of reduced-order observers is that measurement noise can have unintended consequences on the state estimate. In contrast, the *innovation term* $\boldsymbol{y} - \hat{\boldsymbol{y}}$ in full-order observers acts as a feedback mechanism that can have the effect of "filtering out" noise. Nonlinear state estimators such as the extended Kalman filter (EKF) can be viewed in this way, where the model of the dynamics is used to intelligently filter out process and measurement noise. An alternative viewpoint is that of feedback stabilization. To demonstrate, consider the nonlinear system $\dot{\boldsymbol{x}} = \boldsymbol{f}(\boldsymbol{x})$ with output $\boldsymbol{y} = \boldsymbol{h}(\boldsymbol{x})$. For systems defined on $\mathbb{R}^n$, it suffices to consider full-order state estimators and observers of the form

$$\dot{\hat{\boldsymbol{x}}} = \boldsymbol{f}(\hat{\boldsymbol{x}}) + \mathbf{v}(\hat{\boldsymbol{x}}, \boldsymbol{y})$$

where $\mathbf{v}$ is called the *output injection*. From this perspective, the dynamics of the state estimate error $\tilde{\boldsymbol{x}} = \hat{\boldsymbol{x}} - \boldsymbol{x}$ are "controlled" via output feedback

$$\mathbf{v} = \boldsymbol{L}\big(\boldsymbol{y} - \boldsymbol{h}(\hat{\boldsymbol{x}})\big)$$

for some gain matrix $\boldsymbol{L}$. State estimators such as the EKF fall short from this perspective insofar that their stability guarantees are only local [90]. This observation motivates the use of full-order nonlinear observers with *global* stability guarantees.

One method for designing a global nonlinear observer is feedback passivation; that is, $\mathbf{v}$ is chosen to render the state estimation error dynamics *passive*. As first formalized by Willems [153], a dynamical system $\dot{\boldsymbol{x}} = \boldsymbol{f}(\boldsymbol{x}) + \boldsymbol{g}(\boldsymbol{x})\boldsymbol{u}$ with output $\boldsymbol{y} = \boldsymbol{h}(\boldsymbol{x})$ is called *dissipative* with respect to the *supply rate* $w(\boldsymbol{u}, \boldsymbol{y})$ if there exists a non-negative *storage function* $W(\boldsymbol{x})$ such that

$$W(\boldsymbol{x}(t)) - W(\boldsymbol{x}(0)) \leq \int_0^t w(\boldsymbol{u}(\tau), \boldsymbol{y}(\tau))\,\mathrm{d}\tau \tag{8.1}$$

The system is considered *passive* if it is dissipative with respect to the supply rate $w(\boldsymbol{u}, \boldsymbol{y}) = \boldsymbol{u}^\mathsf{T}\boldsymbol{y}$. It is *strictly passive* if there also exists a positive definite function ϕ such that the system is dissipative with respect to $w(\boldsymbol{u}, \boldsymbol{y}) = \boldsymbol{u}^\mathsf{T}\boldsymbol{y} - \phi$. Passive systems exhibit many desirable properties. For example, pure negative output feedback of a zero-state detectable, passive system asymptotically stabilizes the origin. This property among others is described in the seminal work of Byrnes, Isidori, and Willems [29], where the authors also develop

the conditions under which a system can be rendered passive by state feedback. Jiang and Hill [81] extended these conditions to output feedback passivation, which is the mechanism used in the passivity-based observer design approach described by Shim [131] and Shim *et al.* [132]. This chapter is based on reference [75] and details the design of a passivity-based wind observer.

The rest of this chapter is organized as follows. Section 8.2 provides an overview of passivity-based observer theory as presented by Shim *et al.* [132]. Next, Section 8.3 discusses the problem setup and the assumptions required for the observer design. Next, Section 8.4 details the first step of the observer design — rendering the state estimation error dynamics minimum phase. The second step of the observer design is covered in Section 8.5, where the error dynamics are proven to be strictly passive. Finally, Section 8.6 presents both simulation and flight test results for the observer, enabling the evaluation of the observer's performance even when assumptions are violated.

8.2 Observer Design via Passivation of Error Dynamics

In this section, we review the passivity-based observer design method detailed by Shim *et al.* [132]. Suppose the state $\boldsymbol{x} \in \mathbb{R}^n$ can be split into a measured part $\boldsymbol{x}_1 \in \mathbb{R}^p$ and an unmeasured part $\boldsymbol{x}_2 \in \mathbb{R}^{n-p}$ such that $\boldsymbol{x} = (\boldsymbol{x}_1, \boldsymbol{x}_2)$. For the purpose of observer design, assume $\boldsymbol{x}_1$ is measured perfectly as $\boldsymbol{y} = \boldsymbol{x}_1$. Note that we do not consider $\boldsymbol{y}$ to be part of the true state vector like denoted in Chapters 3 and 7, since in implementation, there inevitably exist measurement disturbances causing $\boldsymbol{y} \neq \boldsymbol{x}_1$. As will be seen shortly, the closed-loop properties of passivity-based observers lead to an inherent robustness to this discrepancy.

Consider the nonlinear system

$$\dot{\boldsymbol{x}}_1 = \boldsymbol{f}_1(\boldsymbol{x}_1, \boldsymbol{x}_2, \boldsymbol{u}) \tag{8.2a}$$
$$\dot{\boldsymbol{x}}_2 = \boldsymbol{f}_2(\boldsymbol{x}_1, \boldsymbol{x}_2, \boldsymbol{u}) \tag{8.2b}$$

where $\boldsymbol{u} \in \mathcal{U}$ comprises the inputs to the system. The aim is to design the Luenberger-like observer

$$\dot{\hat{\boldsymbol{x}}}_1 = \boldsymbol{f}_1(\hat{\boldsymbol{x}}_1, \hat{\boldsymbol{x}}_2, \boldsymbol{u}) + \boldsymbol{L}_1 \mathbf{v}(\hat{\boldsymbol{x}}, \boldsymbol{y}, \boldsymbol{u}) \tag{8.3a}$$
$$\dot{\hat{\boldsymbol{x}}}_2 = \boldsymbol{f}_2(\hat{\boldsymbol{x}}_1, \hat{\boldsymbol{x}}_2, \boldsymbol{u}) + \boldsymbol{L}_2 \mathbf{v}(\hat{\boldsymbol{x}}, \boldsymbol{y}, \boldsymbol{u}) \tag{8.3b}$$

with nonlinear output injection

$$\mathbf{v}(\hat{\boldsymbol{x}}, \boldsymbol{y}, \boldsymbol{u}) = -k(\hat{\boldsymbol{x}}, \boldsymbol{y}, \boldsymbol{u})\boldsymbol{y}_\mathrm{p} + \mathbf{v}_\mathrm{p} \tag{8.4}$$

The output error $\boldsymbol{y}_\mathrm{p} = \hat{\boldsymbol{y}} - \boldsymbol{y}$ will become the passive output corresponding to the passive input $\mathbf{v}_\mathrm{p}$, a dummy input, for the observer dynamics. Note that the observer formulation involves two gains — a *constant* gain $\boldsymbol{L} = [\boldsymbol{L}_1^\mathsf{T} \;\; \boldsymbol{L}_2^\mathsf{T}]^\mathsf{T}$ and scalar gain *function* k. For the wind estimation problem, we will generalize the approach by allowing the scalar gain function, k,

to be a matrix-valued function, $\boldsymbol{K}$, and allowing the matrix $\boldsymbol{L}_2$ to depend on measurements as similarly done by Chen and Woolsey [34] and Venkatraman and van der Schaft [151].

Denoting

$$\tilde{\boldsymbol{f}}(\tilde{\boldsymbol{x}};\boldsymbol{x};\boldsymbol{u}) \coloneqq \boldsymbol{f}(\tilde{\boldsymbol{x}}+\boldsymbol{x},\boldsymbol{u}) - \boldsymbol{f}(\boldsymbol{x},\boldsymbol{u}) \tag{8.5}$$

the state estimate error dynamics are

$$\dot{\tilde{\boldsymbol{x}}}_1 = \tilde{\boldsymbol{f}}_1(\tilde{\boldsymbol{x}}_1,\tilde{\boldsymbol{x}}_2;\boldsymbol{x}_1,\boldsymbol{x}_2;\boldsymbol{u}) + \boldsymbol{L}_1\mathbf{v}(\hat{\boldsymbol{x}},\boldsymbol{y},\boldsymbol{u}) \tag{8.6a}$$

$$\dot{\tilde{\boldsymbol{x}}}_2 = \tilde{\boldsymbol{f}}_2(\tilde{\boldsymbol{x}}_1,\tilde{\boldsymbol{x}}_2;\boldsymbol{x}_1,\boldsymbol{x}_2;\boldsymbol{u}) + \boldsymbol{L}_2\mathbf{v}(\hat{\boldsymbol{x}},\boldsymbol{y},\boldsymbol{u}) \tag{8.6b}$$

The observer design involves two main steps. First, with $\boldsymbol{y}_\mathrm{p}$ viewed as the output, a proper Lyapunov function $V^*(\tilde{\boldsymbol{x}}_2,\boldsymbol{x})$ and a positive definite function φ^* are found that prove the error system in Eq. (8.6) augmented with the plant dynamics is globally minimum phase with respect to the set

$$\mathcal{M} = \{(\tilde{\boldsymbol{x}},\boldsymbol{x}) \in \mathbb{R}^n \times \mathbb{R}^n \mid \tilde{\boldsymbol{x}} = \boldsymbol{0}\} \tag{8.7}$$

with

$$\dot{V}^* \leq -\varphi^*(\|\tilde{\boldsymbol{x}}_2\|) \tag{8.8}$$

This step can be thought of like the first step in integrator backstepping, where one stabilizes a subsystem using a state variable as an artificial input [86, Ch. 14], ensuring the unmeasured state estimates asymptotically approach their true values when the measurable states are perfectly known. Second, non-negative functions φ_1 and φ_2 are determined such that

$$\begin{aligned}\left|\frac{\partial V^*}{\partial \tilde{\boldsymbol{x}}_2}[\tilde{\boldsymbol{f}}_2 - \boldsymbol{L}_2\boldsymbol{L}_1^{-1}\tilde{\boldsymbol{f}}_1](\tilde{\boldsymbol{x}}_1,\boldsymbol{L}_2\boldsymbol{L}_1^{-1}\tilde{\boldsymbol{x}}_1;\boldsymbol{x}_1,\hat{\boldsymbol{x}}_2;\boldsymbol{u}) + \tilde{\boldsymbol{x}}_1\boldsymbol{L}_1^{-1}\tilde{\boldsymbol{f}}_1(\tilde{\boldsymbol{x}}_1,\tilde{\boldsymbol{x}}_2+\boldsymbol{L}_2\boldsymbol{L}_1^{-1}\tilde{\boldsymbol{x}}_1;\boldsymbol{x}_1,\hat{\boldsymbol{x}}_2-\tilde{\boldsymbol{x}}_2;\boldsymbol{u})\right| \\ \leq \varphi_1(\tilde{\boldsymbol{x}}_1,\boldsymbol{x}_1,\hat{\boldsymbol{x}}_2,\boldsymbol{u})\|\tilde{\boldsymbol{x}}_1\|^2 + \varphi_2(\tilde{\boldsymbol{x}}_1,\boldsymbol{x}_1,\hat{\boldsymbol{x}}_2,\boldsymbol{u})\sqrt{\varphi^*(\|\tilde{\boldsymbol{x}}_2\|)}\|\tilde{\boldsymbol{x}}_1\|\end{aligned} \tag{8.9}$$

In this expression, parentheses contain arguments for all functions in square brackets. The requirement that there exist these *bounding functions* comes from the sufficient conditions for output feedback passivation developed by Jiang and Hill [81]. It essentially ensures the coupling between the output dynamics ($\dot{\tilde{\boldsymbol{x}}}_1$) and the unmeasurable dynamics ($\dot{\tilde{\boldsymbol{x}}}_2$) preserves strict passivity from $\mathbf{v}_\mathrm{p}$ to $\boldsymbol{y}_\mathrm{p}$, which is a result of the following.

Theorem 8.1 (Theorem 2 by Shim *et al.* [132])**.** *Suppose the Lyapunov function V^* proves that the error dynamics augmented with the system dynamics are (globally) minimum phase with respect to $\mathcal{M}$. Also suppose there exist function φ_1 and φ_2 such that Eq. (8.9) holds. Then, the feedback*

$$\mathbf{v} = -k(\hat{\boldsymbol{x}},\boldsymbol{y})\boldsymbol{y}_\mathrm{p} + \mathbf{v}_\mathrm{p} \tag{8.10}$$

with

$$k(\hat{\boldsymbol{x}},\boldsymbol{y}) = \varepsilon + \varphi_1(\hat{\boldsymbol{x}}_1-\boldsymbol{y},\boldsymbol{y},\hat{\boldsymbol{x}}_2-\boldsymbol{L}_2\boldsymbol{L}_1^{-1}(\hat{\boldsymbol{x}}_1-\boldsymbol{y})) + \varphi_2^2(\hat{\boldsymbol{x}}_1-\boldsymbol{y},\boldsymbol{y},\hat{\boldsymbol{x}}_2-\boldsymbol{L}_2\boldsymbol{L}_1^{-1}(\hat{\boldsymbol{x}}_1-\boldsymbol{y})) \tag{8.11}$$

for some $\varepsilon > 0$ renders the augmented system strictly passive from $\mathbf{v}_\mathrm{p}$ to $\boldsymbol{y}_\mathrm{p}$ with respect to $\mathcal{M}$ with the storage function

$$W = V^*(\tilde{\boldsymbol{x}}_2 - \boldsymbol{L}_2\boldsymbol{L}_1^{-1}\tilde{\boldsymbol{x}}_1, \boldsymbol{x}) + \frac{1}{2}\tilde{\boldsymbol{x}}_1^\mathsf{T}\boldsymbol{L}_1^{-1}\tilde{\boldsymbol{x}}_1 \tag{8.12}$$

Upon setting $\mathbf{v}_\mathrm{p} = \mathbf{0}$, $\mathcal{M}$ becomes positively invariant and (globally) asymptotically attractive.

While we do not use this theorem directly, the results in this chapter follow its proof.

8.3 Problem Statement

We now aim to design a passivity based observer for the aircraft in wind. To avoid geometric complications, the attitude rotation matrix $\boldsymbol{R}_\mathrm{IB}$ is parameterized by the *compass vector* $\boldsymbol{\lambda} = \boldsymbol{R}_\mathrm{IB}^\mathsf{T}\boldsymbol{e}_1$ and *tilt vector* $\boldsymbol{\zeta} = \boldsymbol{R}_\mathrm{IB}^\mathsf{T}\boldsymbol{e}_3$, as done by Woolsey and Techy [155]. The unit vector $\boldsymbol{\lambda} \in \mathsf{S}^2$ is the North direction expressed in the body frame. Similarly, $\boldsymbol{\zeta} \in \mathsf{S}^2$ is the inertial downward direction expressed in the body frame. With this parameterization, the attitude kinematics (2.9) become

$$\dot{\boldsymbol{\lambda}} = \boldsymbol{\lambda} \times \boldsymbol{\omega} \tag{8.13a}$$

$$\dot{\boldsymbol{\zeta}} = \boldsymbol{\zeta} \times \boldsymbol{\omega} \tag{8.13b}$$

where the rotation matrix, $\boldsymbol{R}_\mathrm{IB}$, may be reconstructed as

$$\boldsymbol{R}_\mathrm{IB}(\boldsymbol{\lambda}, \boldsymbol{\zeta}) = \begin{bmatrix} \boldsymbol{\lambda} & \boldsymbol{S}(\boldsymbol{\zeta})\boldsymbol{\lambda} & \boldsymbol{\zeta} \end{bmatrix}^\mathsf{T} \tag{8.14}$$

Like in Section 7.2, we restrict ourselves to the deterministic setting. Therefore, we assume the wind field is uniform and steady. Similar to Assumption 7.1, we affinely decompose the aerodynamic force $\boldsymbol{F}$ and moment $\boldsymbol{M}$ for the purpose of observer design.

Assumption 8.1. *The aerodynamic force and moment satisfy*

$$\boldsymbol{F} = \boldsymbol{F}_0(\boldsymbol{y}, \boldsymbol{u}) + \boldsymbol{F}_v\boldsymbol{v}_\mathrm{r} + \boldsymbol{F}_\omega\boldsymbol{\omega} \tag{8.15}$$

$$\boldsymbol{M} = \boldsymbol{M}_0(\boldsymbol{y}, \boldsymbol{u}) + \boldsymbol{M}_v\boldsymbol{v}_\mathrm{r} + \boldsymbol{M}_\omega\boldsymbol{\omega} \tag{8.16}$$

where $\boldsymbol{F}_v$, $\boldsymbol{F}_\omega$, $\boldsymbol{M}_v\boldsymbol{v}_\mathrm{r}$, and $\boldsymbol{M}_\omega$ are constant matrices.

Assumption 8.1 is that the quantities $\boldsymbol{F}_v$, $\boldsymbol{F}_\omega$, $\boldsymbol{M}_v\boldsymbol{v}_\mathrm{r}$, and $\boldsymbol{M}_\omega$ are treated as slowly-varying parameters. For example, the values of $\boldsymbol{F}_{(\cdot)}$ and $\boldsymbol{M}_{(\cdot)}$ for a fixed-wing aircraft generally depend on dynamic pressure, $\frac{1}{2}\rho\boldsymbol{v}_\mathrm{r}^\mathsf{T}\boldsymbol{v}_\mathrm{r}$, which we can assume to vary slowly compared to the observer and aircraft dynamics. In contrast, $\boldsymbol{F}_0$ and $\boldsymbol{M}_0$ are functions of the known input $\boldsymbol{u}$ and output $\boldsymbol{y}$. For compactness, we will drop the arguments to $\boldsymbol{F}_0$ and $\boldsymbol{M}_0$. The equations

of motion used for the passivity based wind observer design are

$$\dot{\boldsymbol{q}} = \boldsymbol{R}_{\text{IB}}\boldsymbol{v}_{\text{r}} + \boldsymbol{w} \tag{8.17a}$$
$$\dot{\boldsymbol{\lambda}} = \boldsymbol{\lambda} \times \boldsymbol{\omega} \tag{8.17b}$$
$$\dot{\boldsymbol{\zeta}} = \boldsymbol{\zeta} \times \boldsymbol{\omega} \tag{8.17c}$$
$$\dot{\boldsymbol{h}} = \boldsymbol{I}^{-1}\big(\boldsymbol{I}\boldsymbol{\omega} \times \boldsymbol{\omega} + \boldsymbol{M}_0 + \boldsymbol{M}_v\boldsymbol{v}_{\text{r}} + \boldsymbol{M}_\omega\boldsymbol{\omega}\big) \tag{8.17d}$$
$$\dot{\boldsymbol{v}}_{\text{r}} = \boldsymbol{v}_{\text{r}} \times \boldsymbol{\omega} + g\boldsymbol{\zeta} + \frac{1}{m}\big(\boldsymbol{F}_0 + \boldsymbol{F}_v\boldsymbol{v}_{\text{r}} + \boldsymbol{F}_\omega\boldsymbol{\omega}\big) \tag{8.17e}$$
$$\dot{\boldsymbol{w}} = \boldsymbol{0} \tag{8.17f}$$

The state of this system is defined by the vector $\boldsymbol{x} = [\boldsymbol{q}^\mathsf{T}\ \boldsymbol{\lambda}^\mathsf{T}\ \boldsymbol{\zeta}^\mathsf{T}\ \boldsymbol{\omega}^\mathsf{T}\ \boldsymbol{v}_{\text{r}}^\mathsf{T}\ \boldsymbol{w}^\mathsf{T}]^\mathsf{T}$.

Like Chapter 7, we assume the aircraft is instrumented with an accelerometer, gyroscope, magnetometer, and inertial positioning system (i.e. vision-based or GNSS) such that position, attitude, and angular velocity measurements can be readily obtained with negligible noise from a low-level estimation algorithm. In other words, consider Assumption 7.2 to be true. Therefore, let

$$\boldsymbol{y} = \boldsymbol{x}_1 = [\boldsymbol{q}^\mathsf{T}\ \boldsymbol{\lambda}^\mathsf{T}\ \boldsymbol{\zeta}^\mathsf{T}\ \boldsymbol{\omega}^\mathsf{T}]^\mathsf{T} \tag{8.18}$$

meaning the unmeasured part of the state is $\boldsymbol{x}_2 = [\boldsymbol{v}_{\text{r}}^\mathsf{T}\ \boldsymbol{w}^\mathsf{T}]^\mathsf{T}$. Thus, the dynamics (8.17) are in the form (8.2), where $\boldsymbol{f}_1$ contains the right-hand sides of Eqs. (8.17a)–(8.17d) and $\boldsymbol{f}_2$ contains the right-hand sides of Eqs. (8.17e)–(8.17f).

Remark 8.1. *While the outputs $\boldsymbol{y}$ are assumed to be noise-free for the purposes of observer design, the terms $\boldsymbol{F}_0$ and $\boldsymbol{M}_0$ depend on real-time measurements, which may be imperfect in practice. Throughout the remainder of this chapter, we will use $\boldsymbol{y}$ to denote the measured quantities used in the implementation of the observer, whereas $\boldsymbol{x}_1$ refers to the true values used in the design process.*

8.4 Minimum Phase and Relative Degree Sufficient Conditions

Consider the more general form of Eq. (8.3),

$$\dot{\hat{\boldsymbol{x}}}_1 = \boldsymbol{f}_1(\hat{\boldsymbol{x}}_1, \hat{\boldsymbol{x}}_2, \boldsymbol{u}) + \boldsymbol{L}_1\mathbf{v} \tag{8.19a}$$
$$\dot{\hat{\boldsymbol{x}}}_2 = \boldsymbol{f}_2(\hat{\boldsymbol{x}}_1, \hat{\boldsymbol{x}}_2, \boldsymbol{u}) + \boldsymbol{L}_2(\boldsymbol{y})\mathbf{v} \tag{8.19b}$$

which we use to estimate the state of the aircraft in wind. It follows that the components of the error dynamics vector field $\tilde{\boldsymbol{f}}$, appearing in Eq. (8.6), has the components

$$\tilde{\boldsymbol{f}}_{1_q} = \boldsymbol{R}_{\mathrm{IB}}(\tilde{\boldsymbol{\lambda}} + \boldsymbol{\lambda}, \tilde{\boldsymbol{\zeta}} + \boldsymbol{\zeta})(\tilde{\boldsymbol{v}}_{\mathrm{r}} + \boldsymbol{v}_{\mathrm{r}}) - \boldsymbol{R}_{\mathrm{IB}}(\boldsymbol{\lambda}, \boldsymbol{\zeta})\boldsymbol{v}_{\mathrm{r}} + \tilde{\boldsymbol{w}} \tag{8.20a}$$

$$\tilde{\boldsymbol{f}}_{1_\lambda} = \boldsymbol{S}(\tilde{\boldsymbol{\lambda}} + \boldsymbol{\lambda})(\tilde{\boldsymbol{\omega}} + \boldsymbol{\omega}) - \boldsymbol{S}(\boldsymbol{\lambda})\boldsymbol{\omega} \tag{8.20b}$$

$$\tilde{\boldsymbol{f}}_{1_\zeta} = \boldsymbol{S}(\tilde{\boldsymbol{\zeta}} + \boldsymbol{\zeta})(\tilde{\boldsymbol{\omega}} + \boldsymbol{\omega}) - \boldsymbol{S}(\boldsymbol{\zeta})\boldsymbol{\omega} \tag{8.20c}$$

$$\tilde{\boldsymbol{f}}_{1_\omega} = \boldsymbol{I}^{-1}\big(\boldsymbol{S}(\boldsymbol{I}\tilde{\boldsymbol{\omega}} + \boldsymbol{I}\boldsymbol{\omega})(\tilde{\boldsymbol{\omega}} + \boldsymbol{\omega}) - \boldsymbol{S}(\boldsymbol{I}\boldsymbol{\omega})\boldsymbol{\omega} + \boldsymbol{M}_v\tilde{\boldsymbol{v}}_{\mathrm{r}} + \boldsymbol{M}_\omega\tilde{\boldsymbol{\omega}}\big) \tag{8.20d}$$

$$\tilde{\boldsymbol{f}}_{2_{v_{\mathrm{r}}}} = \boldsymbol{S}(\tilde{\boldsymbol{v}}_{\mathrm{r}} + \boldsymbol{v}_{\mathrm{r}})(\tilde{\boldsymbol{\omega}} + \boldsymbol{\omega}) - \boldsymbol{S}(\boldsymbol{v}_{\mathrm{r}})\boldsymbol{\omega} + g\tilde{\boldsymbol{\zeta}} + \frac{1}{m}\left(\boldsymbol{F}_v\tilde{\boldsymbol{v}}_{\mathrm{r}} + \boldsymbol{F}_\omega\tilde{\boldsymbol{\omega}}\right) \tag{8.20e}$$

$$\tilde{\boldsymbol{f}}_{2_w} = \boldsymbol{0} \tag{8.20f}$$

The aim of this section is to design the observer gain matrix $\boldsymbol{L}$ such that the first condition in Theorem 8.1 holds, where $\boldsymbol{L}$ is partitioned as

$$\boldsymbol{L}_1 = \mathbf{diag}\left(\boldsymbol{L}_{1_q}, \boldsymbol{L}_{1_\lambda}, \boldsymbol{L}_{1_\zeta}, \boldsymbol{L}_{1_\omega}\right) \tag{8.21a}$$

$$\boldsymbol{L}_2 = \begin{bmatrix} \boldsymbol{L}_{2_{v_r}} \\ \boldsymbol{L}_{2_w} \end{bmatrix} = \begin{bmatrix} \boldsymbol{L}_{2_{v,q}} & \boldsymbol{L}_{2_{v,\lambda}} & \boldsymbol{L}_{2_{v,\zeta}} & \boldsymbol{L}_{2_{v,\omega}} \\ \boldsymbol{L}_{2_{w,q}} & \boldsymbol{L}_{2_{w,\lambda}} & \boldsymbol{L}_{2_{w,\zeta}} & \boldsymbol{L}_{2_{w,\omega}} \end{bmatrix} \tag{8.21b}$$

That is, we find conditions on $\boldsymbol{L}$ such that a given candidate Lyapunov function proves the error dynamics are minimum phase. Considering the output injection term in Eq. (8.10), the zero dynamics of the *augmented system* composed of Eqs. (8.17) and (8.20) is analyzed in view of the input-output pair $\{\mathbf{v}_{\mathrm{p}}, \boldsymbol{y}_{\mathrm{p}}\}$. In general, the *zero dynamics* of the augmented system with respect to $\boldsymbol{y}_{\mathrm{p}}$ exist in some neighborhood $\mathcal{Z} \subseteq \mathbb{R}^n \times \mathbb{R}^n$ about $\tilde{\boldsymbol{x}} = \boldsymbol{0}$ [29] and evolve on

$$\mathcal{Z}^* = \{(\tilde{\boldsymbol{x}}, \boldsymbol{x}) \in \mathcal{Z} \mid \tilde{\boldsymbol{x}}_1 \equiv \boldsymbol{0}\} \tag{8.22}$$

As discussed by Shim *et al.* [132], the zero dynamics can be shown to satisfy

$$\dot{\tilde{\boldsymbol{x}}}_2 = \tilde{\boldsymbol{f}}_2(\boldsymbol{0}, \tilde{\boldsymbol{x}}_2; \boldsymbol{x}_1, \boldsymbol{x}_2; \boldsymbol{u}) - \boldsymbol{L}_2(\boldsymbol{y})\boldsymbol{L}_1^{-1}\tilde{\boldsymbol{f}}_1(\boldsymbol{0}, \tilde{\boldsymbol{x}}_2; \boldsymbol{x}_1, \boldsymbol{x}_2; \boldsymbol{u}) \tag{8.23a}$$

$$\dot{\boldsymbol{x}} = \boldsymbol{f}(\boldsymbol{x}, \boldsymbol{u}) \tag{8.23b}$$

Therefore, we must choose $\boldsymbol{L}$ such that $\tilde{\boldsymbol{x}}_2 = \boldsymbol{0}$ is asymptotically stable on $\mathcal{Z}^*$. Here, we see that the global existence of the zero dynamics only requires $\boldsymbol{L}_1$ to be invertible, a condition that also implies the error dynamics have vector relative degree $\{1, \cdots, 1\}$ [81]. For convenience, denote

$$\tilde{\boldsymbol{\phi}}_2(\tilde{\boldsymbol{x}}_1, \tilde{\boldsymbol{x}}_2; \boldsymbol{x}_1, \boldsymbol{x}_2; \boldsymbol{u}) \coloneqq \tilde{\boldsymbol{f}}_2(\tilde{\boldsymbol{x}}_1, \tilde{\boldsymbol{x}}_2; \boldsymbol{x}_1, \boldsymbol{x}_2; \boldsymbol{u}) - \boldsymbol{L}_2(\boldsymbol{y})\boldsymbol{L}_1^{-1}\tilde{\boldsymbol{f}}_1(\tilde{\boldsymbol{x}}_1, \tilde{\boldsymbol{x}}_2; \boldsymbol{x}_1, \boldsymbol{x}_2; \boldsymbol{u}) \tag{8.24}$$

$$\implies \tilde{\boldsymbol{\phi}}_2^* \coloneqq \tilde{\boldsymbol{\phi}}_2(\boldsymbol{0}, \tilde{\boldsymbol{x}}_2; \boldsymbol{x}_1, \boldsymbol{x}_2; \boldsymbol{u}) \tag{8.25}$$

where $\tilde{\boldsymbol{\phi}}_2^*$ is called the *zero dynamics vector field*. Referring to (8.21), we compute $\tilde{\boldsymbol{\phi}}_{2_{v_\mathrm{r}}}$ and $\tilde{\boldsymbol{\phi}}_{2_w}$ as

$$\begin{aligned}\tilde{\boldsymbol{\phi}}_{2_{v_\mathrm{r}}}(\tilde{\boldsymbol{x}}_1,\tilde{\boldsymbol{x}}_2;\boldsymbol{x}_1,\boldsymbol{x}_2;\boldsymbol{u}) &= \boldsymbol{S}(\tilde{\boldsymbol{v}}_\mathrm{r}+\boldsymbol{v}_\mathrm{r})(\tilde{\boldsymbol{\omega}}+\boldsymbol{\omega}) - \boldsymbol{S}(\boldsymbol{v}_\mathrm{r})\boldsymbol{\omega} + g\tilde{\boldsymbol{\zeta}} + \frac{1}{m}\left(\boldsymbol{F}_v\tilde{\boldsymbol{v}}_\mathrm{r} + \boldsymbol{F}_\omega\tilde{\boldsymbol{\omega}}\right)\\ &\quad - \boldsymbol{L}_{2_{v,q}}\boldsymbol{L}_{1_q}^{-1}\left(\boldsymbol{R}_\mathrm{IB}(\tilde{\boldsymbol{\lambda}}+\boldsymbol{\lambda},\tilde{\boldsymbol{\zeta}}+\boldsymbol{\zeta})(\tilde{\boldsymbol{v}}_\mathrm{r}+\boldsymbol{v}_\mathrm{r}) - \boldsymbol{R}_\mathrm{IB}(\boldsymbol{\lambda},\boldsymbol{\zeta})\boldsymbol{v}_\mathrm{r} + \tilde{\boldsymbol{w}}\right)\\ &\quad - \boldsymbol{L}_{2_{v,\lambda}}\boldsymbol{L}_{1_\lambda}^{-1}\left(\boldsymbol{S}(\tilde{\boldsymbol{\lambda}}+\boldsymbol{\lambda})(\tilde{\boldsymbol{\omega}}+\boldsymbol{\omega}) - \boldsymbol{S}(\boldsymbol{\lambda})\boldsymbol{\omega}\right)\\ &\quad - \boldsymbol{L}_{2_{v,\zeta}}\boldsymbol{L}_{1_\zeta}^{-1}\left(\boldsymbol{S}(\tilde{\boldsymbol{\zeta}}+\boldsymbol{\zeta})(\tilde{\boldsymbol{\omega}}+\boldsymbol{\omega}) - \boldsymbol{S}(\boldsymbol{\zeta})\boldsymbol{\omega}\right)\\ &\quad - \boldsymbol{L}_{2_{v,\omega}}\boldsymbol{L}_{1_\omega}^{-1}\Big(\boldsymbol{I}^{-1}\left(\boldsymbol{S}(\boldsymbol{I}\tilde{\boldsymbol{\omega}}+\boldsymbol{I}\boldsymbol{\omega})(\tilde{\boldsymbol{\omega}}+\boldsymbol{\omega}) - \boldsymbol{S}(\boldsymbol{I}\boldsymbol{\omega})\boldsymbol{\omega} + \boldsymbol{M}_v\tilde{\boldsymbol{v}}_\mathrm{r} + \boldsymbol{M}_\omega\tilde{\boldsymbol{\omega}}\right)\Big)\end{aligned} \tag{8.26a}$$

$$\begin{aligned}\tilde{\boldsymbol{\phi}}_{2_w}(\tilde{\boldsymbol{x}}_1,\tilde{\boldsymbol{x}}_2;\boldsymbol{x}_1,\boldsymbol{x}_2;\boldsymbol{u}) &= -\boldsymbol{L}_{2_{w,q}}\boldsymbol{L}_{1_q}^{-1}\left(\boldsymbol{R}_\mathrm{IB}(\tilde{\boldsymbol{\lambda}}+\boldsymbol{\lambda},\tilde{\boldsymbol{\zeta}}+\boldsymbol{\zeta})(\tilde{\boldsymbol{v}}_\mathrm{r}+\boldsymbol{v}_\mathrm{r}) - \boldsymbol{R}_\mathrm{IB}(\boldsymbol{\lambda},\boldsymbol{\zeta})\boldsymbol{v}_\mathrm{r} + \tilde{\boldsymbol{w}}\right)\\ &\quad - \boldsymbol{L}_{2_{w,\lambda}}\boldsymbol{L}_{1_\lambda}^{-1}\left(\boldsymbol{S}(\tilde{\boldsymbol{\lambda}}+\boldsymbol{\lambda})(\tilde{\boldsymbol{\omega}}+\boldsymbol{\omega}) - \boldsymbol{S}(\boldsymbol{\lambda})\boldsymbol{\omega}\right)\\ &\quad - \boldsymbol{L}_{2_{w,\zeta}}\boldsymbol{L}_{1_\zeta}^{-1}\left(\boldsymbol{S}(\tilde{\boldsymbol{\zeta}}+\boldsymbol{\zeta})(\tilde{\boldsymbol{\omega}}+\boldsymbol{\omega}) - \boldsymbol{S}(\boldsymbol{\zeta})\boldsymbol{\omega}\right)\\ &\quad - \boldsymbol{L}_{2_{w,\omega}}\boldsymbol{L}_{1_\omega}^{-1}\Big(\boldsymbol{I}^{-1}\left(\boldsymbol{S}(\boldsymbol{I}\tilde{\boldsymbol{\omega}}+\boldsymbol{I}\boldsymbol{\omega})(\tilde{\boldsymbol{\omega}}+\boldsymbol{\omega}) - \boldsymbol{S}(\boldsymbol{I}\boldsymbol{\omega})\boldsymbol{\omega} + \boldsymbol{M}_v\tilde{\boldsymbol{v}}_\mathrm{r} + \boldsymbol{M}_\omega\tilde{\boldsymbol{\omega}}\right)\Big)\end{aligned} \tag{8.26b}$$

The zero dynamics are obtained by simply evaluating Eq. (8.26) at $\boldsymbol{y}_\mathrm{p} = \tilde{\boldsymbol{x}}_1 = \boldsymbol{0}$. They evolve according to

$$\tilde{\boldsymbol{\phi}}_{2_{v_\mathrm{r}}}^* = -\boldsymbol{S}(\boldsymbol{\omega})\tilde{\boldsymbol{v}}_\mathrm{r} + \frac{1}{m}\boldsymbol{F}_v\tilde{\boldsymbol{v}}_\mathrm{r} - \boldsymbol{L}_{2_{v,\omega}}\boldsymbol{L}_{1_\omega}^{-1}\boldsymbol{I}^{-1}\boldsymbol{M}_v\tilde{\boldsymbol{v}}_\mathrm{r} - \boldsymbol{L}_{2_{v,q}}\boldsymbol{L}_{1_q}^{-1}\left(\boldsymbol{R}_\mathrm{IB}(\boldsymbol{\lambda},\boldsymbol{\zeta})\tilde{\boldsymbol{v}}_\mathrm{r} + \tilde{\boldsymbol{w}}\right) \tag{8.27a}$$

$$\tilde{\boldsymbol{\phi}}_{2_w}^* = -\boldsymbol{L}_{2_{w,q}}\boldsymbol{L}_{1_q}^{-1}\left(\boldsymbol{R}_\mathrm{IB}(\boldsymbol{\lambda},\boldsymbol{\zeta})\tilde{\boldsymbol{v}}_\mathrm{r} + \tilde{\boldsymbol{w}}\right) - \boldsymbol{L}_{2_{w,\omega}}\boldsymbol{L}_{1_\omega}^{-1}\boldsymbol{I}^{-1}\boldsymbol{M}_v\tilde{\boldsymbol{v}}_\mathrm{r} \tag{8.27b}$$

Remark 8.2. *The zero dynamics (8.27) are very similar to the invariant error dynamics (7.17.I) for the symmetry-preserving reduced-order wind observer. In fact, the design of a passivity-based observer also yields a reduced-order observer. A similar result was obtained by Venkatraman and van der Schaft [151] for a special class of port-Hamiltonian systems.*

Consider the zero-error set $\mathcal{M}$ defined in Eq. (8.7). We aim to find a proper Lyapunov function $V^*(\tilde{\boldsymbol{x}}_2,\boldsymbol{x})$ that proves $\mathcal{M}^*$ is positively invariant and globally asymptotically attractive on $\mathcal{Z}^*$. That is, we seek V^* such that

$$\psi_1(\|\tilde{\boldsymbol{x}}_2\|) \leq V^*(\tilde{\boldsymbol{x}}_2,\boldsymbol{x}) \leq \psi_2(\|\tilde{\boldsymbol{x}}_2\|) \tag{8.28}$$

$$\dot{V}^* = \frac{\partial V^*}{\partial \tilde{\boldsymbol{x}}_2}\tilde{\boldsymbol{\phi}}_2^* + \frac{\partial V^*}{\partial \boldsymbol{x}}\boldsymbol{f} \leq -\varphi^*(\|\tilde{\boldsymbol{x}}_2\|) \tag{8.29}$$

where ψ_1,ψ_2 are class $\mathcal{K}_\infty$ functions and φ^* is a smooth, positive definite function. Note that V^* does not necessarily depend on $\boldsymbol{x}$, but allowing it to do so may admit observer designs for

a wider class of systems [132]. As a consequence of Assumption 8.1, we need only consider the candidate Lyapunov function

$$V^*(\tilde{\boldsymbol{x}}_2, \boldsymbol{x}) = \frac{1}{2}\tilde{\boldsymbol{x}}_2^\mathsf{T}\tilde{\boldsymbol{x}}_2 \tag{8.30}$$

which satisfies Eq. (8.28). It follows that

$$\begin{aligned}\dot{V}^* = &-\tilde{\boldsymbol{v}}_\mathrm{r}^\mathsf{T}\boldsymbol{S}(\boldsymbol{\omega})\tilde{\boldsymbol{v}}_\mathrm{r} + \tilde{\boldsymbol{v}}_\mathrm{r}^\mathsf{T}\frac{1}{m}\boldsymbol{F}_v\tilde{\boldsymbol{v}}_\mathrm{r} - \tilde{\boldsymbol{v}}_\mathrm{r}^\mathsf{T}\boldsymbol{L}_{2_{v,q}}\boldsymbol{L}_{1_q}^{-1}\tilde{\boldsymbol{w}} - \tilde{\boldsymbol{v}}_\mathrm{r}^\mathsf{T}\boldsymbol{L}_{2_{v,q}}\boldsymbol{L}_{1_q}^{-1}\boldsymbol{R}_\mathrm{IB}\tilde{\boldsymbol{v}}_\mathrm{r} - \tilde{\boldsymbol{v}}_\mathrm{r}^\mathsf{T}\boldsymbol{L}_{2_{v,\omega}}\boldsymbol{L}_{1_\omega}^{-1}\boldsymbol{I}^{-1}\boldsymbol{M}_v\tilde{\boldsymbol{v}}_\mathrm{r} \\ &- \tilde{\boldsymbol{w}}^\mathsf{T}\boldsymbol{L}_{2_{w,q}}\boldsymbol{L}_{1_q}^{-1}\boldsymbol{R}_\mathrm{IB}\tilde{\boldsymbol{v}}_\mathrm{r} - \tilde{\boldsymbol{w}}^\mathsf{T}\boldsymbol{L}_{2_{w,q}}\boldsymbol{L}_{1_q}^{-1}\tilde{\boldsymbol{w}} - \tilde{\boldsymbol{w}}^\mathsf{T}\boldsymbol{L}_{2_{w,\omega}}\boldsymbol{L}_{1_\omega}^{-1}\boldsymbol{I}^{-1}\boldsymbol{M}_v\tilde{\boldsymbol{v}}_\mathrm{r}\end{aligned} \tag{8.31}$$

Here we have dropped the argument to $\boldsymbol{R}_\mathrm{IB}$ for compactness. Henceforth, it is implied that $\boldsymbol{R}_\mathrm{IB} = \boldsymbol{R}_\mathrm{IB}(\boldsymbol{\lambda}, \boldsymbol{\zeta})$ unless explicitly stated. Notice the term $\tilde{\boldsymbol{v}}_\mathrm{r}^\mathsf{T}\boldsymbol{S}(\boldsymbol{\omega})\tilde{\boldsymbol{v}}_\mathrm{r}$ is identically equal to zero since the quadratic form of a skew-symmetric matrix is zero. We may then write Eq. (8.31) as

$$\dot{V}^* = -\tilde{\boldsymbol{x}}_2^\mathsf{T}\boldsymbol{P}\tilde{\boldsymbol{x}}_2 \tag{8.32}$$

where

$$\boldsymbol{P}_{11} = -\frac{1}{m}\boldsymbol{F}_v + \boldsymbol{L}_{2_{v,q}}\boldsymbol{L}_{1_q}^{-1}\boldsymbol{R}_\mathrm{IB} + \boldsymbol{L}_{2_{v,\omega}}\boldsymbol{L}_{1_\omega}^{-1}\boldsymbol{I}^{-1}\boldsymbol{M}_v \tag{8.33a}$$

$$\boldsymbol{P}_{12} = \boldsymbol{L}_{2_{v,q}}\boldsymbol{L}_{1_q}^{-1} \tag{8.33b}$$

$$\boldsymbol{P}_{21} = \boldsymbol{L}_{2_{w,q}}\boldsymbol{L}_{1_q}^{-1}\boldsymbol{R}_\mathrm{IB} + \boldsymbol{L}_{2_{w,\omega}}\boldsymbol{L}_{1_\omega}^{-1}\boldsymbol{I}^{-1}\boldsymbol{M}_v \tag{8.33c}$$

$$\boldsymbol{P}_{22} = \boldsymbol{L}_{2_{w,q}}\boldsymbol{L}_{1_q}^{-1} \tag{8.33d}$$

Therefore, we must choose the gain matrix $\boldsymbol{L}$ such that

$$\begin{bmatrix}\boldsymbol{Q}_{11} & \boldsymbol{Q}_{12} \\ \boldsymbol{Q}_{12}^\mathsf{T} & \boldsymbol{Q}_{22}\end{bmatrix} \coloneqq \boldsymbol{Q} \coloneqq \frac{1}{2}\left(\boldsymbol{P} + \boldsymbol{P}^\mathsf{T}\right) \succ \boldsymbol{0} \tag{8.34}$$

where

$$\begin{aligned}\boldsymbol{Q}_{11} &= \frac{1}{2}\Big(-\frac{1}{m}(\boldsymbol{F}_v + \boldsymbol{F}_v^\mathsf{T}) + \boldsymbol{L}_{2_{v,q}}\boldsymbol{L}_{1_q}^{-1}\boldsymbol{R}_\mathrm{IB} + \boldsymbol{R}_\mathrm{IB}^\mathsf{T}\boldsymbol{L}_{1_q}^{-\mathsf{T}}\boldsymbol{L}_{2_{v,q}}^\mathsf{T} \\ &\qquad + \boldsymbol{L}_{2_{v,\omega}}\boldsymbol{L}_{1_\omega}^{-1}\boldsymbol{I}^{-1}\boldsymbol{M}_v + \boldsymbol{M}_v^\mathsf{T}\boldsymbol{I}^{-1}\boldsymbol{L}_{1_\omega}^{-\mathsf{T}}\boldsymbol{L}_{2_{v,\omega}}^\mathsf{T}\Big) \\ \boldsymbol{Q}_{12} &= \frac{1}{2}\left(\boldsymbol{L}_{2_{v,q}}\boldsymbol{L}_{1_q}^{-1} + \boldsymbol{R}_\mathrm{IB}^\mathsf{T}\boldsymbol{L}_{1_q}^{-\mathsf{T}}\boldsymbol{L}_{2_{w,q}}^\mathsf{T} + \boldsymbol{M}_v^\mathsf{T}\boldsymbol{I}^{-1}\boldsymbol{L}_{1_\omega}^{-\mathsf{T}}\boldsymbol{L}_{2_{w,\omega}}^\mathsf{T}\right) \\ \boldsymbol{Q}_{22} &= \frac{1}{2}\left(\boldsymbol{L}_{2_{w,q}}\boldsymbol{L}_{1_q}^{-1} + \boldsymbol{L}_{1_q}^{-\mathsf{T}}\boldsymbol{L}_{2_{w,q}}^\mathsf{T}\right)\end{aligned}$$

Therefore, choosing $\boldsymbol{L}$ such that $\boldsymbol{Q} \succ \boldsymbol{0}$ is sufficient for proving $\dot{V}^*$ is negative definite. Let

$$\boldsymbol{L}_{2_{v,q}} = \boldsymbol{\Gamma}_{v,q}\boldsymbol{R}_\mathrm{IB}^\mathsf{T}\boldsymbol{L}_{1_q} \tag{8.35a}$$

$$\boldsymbol{L}_{2_{v,\omega}} = \boldsymbol{\Gamma}_{v,\omega}\boldsymbol{M}_v^\mathsf{T}\boldsymbol{I}\boldsymbol{L}_{1_\omega} \tag{8.35b}$$

$$\boldsymbol{L}_{2_{w,q}} = \boldsymbol{R}_\mathrm{IB}\boldsymbol{\Gamma}_{w,q}\boldsymbol{R}_\mathrm{IB}^\mathsf{T}\boldsymbol{L}_{1_q} \tag{8.35c}$$

$$\boldsymbol{L}_{2_{w,\omega}} = \boldsymbol{R}_\mathrm{IB}\boldsymbol{\Gamma}_{w,\omega}\boldsymbol{M}_v^\mathsf{T}\boldsymbol{I}\boldsymbol{L}_{1_\omega} \tag{8.35d}$$

where the matrix

$$\boldsymbol{\Gamma} = \begin{bmatrix} \boldsymbol{\Gamma}_{v,q} & \boldsymbol{\Gamma}_{v,\omega} \\ \boldsymbol{\Gamma}_{w,q} & \boldsymbol{\Gamma}_{w,\omega} \end{bmatrix} \tag{8.36}$$

is a constant parameter used for tuning. Notice we have chosen $\boldsymbol{L}_2$ to make the design of $\boldsymbol{L}_1$ independent of the tuning of the zero dynamics. The matrix $\boldsymbol{Q}$ reduces to

$$\boldsymbol{Q}_{11} = -\frac{1}{2m}\left(\boldsymbol{F}_v + \boldsymbol{F}_v^\mathsf{T}\right) + \frac{1}{2}\left(\boldsymbol{\Gamma}_{v,q} + \boldsymbol{\Gamma}_{v,q}^\mathsf{T}\right) + \frac{1}{2}\left(\boldsymbol{\Gamma}_{v,\omega}\boldsymbol{M}_v^\mathsf{T}\boldsymbol{M}_v + \boldsymbol{M}_v^\mathsf{T}\boldsymbol{M}_v\boldsymbol{\Gamma}_{v,\omega}^\mathsf{T}\right) \tag{8.37a}$$

$$\boldsymbol{Q}_{12} = \frac{1}{2}\left(\boldsymbol{\Gamma}_{v,q} + \boldsymbol{\Gamma}_{w,q}^\mathsf{T} + \boldsymbol{M}_v^\mathsf{T}\boldsymbol{M}_v\boldsymbol{\Gamma}_{w,\omega}^\mathsf{T}\right)\boldsymbol{R}_{\mathrm{IB}}^\mathsf{T} \tag{8.37b}$$

$$\boldsymbol{Q}_{22} = \frac{1}{2}\boldsymbol{R}_{\mathrm{IB}}\left(\boldsymbol{\Gamma}_{w,q} + \boldsymbol{\Gamma}_{w,q}^\mathsf{T}\right)\boldsymbol{R}_{\mathrm{IB}}^\mathsf{T} \tag{8.37c}$$

The rotation matrix, $\boldsymbol{R}_{\mathrm{IB}}$, does not influence the definiteness of $\boldsymbol{Q}$. This can be seen using the Schur complement lemma, stating that $\boldsymbol{Q} \succ \boldsymbol{0}$ if and only if

$$\boldsymbol{\Gamma}_{w,q} + \boldsymbol{\Gamma}_{w,q}^\mathsf{T} \succ \boldsymbol{0} \tag{8.38a}$$

$$\boldsymbol{Q}_{11} - \boldsymbol{Q}_{12}\boldsymbol{Q}_{22}^{-1}\boldsymbol{Q}_{12}^\mathsf{T} \succ \boldsymbol{0} \tag{8.38b}$$

Therefore, we may choose $\boldsymbol{\Gamma}$ such that

$$\begin{bmatrix} -\frac{1}{m}\boldsymbol{F}_v + \boldsymbol{\Gamma}_{v,q} + \boldsymbol{\Gamma}_{v,\omega}\boldsymbol{M}_v^\mathsf{T}\boldsymbol{M}_v & \boldsymbol{\Gamma}_{v,q} \\ \boldsymbol{\Gamma}_{w,q} + \boldsymbol{\Gamma}_{w,\omega}\boldsymbol{M}_v^\mathsf{T}\boldsymbol{M}_v & \boldsymbol{\Gamma}_{w,q} \end{bmatrix} + \begin{bmatrix} -\frac{1}{m}\boldsymbol{F}_v + \boldsymbol{\Gamma}_{v,q} + \boldsymbol{\Gamma}_{v,\omega}\boldsymbol{M}_v^\mathsf{T}\boldsymbol{M}_v & \boldsymbol{\Gamma}_{v,q} \\ \boldsymbol{\Gamma}_{w,q} + \boldsymbol{\Gamma}_{w,\omega}\boldsymbol{M}_v^\mathsf{T}\boldsymbol{M}_v & \boldsymbol{\Gamma}_{w,q} \end{bmatrix}^\mathsf{T} \succ \boldsymbol{0} \tag{8.39}$$

This condition may be stated as the linear matrix inequality (LMI)

$$\boldsymbol{\Gamma}\mathcal{A} + \mathcal{A}^\mathsf{T}\boldsymbol{\Gamma}^\mathsf{T} + \mathcal{Q} \succ \boldsymbol{0} \tag{8.40}$$

where

$$\mathcal{A} = \begin{bmatrix} \mathbb{I} & \mathbb{I} \\ \boldsymbol{M}_v^\mathsf{T}\boldsymbol{M}_v & \boldsymbol{0} \end{bmatrix} \qquad \text{and} \qquad \mathcal{Q} = \begin{bmatrix} -\frac{1}{m}(\boldsymbol{F}_v + \boldsymbol{F}_v^\mathsf{T}) & \boldsymbol{0} \\ \boldsymbol{0} & \boldsymbol{0} \end{bmatrix}$$

Since $\dot{V}^* = -\tilde{\boldsymbol{x}}_2^\mathsf{T}\boldsymbol{Q}\tilde{\boldsymbol{x}}_2$, we choose to lower bound the smallest eigenvalue of $\boldsymbol{Q}$, denoted $\lambda_{\min}(\boldsymbol{Q})$, by some positive constant $\underline{\gamma}$. This constant lower bounds the convergence rate of the zero dynamics. Similarly, we can ensure the observer gain is not arbitrarily large by setting an upper bound, $\overline{\gamma}$, on the largest eigenvalue of $\boldsymbol{Q}$, denoted $\lambda_{\max}(\boldsymbol{Q})$. This is important for ensuring the numerical integration of the observer is well-conditioned. Therefore, we incorporate the additional convex constraints

$$\lambda_{\min}(\bar{\boldsymbol{Q}}) \geq \underline{\gamma} \tag{8.41a}$$

$$\lambda_{\max}(\bar{\boldsymbol{Q}}) \leq \overline{\gamma} \tag{8.41b}$$

where $\bar{\boldsymbol{Q}} \coloneqq \boldsymbol{Q}|_{\boldsymbol{R}_{\mathrm{IB}}=\mathbb{I}}$ is a constant, symmetric matrix. Hence, for some given $\underline{\gamma}$ and $\overline{\gamma}$, we have the convex feasibility problem

$$\text{Find } \boldsymbol{\Gamma} \qquad \text{such that} \qquad \begin{array}{l} \boldsymbol{\Gamma}\mathcal{A} + \mathcal{A}^\mathsf{T}\boldsymbol{\Gamma}^\mathsf{T} + \mathcal{Q} \succ \boldsymbol{0} \\ \boldsymbol{\Gamma}_{w,q} + \boldsymbol{\Gamma}_{w,q}^\mathsf{T} \succ \boldsymbol{0} \\ \lambda_{\min}(\bar{\boldsymbol{Q}}) \geq \underline{\gamma} \\ \lambda_{\max}(\bar{\boldsymbol{Q}}) \leq \overline{\gamma} \end{array} \tag{8.42}$$

It may be desirable to further constrain the set of solutions to (8.42). In some cases, the norm of $\boldsymbol{\Gamma}$ can still be quite large despite the addition of the bound $\overline{\gamma}$. Accordingly, an additional upper bound can be placed on the norm of $\boldsymbol{\Gamma}$. This approach may also be used for the case where one chooses to "gain-schedule" $\boldsymbol{\Gamma}$ based on the current flight condition. This can be done in principle as long as $\boldsymbol{F}_v$, $\boldsymbol{F}_\omega$, $\boldsymbol{M}_v$, and $\boldsymbol{M}_\omega$ vary sufficiently slowly.

If $\underline{\gamma}$ is upper bounded for the aerodynamic model of interest, (8.42) can be optimally solved by maximizing $\underline{\gamma}$ for some given $\overline{\gamma}$ greater then the maximal $\underline{\gamma}$. As seen in Eq. (8.37), the upper bound on the zero dynamics convergence rate then directly depends on the aircraft mass, $\boldsymbol{F}_v$, and $\boldsymbol{M}_v$. In other words, the dissipation rate of relative velocity and wind observation error is dependent on the aircraft's physical dissipation due to drag. Practically, this means there may be an upper limit on the time scale of wind fluctuations that can be accurately resolved. Conversely, if $\overline{\gamma}$ is lower bounded for some given $\underline{\gamma}$ less than the minimal $\overline{\gamma}$, then it may be minimized to ensure $\boldsymbol{Q}$ is well-conditioned.

While we have arrived at Eq. (8.40) assuming perfect knowledge of m, $\boldsymbol{F}_v$, and $\boldsymbol{M}_v$, we may want to prescribe a solution that is more robust to uncertainty or changes in these parameters. Suppose the matrices $\mathcal{A}$, $\mathcal{Q}$, and $\bar{\boldsymbol{Q}}$ are polytopic uncertain with

$$\left\{\mathcal{A},\ \mathcal{Q},\ \bar{\boldsymbol{Q}}\right\} \in \mathbb{P} \coloneqq \sum_{i=1}^{N} \alpha_i \left\{\mathcal{A}_i,\ \mathcal{Q}_i,\ \bar{\boldsymbol{Q}}_i\right\}, \quad \sum_{i=1}^{N} \alpha_i = 1 \tag{8.43}$$

Then, we may choose $\boldsymbol{\Gamma}$ as a solution to the following problem:

$$\text{Find } \boldsymbol{\Gamma} \quad \text{such that} \quad \begin{array}{l} \boldsymbol{\Gamma}\mathcal{A}_i + \mathcal{A}_i^{\mathsf{T}}\boldsymbol{\Gamma}^{\mathsf{T}} + \mathcal{Q}_i \succ \boldsymbol{0} \\ \boldsymbol{\Gamma}_{w,q} + \boldsymbol{\Gamma}_{w,q}^{\mathsf{T}} \succ \boldsymbol{0} \\ \lambda_{\min}(\bar{\boldsymbol{Q}}_i) \geq \underline{\gamma} \\ \lambda_{\max}(\bar{\boldsymbol{Q}}_i) \leq \overline{\gamma} \end{array} \quad \text{for } i = 1, \cdots, N \tag{8.44}$$

With $\boldsymbol{\Gamma}$ chosen such that (8.42) or (8.44) are solved, we see that

$$\dot{V}^* = -\tilde{\boldsymbol{x}}_2^{\mathsf{T}}\boldsymbol{Q}\tilde{\boldsymbol{x}}_2 \leq -\underline{\gamma}\|\tilde{\boldsymbol{x}}_2\|^2 =: -\varphi^*(\|\tilde{\boldsymbol{x}}_2\|) \tag{8.45}$$

proving the error system is globally minimum phase with respect to $\boldsymbol{y}_{\mathrm{p}} = \hat{\boldsymbol{y}} - \boldsymbol{y}$.

8.5 Bounding Functions and Strict Passivity

Having proven that the augmented system is minimum phase, we follow the second step by Shim *et al.* [132] and consider the change of coordinates

$$\boldsymbol{\xi}_1 = \tilde{\boldsymbol{x}}_1 \tag{8.46a}$$

$$\boldsymbol{\xi}_2 = \tilde{\boldsymbol{x}}_2 - \boldsymbol{L}_2(\boldsymbol{y})\boldsymbol{L}_1^{-1}\tilde{\boldsymbol{x}}_1 \tag{8.46b}$$

Specifically, the components of $\boldsymbol{\xi}_2$ for the aircraft in wind are

$$\boldsymbol{\xi}_{2_{v_\mathrm{r}}} = \tilde{\boldsymbol{v}}_\mathrm{r} - \boldsymbol{\Gamma}_{v,q}\boldsymbol{R}_\mathrm{IB}^\mathsf{T}\tilde{\boldsymbol{q}} - \boldsymbol{\Gamma}_{v,\omega}\boldsymbol{M}_v^\mathsf{T}\boldsymbol{I}\tilde{\boldsymbol{\omega}} \tag{8.47a}$$

$$\boldsymbol{\xi}_{2_w} = \tilde{\boldsymbol{w}} - \boldsymbol{R}_\mathrm{IB}\boldsymbol{\Gamma}_{w,q}\boldsymbol{R}_\mathrm{IB}^\mathsf{T}\tilde{\boldsymbol{q}} - \boldsymbol{R}_\mathrm{IB}\boldsymbol{\Gamma}_{w,\omega}\boldsymbol{M}_v^\mathsf{T}\boldsymbol{I}\tilde{\boldsymbol{\omega}} \tag{8.47b}$$

It follows that

$$\dot{\boldsymbol{\xi}}_2 = \tilde{\boldsymbol{\phi}}_2(\boldsymbol{\xi}_1, \boldsymbol{\xi}_2 + \boldsymbol{L}_2\boldsymbol{L}_1^{-1}\boldsymbol{\xi}_1; \boldsymbol{x}_1, \boldsymbol{x}_2; \boldsymbol{u}) - \frac{\mathrm{d}}{\mathrm{d}t}\left(\boldsymbol{L}_2(\boldsymbol{y})\boldsymbol{L}_1^{-1}\right)\tilde{\boldsymbol{x}}_1 \tag{8.48}$$

The only difference here from the results by Shim *et al.* [132] is the second term. We will see shortly that its effect can be incorporated into our choice of gain function, $\boldsymbol{K}$. Consider the storage function

$$W(\boldsymbol{\xi}, \boldsymbol{x}) = V^*(\boldsymbol{\xi}_2, \boldsymbol{x}) + \frac{1}{2}\boldsymbol{\xi}_1^\mathsf{T}\boldsymbol{L}_1^{-1}\boldsymbol{\xi}_1 \tag{8.49}$$

It can be shown the time derivative of W satisfies

$$\begin{aligned}\dot{W} = {} & \frac{\partial V^*}{\partial \boldsymbol{x}}\boldsymbol{f}(\boldsymbol{x}, \boldsymbol{u}) + \frac{\partial V^*}{\partial \boldsymbol{\xi}_2}\tilde{\boldsymbol{\phi}}_2^*(\boldsymbol{\xi}_2, \boldsymbol{x}, \boldsymbol{u}) + \frac{\partial V^*}{\partial \boldsymbol{\xi}_2}\tilde{\boldsymbol{\phi}}_2(\boldsymbol{\xi}_1, \boldsymbol{L}_2\boldsymbol{L}_1^{-1}\boldsymbol{\xi}_1; \boldsymbol{x}_1, \boldsymbol{x}_2; \boldsymbol{u}) \\ & + \boldsymbol{\xi}_1^\mathsf{T}\boldsymbol{L}_1^{-1}\tilde{\boldsymbol{f}}_1(\tilde{\boldsymbol{x}}_1, \tilde{\boldsymbol{x}}_2 + \boldsymbol{L}_2\boldsymbol{L}_1^{-1}\tilde{\boldsymbol{x}}_1; \boldsymbol{x}_1, \hat{\boldsymbol{x}}_2 - \tilde{\boldsymbol{x}}_2; \boldsymbol{u}) + \frac{\partial V^*}{\partial \boldsymbol{\xi}_2}\frac{\mathrm{d}}{\mathrm{d}t}\left(\boldsymbol{L}_2(\boldsymbol{y})\boldsymbol{L}_1^{-1}\right)\boldsymbol{\xi}_1 + \boldsymbol{\xi}_1^\mathsf{T}\mathbf{v}\end{aligned} \tag{8.50}$$

where the term $\frac{\mathrm{d}}{\mathrm{d}t}\left(\boldsymbol{L}_2(\boldsymbol{y})\boldsymbol{L}_1^{-1}\right)$ for the aircraft in wind is

$$\frac{\mathrm{d}}{\mathrm{d}t}\left(\boldsymbol{L}_2(\boldsymbol{y})\boldsymbol{L}_1^{-1}\right) = \begin{bmatrix} -\boldsymbol{\Gamma}_{v,q}\boldsymbol{S}(\boldsymbol{\omega})\boldsymbol{R}_\mathrm{IB}^\mathsf{T} & \mathbf{0} & \mathbf{0} & \mathbf{0} \\ \boldsymbol{R}_\mathrm{IB}\left(\boldsymbol{S}(\boldsymbol{\omega})\boldsymbol{\Gamma}_{w,q} - \boldsymbol{\Gamma}_{w,q}\boldsymbol{S}(\boldsymbol{\omega})\right)\boldsymbol{R}_\mathrm{IB}^\mathsf{T} & \mathbf{0} & \mathbf{0} & \boldsymbol{R}_\mathrm{IB}\boldsymbol{S}(\boldsymbol{\omega})\boldsymbol{\Gamma}_{w,\omega}\boldsymbol{M}_v^\mathsf{T}\boldsymbol{I} \end{bmatrix} \tag{8.51}$$

Then by Eq. (8.45), we have

$$\begin{aligned}\dot{W} \leq {} & -\varphi^*(\|\boldsymbol{\xi}_2\|) + \frac{\partial V^*}{\partial \boldsymbol{\xi}_2}\tilde{\boldsymbol{\phi}}_2(\boldsymbol{\xi}_1, \boldsymbol{L}_2(\boldsymbol{y})\boldsymbol{L}_1^{-1}\boldsymbol{\xi}_1; \boldsymbol{x}_1, \boldsymbol{\xi}_2 + \boldsymbol{x}_2; \boldsymbol{u}) \\ & + \boldsymbol{\xi}_1^\mathsf{T}\boldsymbol{L}_1^{-1}\tilde{\boldsymbol{f}}_1(\boldsymbol{\xi}_1, \boldsymbol{\xi}_2 + \boldsymbol{L}_2(\boldsymbol{y})\boldsymbol{L}_1^{-1}\boldsymbol{\xi}_1; \boldsymbol{x}_1, \boldsymbol{x}_2; \boldsymbol{u}) - \frac{\partial V^*}{\partial \boldsymbol{\xi}_2}\frac{\mathrm{d}}{\mathrm{d}t}\left(\boldsymbol{L}_2(\boldsymbol{y})\boldsymbol{L}_1^{-1}\right)\boldsymbol{\xi}_1 + \boldsymbol{\xi}_1^\mathsf{T}\mathbf{v}\end{aligned} \tag{8.52}$$

Here we see the feedback $\mathbf{v}$ can be chosen to render the augmented dynamics strictly passive. Specifically, consider the following result.

Proposition 8.1. *There exist a symmetric matrix function* $\boldsymbol{\Psi} : \mathbb{R}^p \times \mathbb{R}^{n-p} \times \mathbb{R}^p \times \mathcal{U} \to \mathbb{R}^{p\times p}$ *and a matrix function* $\boldsymbol{\Lambda} : \mathbb{R}^p \times \mathbb{R}^{n-p} \times \mathbb{R}^p \times \mathcal{U} \to \mathbb{R}^{(n-p)\times p}$ *such that*

$$\begin{aligned}& \frac{\partial V^*}{\partial \boldsymbol{\xi}_2}\tilde{\boldsymbol{\phi}}_2(\boldsymbol{\xi}_1, \boldsymbol{L}_2(\boldsymbol{y})\boldsymbol{L}_1^{-1}\boldsymbol{\xi}_1; \boldsymbol{x}_1, \boldsymbol{\xi}_2 + \boldsymbol{x}_2; \boldsymbol{u}) + \boldsymbol{\xi}_1^\mathsf{T}\boldsymbol{L}_1^{-1}\tilde{\boldsymbol{f}}_1(\boldsymbol{\xi}_1, \boldsymbol{\xi}_2 + \boldsymbol{L}_2(\boldsymbol{y})\boldsymbol{L}_1^{-1}\boldsymbol{\xi}_1; \boldsymbol{x}_1, \boldsymbol{x}_2; \boldsymbol{u}) \\ & - \frac{\partial V^*}{\partial \boldsymbol{\xi}_2}\frac{\mathrm{d}}{\mathrm{d}t}\left(\boldsymbol{L}_2(\boldsymbol{y})\boldsymbol{L}_1^{-1}\right)\boldsymbol{\xi}_1 \leq \sqrt{\varphi^*(\|\boldsymbol{\xi}_2\|)}\|\boldsymbol{\Lambda}(\boldsymbol{\xi}_1, \boldsymbol{\xi}_2 + \boldsymbol{x}_2, \boldsymbol{x}_1, \boldsymbol{u})\boldsymbol{\xi}_1\| + \boldsymbol{\xi}_1^\mathsf{T}\boldsymbol{\Psi}(\boldsymbol{\xi}_1, \boldsymbol{\xi}_2 + \boldsymbol{x}_2, \boldsymbol{x}_1, \boldsymbol{u})\boldsymbol{\xi}_1\end{aligned} \tag{8.53}$$

Proof. The proof of Proposition 8.1 is given in Appendix B. □

Using Proposition 8.1, we write Eq. (8.52) as

$$\dot{W} \leq -\varphi^*(\|\boldsymbol{\xi}_2\|) + \sqrt{\varphi^*(\|\boldsymbol{\xi}_2\|)}\|\boldsymbol{\Lambda}(\boldsymbol{\xi}_1, \boldsymbol{\xi}_2 + \boldsymbol{x}_2, \boldsymbol{x}_1, \boldsymbol{u})\boldsymbol{\xi}_1\| + \boldsymbol{\xi}_1^\mathsf{T}\boldsymbol{\Psi}(\boldsymbol{\xi}_1, \boldsymbol{\xi}_2 + \boldsymbol{x}_2, \boldsymbol{x}_1, \boldsymbol{u})\boldsymbol{\xi}_1 + \boldsymbol{\xi}_1^\mathsf{T}\mathbf{v} \tag{8.54}$$

Consider the feedback law

$$\mathbf{v} = -\boldsymbol{K}(\hat{\boldsymbol{x}}, \boldsymbol{y})\boldsymbol{y}_\mathrm{p} + \mathbf{v}_\mathrm{p} \tag{8.55}$$

where

$$\boldsymbol{K}(\hat{\boldsymbol{x}}, \boldsymbol{y}, \boldsymbol{u}) = \varepsilon\mathbb{I} + \left[\boldsymbol{\Psi} + \boldsymbol{\Lambda}^\mathsf{T}\boldsymbol{\Lambda}\right]\left(\hat{\boldsymbol{x}}_1 - \boldsymbol{y}, \hat{\boldsymbol{x}}_2 - \boldsymbol{L}_2(\boldsymbol{y})\boldsymbol{L}_1^{-1}(\hat{\boldsymbol{x}}_1 - \boldsymbol{y}), \boldsymbol{y}, \boldsymbol{u}\right) \tag{8.56}$$

for any $\varepsilon > 0$. Here, parentheses contain arguments for all functions in square brackets. Substituting this feedback law under the coordinate transformation into Eq. (8.54), we obtain

$$\begin{aligned}\dot{W} \leq\ & \boldsymbol{y}_\mathrm{p}^\mathsf{T}\mathbf{v}_\mathrm{p} - \varphi^*(\|\boldsymbol{\xi}_2\|) + \sqrt{\varphi^*(\|\boldsymbol{\xi}_2\|)}\|\boldsymbol{\Lambda}(\boldsymbol{\xi}_1, \boldsymbol{\xi}_2 + \boldsymbol{x}_2, \boldsymbol{x}_1, \boldsymbol{u})\boldsymbol{\xi}_1\| \\ & + \boldsymbol{\xi}_1^\mathsf{T}\boldsymbol{\Psi}(\boldsymbol{\xi}_1, \boldsymbol{\xi}_2 + \boldsymbol{x}_2, \boldsymbol{x}_1, \boldsymbol{u})\boldsymbol{\xi}_1 - \boldsymbol{\xi}_1^\mathsf{T}\left(\varepsilon\mathbb{I} + \left[\boldsymbol{\Psi} + \boldsymbol{\Lambda}^\mathsf{T}\boldsymbol{\Lambda}\right](\boldsymbol{\xi}_1, \boldsymbol{\xi}_2 + \boldsymbol{x}_2, \boldsymbol{x}_1, \boldsymbol{u})\right)\boldsymbol{\xi}_1\end{aligned} \tag{8.57}$$

After writing Eq. (8.57) as

$$\begin{aligned}\dot{W} \leq\ & \boldsymbol{y}_\mathrm{p}^\mathsf{T}\mathbf{v}_\mathrm{p} - \frac{3}{4}\varphi^*(\|\boldsymbol{\xi}_2\|) - \varepsilon\boldsymbol{\xi}_1^\mathsf{T}\boldsymbol{\xi}_1 \\ & - \frac{1}{4}\varphi^*(\|\boldsymbol{\xi}_2\|) + \sqrt{\varphi^*(\|\boldsymbol{\xi}_2\|)}\|\boldsymbol{\Lambda}(\boldsymbol{\xi}_1, \boldsymbol{\xi}_2 + \boldsymbol{x}_2, \boldsymbol{x}_1, \boldsymbol{u})\boldsymbol{\xi}_1\| - \boldsymbol{\xi}_1^\mathsf{T}\left[\boldsymbol{\Lambda}^\mathsf{T}\boldsymbol{\Lambda}\right](\boldsymbol{\xi}_1, \boldsymbol{\xi}_2 + \boldsymbol{x}_2, \boldsymbol{x}_1, \boldsymbol{u})\boldsymbol{\xi}_1\end{aligned} \tag{8.58}$$

and noticing

$$-\frac{1}{4}\varphi^*(\|\boldsymbol{\xi}_2\|) + \sqrt{\varphi^*(\|\boldsymbol{\xi}_2\|)}\|\boldsymbol{\Lambda}\boldsymbol{\xi}_1\| - \boldsymbol{\xi}_1^\mathsf{T}\boldsymbol{\Lambda}^\mathsf{T}\boldsymbol{\Lambda}\boldsymbol{\xi}_1 = -\left(\frac{1}{2}\sqrt{\varphi^*(\|\boldsymbol{\xi}_2\|)} - \|\boldsymbol{\Lambda}\boldsymbol{\xi}_1\|\right)^2$$

it can be seen that

$$\dot{W} \leq \boldsymbol{y}_\mathrm{p}^\mathsf{T}\mathbf{v}_\mathrm{p} - \frac{3}{4}\varphi^*(\|\boldsymbol{\xi}_2\|) - \varepsilon\boldsymbol{\xi}_1^\mathsf{T}\boldsymbol{\xi}_1 - \left(\frac{1}{2}\sqrt{\varphi^*(\|\boldsymbol{\xi}_2\|)} - \|\boldsymbol{\Lambda}\boldsymbol{\xi}_1\|\right)^2 \tag{8.59}$$

Therefore, the storage function

$$W = V^*(\tilde{\boldsymbol{x}}_2 - \boldsymbol{L}_2\boldsymbol{L}_1^{-1}\tilde{\boldsymbol{x}}_1, \boldsymbol{x}) + \frac{1}{2}\tilde{\boldsymbol{x}}_1^\mathsf{T}\boldsymbol{L}_1^{-1}\tilde{\boldsymbol{x}}_1 \tag{8.60}$$

proves the feedback law (8.55) renders the augmented system strictly passive from $\mathbf{v}_\mathrm{p}$ to $\boldsymbol{y}_\mathrm{p}$ with respect to $\mathcal{M}$. Upon setting $\mathbf{v}_\mathrm{p} = \mathbf{0}$, $\mathcal{M}$ becomes positively invariant and globally asymptotically attractive [97]. In other words, the origin of the error system (8.6) is asymptotically stable. In fact, since $\boldsymbol{L}_2(\boldsymbol{y})$ is bounded, there exist positive constants κ_1, κ_2, and

κ_3 such that $\kappa_1\|\tilde{\boldsymbol{x}}\|^2 \leq W \leq \kappa_2\|\tilde{\boldsymbol{x}}\|^2$ and $\dot{W} \leq -\kappa_3\|\tilde{\boldsymbol{x}}\|^2$. Specifically, define the constant symmetric matrices

$$\boldsymbol{G}_{1,2} = \begin{bmatrix} \boldsymbol{L}_1^{-\mathsf{T}}\bar{\boldsymbol{L}}_2^{\mathsf{T}}\bar{\boldsymbol{L}}_2\boldsymbol{L}_1^{-1} + (\boldsymbol{L}_1^{-1} + \boldsymbol{L}_1^{-\mathsf{T}})/2 & \boldsymbol{L}_1^{-\mathsf{T}}\bar{\boldsymbol{L}}_2^{\mathsf{T}} \\ \bar{\boldsymbol{L}}_2\boldsymbol{L}_1^{-1} & \mathbb{I} \end{bmatrix} \tag{8.61}$$

$$\boldsymbol{G}_3 = \begin{bmatrix} \frac{3}{4}\underline{\gamma}\boldsymbol{L}_1^{-\mathsf{T}}\bar{\boldsymbol{L}}_2^{\mathsf{T}}\bar{\boldsymbol{L}}_2\boldsymbol{L}_1^{-1} + \varepsilon\mathbb{I} & \frac{3}{8}\underline{\gamma}\boldsymbol{L}_1^{-\mathsf{T}}\bar{\boldsymbol{L}}_2^{\mathsf{T}} \\ \frac{3}{4}\underline{\gamma}\bar{\boldsymbol{L}}_2\boldsymbol{L}_1^{-1} & \frac{3}{4}\underline{\gamma}\mathbb{I} \end{bmatrix} \tag{8.62}$$

where

$$\bar{\boldsymbol{L}}_2 \coloneqq \boldsymbol{L}_2|_{\boldsymbol{R}_{\mathrm{IB}}=\mathbb{I}}$$

Then, the origin of the error system (8.6) is proven globally exponentially stable with trajectories satisfying

$$\|\tilde{\boldsymbol{x}}(t)\| \leq \sqrt{\frac{\kappa_2}{\kappa_1}}\|\tilde{\boldsymbol{x}}(0)\|e^{-\frac{1}{2}\frac{\kappa_3}{\kappa_2}t} \tag{8.63}$$

where $\kappa_1 = \frac{1}{2}\lambda_{\min}(\boldsymbol{G}_{1,2})$, $\kappa_2 = \frac{1}{2}\lambda_{\max}(\boldsymbol{G}_{1,2})$, and $\kappa_3 = \lambda_{\min}(\boldsymbol{G}_3)$. These results give an explicit upper bound for the convergence rate of the state estimate error. Note that this upper bound may be conservative since the contribution of the last term in Eq. (8.59) is neglected.

The matrix $\boldsymbol{L}_1$ is left as a tuning parameter that can be chosen using familiar methods of observer gain design by linearizing about a nominal flight condition and defining weighted objectives (similar to the process and measurement noise covariance matrices for a Kalman filter). Also note the choice of bounding matrix functions $\boldsymbol{\Psi}$ and $\boldsymbol{\Lambda}$ given in Appendix B hold for any finite $\boldsymbol{L}_{2_{v,\lambda}}$, $\boldsymbol{L}_{2_{v,\zeta}}$, $\boldsymbol{L}_{2_{w,\lambda}}$, $\boldsymbol{L}_{2_{w,\zeta}}$. However, the observer gain is then also arbitrarily large. Therefore, it is judicious to choose these gains to make $\boldsymbol{\Psi}$ and $\boldsymbol{\Lambda}$ as small as possible. Setting $\boldsymbol{L}_{2_{v,\lambda}}$, $\boldsymbol{L}_{2_{v,\zeta}}$, $\boldsymbol{L}_{2_{w,\lambda}}$, and $\boldsymbol{L}_{2_{w,\zeta}}$ to be zero matrices is sufficient for this task. Intuitively, this is because the attitude innovation does not depend on the air-relative velocity or wind. Altogether, the injection gain matrix $\boldsymbol{L}$ is

$$\boldsymbol{L} = \begin{bmatrix} \boldsymbol{L}_{1_q} & \boldsymbol{0} & \boldsymbol{0} & \boldsymbol{0} \\ \boldsymbol{0} & \boldsymbol{L}_{1_\lambda} & \boldsymbol{0} & \boldsymbol{0} \\ \boldsymbol{0} & \boldsymbol{0} & \boldsymbol{L}_{1_\zeta} & \boldsymbol{0} \\ \boldsymbol{0} & \boldsymbol{0} & \boldsymbol{0} & \boldsymbol{L}_{1_\omega} \\ \boldsymbol{\Gamma}_{v,q}\boldsymbol{R}_{\mathrm{IB}}^{\mathsf{T}}(\boldsymbol{\lambda},\boldsymbol{\zeta})\boldsymbol{L}_{1_q} & \boldsymbol{0} & \boldsymbol{0} & \boldsymbol{\Gamma}_{v,\omega}\boldsymbol{M}_v^{\mathsf{T}}\boldsymbol{I}\boldsymbol{L}_{1_\omega} \\ \boldsymbol{R}_{\mathrm{IB}}(\boldsymbol{\lambda},\boldsymbol{\zeta})\boldsymbol{\Gamma}_{w,q}\boldsymbol{R}_{\mathrm{IB}}^{\mathsf{T}}(\boldsymbol{\lambda},\boldsymbol{\zeta})\boldsymbol{L}_{1_q} & \boldsymbol{0} & \boldsymbol{0} & \boldsymbol{R}_{\mathrm{IB}}(\boldsymbol{\lambda},\boldsymbol{\zeta})\boldsymbol{\Gamma}_{w,\omega}\boldsymbol{M}_v^{\mathsf{T}}\boldsymbol{I}\boldsymbol{L}_{1_\omega} \end{bmatrix} \tag{8.64}$$

8.6 Fixed-Wing Aircraft Demonstration

8.6.1 Research Aircraft

The proposed observer was implemented both in simulation and flight test of a small fixed-wing UAS called the My Twin Dream (MTD), shown in Figure 8.1. It is a radio-controlled foam aircraft with counter-rotating electric motors and 10 in. diameter, 6 in. pitch (10x6)

propellers. The aircraft was instrumented with a Cubepilot CubeOrange flight computer running PX4 firmware. The sensors onboard the aircraft include triple-redundant accelerometers and gyroscopes, two magnetometers, a Real-Time Kinematic (RTK) global navigation satellite system (GNSS) receiver, and a vaned air data unit for validation. The MTD was chosen for its simple construction, propeller location to accommodate the air data boom, and endurance of approximately 25 minutes. The MTD's physical properties are listed in Table 8.1.

Figure 8.1: My Twin Dream (MTD) research aircraft

Table 8.1: My Twin Dream (MTD) properties

Property	Symbol	Value	Units
Mass	m	3.311	kg
Mean aerodynamic chord	$\bar{c}$	0.254	m
Projected wing span	b	1.800	m
Wing planform area	S	0.457	m^2
Roll moment of inertia	I_{xx}	0.319	$\text{kg} \cdot \text{m}^2$
Pitch moment of inertia	I_{yy}	0.267	$\text{kg} \cdot \text{m}^2$
Yaw moment of inertia	I_{zz}	0.471	$\text{kg} \cdot \text{m}^2$
x-z product of inertia	I_{xz}	0.024	$\text{kg} \cdot \text{m}^2$
Other products of inertia	I_{xy}, I_{yz}	≈ 0	$\text{kg} \cdot \text{m}^2$

A nonlinear aero-propulsive model for the MTD was identified from flight data using the methods detailed in references [62], [135], [136]. Flight data was collected for the MTD in calm conditions using orthogonal phase-optimized multisine inputs [113] and was processed according to Gresham *et al.* [62] and Simmons *et al.* [136]. Next, multivariate orthogonal function modeling was used to determine the model structure with the minimum predicted

squared error [108]. Similar to the eSPAARO model in Section 7.6.2, the resulting non-dimensional force and moment coefficient model is

$$C_x = C_{x_\alpha}\alpha + C_{x_q}\breve{q} + C_{x_{\alpha^2}}\alpha^2 + C_{x_{\mathcal{J}_c}}\mathcal{J}_c + C_{x_0} \tag{8.65a}$$
$$C_y = C_{y_\beta}\beta + C_{y_r}\breve{r} + C_{y_{\delta a}}\delta a + C_{y_{\delta r}}\delta r \tag{8.65b}$$
$$C_z = C_{z_\alpha}\alpha + C_{z_q}\breve{q} + C_{z_{\delta e}}\delta e + C_{z_0} \tag{8.65c}$$
$$C_l = C_{l_\beta}\beta + C_{l_p}\breve{p} + C_{l_{\delta a}}\delta a \tag{8.65d}$$
$$C_m = C_{m_\alpha}\alpha + C_{m_q}\breve{q} + C_{m_{\delta e}}\delta e + C_{m_{\alpha^3}}\alpha^3 + C_{m_0} \tag{8.65e}$$
$$C_n = C_{n_\beta}\beta + C_{n_r}\breve{r} + C_{n_{\delta a}}\delta a + C_{n_{\delta r}}\delta r \tag{8.65f}$$

Next, maximum likelihood parameter estimates were obtained using the output error method [113] in MATLAB using the System IDentification Programs for AirCraft (SIDPAC) software toolbox [111]. The final model structure is given in Appendix A.5. The model parameter estimates are shown in Table A.3 and the valid model domain is given in Table A.4. Figure A.1 shows state prediction results obtained by integrating the final model with input data that were used in obtaining the model.

8.6.2 Simulation Results

First, the proposed observer was implemented in simulation with all assumptions satisfied in order to demonstrate the theoretical convergence guarantees. That is, the model is perfectly known, there is no measurement noise, and the wind is constant. The nonlinear system (8.17) with linearized aerodynamics was simulated in a uniform wind field with components $W_N = 10$ m/s, $W_E = -15$ m/s, and $W_D = -3$ m/s using MATLAB. The aircraft was given large-amplitude open loop controls resulting in the trajectory shown in Figure 8.2. The nonlinear

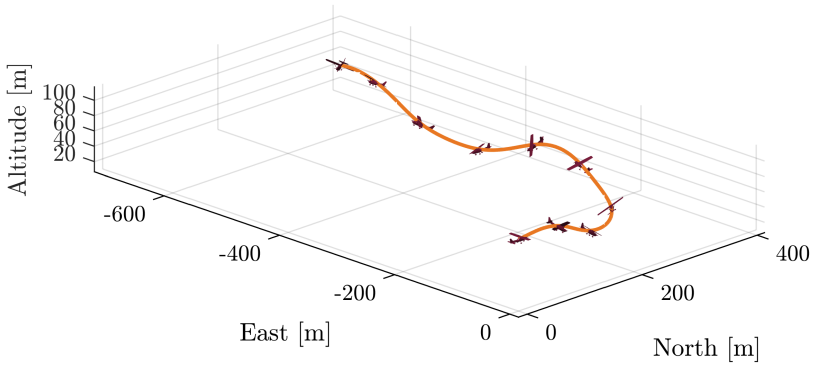

Figure 8.2: Simulated aircraft trajectory in wind

passivity-based observer was implemented on this data. The LMIs in (8.42) were solved using CVX [58], [60] with the Mosek solver [7]. The lower bound $\underline{\gamma}$ was maximized for a fixed upper bound of $\overline{\gamma} = 5$, resulting in an optimal value of $\underline{\gamma} = 0.27$. The time history of wind estimate results are shown in Figure 8.3. The storage function, W, for the simulation

data is shown in Figure 8.4. Here, we see that W is strictly decreasing in time — consistent with Eq. (8.59).

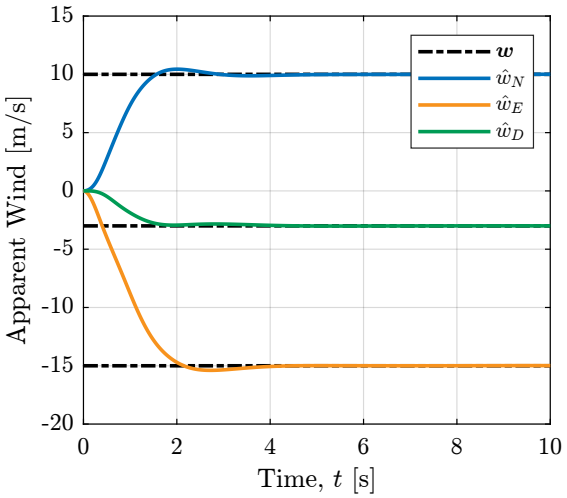

Figure 8.3: Simulated wind estimates

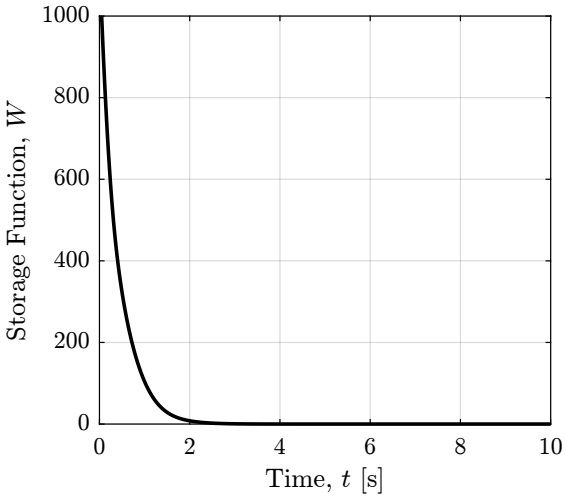

Figure 8.4: Storage function time history

8.6.3 Flight Test Results

Next, the proposed observer was implemented on flight test data for the MTD. These data were collected as part of a flight test campaign at Virginia Tech's Kentland Experimental Aerial Systems (KEAS) airfield on September 28th, 2022. The wind conditions were moderately turbulent for the aircraft's size, varying between 3 and 12 m/s, with a mean wind speed of 7.5 m/s coming from the northwest.

Data were gathered in a grid pattern for two flights — one at 400 ft and the other at 700 ft above ground level (AGL). Since we are interested in maneuvering flight, nine maneuvers were selected in which the aircraft executed a sharp banked turn resulting in a heading change of 180 degrees.

The robust feasibility problem (8.44) was solved over the valid range of state and input values for the aerodynamic model (Table A.4). The upper bound $\overline{\gamma}$ was fixed at 5, while the lower bound $\underline{\gamma}$ was maximized to yield an optimal value of 0.056. An additional constraint was placed such that the norm of $\boldsymbol{\Gamma}$ was less than 20 in order to maintain efficient and accurate numerical integration of the observer. The injection gain of the measured states, $\boldsymbol{L}_1$, was found by linearizing the aircraft dynamics about the nominal cruise flight condition, $(\boldsymbol{x}_0, \boldsymbol{u}_0)$, for the MTD and solving the algebraic Riccati equation, $\boldsymbol{AP}+\boldsymbol{PA}^\mathsf{T}-\boldsymbol{PC}^\mathsf{T}\boldsymbol{R}_c^{-1}\boldsymbol{CP}+\boldsymbol{Q}_c=\boldsymbol{0}$. Here, $\boldsymbol{A}=\partial \boldsymbol{f}/\partial \boldsymbol{x}|_{\boldsymbol{x}_0,\boldsymbol{u}_0}$ and $\boldsymbol{C}=[\mathbb{I}\ \ \boldsymbol{0}]^\mathsf{T}$. Using historical data collected for the MTD, the $\boldsymbol{Q}_c$ and $\boldsymbol{R}_c$ matrices were selected as typically done for a Kalman-Bucy filter. That is, $\boldsymbol{Q}_c$ was selected as the maximum power spectral density of the difference between the modeled and measured state derivatives over the frequency range of interest. The matrix $\boldsymbol{R}_c$ was

chosen to be a time-averaged state estimate error covariance of $\boldsymbol{y} = \boldsymbol{x}_1$ from the autopilot's extended Kalman filter. The block-diagonal elements of the resulting gain matrix, $\boldsymbol{P}\boldsymbol{C}^{\mathsf{T}}\boldsymbol{R}_c^{-1}$, were checked for invertibility and then selected to be the respective block-diagonal elements of $\boldsymbol{L}_1$. The initial conditions of the measured states, $\hat{\boldsymbol{x}}_1(0)$ were set to their initial measured values, $\boldsymbol{y}(0)$. The initial condition for the relative velocity, $\hat{\boldsymbol{v}}_{\mathrm{r}}(0)$ was set to be the aircraft's nominal trim value in calm air, while the initial wind estimate, $\hat{\boldsymbol{w}}$ was set to zero.

The passivity-based observer was implemented on all nine turn maneuvers with the same tuning parameters. The root-mean-squared error (RMSE) of the wind components were computed for each 40 second maneuver, as tabulated in Table 8.2. The typical RMSE value is less than 1 m/s. The RMSE for the vertical component is typically smaller than for the horizontal components, due to a fixed-wing aircraft's inherent sensitivity to vertical velocity fluctuations.

Table 8.2: Flight test maneuvers

Maneuver	Flight Number	RMSE(w_N) [m/s]	RMSE(w_E) [m/s]	RMSE(w_D) [m/s]
1	1	0.97	0.58	0.59
2	1	0.83	0.70	0.68
3	1	0.86	0.76	0.69
4	1	0.74	0.55	0.56
5	1	0.75	0.75	0.56
6	2	1.06	0.68	0.41
7	2	1.11	0.81	0.46
8	2	0.84	0.93	0.70
9	2	1.32	1.04	0.63

As an example, the passivity-based observer results for Maneuver 9 are considered. The trajectory that the aircraft followed during this maneuver is shown in Figure 8.5. The time

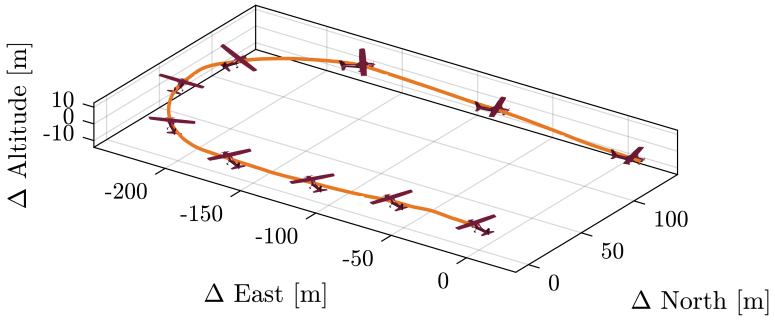

Figure 8.5: Trajectory of maneuver 9

histories of the apparent wind estimates are shown in Figure 8.6 along with the "truth values" reconstructed according to Eq. (6.25). Examining Figure 8.6, the wind estimates

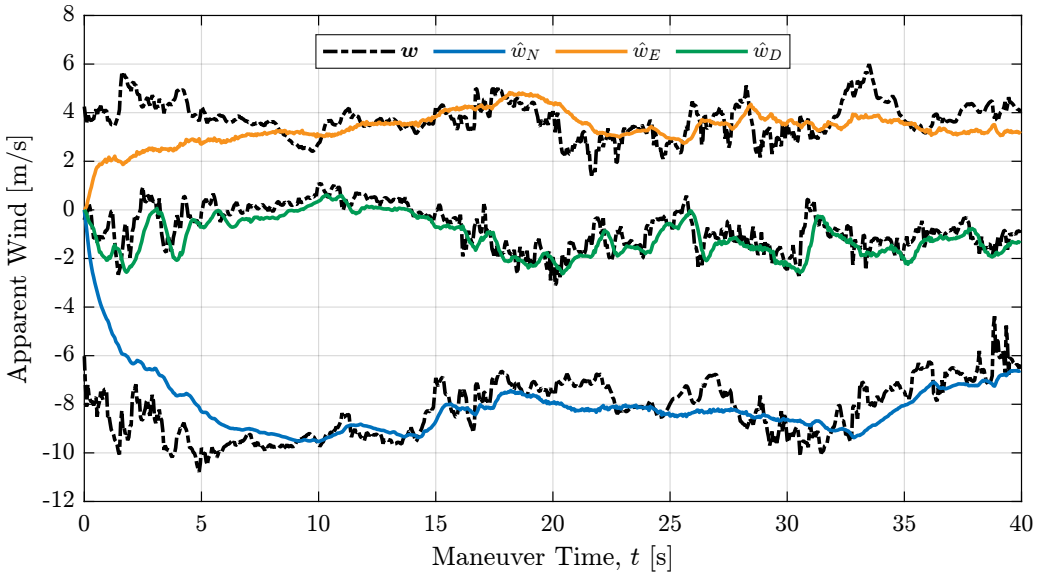

Figure 8.6: Wind estimates for maneuver 9

appear to converge within an ultimate bound around the true values. Suppose we consider the modeling error as a disturbance to the error system, on which we can place some upper bound. Then since the state estimate error is globally asymptotically stable for the ideal system, there exists some neighborhood about the origin in which the error system is locally input-to-state stable with respect to these disturbances [86, Ch. 5]. The norms of the matrix-valued bounding functions, $\boldsymbol{\Psi}$ and $\boldsymbol{\Lambda}$, are also plotted in Figure 8.7. Recall, the function $\boldsymbol{\Psi}$

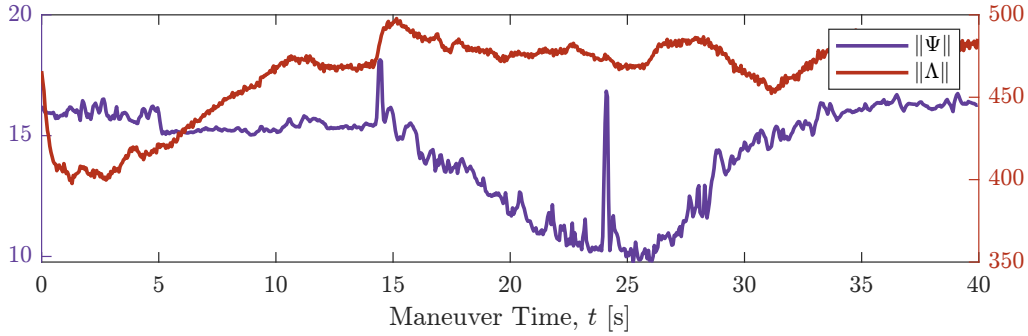

Figure 8.7: Bounding functions for maneuver 9

bounds the nonlinear growth of $\tilde{\boldsymbol{x}}_1$, which is typically smaller than that of $\tilde{\boldsymbol{x}}_2$ (bounded by $\boldsymbol{\Lambda}$).

The variation in convergence among the set of maneuvers was also analyzed. Point-wise in time, the sample mean and standard deviations were computed across the set of wind estimate error trajectories. Time histories for the first one second of these data are shown in Figure 8.8, where we see consistent convergence towards some ultimate bound about zero

error.

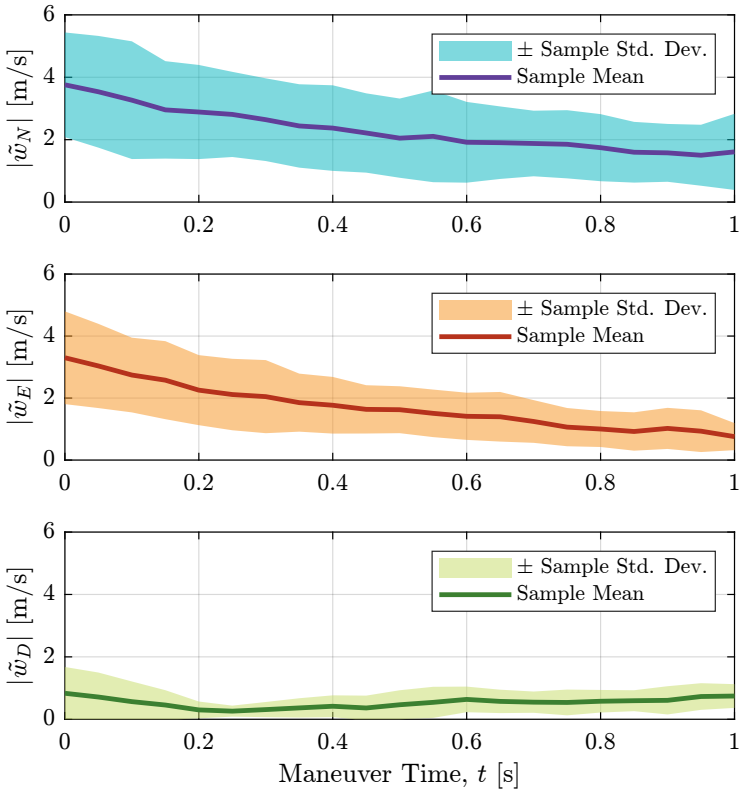

Figure 8.8: Variation in wind estimate error transients

Chapter 9

Conclusions and Future Directions

This dissertation has explored the theory and application of nonlinear observers for wind estimation. Particular emphasis has been placed on expanding operating conditions for which flight dynamic models and state estimation techniques remain accurate and mathematically valid. We have shown that carefully designed nonlinear observers informed by large-domain aerodynamic models can yield strong mathematical guarantees on the convergence of wind estimates, even in a stochastic setting. As autonomy grows increasingly vital for both small UAVs and larger commercial or urban air mobility platforms, these techniques provide strong guarantees that can be incorporated into a wide variety of applications, such as synthetic air data systems, path planning algorithms, safety monitoring solutions, and numerical weather models.

9.1 Conclusions and Summary of Contributions

Symmetry-Preserving Reduced-Order Observers

A symmetry-preserving, reduced-order observer was introduced in Chapter 3. Nonlinear reduced-order observers are beneficial when part of the system's state is known with negligible error, reducing the dimension of the observer and possibly computational complexity. The core innovation of this work lies in leveraging symmetries in the system dynamics to construct the nonlinear dynamics and output of the reduced-order observer. The observer ensures that the state estimate error system also inherits invariance under a Lie group's action, which simplifies both the design process and stability analysis. In cases where the system's nonlinearities comprise the Lie group's action, the nonlinear observer may even yield linear state estimation error dynamics to enable a multitude of design and optimization techniques that improve performance. These benefits were demonstrated in the example of a rigid-body velocity observer.

Nonlinear Multirotor Flight Dynamic Modeling

Multirotor flight dynamic models for control and estimation have typically been limited to a small operating domain near a nominal equilibrium state (usually hover). Chapter 4 addresses this limitation by carefully bridging established rotor aerodynamic theory and empirical modeling methods to obtain a quasi-steady, nonlinear model that is both accurate over a large domain and identifiable from flight data. Additional assumptions led to further

simplified models that can more easily be identified from flight data and used in control and estimation applications. While these steps demonstrate the general applicability and utility of our physics-based modeling approach, several assumptions, such as uniform inflow conditions and steady-flight rotor loads, may limit its applicability to more extreme flight regimes or motion on fast time scales. To ensure reliable parameter identification, a simulation study was conducted based on wind tunnel data. The modeling results not only reveal the relative significance of model regressors through a forward selection-like algorithm, but also statistically inform a two-step procedure for identifying model parameters using all force and moment data. The model fit and predictive skill of the derived models were validated, demonstrating the utility of the physics-based model structure. Finally, by examining the relative contribution of individual terms over a range of forward-flight speeds, we have shown which effects may or may not be critical for a given application, thereby informing a hierarchical approach to model selection that can be used in conjunction with data-driven model structure determination techniques.

Robust Control for System Identification

Identifying parameters for large-domain flight dynamic models for unstable aircraft is challenging, particularly because stabilizing controllers can introduce regressor correlation and suppress dynamics of interest. In Chapter 5, a modeling methodology was presented that supports data collection for the experimental identification of large-domain nonlinear flight dynamic models using a robust linear, parameter-varying control law. This methodology thus constitutes a *safe* (prescribed bound on the excitation-to-state amplification) and *effective* (with sufficient excitation to identify model parameters) approach that has a low barrier to implementation. It requires only an initial set of locally stabilizing control laws, such as PID controllers, which are then used to collect flight data to identify a polytopic LPV model for the aircraft dynamics. For a multirotor, it was shown that this step involves only eight maneuvers, each corresponding to a body velocity reference condition. The next step of this process consists of excitation and reference signal design and robust H_∞ control law synthesis. For the multirotor, a 7-axis multisine signal was designed to ensure the body velocity reference is uncorrelated from the actuator commands. With this control law, one can conduct the second (and final) phase of data collection to obtain rich data over the entire flight envelope.

Symmetry-Preserving Reduced-Order Observers for Wind Estimation

Chapters 6–7 applied the reduced-order observer presented in Chapter 3 to wind estimation for maneuvering aircraft. The rotational symmetries in rigid-body dynamics allowed for exponential convergence *without* a small-perturbation assumption on the rigid-body dynamics, significantly expanding the observer's domain of guaranteed stability. In practice, this means the proposed observer can handle scenarios with large changes in wind velocity or aggressive vehicle maneuvers. The observer's theoretical guarantees were demonstrated through simulation of a nonlinear quadrotor aircraft model. Observers synthesized using both body-frame

and inertial-frame transformation groups yielded comparable results. Through these simulations, the observer was found to be robust to turbulence, measurement noise, and sampled position data.

Furthermore, an extension of the observer to the stochastic aircraft dynamics accounts for turbulence and uncertain aerodynamics in a principled manner. Through this perspective, the gain selection problem reduced to that of the Kalman-Bucy filter, greatly simplifying the design process for the practitioner. Noise-to-state stability guarantees provide probabilistic bounds on the convergence of the invariant error, although Monte-Carlo simulation of the nonlinear quadrotor model revealed these bounds to be conservative. Nonetheless, these probabilistic convergence guarantees support the use of the observer in safety-critical applications. Applying the observers to flight data for a fixed-wing UAV further demonstrated the observer's practical utility and robustness. These flight test results showed the observer's applicability to general maneuvering flight — a result afforded by the exponential (stochastic) stability guarantees on the invariant error dynamics. In these flight test results, it was found that the body-frame transformation group yielded more robust wind estimates. Overall, this provably stable observer provides strong guarantees that can be incorporated into a wide variety of applications, such as synthetic air data systems, path planning algorithms, safety monitoring solutions, and numerical weather models.

Passivity-Based Wind Observer

Finally, in Chapter 8, a global nonlinear passivity-based observer for wind estimation was presented. Under mild assumptions about the wind field and aircraft aerodynamics, we obtain rigorous guarantees on the convergence of wind estimates across the entire flight envelope. Such strong results help expand the range of flight conditions for which accurate wind estimates can be made. Through a judicious choice of the output error injection gain matrix (specifically, the component denoted $\boldsymbol{L}_2$ in the chapter), linear matrix inequality conditions were obtained that not only prove the observer error dynamics are globally minimum phase, but also provide a constructive design procedure. Explicit formulas were derived for the bounding functions that define the matrix-valued output error scaling (denoted $\boldsymbol{K}$ in the chapter), allowing the observer to be implemented on flight data. Implementing the observer on both simulation and flight data demonstrated its potential to estimate wind with rigorous guarantees, even in maneuvering flight.

9.2 Future Directions

As advancements in aerospace systems push the boundaries of autonomy, safety must remain a top priority. Building on the theoretical and practical developments of this dissertation, future research will center on obtaining probabilistic stability guarantees by integrating nonlinear modeling, control, and estimation methods in the stochastic setting. This work will allow future aerospace systems, particularly aerial robotics and urban air mobility vehicles,

to operate freely in complex and uncertain conditions. A primary goal is to extend nonlinear observers to stochastic differential equations, thereby incorporating random disturbances directly into the observer design. Parallel to these observer-centric efforts, stochastic extensions of geometric and energy-based control using passivity will be pursued. By leveraging the structure of such systems, the burden of proving stochastic stability for nonlinear systems can be partially alleviated, simplifying conditions for stabilizing controllers.

A complementary focus area lies in modeling, control, and estimation of atmospheric vehicles in uncertain environments, particularly where parametric uncertainty, unmodeled dynamics, and atmospheric turbulence significantly affect the vehicle's motion. In deriving the quasi-steady models in Chapter 4, certain assumptions (uniform inflow, quasi-steady rotor loads) may not hold for severe maneuvers or very fast transient dynamics. Extending the validity of these models by incorporating (possibly stochastic) unsteady aerodynamics is a natural next step. Similarly, the stochastic observer design in Chapter 7 demonstrated noise-to-state stability under an idealized assumption on turbulence and modeling error. Real-world atmospheric phenomena can be far more complex, especially in urban environments. Incorporating more accurate turbulence models can refine stability bounds and strengthen the guarantees of nonlinear observers. Although simulation data for multirotor UAVs and preliminary flight data for fixed-wing aircraft are presented, there is also a further need to validate the techniques in this dissertation across a broader range of platforms, such as eVTOL vehicles or flexible aircraft.

9.3 Final Remarks

Overall, this dissertation highlights the importance of merging rigorous theoretical perspectives with practical modeling and experimental methods to enable *provably effective* state estimation over large domains in stochastic environments. As aircraft operating envelopes continue to expand, the methods introduced in this dissertation provide a clear path to ensuring both accuracy and robustness in safety-critical applications. Continued advances in stochastic observer design and flight dynamic modeling will be crucial for shaping the operation of autonomous vehicles.

Bibliography

[1] K. A. Adkins, M. Akbas, and M. Compere, "Real-time urban weather observations for urban air mobility," *International Journal of Aviation, Aeronautics, and Aerospace*, vol. 7, no. 4, 2020. DOI: 10.15394/ijaaa.2020.1540 (cit. on p. 1).

[2] N. Aghannan and P. Rouchon, "An intrinsic observer for a class of Lagrangian systems," *IEEE Transactions on Automatic Control*, vol. 48, no. 6, pp. 936–945, Jun. 2003. DOI: 10.1109/TAC.2003.812778 (cit. on p. 24).

[3] M. I. Alabsi and T. D. Fields, "Real-time closed-loop system identification of a quadcopter," *Journal of Aircraft*, vol. 56, no. 1, pp. 324–335, Jan. 2019. DOI: 10.2514/1.C034219 (cit. on p. 39).

[4] B. Anderson, "Stability properties of Kalman-Bucy filters," *Journal of the Franklin Institute*, vol. 291, no. 2, pp. 137–144, Feb. 1971. DOI: 10.1016/0016-0032(71)90016-0 (cit. on p. 113).

[5] B. D. O. Anderson and J. B. Moore, *Linear Optimal Control* (Prentice-Hall Networks Series). Englewood Cliffs, N.J: Prentice-Hall, 1971, ISBN: 978-0-13-536870-1 (cit. on p. 103).

[6] M. J. Anderson and P. J. Whitcomb, *RSM Simplified: Optimizing Processes Using Response Surface Methods for Design of Experiments*, 2nd ed. Boca Raton, FL: CRC Press, 2017. DOI: 10.1201/9781315382326 (cit. on p. 59).

[7] M. ApS, *The MOSEK optimization toolbox for MATLAB manual*, 2022. [Online]. Available: https://docs.mosek.com/latest/intro/index.html (cit. on pp. 84, 143).

[8] L.-P. Arguin, *A First Course in Stochastic Calculus* (Pure and Applied Undergraduate Texts volume 53). Providence, RI: American Mathematical Society, 2022, ISBN: 978-1-4704-6488-2 (cit. on p. 15).

[9] J. Armstrong and D. Brigo, "Intrinsic stochastic differential equations as jets," *Proceedings of the Royal Society A: Mathematical, Physical and Engineering Sciences*, vol. 474, no. 2210, p. 20 170 559, Feb. 2018. DOI: 10.1098/rspa.2017.0559 (cit. on p. 94).

[10] L. Arnold, *Stochastic Differential Equations: Theory and Applications*. New York: Wiley, 1974, ISBN: 978-0-471-03359-2 (cit. on pp. 17, 18, 22).

[11] A. Asignacion, S. Suzuki, R. Noda, T. Nakata, and H. Liu, "Frequency-based wind gust estimation for quadrotors using a nonlinear disturbance observer," *IEEE Robotics and Automation Letters*, vol. 7, no. 4, pp. 9224–9231, Oct. 2022. DOI: 10.1109/LRA.2022.3190073 (cit. on p. 88).

[12] A. Astolfi, D. Karagiannis, and R. Ortega, "Chapter 5: Reduced-order observers," in *Nonlinear and Adaptive Control with Applications*, ser. Communications and Control Engineering, London: Springer-Verlag, 2008, pp. 91–114, ISBN: 978-1-84800-065-0 (cit. on pp. 25, 28).

[13] S. I. Azid, K. Kumar, M. Cirrincione, and A. Fagiolini, "Wind gust estimation for precise quasi-hovering control of quadrotor aircraft," *Control Engineering Practice*, vol. 116, p. 104 930, Nov. 2021. DOI: 10.1016/j.conengprac.2021.104930 (cit. on p. 88).

[14] M. Bangura, "Aerodynamics and Control of Quadrotors," Ph.D. dissertation, The Australian National University, Feb. 2017 (cit. on p. 39).

[15] J. X. J. Bannwarth, Z. Jeremy Chen, K. A. Stol, B. A. MacDonald, and P. J. Richards, "Aerodynamic force modeling of multirotor unmanned aerial vehicles," *AIAA Journal*, vol. 57, no. 3, pp. 1250–1259, Mar. 2019. DOI: 10.2514/1.J057165 (cit. on pp. 39, 47).

[16] Y. Bar-Shalom, X.-R. Li, and T. Kirubarajan, *Estimation with Applications to Tracking and Navigation*. New York: John Wiley and Sons, Inc., 2001, ISBN: 978-0-471-41655-5 (cit. on p. 66).

[17] L. Barbieri *et al.*, "Intercomparison of small unmanned aircraft system (sUAS) measurements for atmospheric science during the LAPSE-RATE campaign," *Sensors*, vol. 19, no. 9, p. 2179, May 2019. DOI: 10.3390/s19092179 (cit. on p. 1).

[18] D. F. Barcelos, G. Bramesfeld, B. Isaac, and S. Waslander, "Physics-based approach to multirotor vehicle flight-dynamics prediction," in *AIAA AVIATION 2021 Forum*, American Institute of Aeronautics and Astronautics, Aug. 2021. DOI: 10.2514/6.2021-2532 (cit. on p. 49).

[19] D. F. Barcelos, A. Kolaei, and G. Bramesfeld, "Aerodynamic interactions of quadrotor configurations," *Journal of Aircraft*, vol. 57, no. 6, pp. 1074–1090, Nov. 2020. DOI: 10.2514/1.C035614 (cit. on pp. 38, 49).

[20] A. Barrau and S. Bonnabel, "The invariant extended Kalman filter as a stable observer," *IEEE Transactions on Automatic Control*, vol. 62, no. 4, pp. 1797–1812, Apr. 2017. DOI: 10.1109/TAC.2016.2594085 (cit. on p. 24).

[21] Y. I. Belopolskaya and Y. L. Dalecky, *Stochastic Equations and Differential Geometry* (Mathematics and Its Applications), M. Hazewinkel, Ed. Dordrecht: Springer, 1990, vol. 30, ISBN: 978-94-010-7493-3. DOI: 10.1007/978-94-009-2215-0 (cit. on p. 94).

[22] S. Bonnabel, P. Martin, and P. Rouchon, "Non-linear symmetry-preserving observers on Lie groups," *IEEE Transactions on Automatic Control*, vol. 54, no. 7, pp. 1709–1713, Jul. 2009. DOI: 10.1109/TAC.2009.2020646 (cit. on p. 24).

[23] S. Bonnabel, P. Martin, and E. Salaun, "Invariant extended Kalman filter: Theory and application to a velocity-aided attitude estimation problem," in *Proceedings of the 48th IEEE Conference on Decision and Control*, Shanghai: IEEE, Dec. 2009, pp. 1297–1304. DOI: 10.1109/CDC.2009.5400372 (cit. on p. 24).

[24] S. Bonnabel, P. Martin, and P. Rouchon, "Symmetry-preserving observers," *IEEE Transactions on Automatic Control*, vol. 53, no. 11, pp. 2514–2526, Dec. 2008. DOI: 10.1109/TAC.2008.2006929 (cit. on pp. 24, 26, 27, 30, 33).

[25] W. M. Boothby, *An Introduction to Differentiable Manifolds and Riemannian Geometry*, Revised Second. San Diego: Academic Press, 2003, ISBN: 978-0-12-116051-7 (cit. on pp. 7, 9).

[26] V. S. Borkar, *Probability Theory: An Advanced Course*. New York: Springer, 1995, ISBN: 978-0-387-94558-3. DOI: 10.1007/978-1-4612-0791-7 (cit. on p. 23).

[27] P.-J. Bristeau, P. Martin, E. Salaun, and N. Petit, "The role of propeller aerodynamics in the model of a quadrotor UAV," in *2009 European Control Conference (ECC)*, Budapest: IEEE, Aug. 2009, pp. 683–688. DOI: 10.23919/ECC.2009.7074482 (cit. on p. 39).

[28] F. Bullo and A. D. Lewis, *Geometric Control of Mechanical Systems: Modeling, Analysis, and Design for Simple Mechanical Control Systems* (Texts in Applied Mathematics 49). New York, NY: Springer, 2009, ISBN: 978-0-387-22195-3 (cit. on p. 13).

[29] C. I. Byrnes, A. Isidori, and J. C. Willems, "Passivity, feedback equivalence, and the global stabilization of minimum phase nonlinear systems," *IEEE Transactions on Automatic Control*, vol. 36, no. 11, pp. 1228–1240, Nov. 1991. DOI: 10.1109/9.100932 (cit. on pp. 129, 134).

[30] D.-G. Caprace, A. Ning, P. Chatelain, and G. Winckelmans, "Effects of rotor-airframe interaction on the aeromechanics and wake of a quadcopter in forward flight," *Aerospace Science and Technology*, vol. 130, p. 107 899, Nov. 2022. DOI: 10.1016/j.ast.2022.107899 (cit. on p. 49).

[31] H. Chen and H. Bai, "Incorporating thrust models for quadcopter wind estimation," *IFAC-PapersOnLine*, vol. 55, no. 37, pp. 19–24, 2022. DOI: 10.1016/j.ifacol.2022.11.155 (cit. on p. 88).

[32] H. Chen, H. Bai, and C. N. Taylor, "Invariant-EKF design for quadcopter wind estimation," in *2022 American Control Conference (ACC)*, Atlanta, GA, USA: IEEE, Jun. 2022, pp. 1236–1241. DOI: 10.23919/ACC53348.2022.9867417 (cit. on pp. 24, 88, 98).

[33] Y.-C. Chen and C. A. Woolsey, "A structure-inspired disturbance observer for finite-dimensional mechanical systems," *IEEE Transactions on Control Systems Technology*, vol. 32, no. 2, pp. 440–455, Mar. 2024. DOI: 10.1109/TCST.2023.3327510 (cit. on p. 24).

[34] Y.-C. Chen and C. Woolsey, "Passivity-based disturbance observer design," in *ASME 2020 Dynamic Systems and Control Conference*, Virtual: American Society of Mechanical Engineers, Oct. 2020. DOI: 10.1115/DSCC2020-3287 (cit. on p. 131).

[35] S. Chintalapati, S. Rock, and S. Habchi, "Unsteady aerodynamics of a rapidly tumbling bluff body," in *37th Aerospace Sciences Meeting and Exhibit*, Reno, NV: American Institute of Aeronautics and Astronautics, Jan. 1999. DOI: 10.2514/6.1999-659 (cit. on p. 49).

[36] J. Cooper, J. W. Hopwood, C. A. Woolsey, S. F. J. De Wekker, and M. DeVore, "Intelligent wind estimation for chemical source localization," in *79th Annual Forum & Technology Display*, West Palm Beach, FL: Vertical Flight Society, May 2023, pp. 1–20. DOI: 10.4050/F-0079-2023-18194 (cit. on pp. 5, 43, 72).

[37] M. A. Cunningham and J. E. Hubbard, "Open-loop linear model identification of a multirotor vehicle with active feedback control," *Journal of Aircraft*, vol. 57, no. 6, pp. 1044–1061, Nov. 2020. DOI: 10.2514/1.C035834 (cit. on pp. 39, 46, 47, 58, 72).

[38] R. Durrett, *Probability: Theory and Examples* (Cambridge Series in Statistical and Probabilistic Mathematics), 4th. Cambridge: Cambridge University Press, 2010, ISBN: 978-0-521-76539-8 (cit. on p. 15).

[39] M. Emery, *An Invitation to Second-Order Stochastic Differential Geometry*, May 2007. HAL Open Science: hal-00145073f (cit. on p. 94).

[40] B. Etkin, *Dynamics of Atmospheric Flight*. New York: Wiley, 1972, ISBN: 978-0-471-24620-6 (cit. on pp. 12, 89).

[41] B. Etkin, "Turbulent wind and its effect on flight," *Journal of Aircraft*, vol. 18, no. 5, pp. 327–345, May 1981. DOI: 10.2514/3.57498 (cit. on p. 90).

[42] L. C. Evans, *An Introduction to Stochastic Differential Equations*, v1.2. Providence, RI: American Mathematical Society, 2013 (cit. on pp. 15, 18).

[43] G. Fay, "Derivation of the aerodynamic forces for the mesicopter simulation," Stanford University: Stanford University, Feb. 2001 (cit. on pp. 39, 43).

[44] J. V. Foster and D. Hartman, "High-fidelity multi-rotor unmanned aircraft system (UAS) simulation development for trajectory prediction under off-nominal flight dynamics," in *17th AIAA Aviation Technology, Integration, and Operations Conference*, Denver, CO: American Institute of Aeronautics and Astronautics, Jun. 2017, pp. 1–19. DOI: 10.2514/6.2017-3271 (cit. on pp. 44, 58, 68).

[45] W. Frost and R. L. Bowles, "Wind shear terms in the equations of aircraft motion," *Journal of Aircraft*, vol. 21, no. 11, pp. 866–872, Nov. 1984. DOI: 10.2514/3.45056 (cit. on p. 90).

[46] G. Gaeta and C. Lunini, "On Lie-point symmetries for Itô stochastic differential equations," *Journal of Nonlinear Mathematical Physics*, vol. 24, no. Supplement 1, pp. 90–102, 2017. DOI: 10.1080/14029251.2017.1418056 (cit. on p. 109).

[47] K. Gahan, J. W. Hopwood, and C. A. Woolsey, "Wind estimation using an H_∞ filter with fixed-wing aircraft flight test results," in *AIAA SciTech 2023 Forum*, National Harbor, MD: American Institute of Aeronautics and Astronautics, Jan. 2023. DOI: 10.2514/6.2023-2252 (cit. on p. 5).

[48] K. C. Gahan, J. W. Hopwood, and C. A. Woolsey, "Uncertainty in wind estimates, part 1: Analysis using generalized polynomial chaos," in *AIAA SciTech 2024 Forum*, Orlando, FL: American Institute of Aeronautics and Astronautics, Jan. 2024. DOI: 10.2514/6.2024-2824 (cit. on pp. 5, 88).

[49] K. C. Gahan, J. W. Hopwood, and C. A. Woolsey, "Uncertainty in wind estimates, part 2: H_∞ filtering using generalized polynomial chaos," in *AIAA SciTech 2024 Forum*, Orlando, FL: American Institute of Aeronautics and Astronautics, Jan. 2024. DOI: 10.2514/6.2024-2825 (cit. on pp. 5, 88).

[50] K. C. Gahan, J. W. Hopwood, and C. A. Woolsey, "Model-based wind estimation using H_∞ filtering with flight-test results," *Journal of Guidance, Control, and Dynamics*, vol. 48, no. 3, pp. 630–637, Mar. 2025. DOI: 10.2514/1.G007735 (cit. on pp. 5, 88).

[51] P. Gahinet, A. Nemirovski, A. J. Laub, and M. Chilali, *LMI Control Toolbox User's Guide*, May 1995 (cit. on p. 76).

[52] Y. E. Gliklikh, *Ordinary and Stochastic Differential Geometry as a Tool for Mathematical Physics*. Dordrecht: Springer Netherlands, 1996, ISBN: 978-90-481-4731-1. DOI: 10.1007/978-94-015-8634-4 (cit. on p. 94).

[53] H. Goldstein, *Classical Mechanics*, 2nd. Reading, MA: Addison-Wesley, 1980, ISBN: 978-0-201-02918-5 (cit. on p. 12).

[54] A. Gong, F. C. Sanders, R. A. Hess, and M. B. Tischler, "System identification and full flight-envelope model stitching of a package-delivery octocopter," in *AIAA Scitech 2019 Forum*, San Diego, CA: American Institute of Aeronautics and Astronautics, Jan. 2019. DOI: 10.2514/6.2019-1076 (cit. on p. 39).

[55] J. González-Rocha, S. F. J. De Wekker, S. D. Ross, and C. A. Woolsey, "Wind profiling in the lower atmosphere from wind-induced perturbations to multirotor UAS," *Sensors*, vol. 20, no. 5, p. 1341, Feb. 2020. DOI: 10.3390/s20051341 (cit. on p. 1).

[56] J. González-Rocha, C. A. Woolsey, C. Sultan, and S. F. J. De Wekker, "Sensing wind from quadrotor motion," *Journal of Guidance, Control, and Dynamics*, vol. 42, no. 4, pp. 836–852, Apr. 2019. DOI: 10.2514/1.G003542 (cit. on pp. 24, 88, 92).

[57] P. Goos and B. Jones, *Optimal Design of Experiments: A Case Study Approach*. West Sussex, United Kingdom: John Wiley & Sons, 2011, ISBN: 978-0-470-74461-1 (cit. on p. 59).

[58] M. Grant and S. Boyd, *CVX: Matlab Software for Disciplined Convex Programming, version 2.1*, Mar. 2014. [Online]. Available: http://cvxr.com/cvx (cit. on pp. 84, 143).

[59] M. C. Grant and S. P. Boyd, "Graph Implementations for Nonsmooth Convex Programs," in *Recent Advances in Learning and Control*, ser. Lecture Notes in Control and Information Sciences, V. D. Blondel, S. P. Boyd, and H. Kimura, Eds., vol. 371, London: Springer, 2008, pp. 95–110, ISBN: 978-1-84800-154-1. DOI: 10.1007/978-1-84800-155-8 (cit. on p. 84).

[60] J. A. Grauer and E. A. Morelli, "Generic global aerodynamic model for aircraft," *Journal of Aircraft*, vol. 52, no. 1, pp. 13–20, Jan. 2015. DOI: 10.2514/1.C032888 (cit. on pp. 38, 71, 103, 143).

[61] J. L. Gresham, "Aerodynamic Modeling in Nonlinear Regions, including Stall Spins, for Fixed-Wing Unmanned Aircraft from Experimental Flight Data," Ph.D. dissertation, Virginia Polytechnic Institute and State University, Blacksburg, VA, Mar. 2022 (cit. on p. 120).

[62] J. L. Gresham, J.-M. W. Fahmi, B. M. Simmons, J. W. Hopwood, W. Foster, and C. A. Woolsey, "Flight test approach for modeling and control law validation for unmanned aircraft," in *AIAA SciTech 2022 Forum*, San Diego, CA: American Institute of Aeronautics and Astronautics, Jan. 2022, pp. 1–23. DOI: 10.2514/6.2022-2406 (cit. on pp. 5, 74, 120, 142).

[63] J. L. Gresham, B. M. Simmons, J.-M. W. Fahmi, J. W. Hopwood, and C. A. Woolsey, "Remote uncorrelated pilot input excitation assessment for unmanned aircraft aerodynamic modeling," *Journal of Aircraft*, vol. 60, no. 3, pp. 955–967, 2023. DOI: 10.2514/1.C036942 (cit. on p. 5).

[64] J. L. Gresham, B. M. Simmons, J.-M. W. Fahmi, and C. A. Woolsey, "Remote uncorrelated pilot inputs for nonlinear aerodynamic model identification from flight data," in *AIAA AVIATION 2021 Forum*, Virtual: American Institute of Aeronautics and Astronautics, Aug. 2021. DOI: 10.2514/6.2021-2792 (cit. on p. 5).

[65] J. L. Gresham, B. M. Simmons, J. W. Hopwood, and C. A. Woolsey, "Spin aerodynamic modeling for a fixed-wing aircraft using flight data," in *AIAA SciTech 2022 Forum*, San Diego, CA: American Institute of Aeronautics and Astronautics, Jan. 2022. DOI: 10.2514/6.2022-1160 (cit. on p. 5).

[66] J. L. Gresham, B. M. Simmons, J. W. Hopwood, and C. A. Woolsey, "Spin aerodynamic modeling for a fixed-wing aircraft using flight data," *Journal of Aircraft*, vol. 61, no. 1, pp. 128–139, 2024. DOI: 10.2514/1.C036835 (cit. on p. 5).

[67] M. H. Halefom, J. W. Hopwood, and C. A. Woolsey, "Unsteady aerodynamics in model-based wind estimation from fixed-wing aircraft motion," *Journal of Guidance, Control, and Dynamics*, vol. 47, no. 8, pp. 1556–1568, 2024. DOI: 10.2514/1.G007836 (cit. on pp. 4, 5, 88, 95).

[68] *High-fidelity unmanned multirotor flight dynamics simulation for off-nominal conditions*. Accessed: May 20, 2023. [Online]. Available: https://software.nasa.gov/software/LAR-19479-1 (cit. on pp. 39, 58).

[69] D. D. Holm, T. Schmah, and C. Stoica, *Geometric Mechanics and Symmetry: From Finite to Infinite Dimensions* (Oxford Texts in Applied and Engineering Mathematics). New York: Oxford University Press, 2009, ISBN: 978-0-19-921291-0 (cit. on p. 11).

[70] J. Hopwood and C. Woolsey, "A symmetry-preserving reduced-order observer," in *2025 American Control Conference*, Denver, CO, Jul. 2025. DOI: 10.48550/arXiv.2411.07998 (cit. on pp. 3, 4, 25).

[71] J. W. Hopwood and C. A. Woolsey, "A noise-to-state stable symmetry-preserving reduced-order observer for wind estimation," in *AIAA SciTech 2025 Forum*, Orlando, FL, Jan. 2025. DOI: 10.2514/6.2025-1625 (cit. on pp. 4, 38, 96).

[72] J. W. Hopwood, J. L. Gresham, and C. A. Woolsey, "Stall spin flight path control using parallel yaw-periodic linear quadratic and robust H∞ controllers," in *AIAA SciTech 2022 Forum*, San Diego, CA: American Institute of Aeronautics and Astronautics, Jan. 2022. DOI: 10.2514/6.2022-1159 (cit. on p. 4).

[73] J. W. Hopwood, J. L. Gresham, and C. A. Woolsey, "Robust stall spin flight path control with flight test validation," *Journal of Guidance, Control, and Dynamics*, vol. 46, no. 3, pp. 553–559, Mar. 2023. DOI: 10.2514/1.G007016 (cit. on p. 4).

[74] J. W. Hopwood, B. M. Simmons, J. K. Cooper, and C. A. Woolsey, "Practical nonlinear flight dynamic modeling for multirotor aircraft," *Journal of Aircraft*, Accepted, 2025 (cit. on pp. 4, 38, 40).

[75] J. W. Hopwood and C. A. Woolsey, "Passivity-based wind estimation for aircraft maneuvering in steady and uniform wind fields," in *AIAA SciTech 2024 Forum*, Orlando, FL: American Institute of Aeronautics and Astronautics, Jan. 2024. DOI: 10.2514/6.2024-2654 (cit. on pp. 4, 130).

[76] J. W. Hopwood and C. A. Woolsey, "Robust linear parameter-varying control for safe and effective unstable aircraft system identification," in *AIAA SciTech 2024 Forum*, Orlando, FL: American Institute of Aeronautics and Astronautics, Jan. 2024. DOI: 10.2514/6.2024-1305 (cit. on pp. 4, 72).

[77] J. W. Hopwood and C. A. Woolsey, "Nonlinear wind estimation using a symmetry-preserving reduced-order observer," in *AIAA SciTech 2025 Forum*, Orlando, FL, Jan. 2025. DOI: 10.2514/6.2025-1626 (cit. on pp. 4, 38, 96).

[78] C. M. Ivler, E. S. Rowe, J. Martin, M. J. Lopez, and M. B. Tischler, "System identification guidance for multirotor aircraft: Dynamic scaling and test techniques," *Journal of the American Helicopter Society*, 2021. DOI: 10.4050/JAHS.66.022006 (cit. on pp. 39, 81).

[79] J. Jacob, P. Chilson, A. Houston, and S. Smith, "Considerations for atmospheric measurements with small unmanned aircraft systems," *Atmosphere*, vol. 9, no. 7, p. 252, Jul. 2018. DOI: 10.3390/atmos9070252 (cit. on p. 1).

[80] R. V. Jategaonkar, *Flight Vehicle System Identification: A Time-Domain Methodology* (Progress in Astronautics and Aeronautics), Second. Reston, VA: American Institute of Aeronautics and Astronautics, Inc., 2015, ISBN: 978-1-62410-278-3 (cit. on pp. 61, 65, 67, 71).

[81] Z.-P. Jiang and D. J. Hill, "Passivity and disturbance attenuation via output feedback for uncertain nonlinear systems," *IEEE Transactions on Automatic Control*, vol. 43, no. 7, pp. 992–997, Jul. 1998. DOI: 10.1109/9.701109 (cit. on pp. 130, 131, 134).

[82] T. A. Johansen and T. I. Fossen, "The eXogenous Kalman filter (XKF)," *International Journal of Control*, vol. 90, no. 2, pp. 161–167, Feb. 2017. DOI: 10.1080/00207179.2016.1172390 (cit. on p. 128).

[83] W. Johnson, *Helicopter Theory*. Princeton, N. J: Princeton Univ. Pr, 1980, ISBN: 978-0-691-07971-4 (cit. on pp. 42, 64).

[84] D. Karagiannis and A. Astolfi, "Nonlinear observer design using invariant manifolds and applications," in *Proceedings of the 44th IEEE Conference on Decision and Control*, Seville, Spain: IEEE, 2005, pp. 7775–7780. DOI: 10.1109/CDC.2005.1583418 (cit. on pp. 25, 27).

[85] D. A. Karr, D. J. Wing, T. L. Barney, V. Sharma, T. J. Etherington, and J. L. Sturdy, "Initial design guidelines for onboard automation of flight path management," in *AIAA AVIATION 2021 Forum*, Virtual, Jul. 2021. DOI: 10.2514/6.2021-2326 (cit. on p. 1).

[86] H. K. Khalil, *Nonlinear Systems*, Second. Upper Saddle Ridge, NJ: Prentice Hall, 1996, ISBN: 0-13-228024-8 (cit. on pp. 13, 56, 107, 131, 146).

[87] W. Khan and M. Nahon, "Toward an accurate physics-based UAV thruster model," *IEEE/ASME Transactions on Mechatronics*, vol. 18, no. 4, pp. 1269–1279, Aug. 2013. DOI: 10.1109/TMECH.2013.2264105 (cit. on p. 46).

[88] R. Khasminskii, *Stochastic Stability of Differential Equations* (Stochastic Modelling and Applied Probability). Berlin: Springer-Verlag, 2012, vol. 66, ISBN: 978-3-642-23279-4. DOI: 10.1007/978-3-642-23280-0 (cit. on p. 22).

[89] P. E. Kloeden and E. Platen, *Numerical Solution of Stochastic Differential Equations*. Berlin, Heidelberg: Springer Berlin Heidelberg, 1992, ISBN: 978-3-642-08107-1. DOI: 10.1007/978-3-662-12616-5 (cit. on p. 21).

[90] A. J. Krener, "The convergence of the extended Kalman filter," in *Directions in Mathematical Systems Theory and Optimization*, A. Rantzer and C. I. Byrnes, Eds., vol. 286, Berlin, Heidelberg: Springer Berlin Heidelberg, 2003, pp. 173–182, ISBN: 978-3-540-00065-5 (cit. on pp. 2, 129).

[91] J. W. Langelaan, N. Alley, and J. Neidhoefer, "Wind field estimation for small unmanned aerial vehicles," *Journal of Guidance, Control, and Dynamics*, vol. 34, no. 4, pp. 1016–1030, Jul. 2011. DOI: 10.2514/1.52532 (cit. on p. 88).

[92] N. R. Lawrance and S. Sukkarieh, "Path planning for autonomous soaring flight in dynamic wind fields," in *2011 IEEE International Conference on Robotics and Automation*, Shanghai, China: IEEE, May 2011, pp. 2499–2505. DOI: 10.1109/ICRA.2011.5979966 (cit. on p. 1).

[93] J. H. Lee, H. E. Sevil, A. Dogan, and D. Hullender, "Estimation of maneuvering aircraft states and time-varying wind with turbulence," *Aerospace Science and Technology*, vol. 31, no. 1, pp. 87–98, Dec. 2013. DOI: 10.1016/j.ast.2013.09.009 (cit. on p. 88).

[94] E. Lefferts, F. Markley, and M. Shuster, "Kalman filtering for spacecraft attitude estimation," *Journal of Guidance, Control, and Dynamics*, vol. 5, no. 5, pp. 417–429, Sep. 1982. DOI: 10.2514/3.56190 (cit. on p. 24).

[95] J. G. Leishman, *Principles of Helicopter Aerodynamics*, Second. Cambridge: Cambridge University Press, 2006, ISBN: 978-1-107-01335-3 (cit. on p. 43).

[96] F. A. P. Lie and D. Gebre-Egziabher, "Synthetic air data system," *Journal of Aircraft*, vol. 50, no. 4, pp. 1234–1249, Jul. 2013. DOI: 10.2514/1.C032177 (cit. on pp. 1, 88).

[97] Y. Lin, E. D. Sontag, and Y. Wang, "A smooth converse Lyapunov theorem for robust stability," *SIAM Journal on Control and Optimization*, vol. 34, no. 1, pp. 124–160, Jan. 1996. DOI: 10.1137/S0363012993259981 (cit. on p. 140).

[98] P. Mahapatra and D. Zrnic, "Sensors and systems to enhance aviation safety against weather hazards," *Proceedings of the IEEE*, vol. 79, no. 9, pp. 1234–1267, Sep. 1991. DOI: 10.1109/5.97295 (cit. on p. 2).

[99] R. Mahony, T. Hamel, and J.-M. Pflimlin, "Nonlinear complementary filters on the special orthogonal group," *IEEE Transactions on Automatic Control*, vol. 53, no. 5, pp. 1203–1218, Jun. 2008. DOI: 10.1109/TAC.2008.923738 (cit. on p. 24).

[100] R. Mahony, J. Trumpf, and T. Hamel, "Observers for kinematic systems with symmetry," *IFAC Proceedings Volumes*, vol. 46, no. 23, pp. 617–633, 2013. DOI: 10.3182/20130904-3-FR-2041.00212 (cit. on p. 24).

[101] E. Mansfield and J. Zhao, "On the Modern Notion of a Moving Frame," in *Guide to Geometric Algebra in Practice*, L. Dorst and J. Lasenby, Eds., London: Springer London, 2011, pp. 411–434, ISBN: 978-0-85729-811-9. DOI: 10.1007/978-0-85729-811-9_20 (cit. on pp. 25, 26).

[102] J. E. Marsden and T. S. Ratiu, *Introduction to Mechanics and Symmetry* (Texts in Applied Mathematics 17), 2nd. New York: Springer, 1999, ISBN: 978-0-387-98643-2 (cit. on pp. 7, 9, 11, 12).

[103] D. Mateos-Núñez and J. Cortés, "Pth moment noise-to-state stability of stochastic differential equations with persistent noise," *SIAM Journal on Control and Optimization*, vol. 52, no. 4, pp. 2399–2421, Jan. 2014. DOI: 10.1137/130924652 (cit. on p. 23).

[104] A. Medina *et al.*, "Evaluation of Doppler wind lidar for advanced air mobility," *Journal of Applied Remote Sensing*, vol. 19, no. 01, Jan. 2025. DOI: 10.1117/1.JRS.19.014509 (cit. on p. 5).

[105] R. H. Miller, "Unsteady air loads on helicopter rotor blades," *The Journal of the Royal Aeronautical Society*, vol. 68, no. 640, pp. 217–229, Apr. 1964. DOI: 10.1017/S0001924000060887 (cit. on p. 38).

[106] D. C. Montgomery, *Design And Analysis of Experiments*, 8th edition. Hoboken, NJ: John Wiley & Sons, Inc., 2013 (cit. on pp. 39, 59, 67).

[107] E. Morelli, "Efficient global aerodynamic modeling from flight data," in *50th AIAA Aerospace Sciences Meeting Including the New Horizons Forum and Aerospace Exposition*, Nashville, TN: American Institute of Aeronautics and Astronautics, Jan. 2012, pp. 1–26. DOI: 10.2514/6.2012-1050 (cit. on p. 71).

[108] E. A. Morelli, "Global nonlinear aerodynamic modeling using multivariate orthogonal functions," *Journal of Aircraft*, vol. 32, no. 2, pp. 270–277, Mar. 1995. DOI: 10.2514/3.46712 (cit. on pp. 121, 143).

[109] E. A. Morelli, "Multiple input design for real-time parameter estimation in the frequency domain," *IFAC Proceedings Volumes*, vol. 36, no. 16, pp. 639–644, Sep. 2003. DOI: 10.1016/S1474-6670(17)34833-4 (cit. on p. 120).

[110] E. A. Morelli, "Flight-test experiment design for characterizing stability and control of hypersonic vehicles," *Journal of Guidance, Control, and Dynamics*, vol. 32, no. 3, pp. 949–959, May 2009. DOI: 10.2514/1.37092 (cit. on p. 120).

[111] E. A. Morelli, *System IDentification Programs for AirCraft (SIDPAC), Version 4.0*, NASA Langley Research Center, 2018 (cit. on pp. 78, 143).

[112] E. A. Morelli, "Practical aspects of multiple-input design for aircraft system identification flight tests," in *AIAA AVIATION 2021 Forum*, VIRTUAL EVENT: American Institute of Aeronautics and Astronautics, Aug. 2021, pp. 1–25. DOI: 10.2514/6.2021-2795 (cit. on p. 81).

[113] E. A. Morelli and V. Klein, *Aircraft System Identification: Theory and Practice*, Second. Williamsburg, Virginia: Sunflyte Enterprises, 2016, ISBN: 0-9974306-1-3 (cit. on pp. 38, 61, 65, 71, 92, 120–122, 124, 142, 143).

[114] D. Morris and C. Pretty, "An experimental study of drag coefficients of a quadrotor airframe," in *Volume 7: 19th IEEE/ASME International Conference on Mechatronic and Embedded Systems and Applications (MESA)*, Boston, MA: American Society of Mechanical Engineers, Aug. 2023. DOI: 10.1115/DETC2023-114020 (cit. on p. 49).

[115] P. Moylan, "A note on Kalman-Bucy filters with zero measurement noise," *IEEE Transactions on Automatic Control*, vol. 19, no. 3, pp. 263–264, Jun. 1974. DOI: 10.1109/TAC.1974.1100570 (cit. on p. 112).

[116] R. M. Murray, Z. Li, and S. S. Sastry, *A Mathematical Introduction to Robotic Manipulation*. CRC Press, Dec. 2017, ISBN: 978-1-315-13637-0. DOI: 10.1201/9781315136370 (cit. on p. 7).

[117] R. H. Myers, D. C. Montgomery, and C. M. Anderson-Cook, *Response Surface Methodology: Process and Product Optimization Using Designed Experiments*, 4th ed. John Wiley & Sons, 2016 (cit. on pp. 39, 59).

[118] N. Nguyen and B. Webb, "Analytical flight dynamic model development for eVTOL aircraft," in *AIAA SciTech 2025 Forum*, Orlando, FL: American Institute of Aeronautics and Astronautics, Jan. 2025, pp. 1–28. DOI: 10.2514/6.2025-0657 (cit. on p. 39).

[119] R. Niemiec, C. Ivler, F. Gandhi, and F. Sanders, "Multirotor electric aerial vehicle model identification with flight data with corrections to physics-based models," *CEAS Aeronautical Journal*, vol. 13, no. 3, pp. 575–596, Jul. 2022. DOI: 10.1007/s13272-022-00583-5 (cit. on p. 39).

[120] P. Niermeyer, T. Raffler, and F. Holzapfel, "Open-loop quadrotor flight dynamics identification in frequency domain via closed-loop flight testing," in *AIAA Guidance, Navigation, and Control Conference*, Kissimmee, FL: American Institute of Aeronautics and Astronautics, Jan. 2015, p. 14. DOI: 10.2514/6.2015-1539 (cit. on p. 39).

[121] B. Øksendal, *Stochastic Differential Equations* (Universitext). Berlin, Heidelberg: Springer Berlin Heidelberg, 2003, ISBN: 978-3-540-04758-2. DOI: 10.1007/978-3-642-14394-6 (cit. on p. 18).

[122] P. J. Olver, *Classical Invariant Theory*. Cambridge University Press, Jan. 1999, ISBN: 978-0-521-55243-1. DOI: 10.1017/CBO9780511623660 (cit. on pp. 9, 25, 26, 31, 33).

[123] R. T. Palomaki, N. T. Rose, M. van den Bossche, T. J. Sherman, and S. F. J. De Wekker, "Wind estimation in the lower atmosphere using multirotor aircraft," *Journal of Atmospheric and Oceanic Technology*, vol. 34, no. 5, pp. 1183–1191, May 2017. DOI: 10.1175/JTECH-D-16-0177.1 (cit. on pp. 1, 94).

[124] V. S. Pappu, Y. Liu, J. S. Horn, and J. Cooper, "Wind gust estimation on a small VTOL UAV," in *7th AHS Technical Meeting on VTOL Unmanned Aircraft Systems*, Fairfax, VA: American Helicopter Society, 2017, p. 19 (cit. on p. 88).

[125] G. A. Pavliotis, *Stochastic Processes and Applications: Diffusion Processes, the Fokker-Planck and Langevin Equations* (Texts in Applied Mathematics). New York, NY: Springer, 2014, vol. 60, ISBN: 978-1-4939-1322-0. DOI: 10.1007/978-1-4939-1323-7 (cit. on pp. 18, 21).

[126] G. Perozzi, D. Efimov, J.-M. Biannic, and L. Planckaert, "Using a quadrotor as wind sensor: Time-varying parameter estimation algorithms," *International Journal of Control*, vol. 95, no. 1, pp. 126–137, Jan. 2022. DOI: 10.1080/00207179.2020.1780324 (cit. on p. 88).

[127] D. A. Peters and C. J. He, "Finite state induced flow models Part II: Three-dimensional rotor disk," *Journal of Aircraft*, vol. 32, no. 2, pp. 323–333, Mar. 1995. DOI: 10.2514/3.46719 (cit. on p. 38).

[128] C. Reiche, A. P. Cohen, and C. Fernando, "An initial assessment of the potential weather barriers of urban air mobility," *IEEE Transactions on Intelligent Transportation Systems*, vol. 22, no. 9, pp. 6018–6027, Sep. 2021. DOI: 10.1109/TITS.2020.3048364 (cit. on p. 1).

[129] D. Rotondo, F. Nejjari, and V. Puig, "Robust state-feedback control of uncertain LPV systems: An LMI-based approach," *Journal of the Franklin Institute*, vol. 351, no. 5, pp. 2781–2803, May 2014. DOI: 10.1016/j.jfranklin.2014.01.018 (cit. on p. 84).

[130] W. J. Rugh, *Linear System Theory* (Prentice Hall Information and System Sciences Series), Second. Upper Saddle River, N.J: Prentice Hall, 1996, ISBN: 978-0-13-441205-4 (cit. on pp. 24, 104).

[131] H. Shim, "A Passivity-based Nonlinear Observer and a Semi-global Separation Principle," Ph.D. dissertation, School of Electrical Engineering, Seoul National University, Feb. 2000 (cit. on p. 130).

[132] H. Shim, J. H. Seo, and A. R. Teel, "Nonlinear observer design via passivation of error dynamics," *Automatica*, vol. 39, no. 5, pp. 885–892, May 2003. DOI: 10.1016/S0005-1098(03)00023-2 (cit. on pp. 130, 131, 134, 136, 138, 139).

[133] B. M. Simmons, "Advances in Aero-Propulsive Modeling for Fixed-Wing and eVTOL Aircraft Using Experimental Data," Ph.D. dissertation, Virginia Polytechnic Institute and State University, Blacksburg, VA, Apr. 2023 (cit. on pp. 120, 122).

[134] B. M. Simmons, "System identification approach for eVTOL aircraft demonstrated using simulated flight data," *Journal of Aircraft*, pp. 1–16, Feb. 2023. DOI: 10.2514/1.C036896 (cit. on p. 39).

[135] B. M. Simmons, J. L. Gresham, and C. A. Woolsey, "Aero-propulsive modeling for propeller aircraft using flight data," *Journal of Aircraft*, vol. 60, no. 1, pp. 81–96, Jan. 2023. DOI: 10.2514/1.C036773 (cit. on pp. 38, 81, 120, 142).

[136] B. M. Simmons, J. L. Gresham, and C. A. Woolsey, "Flight-test system identification techniques and applications for small, low-cost, fixed-wing aircraft," *Journal of Aircraft*, vol. 60, no. 5, pp. 1503–1521, Sep. 2023. DOI: 10.2514/1.C037260 (cit. on pp. 74, 122, 142).

[137] B. M. Simmons, H. G. McClelland, and C. A. Woolsey, "Nonlinear model identification methodology for small, fixed-wing, unmanned aircraft," *Journal of Aircraft*, vol. 56, no. 3, pp. 1056–1067, May 2019. DOI: 10.2514/1.C035160 (cit. on p. 72).

[138] E. J. J. Smeur, Q. Chu, and G. C. H. E. de Croon, "Adaptive incremental nonlinear dynamic inversion for attitude control of micro air vehicles," *Journal of Guidance, Control, and Dynamics*, vol. 39, no. 3, pp. 450–461, Mar. 2016. DOI: 10.2514/1.G001490 (cit. on pp. 38, 47).

[139] Stat-Ease, *Design-expert*. Accessed: May 21, 2023. [Online]. Available: https://www.statease.com/software/design-expert/ (cit. on p. 59).

[140] D. Stratton and R. Stengel, "Real-time decision aiding: Aircraft guidance for wind shear avoidance," *IEEE Transactions on Aerospace and Electronic Systems*, vol. 31, no. 1, pp. 117–124, Jan. 1995. DOI: 10.1109/7.366298 (cit. on p. 2).

[141] K. Sun, C. D. Regan, and D. Gebre-Egziabher, "Observability and performance analysis of a model-free synthetic air data estimator," *Journal of Aircraft*, vol. 56, no. 4, pp. 1471–1486, Jul. 2019. DOI: 10.2514/1.C035290 (cit. on p. 1).

[142] S. Sun, C. C. de Visser, and Q. Chu, "Quadrotor gray-box model identification from high-speed flight data," *Journal of Aircraft*, vol. 56, no. 2, pp. 645–661, Mar. 2019. DOI: 10.2514/1.C035135 (cit. on p. 39).

[143] T. Tao, *An Introduction to Measure Theory* (Graduate Studies in Mathematics vol. 126). Providence, RI: American Mathematical Society, 2011, ISBN: 978-0-8218-6919-2 (cit. on p. 15).

[144] D. P. Thipphavong *et al.*, "Urban air mobility airspace integration concepts and considerations," in *2018 Aviation Technology, Integration, and Operations Conference*, Atlanta, GA: American Institute of Aeronautics and Astronautics, Jun. 2018. DOI: 10.2514/6.2018-3676 (cit. on p. 1).

[145] P. Tian, H. Chao, M. Rhudy, J. Gross, and H. Wu, "Wind sensing and estimation using small fixed-wing unmanned aerial vehicles: A survey," *Journal of Aerospace Information Systems*, vol. 18, no. 3, pp. 132–143, Mar. 2021. DOI: 10.2514/1.I010885 (cit. on p. 88).

[146] R. Trub, D. Moser, M. Schafer, R. Pinheiro, and V. Lenders, "Monitoring meteorological parameters with crowdsourced air traffic control data," in *2018 17th ACM/IEEE International Conference on Information Processing in Sensor Networks (IPSN)*, Porto: IEEE, Apr. 2018, pp. 25–36. DOI: 10.1109/IPSN.2018.00010 (cit. on p. 1).

[147] L. W. Tu, *An Introduction to Manifolds* (Universitext). New York, NY: Springer, 2011, ISBN: 978-1-4419-7399-3. DOI: 10.1007/978-1-4419-7400-6 (cit. on pp. 7, 8).

[148] U.S. Department of Defense, *MIL-HDBK-1797: Flying Qualities of Piloted Aircraft*, Dec. 1997 (cit. on p. 91).

[149] P. M. Van Den Hof and R. J. Schrama, "Identification and control — Closed-loop issues," *Automatica*, vol. 31, no. 12, pp. 1751–1770, Dec. 1995. DOI: 10.1016/0005-1098(95)00094-X (cit. on p. 71).

[150] P. Van Goor, T. Hamel, and R. Mahony, "Equivariant filter (EqF)," *IEEE Transactions on Automatic Control*, vol. 68, no. 6, pp. 3501–3512, Jun. 2023. DOI: 10.1109/TAC.2022.3194094 (cit. on p. 24).

[151] A. Venkatraman and A. van der Schaft, "Full-order observer design for a class of port-Hamiltonian systems," *Automatica*, vol. 46, no. 3, pp. 555–561, Mar. 2010. DOI: 10.1016/j.automatica.2010.01.019 (cit. on pp. 131, 135).

[152] P. Wei, X. Lin, and Z. Kong, "System identification of wind effects on multirotor aircraft," *International Journal of Intelligent Robotics and Applications*, vol. 6, no. 1, pp. 104–118, Mar. 2022. DOI: 10.1007/s41315-021-00185-0 (cit. on p. 39).

[153] J. C. Willems, "Dissipative Dynamical Systems Part I: General Theory," *Archive for Rational Mechanics and Analysis*, vol. 45, no. 5, pp. 321–351, Jan. 1972. DOI: 10.1007/BF00276493 (cit. on p. 129).

[154] J. Wolkovitch, "Analytical prediction of vortex-ring boundaries for helicopters in steep descents," *Journal of the American Helicopter Society*, vol. 17, no. 3, pp. 13–19, Jul. 1972. DOI: 10.4050/JAHS.17.13 (cit. on p. 60).

[155] C. Woolsey and L. Techy, "Cross-track control of a slender, underactuated AUV using potential shaping," *Ocean Engineering*, vol. 36, no. 1, pp. 82–91, Jan. 2009. DOI: 10.1016/j.oceaneng.2008.07.010 (cit. on p. 132).

[156] X. Xiang, Z. Wang, Z. Mo, G. Chen, K. Pham, and E. Blasch, "Wind field estimation through autonomous quadcopter avionics," in *2016 IEEE/AIAA 35th Digital Avionics Systems Conference (DASC)*, Sacramento, CA, USA: IEEE, Sep. 2016, pp. 1–6. DOI: 10.1109/DASC.2016.7778071 (cit. on p. 88).

[157] S. Yang and S. Jeon, "Recursive path planning and wind field estimation for precision airdrop," *Journal of Guidance, Control, and Dynamics*, vol. 42, no. 6, pp. 1429–1437, Jun. 2019. DOI: 10.2514/1.G003944 (cit. on p. 1).

[158] H. D. Young, *Statistical Treatment of Experimental Data: An Introduction to Statistical Methods*. New York: McGraw-Hill, 1962, ISBN: 978-0-07-072646-8 (cit. on p. 64).

[159] H. Yu, X. Liang, and X. Lyu, "DOB-based wind estimation of a UAV using its onboard sensor," in *2024 IEEE/RSJ International Conference on Intelligent Robots and Systems (IROS)*, Abu Dhabi: IEEE, Oct. 2024, pp. 8126–8133. DOI: 10.1109/IROS58592.2024.10801906 (cit. on p. 88).

Appendix A

Modeling and System Identification

A.1 Derivation of Model 1

We begin by computing the rigid body force vector (4.22) using the rotor force components in Eq. (4.15) evaluated at the local rotor velocities, $\boldsymbol{v}_i$, as approximated by Eq. (4.27).

$$\begin{aligned}
X_{\mathrm{r}} &= \rho\pi R^2 u \sum_{i=1}^{N_{\mathrm{r}}} \Big(-C_{H_{\mu_x}} R\Omega_i - C_{H_{\mu_0,\mu_x}} \nu_0 - C_{H_{\mu_x^2}} v_x - C_{H_{\mu_x,\mu_z}} (w + py_i - qx_i) \Big) \\
Y_{\mathrm{r}} &= \rho\pi R^2 v \sum_{i=1}^{N_{\mathrm{r}}} \Big(-C_{H_{\mu_x}} R\Omega_i - C_{H_{\mu_0,\mu_x}} \nu_0 - C_{H_{\mu_x^2}} v_x - C_{H_{\mu_x,\mu_z}} (w + py_i - qx_i) \Big) \\
Z_{\mathrm{r}} &= \rho\pi R^2 \sum_{i=1}^{N_{\mathrm{r}}} \Big(- C_{T_0} R^2 \Omega_i^2 + C_{T_{\mu_0}} R\nu_0 \Omega_i - C_{T_{\mu_x}} R v_x \Omega_i \\
&\qquad + C_{T_{\mu_z}} R(w + py_i - qx_i)\Omega_i - C_{T_{\mu_x^2}} v_x^2 \Big)
\end{aligned} \tag{A.1}$$

Recall from the virtual actuator definitions in Eqs. (4.28) and (4.30) that $\delta^2 t = \frac{1}{N_{\mathrm{r}}} \sum_{i=1}^{N_{\mathrm{r}}} \Omega_i^2$, $\delta t = \frac{1}{N_{\mathrm{r}}} \sum_{i=1}^{N_{\mathrm{r}}} \Omega_i$, $\delta a = -\sum_{i=1}^{N_{\mathrm{r}}} y_i \Omega_i$, and $\delta e = \sum_{i=1}^{N_{\mathrm{r}}} x_i \Omega_i$. Additionally, Assumption 4.4c implies $\sum_{i=1}^{N_{\mathrm{r}}} x_i = \sum_{i=1}^{N_{\mathrm{r}}} y_i = 0$. Thus, Eq. (A.1) reduces to

$$\begin{aligned}
X_{\mathrm{r}} &= \rho\pi R^2 N_{\mathrm{r}} u \Big(-C_{H_{\mu_x}} R\delta t - C_{H_{\mu_0,\mu_x}} \nu_0 + C_{H_{\mu_x^2}} v_x - C_{H_{\mu_x,\mu_z}} w \Big) \\
Y_{\mathrm{r}} &= \rho\pi R^2 N_{\mathrm{r}} v \Big(-C_{H_{\mu_x}} R\delta t - C_{H_{\mu_0,\mu_x}} \nu_0 + C_{H_{\mu_x^2}} v_x - C_{H_{\mu_x,\mu_z}} w \Big) \\
Z_{\mathrm{r}} &= \rho\pi R^2 \Big(- C_{T_0} R^2 N_{\mathrm{r}} \delta^2 t + C_{T_{\mu_0}} R N_{\mathrm{r}} \nu_0 \delta t - C_{T_{\mu_x}} R N_{\mathrm{r}} v_x \delta t + C_{T_{\mu_z}} R(N_{\mathrm{r}} w \delta t - \Delta\nu_Z) - C_{T_{\mu_x^2}} N_{\mathrm{r}} v_x^2 \Big)
\end{aligned}$$

Finally, adding the airframe-specific force $\boldsymbol{F}_{\mathrm{a}}$, we obtain the force components in Model 1.

Recall from Eq. (4.23), the total rotor-based moment about the body frame origin is the sum of the rotor moments plus the sum of the moments due to the rotor forces. We first write the components of the moment vector due to rotor aerodynamic moments, given by Eq. (4.19), as

$$\begin{aligned}
-\sum_{i=1}^{N_{\mathrm{r}}} \sigma_i \mathcal{L}_{\mathrm{r},i} = \rho\pi R^2 \sum_{i=1}^{N_{\mathrm{r}}} \sigma_i \Big(& C_{R_{\mu_x}} R^2 \Omega_i u - C_{R_{\mu_0,\mu_x}} R\nu_0 u + C_{R_{\mu_x^2}} R v_x u \\
& - C_{R_{\mu_x,\mu_z}} Ru(w + py_i - qx_i) \Big)
\end{aligned}$$

$$-\sum_{i=1}^{N_\mathrm{r}}\sigma_i\mathcal{M}_{\mathrm{r},i}=\rho\pi R^2\sum_{i=1}^{N_\mathrm{r}}\sigma_i\Big(C_{R_{\mu_x}}R^2\Omega_i v-C_{R_{\mu_0,\mu_x}}R\nu_0 v+C_{R_{\mu_x^2}}Rv_x v \\ -C_{R_{\mu_x,\mu_z}}Rv(w+py_i-qx_i)\Big)$$

$$-\sum_{i=1}^{N_\mathrm{r}}\sigma_i\mathcal{N}_{\mathrm{r},i}=\rho\pi R^2\sum_{i=1}^{N_\mathrm{r}}\sigma_i\Big(-C_{Q_0}R^3\Omega_i^2-C_{Q_{\mu_0}}R^2\nu_0\Omega_i+C_{Q_{\mu_x}}R^2v_x\Omega_i-C_{Q_{\mu_z}}R^2(w+py_i-qx_i)\Omega_i \\ +C_{Q_{\mu_0^2}}R\nu_0^2+C_{Q_{\mu_x^2}}Rv_x^2+C_{Q_{\mu_z^2}}R(w+py_i-qx_i)^2-C_{Q_{\mu_0,\mu_x}}R\nu_0 v_x \\ +C_{Q_{\mu_0,\mu_z}}R\nu_0(w+py_i-qx_i)-C_{Q_{\mu_x,\mu_z}}Rv_x(w+py_i-qx_i)\Big)$$

By Assumption 4.4b, $\sum_{i=1}^{N_\mathrm{r}}\sigma_i=0$. Additionally, the combination of Assumptions 4.4a, 4.4c, and 4.4d imply $\sum_{i=1}^{N_\mathrm{r}}\sigma_i x_i=\sum_{i=1}^{N_\mathrm{r}}\sigma_i y_i=0$. Therefore, we have

$$\begin{aligned}
-\sum_{i=1}^{N_\mathrm{r}}\sigma_i\mathcal{L}_{\mathrm{r},i}&=\rho\pi R^2\left(C_{R_{\mu_x}}R^2u\sum_{i=1}^{N_\mathrm{r}}\sigma_i\Omega_i\right)\\
-\sum_{i=1}^{N_\mathrm{r}}\sigma_i\mathcal{M}_{\mathrm{r},i}&=\rho\pi R^2\left(C_{R_{\mu_x}}R^2v\sum_{i=1}^{N_\mathrm{r}}\sigma_i\Omega_i\right)\\
-\sum_{i=1}^{N_\mathrm{r}}\sigma_i\mathcal{N}_{\mathrm{r},i}&=\rho\pi R^2\sum_{i=1}^{N_\mathrm{r}}\sigma_i\Big(-C_{Q_0}R^3\Omega_i^2-C_{Q_{\mu_0}}R^2\nu_0\Omega_i+C_{Q_{\mu_x}}R^2v_x\Omega_i\\
&\qquad -C_{Q_{\mu_z}}R^2(w+py_i-qx_i)\Omega_i+C_{Q_{\mu_z^2}}R(py_i-qx_i)^2\Big)
\end{aligned}$$

From the virtual actuator definitions in Eqs. (4.28) and (4.30), $\delta^2 r=-\sum_{i=1}^{N_\mathrm{r}}\sigma_i\Omega_i^2$ and $\delta r=-\sum_{i=1}^{N_\mathrm{r}}\sigma_i\Omega_i$. Thus,

$$\begin{aligned}
-\sum_{i=1}^{N_\mathrm{r}}\sigma_i\mathcal{L}_{\mathrm{r},i}&=\rho\pi R^2\left(-C_{R_{\mu_x}}R^2u\delta r\right)\\
-\sum_{i=1}^{N_\mathrm{r}}\sigma_i\mathcal{M}_{\mathrm{r},i}&=\rho\pi R^2\left(-C_{R_{\mu_x}}R^2v\delta r\right)\\
-\sum_{i=1}^{N_\mathrm{r}}\sigma_i\mathcal{N}_{\mathrm{r},i}&=\rho\pi R^2\Big(C_{Q_0}R^3\delta^2 r+C_{Q_{\mu_0}}R^2\nu_0\delta r-C_{Q_{\mu_x}}R^2v_x\delta r\\
&\qquad +C_{Q_{\mu_z}}R^2\Big(w\delta r-\Delta\nu_w\Big)-C_{Q_{\mu_z^2}}R\Delta\nu_{\mathcal{N}}^2\Big)
\end{aligned}\tag{A.2}$$

where

$$\Delta\nu_{\mathcal{N}}\coloneqq\sum_{i=1}^{N_\mathrm{r}}\sigma_i(py_i-qx_i)\Omega_i$$

$$\Delta\nu_{\mathcal{N}}^2\coloneqq-\sum_{i=1}^{N_\mathrm{r}}\sigma_i(py_i-qx_i)^2$$

Next, the contribution of rotor forces to the total aerodynamic moment is

$$\sum_{i=1}^{N_\mathrm{r}} \boldsymbol{p}_i \times \boldsymbol{F}_{\mathrm{r},i} = \sum_{i=1}^{N_\mathrm{r}} \begin{bmatrix} y_i Z_{\mathrm{r},i} + h Y_{\mathrm{r},i} \\ -x_i Z_{\mathrm{r},i} - h X_{\mathrm{r},i} \\ x_i Y_{\mathrm{r},i} - y_i X_{\mathrm{r},i} \end{bmatrix}$$

where we have made use of Assumption 4.4e that $z_i = -h$. Using the rotor force components from Eq. (4.15) evaluated at the local rotor velocities, it follows that

$$\begin{aligned}
\sum_{i=1}^{N_\mathrm{r}} (y_i Z_{\mathrm{r},i} + h Y_{\mathrm{r},i}) &= \rho\pi R^2 \sum_{i=1}^{N_\mathrm{r}} \Big(- C_{T_0} R^2 y_i \Omega_i^2 + C_{T_{\mu_0}} R \nu_0 y_i \Omega_i - C_{T_{\mu_x}} R v_x y_i \Omega_i \\
&\qquad + C_{T_{\mu_z}} R y_i (w + p y_i - q x_i) \Omega_i - C_{T_{\mu_x^2}} v_x^2 y_i - C_{H_{\mu_x}} R h \Omega_i v \\
&\qquad - C_{H_{\mu_0,\mu_x}} h \nu_0 v + C_{H_{\mu_x^2}} h v_x v - C_{H_{\mu_x,\mu_z}} h v (w + p y_i - q x_i) \Big) \\
\sum_{i=1}^{N_\mathrm{r}} (-x_i Z_{\mathrm{r},i} - h X_{\mathrm{r},i}) &= \rho\pi R^2 \sum_{i=1}^{N_\mathrm{r}} \Big(C_{T_0} R^2 x_i \Omega_i^2 - C_{T_{\mu_0}} R \nu_0 x_i \Omega_i + C_{T_{\mu_x}} R v_x x_i \Omega_i \\
&\qquad - C_{T_{\mu_z}} R x_i (w + p y_i - q x_i) \Omega_i + C_{T_{\mu_x^2}} v_x^2 x_i + C_{H_{\mu_x}} R h \Omega_i u \\
&\qquad + C_{H_{\mu_0,\mu_x}} h \nu_0 u - C_{H_{\mu_x^2}} h v_x u + C_{H_{\mu_x,\mu_z}} h u (w + p y_i - q x_i) \Big) \\
\sum_{i=1}^{N_\mathrm{r}} (x_i Y_{\mathrm{r},i} - y_i X_{\mathrm{r},i}) &= \rho\pi R^2 \sum_{i=1}^{N_\mathrm{r}} \Big(C_{H_{\mu_x}} R (u y_i - v x_i) \Omega_i + C_{H_{\mu_0,\mu_x}} \nu_0 (u y_i - v x_i) \\
&\qquad + C_{H_{\mu_x,\mu_z}} (u y_i - v x_i)(w + p y_i - q x_i) + C_{H_{\mu_x^2}} v_x (u y_i - v x_i) \Big)
\end{aligned} \tag{A.3}$$

Recall, Assumption 4.4c implies $\sum_{i=1}^{N_\mathrm{r}} x_i = \sum_{i=1}^{N_\mathrm{r}} y_i = 0$. Furthermore, Assumptions 4.4c and 4.4d together imply $\sum_{i=1}^{N_\mathrm{r}} x_i y_i = 0$ and $\sum_{i=1}^{N_\mathrm{r}} x_i^2 = \sum_{i=1}^{N_\mathrm{r}} y_i^2 = \frac{1}{2} N_\mathrm{r} \ell^2$. Using these facts and the virtual actuator definitions, Eq. (A.3) simplifies to

$$\begin{aligned}
\sum_{i=1}^{N_\mathrm{r}} (y_i Z_{\mathrm{r},i} + h Y_{\mathrm{r},i}) &= \rho\pi R^2 \Big(C_{T_0} R^2 \delta^2 a - C_{T_{\mu_0}} R \nu_0 \delta a + C_{T_{\mu_x}} R v_x \delta a \\
&\qquad - C_{T_{\mu_z}} R \Big(w \delta a - \Delta\nu_{\mathcal{L}} \Big) - C_{H_{\mu_x}} R N_\mathrm{r} h v \delta t \\
&\qquad - C_{H_{\mu_0,\mu_x}} N_\mathrm{r} h \nu_0 v - C_{H_{\mu_x,\mu_z}} N_\mathrm{r} h v w - C_{H_{\mu_x^2}} N_\mathrm{r} h v_x v \Big) \\
\sum_{i=1}^{N_\mathrm{r}} (-x_i Z_{\mathrm{r},i} - h X_{\mathrm{r},i}) &= \rho\pi R^2 \Big(C_{T_0} R^2 \delta^2 e - C_{T_{\mu_0}} R \nu_0 \delta e + C_{T_{\mu_x}} R v_x \delta e \\
&\qquad - C_{T_{\mu_z}} R \Big(w \delta e - \Delta\nu_{\mathcal{M}} \Big) + C_{H_{\mu_x}} R N_\mathrm{r} h u \delta t \\
&\qquad + C_{H_{\mu_0,\mu_x}} N_\mathrm{r} h \nu_0 u + C_{H_{\mu_x,\mu_z}} N_\mathrm{r} h u w + C_{H_{\mu_x^2}} N_\mathrm{r} h v_x u \Big) \\
\sum_{i=1}^{N_\mathrm{r}} (x_i Y_{\mathrm{r},i} - y_i X_{\mathrm{r},i}) &= \rho\pi R^2 \Big(- C_{H_{\mu_x}} R (u \delta a + v \delta e) + \frac{1}{2} C_{H_{\mu_x,\mu_z}} N_\mathrm{r} \ell^2 (u p + v q) \Big)
\end{aligned} \tag{A.4}$$

where

$$\Delta\nu_{\mathcal{L}} \coloneqq \sum_{i=1}^{N_\mathrm{r}} y_i(py_i - qx_i)\Omega_i$$
$$\Delta\nu_{\mathcal{M}} \coloneqq \sum_{i=1}^{N_\mathrm{r}} x_i(qx_i - py_i)\Omega_i$$

Altogether, Eqs. (A.2) and (A.4) are substituted into the total rotor-based aerodynamic moment given by Eq. (4.23) to obtain

$$\begin{aligned}
\mathcal{L}_\mathrm{r} = \rho\pi R^2\Big(&- C_{R_{\mu_x}} R^2 u\delta r + C_{T_0} R^2\delta^2 a - C_{T_{\mu_0}} R\nu_0\delta a + C_{T_{\mu_x}} Rv_x\delta a \\
&- C_{T_{\mu_z}} R\Big(w\delta a - \Delta\nu_{\mathcal{L}}\Big) - C_{H_{\mu_x}} RN_\mathrm{r} hv\delta t - C_{H_{\mu_0,\mu_x}} N_\mathrm{r} hv\nu_0 \\
&+ C_{H_{\mu_x^2}} N_\mathrm{r} hvv_x - C_{H_{\mu_x,\mu_z}} N_\mathrm{r} hvw\Big) \\
\mathcal{M}_\mathrm{r} = \rho\pi R^2\Big(&- C_{R_{\mu_x}} R^2 v\delta r + C_{T_0} R^2\delta^2 e - C_{T_{\mu_0}} R\nu_0\delta e + C_{T_{\mu_x}} Rv_x\delta e \\
&- C_{T_{\mu_z}} R\Big(w\delta e - \Delta\nu_{\mathcal{M}}\Big) + C_{H_{\mu_x}} RN_\mathrm{r} hu\delta t + C_{H_{\mu_0,\mu_x}} N_\mathrm{r} hu\nu_0 \\
&- C_{H_{\mu_x^2}} N_\mathrm{r} huv_x + C_{H_{\mu_x,\mu_z}} N_\mathrm{r} huw\Big) \\
\mathcal{N}_\mathrm{r} = \rho\pi R^2\Big(&C_{Q_0} R^3\delta^2 r + C_{Q_{\mu_0}} R^2\nu_0\delta r - C_{Q_{\mu_x}} R^2 v_x\delta r + C_{Q_{\mu_z}} R^2\Big(w\delta r - \Delta\nu_{\mathcal{N}}\Big) \\
&- C_{Q_{\mu_z^2}} R\Delta\nu_{\mathcal{N}}^2 - C_{H_{\mu_x}} R(u\delta a + v\delta e) + \frac{1}{2} C_{H_{\mu_x,\mu_z}} N_\mathrm{r}\ell^2(up + vq)\Big)
\end{aligned}$$

The airframe and gyroscopic moments are added to Eq. (A.5) according to Eq. (4.25) to yield the moment components given in Model 1.

Finally, we derive expressions for $\Delta\nu_{\mathcal{L}}$, $\Delta\nu_{\mathcal{M}}$, $\Delta\nu_{\mathcal{N}}$, and $\Delta\nu_{\mathcal{N}}^2$ in terms of virtual actuators and show how their expressions depend on the class of configurations given in Definition 4.1. It turns out the structure of $\mathbf{M_{ix}}$ under Assumption 4.4 allows us to readily compute its pseudoinverse. First, notice that Assumption 4.4 implies $\mathbf{M_{ix}}$ can be written as

$$\mathbf{M_{ix}} = \begin{bmatrix} \frac{1}{N_\mathrm{r}} & \frac{1}{N_\mathrm{r}} & \cdots & \frac{1}{N_\mathrm{r}} & \frac{1}{N_\mathrm{r}} \\ -\ell\sin\theta_1 & -\ell\sin\theta_2 & \cdots & -\ell\sin\theta_{N_\mathrm{r}-1} & -\ell\sin\theta_{N_\mathrm{r}} \\ \ell\cos\theta_1 & \ell\cos\theta_2 & \cdots & \ell\cos\theta_{N_\mathrm{r}-1} & \ell\cos\theta_{N_\mathrm{r}} \\ -1 & +1 & \cdots & -1 & +1 \end{bmatrix}$$

where θ_i is the angle from the $\boldsymbol{b}_1$ axis of the ith rotor arm. Therefore,

$$\mathbf{M_{ix}}\mathbf{M_{ix}}^\mathsf{T} = \begin{bmatrix} \frac{1}{N_\mathrm{r}} & -\frac{\ell}{N_\mathrm{r}}\sum\cos\theta_i & \frac{\ell}{N_\mathrm{r}}\sum\sin\theta_i & 0 \\ -\frac{\ell}{N_\mathrm{r}}\sum\cos\theta_i & \ell^2\sum\cos^2\theta_i & -\frac{\ell}{2}\sum\sin(2\theta_i) & \ell\sum(-1)^{i-1}\cos\theta_i \\ \frac{\ell}{N_\mathrm{r}}\sum\sin\theta_i & -\frac{\ell}{2}\sum\sin(2\theta_i) & \ell^2\sum\sin^2\theta_i & -\ell\sum(-1)^{i-1}\sin\theta_i \\ 0 & \ell\sum(-1)^{i-1}\cos\theta_i & -\ell\sum(-1)^{i-1}\sin\theta_i & N_\mathrm{r} \end{bmatrix}$$

where the sum, $\sum$, is from $i = 1$ to N_r. By the symmetry implied by Assumption 4.4,

$$\mathbf{M_{ix}}\mathbf{M_{ix}^\mathsf{T}} = \mathbf{diag}\left(\frac{1}{N_\mathrm{r}}, \frac{N_\mathrm{r}}{2}\ell^2, \frac{N_\mathrm{r}}{2}\ell^2, N_\mathrm{r}\right) \implies \left(\mathbf{M_{ix}}\mathbf{M_{ix}^\mathsf{T}}\right)^{-1} = \mathbf{diag}\left(N_\mathrm{r}, \frac{2}{N_\mathrm{r}\ell^2}, \frac{2}{N_\mathrm{r}\ell^2}, \frac{1}{N_\mathrm{r}}\right)$$

Finally, the pseudoinverse of $\mathbf{M_{ix}}$ is

$$\mathbf{M_{ix}^\dagger} = \mathbf{M_{ix}^\mathsf{T}}\,\mathbf{diag}\left(N_\mathrm{r}, \frac{2}{N_\mathrm{r}\ell^2}, \frac{2}{N_\mathrm{r}\ell^2}, \frac{1}{N_\mathrm{r}}\right) \tag{A.5}$$

Consider the configuration-dependent term $\Delta\nu_\mathcal{L} := \sum_{i=1}^{N_\mathrm{r}} y_i(py_i - qx_i)\Omega_i$. Using Eq. (A.5), we have

$$\begin{aligned}\Delta\nu_\mathcal{L} &:= \sum_{i=1}^{N_\mathrm{r}} y_i(py_i - qx_i)\Omega_i \\ &= \sum_{i=1}^{N_\mathrm{r}} \ell\sin\theta_i(p\ell\sin\theta_i - q\ell\cos\theta_i)(\delta t - \delta a\frac{2}{N_\mathrm{r}\ell}\sin\theta_i + \delta e\frac{2}{N_\mathrm{r}\ell}\cos\theta_i - \frac{1}{N_\mathrm{r}}\delta r(-1)^{i-1})\end{aligned}$$

Expanding, we have

$$\begin{aligned}\Delta\nu_\mathcal{L} = p\ell^2\delta t\sum\sin^2\theta_i - p\ell^2\frac{1}{N_\mathrm{r}}\delta r\sum(-1)^{i-1}\sin^2\theta_i + q\frac{\ell^2}{2}\frac{1}{N_\mathrm{r}}\delta r\sum(-1)^{i-1}\sin(2\theta_i) \\ - q\frac{\ell^2}{2}\delta t\sum\sin(2\theta_i) - p\frac{\ell}{2}(\delta a\sum\sin^3\theta_i - \delta e\sum\sin^2\theta_i\cos\theta_i) \\ + q\frac{\ell}{2}(\delta a\sum\sin^2\theta_i\cos\theta_i - \delta e\sum\sin\theta_i\cos^2\theta_i)\end{aligned} \tag{A.6}$$

By Assumption 4.4, the second and third lines of Eq. (A.6) vanish. Thus, we have

$$\Delta\nu_\mathcal{L} = \frac{1}{2}\ell^2 pN_\mathrm{r}\delta t - p\ell^2\frac{1}{N_\mathrm{r}}\delta r\sum(-1)^{i-1}\sin^2\theta_i + q\frac{\ell^2}{2}\frac{1}{N_\mathrm{r}}\delta r\sum(-1)^{i-1}\sin(2\theta_i) \tag{A.7}$$

The second two terms in Eq. (A.7) are zero for $N_\mathrm{r} \geq 6$. For $N_\mathrm{r} = 4$, they are $\frac{1}{2}\ell^2\left(p\cos(2\theta_0) + q\sin(2\theta_0)\right)\delta r$, where θ_0 is either zero (+ configuration) or π/N_r ($\times$ configuration). Finally using Definition 4.1,

$$\Delta\nu_\mathcal{L} = \begin{cases}\frac{1}{2}\ell^2 p(N_\mathrm{r}\delta t - \delta r) & \text{quadrotor}_+ \\ \frac{1}{2}\ell^2(N_\mathrm{r}p\delta t + q\delta r) & \text{quadrotor}_\times \\ \frac{1}{2}\ell^2 pN_\mathrm{r}\delta t & \text{multirotor}_{\geq 6}\end{cases}$$

The remainder of the configuration-dependent terms are found similarly. □

A.2 Quadrotor LPV Aerodynamic Model Structure

The non-zero elements of the matrices $\boldsymbol{\mathcal{A}}_{(\cdot)}$ and $\boldsymbol{\mathcal{B}}_{(\cdot)}$ from Eq. (5.8) (which are also functions of the unknown parameter vector $\boldsymbol{\vartheta}$) are indicated with a "$\bullet$" as follows.

$$\boldsymbol{\mathcal{A}}_0 = \begin{bmatrix} \bullet & 0 & 0 & 0 & 0 & 0 \\ 0 & \bullet & 0 & 0 & 0 & 0 \\ 0 & 0 & \bullet & 0 & 0 & 0 \\ 0 & \bullet & 0 & \bullet & 0 & 0 \\ \bullet & 0 & 0 & 0 & \bullet & 0 \\ 0 & 0 & 0 & 0 & 0 & 0 \end{bmatrix} \qquad \boldsymbol{\mathcal{A}}_u = \begin{bmatrix} \bullet & 0 & \bullet & 0 & 0 & 0 \\ 0 & \bullet & 0 & 0 & 0 & 0 \\ \bullet & 0 & \bullet & \bullet & \bullet & 0 \\ \bullet & \bullet & \bullet & \bullet & \bullet & 0 \\ \bullet & \bullet & \bullet & \bullet & \bullet & 0 \\ \bullet & \bullet & \bullet & \bullet & \bullet & 0 \end{bmatrix}$$

$$\boldsymbol{\mathcal{A}}_v = \begin{bmatrix} \bullet & 0 & 0 & 0 & 0 & 0 \\ 0 & \bullet & \bullet & 0 & 0 & 0 \\ 0 & \bullet & \bullet & \bullet & \bullet & 0 \\ \bullet & \bullet & \bullet & \bullet & \bullet & 0 \\ \bullet & \bullet & \bullet & \bullet & \bullet & 0 \\ \bullet & \bullet & \bullet & \bullet & \bullet & 0 \end{bmatrix} \qquad \boldsymbol{\mathcal{A}}_w = \begin{bmatrix} \bullet & 0 & 0 & 0 & 0 & 0 \\ 0 & \bullet & 0 & 0 & 0 & 0 \\ 0 & 0 & \bullet & \bullet & \bullet & 0 \\ \bullet & \bullet & \bullet & \bullet & \bullet & 0 \\ \bullet & \bullet & \bullet & \bullet & \bullet & 0 \\ \bullet & \bullet & \bullet & \bullet & \bullet & 0 \end{bmatrix}$$

$$\boldsymbol{\mathcal{B}}_0 = \begin{bmatrix} 0 & 0 & 0 & 0 \\ 0 & 0 & 0 & 0 \\ \bullet & 0 & 0 & 0 \\ 0 & \bullet & 0 & 0 \\ 0 & 0 & \bullet & 0 \\ 0 & 0 & 0 & \bullet \end{bmatrix} \quad \boldsymbol{\mathcal{B}}_u = \begin{bmatrix} \bullet & 0 & 0 & 0 \\ 0 & 0 & 0 & 0 \\ \bullet & \bullet & \bullet & \bullet \\ \bullet & \bullet & \bullet & \bullet \\ \bullet & \bullet & \bullet & \bullet \\ \bullet & \bullet & \bullet & \bullet \end{bmatrix} \quad \boldsymbol{\mathcal{B}}_v = \begin{bmatrix} 0 & 0 & 0 & 0 \\ \bullet & 0 & 0 & 0 \\ \bullet & \bullet & \bullet & \bullet \\ \bullet & \bullet & \bullet & \bullet \\ \bullet & \bullet & \bullet & \bullet \\ \bullet & \bullet & \bullet & \bullet \end{bmatrix} \quad \boldsymbol{\mathcal{B}}_w = \begin{bmatrix} 0 & 0 & 0 & 0 \\ 0 & 0 & 0 & 0 \\ \bullet & \bullet & \bullet & \bullet \\ \bullet & \bullet & \bullet & \bullet \\ \bullet & \bullet & \bullet & \bullet \\ \bullet & \bullet & \bullet & \bullet \end{bmatrix}$$

A.3 Equation-Error Gray-Box Identification

Consider the linear, time-invariant state equation

$$\dot{\boldsymbol{x}} = \boldsymbol{A}\boldsymbol{x} + \boldsymbol{B}\boldsymbol{u} \tag{A.8}$$

where the elements of $\boldsymbol{A}$ and $\boldsymbol{B}$ depend on both known constants (e.g. gravitational acceleration) and unknown parameters (e.g. aerodynamic coefficients). Let $\boldsymbol{x} = [x_1 \ \cdots \ x_{n_x}]^\mathsf{T}$ and $\boldsymbol{u} = [u_1 \ \cdots \ u_{n_u}]^\mathsf{T}$. Define the index sets

$$\mathcal{I}_A = \{(i,j) \mid A_{ij} \text{ unknown}, \ i,j = 1, \cdots, n_x\} \tag{A.9}$$

$$\mathcal{I}_B = \{(i,j) \mid B_{ij} \text{ unknown}, \ i = 1, \cdots, n_x, \ j = 1, \cdots, n_u\} \tag{A.10}$$

and their "complements"

$$\overline{\mathcal{I}}_A = \{(i,j) \mid A_{ij} \text{ known}, \ i,j = 1, \cdots, n_x\} \tag{A.11}$$

$$\overline{\mathcal{I}}_B = \{(i,j) \mid B_{ij} \text{ known}, \ i = 1, \cdots, n_x, \ j = 1, \cdots, n_u\} \tag{A.12}$$

Let the row vector of regressors for the ith row of the state equation be

$$\boldsymbol{h}_i = \begin{bmatrix} \boldsymbol{x}_j^\mathsf{T} & \boldsymbol{u}_k^\mathsf{T} \end{bmatrix}, \quad (i,j) \in \mathcal{I}_A, \quad (i,k) \in \mathcal{I}_B \tag{A.13}$$

where for each i, $\boldsymbol{x}_j$ and $\boldsymbol{u}_k$ are column vectors containing the components of $\boldsymbol{x}$ and $\boldsymbol{u}$ defined by the index sets $\mathcal{I}_A$ and $\mathcal{I}_B$. Then, let the measurement for the ith row of the state equation be

$$y_i = \dot{x}_i - \sum_j A_{ij} x_j - \sum_k B_{ik} u_k, \quad (i,j) \in \overline{\mathcal{I}}_A, \quad (i,k) \in \overline{\mathcal{I}}_B \tag{A.14}$$

For each row of the state equation, define the column vector of parameters

$$\boldsymbol{\theta}^{(i)} = \begin{bmatrix} \boldsymbol{A}_j^\mathsf{T} \\ \boldsymbol{B}_k^\mathsf{T} \end{bmatrix}, \quad (i,j) \in \mathcal{I}_A, \quad (i,k) \in \mathcal{I}_B \tag{A.15}$$

where for each i, $\boldsymbol{A}_j$ and $\boldsymbol{B}_k$ are constructed from the elements of the ith rows of $\boldsymbol{A}$ and $\boldsymbol{B}$ according to the index sets $\mathcal{I}_A$ and $\mathcal{I}_B$, respectively. *Note: The preceding derivation and notation is presented for easy implementation in* MATLAB.

With these definitions, a sample has the model

$$y_i = \boldsymbol{h}_i \boldsymbol{\theta}^{(i)}, \quad i = 1, \cdots, n_x \tag{A.16}$$

for each $i = 1, \cdots, n_x$. Now suppose we take K samples of y_i and $\boldsymbol{h}_i$, where the kth sample is denoted $y_i(k)$, $\boldsymbol{x}(k)$, and $\boldsymbol{u}(k)$, etc. Let the measurements be subjected to additive, white, Gaussian noise such that

$$z_i(k) = y_i(k) + w_i(k), \quad k = 1, \cdots, K, \quad i = 1, \cdots, n_x \tag{A.17}$$

Stacking the K measurements and regressors, we obtain

$$\boldsymbol{y}_i = \begin{bmatrix} y_i(1) \\ y_i(2) \\ \vdots \\ y_i(K) \end{bmatrix}, \qquad \boldsymbol{H}_i = \begin{bmatrix} \boldsymbol{h}_i(1) \\ \boldsymbol{h}_i(2) \\ \vdots \\ \boldsymbol{h}_i(K) \end{bmatrix}, \qquad \text{and} \qquad \boldsymbol{w}_i = \begin{bmatrix} w_i(1) \\ w_i(2) \\ \vdots \\ w_i(K) \end{bmatrix} \tag{A.18}$$

Then, the measurement equations are

$$\boldsymbol{y}_i = \boldsymbol{H}_i \boldsymbol{\theta}^{(i)}, \quad i = 1, \cdots, n_x \tag{A.19}$$

from which one obtains the least square error parameter estimates

$$\boldsymbol{\theta}^{(i)} = (\boldsymbol{H}_i^\mathsf{T} \boldsymbol{H}_i)^{-1} \boldsymbol{H}_i^\mathsf{T} \boldsymbol{y}_i, \quad i = 1, \cdots, n_x \tag{A.20}$$

A.4 eSPAARO System Identification Results

The Equation Error parameter estimates for the eSPAARO model given in Eq. (7.62) are tabulated in Table A.1. This model's valid domain is given in Table A.2.

A.5 MTD System Identification Results

The Output Error parameter estimates for the MTD model given in Eq. (8.65) are tabulated in Table A.3. This model's valid domain is given in Table A.4. The predicted outputs for the training data using this model are shown in Figure A.1.

Table A.1: eSPAARO parameter estimates

Parameter	Estimate	Std. Dev.
C_{x_α}	2.16×10^{-1}	1.44×10^{-2}
$C_{x_{\alpha^2}}$	1.94	1.78×10^{-1}
$C_{x_{\mathcal{J}_c}}$	2.10×10^{-2}	2.02×10^{-4}
$C_{x_{\mathcal{J}_c^2}}$	6.07×10^{-4}	3.57×10^{-5}
C_{x_0}	5.93×10^{-2}	3.93×10^{-3}
C_{y_β}	-3.53×10^{-1}	1.13×10^{-2}
C_{y_r}	1.29×10^{-1}	3.51×10^{-2}
$C_{y_{\delta v_\mathrm{L}}}$	-7.58×10^{-2}	6.97×10^{-3}
$C_{y_{\delta v_\mathrm{R}}}$	8.16×10^{-2}	7.32×10^{-3}
C_{y_0}	-2.99×10^{-2}	9.63×10^{-4}
C_{z_α}	-3.43	2.53×10^{-1}
C_{z_q}	-1.09×10^{1}	3.11
$C_{z_{\dot{\alpha}}}$	1.63×10^{1}	3.21
C_{z_0}	-6.10×10^{-1}	2.55×10^{-2}
C_{l_β}	7.71×10^{-3}	3.60×10^{-3}
C_{l_p}	-4.22×10^{-1}	1.71×10^{-2}
C_{l_r}	1.29×10^{-1}	1.10×10^{-2}
$C_{l_{\delta a}}$	-2.75×10^{-1}	9.41×10^{-3}
C_{l_0}	7.99×10^{-4}	9.09×10^{-5}
C_{m_α}	-5.38×10^{-1}	4.93×10^{-2}
C_{m_q}	-1.01×10^{1}	7.11×10^{-1}
$C_{m_{\delta v_\mathrm{L}}}$	-4.41×10^{-1}	1.55×10^{-2}
$C_{m_{\delta v_\mathrm{R}}}$	-4.80×10^{-1}	1.66×10^{-2}
C_{m_0}	-1.87×10^{-3}	1.10×10^{-3}
C_{n_β}	7.90×10^{-2}	1.86×10^{-3}
C_{n_p}	-4.05×10^{-2}	8.81×10^{-3}
C_{n_r}	-5.91×10^{-2}	5.90×10^{-3}
$C_{n_{\delta a}}$	1.48×10^{-2}	4.82×10^{-3}
$C_{n_{\delta v_\mathrm{L}}}$	3.83×10^{-2}	1.16×10^{-3}
$C_{n_{\delta v_\mathrm{R}}}$	-3.59×10^{-2}	1.20×10^{-3}
C_{n_0}	-1.82×10^{-3}	2.69×10^{-4}

Table A.2: eSPAARO model domain

Variable	Min	Median	Max	Units
V	12.12	20.83	31.87	m/s
α	−9.36	−0.25	8.60	deg
β	−29.60	−3.83	21.62	deg
p	−38.37	−0.12	37.79	deg/s
q	−29.64	1.38	32.20	deg/s
r	−34.59	−2.15	28.55	deg/s
δv_{L}	−16.03	−0.57	15.30	deg
δv_{R}	−12.12	0.89	14.63	deg
δa	−5.92	0.04	6.45	deg
Ω	190.3	479.2	778.0	rad/s

Table A.3: MTD parameter estimates

Parameter	Estimate	Standard Deviation
C_{x_α}	-3.07×10^{-1}	4.45×10^{-3}
C_{x_q}	2.54	4.06×10^{-2}
$C_{x_{\alpha^2}}$	3.55	3.73×10^{-2}
$C_{x_{\mathcal{J}_c}}$	9.45×10^{-2}	5.33×10^{-4}
C_{x_0}	1.03×10^{-2}	1.87×10^{-4}
C_{y_β}	-4.62×10^{-1}	3.04×10^{-3}
$C_{y_{\mathrm{r}}}$	5.37×10^{-1}	6.86×10^{-3}
$C_{y_{\delta a}}$	5.95×10^{-2}	1.02×10^{-3}
$C_{y_{\delta r}}$	-1.54×10^{-1}	2.15×10^{-3}
C_{z_α}	−4.95	2.29×10^{-2}
C_{z_q}	−8.80	1.45×10^{-1}
$C_{z_{\delta e}}$	7.90×10^{-2}	1.47×10^{-3}
C_{z_0}	1.32×10^{-1}	1.90×10^{-3}
C_{l_β}	-9.21×10^{-3}	1.49×10^{-4}
C_{l_p}	-3.97×10^{-1}	3.12×10^{-3}
$C_{l_{\delta a}}$	-1.16×10^{-1}	8.04×10^{-4}
C_{m_α}	-4.27×10^{-1}	4.08×10^{-3}
C_{m_q}	−4.88	6.11×10^{-2}
$C_{m_{\delta e}}$	2.66×10^{-1}	1.69×10^{-3}
$C_{m_{\alpha^3}}$	−2.16	4.53×10^{-2}
C_{m_0}	4.17×10^{-2}	3.92×10^{-4}
C_{n_β}	7.78×10^{-2}	4.32×10^{-4}
$C_{n_{\mathrm{r}}}$	-1.61×10^{-1}	1.63×10^{-3}
$C_{n_{\delta a}}$	1.61×10^{-2}	2.57×10^{-4}
$C_{n_{\delta r}}$	5.51×10^{-2}	4.72×10^{-4}

Table A.4: MTD model domain

Variable	Min	Mean	Max	Units
V	13.9	18.7	23.4	m/s
α	1.43	6.08	10.72	deg
β	-8.89	2.83	14.54	deg
p	-90.0	7.9	105.8	deg/s
q	-44.5	9.2	62.9	deg/s
r	-67.6	-0.03	67.5	deg/s
δa	-16.7	-1.2	14.3	deg
δe	-12.2	1.9	16.1	deg
δr	-13.0	-0.1	12.9	deg
Ω	196.7	212.6	228.5	rad/s

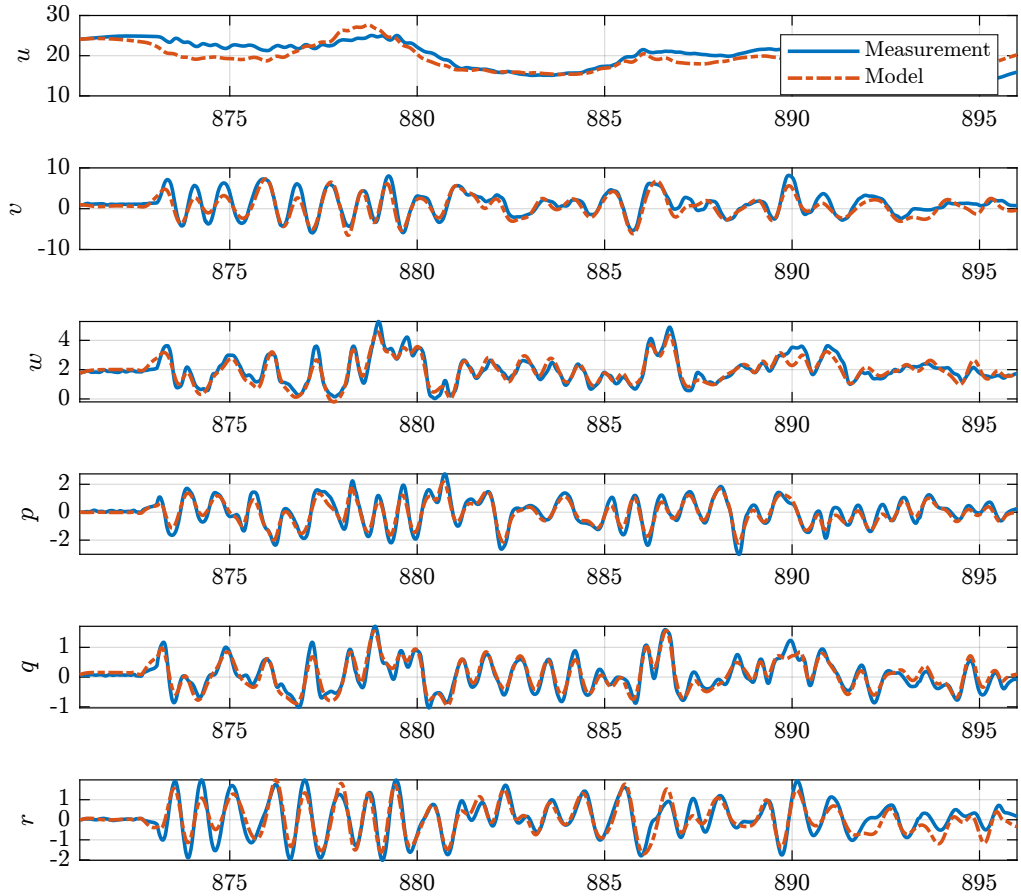

Figure A.1: MTD output error model prediction

Appendix B

Passivity-Based Wind Observer Bounding Functions

Proof of Proposition 8.1.

We start by expanding

$$\frac{\partial V^*}{\partial \tilde{\boldsymbol{x}}_2}\tilde{\boldsymbol{\phi}}_2(\tilde{\boldsymbol{x}}_1, \boldsymbol{L}_2(\boldsymbol{y})\boldsymbol{L}_1^{-1}\tilde{\boldsymbol{x}}_1; \boldsymbol{x}_1, \tilde{\boldsymbol{x}}_2 + \boldsymbol{x}_2; \boldsymbol{u}) - \frac{\partial V^*}{\partial \tilde{\boldsymbol{x}}_2}\frac{\mathrm{d}}{\mathrm{d}t}\left(\boldsymbol{L}_2(\boldsymbol{y})\boldsymbol{L}_1^{-1}\right)\tilde{\boldsymbol{x}}_1 + \tilde{\boldsymbol{x}}_1^{\mathsf{T}}\boldsymbol{L}_1^{-1}\tilde{\boldsymbol{f}}_1(\tilde{\boldsymbol{x}}_1, \tilde{\boldsymbol{x}}_2 + \boldsymbol{L}_2(\boldsymbol{y})\boldsymbol{L}_1^{-1}\tilde{\boldsymbol{x}}_1; \boldsymbol{x}_1, \boldsymbol{x}_2; \boldsymbol{u}) \tag{B.1}$$

and replacing $\boldsymbol{x}_2$ with $\hat{\boldsymbol{x}}_2 - \tilde{\boldsymbol{x}}_2$ to yield

$$\begin{aligned}
&- \tilde{\boldsymbol{x}}_2^{\mathsf{T}}\frac{\mathrm{d}}{\mathrm{d}t}\left(\boldsymbol{L}_2(\boldsymbol{y})\boldsymbol{L}_1^{-1}\right)\tilde{\boldsymbol{x}}_1 + \tilde{\boldsymbol{v}}_{\mathrm{r}}^{\mathsf{T}}\tilde{\boldsymbol{\phi}}_{2_{v_{\mathrm{r}}}}(\tilde{\boldsymbol{x}}_1, \boldsymbol{L}_2\boldsymbol{L}_1^{-1}\tilde{\boldsymbol{x}}_1; \boldsymbol{x}_1, \hat{\boldsymbol{x}}_2; \boldsymbol{u}) + \tilde{\boldsymbol{w}}^{\mathsf{T}}\tilde{\boldsymbol{\phi}}_{2_w}(\tilde{\boldsymbol{x}}_1, \boldsymbol{L}_2\boldsymbol{L}_1^{-1}\tilde{\boldsymbol{x}}_1; \boldsymbol{x}_1, \hat{\boldsymbol{x}}_2; \boldsymbol{u}) \\
&\quad + \tilde{\boldsymbol{q}}^{\mathsf{T}}\boldsymbol{L}_{1_q}^{-1}\tilde{\boldsymbol{f}}_{1_q}(\tilde{\boldsymbol{x}}_1, \tilde{\boldsymbol{x}}_2 + \boldsymbol{L}_2\boldsymbol{L}_1^{-1}\tilde{\boldsymbol{x}}_1; \boldsymbol{x}_1, \hat{\boldsymbol{x}}_2 - \tilde{\boldsymbol{x}}_2; \boldsymbol{u}) \\
&\quad + \tilde{\boldsymbol{\lambda}}^{\mathsf{T}}\boldsymbol{L}_{1_\lambda}^{-1}\tilde{\boldsymbol{f}}_{1_\lambda}(\tilde{\boldsymbol{x}}_1, \tilde{\boldsymbol{x}}_2 + \boldsymbol{L}_2\boldsymbol{L}_1^{-1}\tilde{\boldsymbol{x}}_1; \boldsymbol{x}_1, \hat{\boldsymbol{x}}_2 - \tilde{\boldsymbol{x}}_2; \boldsymbol{u}) \\
&\quad + \tilde{\boldsymbol{\zeta}}^{\mathsf{T}}\boldsymbol{L}_{1_\zeta}^{-1}\tilde{\boldsymbol{f}}_{1_\zeta}(\tilde{\boldsymbol{x}}_1, \tilde{\boldsymbol{x}}_2 + \boldsymbol{L}_2\boldsymbol{L}_1^{-1}\tilde{\boldsymbol{x}}_1; \boldsymbol{x}_1, \hat{\boldsymbol{x}}_2 - \tilde{\boldsymbol{x}}_2; \boldsymbol{u}) \\
&\quad + \tilde{\boldsymbol{\omega}}^{\mathsf{T}}\boldsymbol{L}_{1_\omega}^{-1}\tilde{\boldsymbol{f}}_{1_\omega}(\tilde{\boldsymbol{x}}_1, \tilde{\boldsymbol{x}}_2 + \boldsymbol{L}_2\boldsymbol{L}_1^{-1}\tilde{\boldsymbol{x}}_1; \boldsymbol{x}_1, \hat{\boldsymbol{x}}_2 - \tilde{\boldsymbol{x}}_2; \boldsymbol{u})
\end{aligned} \tag{B.2}$$

For compactness, note that $\hat{\boldsymbol{R}}_{\mathrm{IB}} = \boldsymbol{R}_{\mathrm{IB}}(\tilde{\boldsymbol{\lambda}} + \boldsymbol{\lambda}, \tilde{\boldsymbol{\zeta}} + \boldsymbol{\zeta})$ and denote $\boldsymbol{R}_{\mathrm{IB}} = \boldsymbol{R}_{\mathrm{IB}}(\boldsymbol{\lambda}, \boldsymbol{\zeta})$. Then with $\boldsymbol{L}_2$ given in Eq. (8.35), the components of $\tilde{\boldsymbol{\phi}}_2$ from Eq. (8.26) are written as

$$\begin{aligned}
\tilde{\boldsymbol{\phi}}_{2_{v_{\mathrm{r}}}}(\tilde{\boldsymbol{x}}_1, \tilde{\boldsymbol{x}}_2; \boldsymbol{x}_1, \boldsymbol{x}_2; \boldsymbol{u}) &= \boldsymbol{S}(\boldsymbol{v}_{\mathrm{r}})\tilde{\boldsymbol{\omega}} - \boldsymbol{S}(\tilde{\boldsymbol{\omega}} + \boldsymbol{\omega})\tilde{\boldsymbol{v}}_{\mathrm{r}} + g\tilde{\boldsymbol{\zeta}} + \frac{1}{m}\boldsymbol{F}_v\tilde{\boldsymbol{v}}_{\mathrm{r}} + \frac{1}{m}\boldsymbol{F}_\omega\tilde{\boldsymbol{\omega}} \\
&\quad - \boldsymbol{\Gamma}_{v,q}\boldsymbol{R}_{\mathrm{IB}}^{\mathsf{T}}\left(\hat{\boldsymbol{R}}_{\mathrm{IB}}\tilde{\boldsymbol{v}}_{\mathrm{r}} + \left(\hat{\boldsymbol{R}}_{\mathrm{IB}} - \boldsymbol{R}_{\mathrm{IB}}\right)\boldsymbol{v}_{\mathrm{r}} + \tilde{\boldsymbol{w}}\right) \\
&\quad - \boldsymbol{\Gamma}_{v,\omega}\boldsymbol{M}_v^{\mathsf{T}}\Big(\boldsymbol{S}(\boldsymbol{I}(\tilde{\boldsymbol{\omega}} + \boldsymbol{\omega}))\tilde{\boldsymbol{\omega}} - \boldsymbol{S}(\boldsymbol{\omega})\boldsymbol{I}\tilde{\boldsymbol{\omega}} + \boldsymbol{M}_v\tilde{\boldsymbol{v}}_{\mathrm{r}} + \boldsymbol{M}_\omega\tilde{\boldsymbol{\omega}}\Big)
\end{aligned} \tag{B.3a}$$

$$\begin{aligned}
\tilde{\boldsymbol{\phi}}_{2_w}(\tilde{\boldsymbol{x}}_1, \tilde{\boldsymbol{x}}_2; \boldsymbol{x}_1, \boldsymbol{x}_2; \boldsymbol{u}) &= -\boldsymbol{R}_{\mathrm{IB}}\boldsymbol{\Gamma}_{w,q}\boldsymbol{R}_{\mathrm{IB}}^{\mathsf{T}}\Big(\hat{\boldsymbol{R}}_{\mathrm{IB}}\tilde{\boldsymbol{v}}_{\mathrm{r}} + \left(\hat{\boldsymbol{R}}_{\mathrm{IB}} - \boldsymbol{R}_{\mathrm{IB}}\right)\boldsymbol{v}_{\mathrm{r}} + \tilde{\boldsymbol{w}}\Big) \\
&\quad - \boldsymbol{R}_{\mathrm{IB}}\boldsymbol{\Gamma}_{w,\omega}\boldsymbol{M}_v^{\mathsf{T}}\Big(\boldsymbol{S}(\boldsymbol{I}(\tilde{\boldsymbol{\omega}} + \boldsymbol{\omega}))\tilde{\boldsymbol{\omega}} - \boldsymbol{S}(\boldsymbol{\omega})\boldsymbol{I}\tilde{\boldsymbol{\omega}} + \boldsymbol{M}_v\tilde{\boldsymbol{v}}_{\mathrm{r}} + \boldsymbol{M}_\omega\tilde{\boldsymbol{\omega}}\Big)
\end{aligned} \tag{B.3b}$$

Using

$$\boldsymbol{L}_2\boldsymbol{L}_1^{-1}\tilde{\boldsymbol{x}}_1 = \begin{bmatrix} \boldsymbol{L}_{2_{v,q}}\boldsymbol{L}_{1_q}^{-1}\tilde{\boldsymbol{q}} + \boldsymbol{L}_{2_{v,\omega}}\boldsymbol{L}_{1_\omega}^{-1}\tilde{\boldsymbol{\omega}} \\ \boldsymbol{L}_{2_{w,q}}\boldsymbol{L}_{1_q}^{-1}\tilde{\boldsymbol{q}} + \boldsymbol{L}_{2_{w,\omega}}\boldsymbol{L}_{1_\omega}^{-1}\tilde{\boldsymbol{\omega}} \end{bmatrix} = \begin{bmatrix} \boldsymbol{\Gamma}_{v,q}\boldsymbol{R}_{\mathrm{IB}}^{\mathsf{T}}\tilde{\boldsymbol{q}} + \boldsymbol{\Gamma}_{v,\omega}\boldsymbol{M}_v^{\mathsf{T}}\boldsymbol{I}\tilde{\boldsymbol{\omega}} \\ \boldsymbol{R}_{\mathrm{IB}}\boldsymbol{\Gamma}_{w,q}\boldsymbol{R}_{\mathrm{IB}}^{\mathsf{T}}\tilde{\boldsymbol{q}} + \boldsymbol{R}_{\mathrm{IB}}\boldsymbol{\Gamma}_{w,\omega}\boldsymbol{M}_v^{\mathsf{T}}\boldsymbol{I}\tilde{\boldsymbol{\omega}} \end{bmatrix}$$

and the expressions for $\tilde{\boldsymbol{\phi}}_2$ in Eq. (B.3), we compute the necessary terms in Eq. (B.2) as

$$\begin{aligned}\tilde{\boldsymbol{\phi}}_{2_{v_\mathrm{r}}}(\tilde{\boldsymbol{x}}_1, \boldsymbol{L}_2\boldsymbol{L}_1^{-1}\tilde{\boldsymbol{x}}_1; \boldsymbol{x}_1, \hat{\boldsymbol{x}}_2; \boldsymbol{u}) = &\bigg(\Big(\frac{1}{m}\boldsymbol{F}_v - \boldsymbol{S}(\tilde{\boldsymbol{\omega}}+\boldsymbol{\omega})\Big)\boldsymbol{\Gamma}_{v,q} - \boldsymbol{\Gamma}_{v,q}\boldsymbol{R}_{\mathrm{IB}}^{\mathsf{T}}\hat{\boldsymbol{R}}_{\mathrm{IB}}\boldsymbol{\Gamma}_{v,q} - \boldsymbol{\Gamma}_{v,q}\boldsymbol{\Gamma}_{w,q} \\ &- \boldsymbol{\Gamma}_{v,\omega}\boldsymbol{M}_v^{\mathsf{T}}\boldsymbol{M}_v\boldsymbol{\Gamma}_{v,q}\bigg)\boldsymbol{R}_{\mathrm{IB}}^{\mathsf{T}}\tilde{\boldsymbol{q}} + g\tilde{\boldsymbol{\zeta}} + \bigg(\Big(\frac{1}{m}\boldsymbol{F}_v - \boldsymbol{S}(\tilde{\boldsymbol{\omega}}+\boldsymbol{\omega})\Big)\boldsymbol{\Gamma}_{v,\omega}\boldsymbol{M}_v^{\mathsf{T}}\boldsymbol{I} \\ &+ \frac{1}{m}\boldsymbol{F}_\omega + \boldsymbol{S}(\hat{\boldsymbol{v}}_\mathrm{r}) - \boldsymbol{\Gamma}_{v,q}\Big(\boldsymbol{R}_{\mathrm{IB}}^{\mathsf{T}}\hat{\boldsymbol{R}}_{\mathrm{IB}}\boldsymbol{\Gamma}_{v,\omega} + \boldsymbol{\Gamma}_{w,\omega}\Big)\boldsymbol{M}_v^{\mathsf{T}}\boldsymbol{I} \\ &- \boldsymbol{\Gamma}_{v,\omega}\boldsymbol{M}_v^{\mathsf{T}}\Big(\boldsymbol{S}(\boldsymbol{I}(\tilde{\boldsymbol{\omega}}+\boldsymbol{\omega})) - \boldsymbol{S}(\boldsymbol{\omega})\boldsymbol{I} + \boldsymbol{M}_\omega + \boldsymbol{M}_v\boldsymbol{\Gamma}_{v,\omega}\boldsymbol{M}_v^{\mathsf{T}}\boldsymbol{I}\Big)\bigg)\tilde{\boldsymbol{\omega}} \\ &- \boldsymbol{\Gamma}_{v,q}\boldsymbol{R}_{\mathrm{IB}}^{\mathsf{T}}\Big(\hat{\boldsymbol{R}}_{\mathrm{IB}} - \boldsymbol{R}_{\mathrm{IB}}\Big)\hat{\boldsymbol{v}}_\mathrm{r} \end{aligned} \tag{B.4a}$$

$$\begin{aligned}\tilde{\boldsymbol{\phi}}_{2_w}(\tilde{\boldsymbol{x}}_1, \boldsymbol{L}_2\boldsymbol{L}_1^{-1}\tilde{\boldsymbol{x}}_1; \boldsymbol{x}_1, \hat{\boldsymbol{x}}_2; \boldsymbol{u}) = &\boldsymbol{R}_{\mathrm{IB}}\bigg(-\boldsymbol{\Gamma}_{w,q}\Big(\boldsymbol{R}_{\mathrm{IB}}^{\mathsf{T}}\hat{\boldsymbol{R}}_{\mathrm{IB}}\boldsymbol{\Gamma}_{v,q} + \boldsymbol{\Gamma}_{w,q}\Big) - \boldsymbol{\Gamma}_{w,\omega}\boldsymbol{M}_v^{\mathsf{T}}\boldsymbol{M}_v\boldsymbol{\Gamma}_{v,q}\bigg)\boldsymbol{R}_{\mathrm{IB}}^{\mathsf{T}}\tilde{\boldsymbol{q}} \\ &+ \boldsymbol{R}_{\mathrm{IB}}\bigg(-\boldsymbol{\Gamma}_{w,q}\Big(\boldsymbol{R}_{\mathrm{IB}}^{\mathsf{T}}\hat{\boldsymbol{R}}_{\mathrm{IB}}\boldsymbol{\Gamma}_{v,\omega} + \boldsymbol{\Gamma}_{w,\omega}\Big)\boldsymbol{M}_v^{\mathsf{T}}\boldsymbol{I} \\ &- \boldsymbol{\Gamma}_{w,\omega}\boldsymbol{M}_v^{\mathsf{T}}\Big(\boldsymbol{S}(\boldsymbol{I}(\tilde{\boldsymbol{\omega}}+\boldsymbol{\omega})) - \boldsymbol{S}(\boldsymbol{\omega})\boldsymbol{I} + \boldsymbol{M}_\omega + \boldsymbol{M}_v\boldsymbol{\Gamma}_{v,\omega}\boldsymbol{M}_v^{\mathsf{T}}\boldsymbol{I}\Big)\bigg)\tilde{\boldsymbol{\omega}} \\ &- \boldsymbol{R}_{\mathrm{IB}}\boldsymbol{\Gamma}_{w,q}\boldsymbol{R}_{\mathrm{IB}}^{\mathsf{T}}\Big(\hat{\boldsymbol{R}}_{\mathrm{IB}} - \boldsymbol{R}_{\mathrm{IB}}\Big)\hat{\boldsymbol{v}}_\mathrm{r} \end{aligned} \tag{B.4b}$$

$$\begin{aligned}\tilde{\boldsymbol{f}}_{1_q}(\tilde{\boldsymbol{x}}_1, \tilde{\boldsymbol{x}}_2 + \boldsymbol{L}_2\boldsymbol{L}_1^{-1}\tilde{\boldsymbol{x}}_1; \boldsymbol{x}_1, \hat{\boldsymbol{x}}_2 - \tilde{\boldsymbol{x}}_2; \boldsymbol{u}) = &\Big(\boldsymbol{R}_{\mathrm{IB}}\boldsymbol{\Gamma}_{w,q}\boldsymbol{R}_{\mathrm{IB}}^{\mathsf{T}} + \hat{\boldsymbol{R}}_{\mathrm{IB}}\boldsymbol{\Gamma}_{v,q}\boldsymbol{R}_{\mathrm{IB}}^{\mathsf{T}}\Big)\tilde{\boldsymbol{q}} \\ &+ \Big(\boldsymbol{R}_{\mathrm{IB}}\boldsymbol{\Gamma}_{w,\omega} + \hat{\boldsymbol{R}}_{\mathrm{IB}}\boldsymbol{\Gamma}_{v,\omega}\Big)\boldsymbol{M}_v^{\mathsf{T}}\boldsymbol{I}\tilde{\boldsymbol{\omega}} + \tilde{\boldsymbol{w}} \\ &+ \boldsymbol{R}_{\mathrm{IB}}\tilde{\boldsymbol{v}}_\mathrm{r} + \Big(\hat{\boldsymbol{R}}_{\mathrm{IB}} - \boldsymbol{R}_{\mathrm{IB}}\Big)\hat{\boldsymbol{v}}_\mathrm{r} \end{aligned} \tag{B.4c}$$

$$\tilde{\boldsymbol{f}}_{1_\lambda}(\tilde{\boldsymbol{x}}_1, \tilde{\boldsymbol{x}}_2 + \boldsymbol{L}_2\boldsymbol{L}_1^{-1}\tilde{\boldsymbol{x}}_1; \boldsymbol{x}_1, \hat{\boldsymbol{x}}_2 - \tilde{\boldsymbol{x}}_2; \boldsymbol{u}) = \boldsymbol{S}(\tilde{\boldsymbol{\lambda}}+\boldsymbol{\lambda})\tilde{\boldsymbol{\omega}} - \boldsymbol{S}(\boldsymbol{\omega})\tilde{\boldsymbol{\lambda}} \tag{B.4d}$$

$$\tilde{\boldsymbol{f}}_{1_\zeta}(\tilde{\boldsymbol{x}}_1, \tilde{\boldsymbol{x}}_2 + \boldsymbol{L}_2\boldsymbol{L}_1^{-1}\tilde{\boldsymbol{x}}_1; \boldsymbol{x}_1, \hat{\boldsymbol{x}}_2 - \tilde{\boldsymbol{x}}_2; \boldsymbol{u}) = \boldsymbol{S}(\tilde{\boldsymbol{\zeta}}+\boldsymbol{\zeta})\tilde{\boldsymbol{\omega}} - \boldsymbol{S}(\boldsymbol{\omega})\tilde{\boldsymbol{\zeta}} \tag{B.4e}$$

$$\begin{aligned}\tilde{\boldsymbol{f}}_{1_\omega}(\tilde{\boldsymbol{x}}_1, \tilde{\boldsymbol{x}}_2 + \boldsymbol{L}_2\boldsymbol{L}_1^{-1}\tilde{\boldsymbol{x}}_1; \boldsymbol{x}_1, \hat{\boldsymbol{x}}_2 - \tilde{\boldsymbol{x}}_2; \boldsymbol{u}) = &\boldsymbol{I}^{-1}\boldsymbol{M}_v\boldsymbol{\Gamma}_{v,q}\boldsymbol{R}_{\mathrm{IB}}^{\mathsf{T}}\tilde{\boldsymbol{q}} + \boldsymbol{I}^{-1}\boldsymbol{M}_v\tilde{\boldsymbol{v}}_\mathrm{r} \\ &+ \boldsymbol{I}^{-1}\Big(\boldsymbol{S}(\boldsymbol{I}(\tilde{\boldsymbol{\omega}}+\boldsymbol{\omega})) - \boldsymbol{S}(\boldsymbol{\omega})\boldsymbol{I} \\ &+ \boldsymbol{M}_\omega + \boldsymbol{M}_v\boldsymbol{\Gamma}_{v,\omega}\boldsymbol{M}_v^{\mathsf{T}}\boldsymbol{I}\Big)\tilde{\boldsymbol{\omega}} \end{aligned} \tag{B.4f}$$

These expressions (B.4) are then substituted into Eq. (B.2) along with the expression for

$\frac{\mathrm{d}}{\mathrm{d}t}(\boldsymbol{L}_2(\boldsymbol{y})\boldsymbol{L}_1^{-1})$ from Eq. (8.51) to yield

$$
\begin{aligned}
&\tilde{\boldsymbol{v}}_{\mathrm{r}}^{\mathsf{T}}\boldsymbol{\Gamma}_{v,q}\boldsymbol{S}(\boldsymbol{\omega})\boldsymbol{R}_{\mathrm{IB}}^{\mathsf{T}}\tilde{\boldsymbol{q}} - \tilde{\boldsymbol{w}}^{\mathsf{T}}\boldsymbol{R}_{\mathrm{IB}}\left(\boldsymbol{S}(\boldsymbol{\omega})\boldsymbol{\Gamma}_{w,q} - \boldsymbol{\Gamma}_{w,q}\boldsymbol{S}(\boldsymbol{\omega})\right)\boldsymbol{R}_{\mathrm{IB}}^{\mathsf{T}}\tilde{\boldsymbol{q}} - \tilde{\boldsymbol{w}}^{\mathsf{T}}\boldsymbol{R}_{\mathrm{IB}}\boldsymbol{S}(\boldsymbol{\omega})\boldsymbol{\Gamma}_{w,\omega}\boldsymbol{M}_v^{\mathsf{T}}\boldsymbol{I}\tilde{\boldsymbol{\omega}} \\
&\quad + \tilde{\boldsymbol{v}}_{\mathrm{r}}^{\mathsf{T}}\left(\left(\frac{1}{m}\boldsymbol{F}_v - \boldsymbol{S}(\tilde{\boldsymbol{\omega}}+\boldsymbol{\omega})\right)\boldsymbol{\Gamma}_{v,q} - \boldsymbol{\Gamma}_{v,q}\boldsymbol{R}_{\mathrm{IB}}^{\mathsf{T}}\hat{\boldsymbol{R}}_{\mathrm{IB}}\boldsymbol{\Gamma}_{v,q} - \boldsymbol{\Gamma}_{v,q}\boldsymbol{\Gamma}_{w,q} - \boldsymbol{\Gamma}_{v,\omega}\boldsymbol{M}_v^{\mathsf{T}}\boldsymbol{M}_v\boldsymbol{\Gamma}_{v,q}\right)\boldsymbol{R}_{\mathrm{IB}}^{\mathsf{T}}\tilde{\boldsymbol{q}} \\
&\quad + \tilde{\boldsymbol{v}}_{\mathrm{r}}^{\mathsf{T}}g\tilde{\boldsymbol{\zeta}} + \tilde{\boldsymbol{v}}_{\mathrm{r}}^{\mathsf{T}}\left(\left(\frac{1}{m}\boldsymbol{F}_v - \boldsymbol{S}(\tilde{\boldsymbol{\omega}}+\boldsymbol{\omega})\right)\boldsymbol{\Gamma}_{v,\omega}\boldsymbol{M}_v^{\mathsf{T}}\boldsymbol{I} - \boldsymbol{\Gamma}_{v,q}\left(\boldsymbol{R}_{\mathrm{IB}}^{\mathsf{T}}\hat{\boldsymbol{R}}_{\mathrm{IB}}\boldsymbol{\Gamma}_{v,\omega} + \boldsymbol{\Gamma}_{w,\omega}\right)\boldsymbol{M}_v^{\mathsf{T}}\boldsymbol{I}\right. \\
&\quad \left. + \frac{1}{m}\boldsymbol{F}_\omega + \boldsymbol{S}(\hat{\boldsymbol{v}}_{\mathrm{r}}) - \boldsymbol{\Gamma}_{v,\omega}\boldsymbol{M}_v^{\mathsf{T}}\left(\boldsymbol{S}(\boldsymbol{I}(\tilde{\boldsymbol{\omega}}+\boldsymbol{\omega})) - \boldsymbol{S}(\boldsymbol{\omega})\boldsymbol{I} + \boldsymbol{M}_\omega + \boldsymbol{M}_v\boldsymbol{\Gamma}_{v,\omega}\boldsymbol{M}_v^{\mathsf{T}}\boldsymbol{I}\right)\right)\tilde{\boldsymbol{\omega}} \\
&\quad - \tilde{\boldsymbol{v}}_{\mathrm{r}}^{\mathsf{T}}\boldsymbol{\Gamma}_{v,q}\boldsymbol{R}_{\mathrm{IB}}^{\mathsf{T}}\left(\hat{\boldsymbol{R}}_{\mathrm{IB}} - \boldsymbol{R}_{\mathrm{IB}}\right)\hat{\boldsymbol{v}}_{\mathrm{r}} + \tilde{\boldsymbol{w}}^{\mathsf{T}}\boldsymbol{R}_{\mathrm{IB}}\left(-\boldsymbol{\Gamma}_{w,\omega}\boldsymbol{M}_v^{\mathsf{T}}\boldsymbol{M}_v\boldsymbol{\Gamma}_{v,q}\right. \\
&\quad \left.-\boldsymbol{\Gamma}_{w,q}\left(\boldsymbol{R}_{\mathrm{IB}}^{\mathsf{T}}\hat{\boldsymbol{R}}_{\mathrm{IB}}\boldsymbol{\Gamma}_{v,q} + \boldsymbol{\Gamma}_{w,q}\right)\right)\boldsymbol{R}_{\mathrm{IB}}^{\mathsf{T}}\tilde{\boldsymbol{q}} + \tilde{\boldsymbol{w}}^{\mathsf{T}}\boldsymbol{R}_{\mathrm{IB}}\left(-\boldsymbol{\Gamma}_{w,q}\left(\boldsymbol{R}_{\mathrm{IB}}^{\mathsf{T}}\hat{\boldsymbol{R}}_{\mathrm{IB}}\boldsymbol{\Gamma}_{v,\omega} + \boldsymbol{\Gamma}_{w,\omega}\right)\boldsymbol{M}_v^{\mathsf{T}}\boldsymbol{I}\right. \\
&\quad \left.-\boldsymbol{\Gamma}_{w,\omega}\boldsymbol{M}_v^{\mathsf{T}}\left(\boldsymbol{S}(\boldsymbol{I}(\tilde{\boldsymbol{\omega}}+\boldsymbol{\omega})) - \boldsymbol{S}(\boldsymbol{\omega})\boldsymbol{I} + \boldsymbol{M}_\omega + \boldsymbol{M}_v\boldsymbol{\Gamma}_{v,\omega}\boldsymbol{M}_v^{\mathsf{T}}\boldsymbol{I}\right)\right)\tilde{\boldsymbol{\omega}} \\
&\quad - \tilde{\boldsymbol{w}}^{\mathsf{T}}\boldsymbol{R}_{\mathrm{IB}}\boldsymbol{\Gamma}_{w,q}\boldsymbol{R}_{\mathrm{IB}}^{\mathsf{T}}\left(\hat{\boldsymbol{R}}_{\mathrm{IB}} - \boldsymbol{R}_{\mathrm{IB}}\right)\hat{\boldsymbol{v}}_{\mathrm{r}} + \tilde{\boldsymbol{q}}^{\mathsf{T}}\boldsymbol{L}_{1_q}^{-1}\left(\boldsymbol{R}_{\mathrm{IB}}\boldsymbol{\Gamma}_{w,q}\boldsymbol{R}_{\mathrm{IB}}^{\mathsf{T}} + \hat{\boldsymbol{R}}_{\mathrm{IB}}\boldsymbol{\Gamma}_{v,q}\boldsymbol{R}_{\mathrm{IB}}^{\mathsf{T}}\right)\tilde{\boldsymbol{q}} \\
&+ \tilde{\boldsymbol{q}}^{\mathsf{T}}\boldsymbol{L}_{1_q}^{-1}\left(\boldsymbol{R}_{\mathrm{IB}}\boldsymbol{\Gamma}_{w,\omega} + \hat{\boldsymbol{R}}_{\mathrm{IB}}\boldsymbol{\Gamma}_{v,\omega}\right)\boldsymbol{M}_v^{\mathsf{T}}\boldsymbol{I}\tilde{\boldsymbol{\omega}} + \tilde{\boldsymbol{q}}^{\mathsf{T}}\boldsymbol{L}_{1_q}^{-1}\boldsymbol{R}_{\mathrm{IB}}\tilde{\boldsymbol{v}}_{\mathrm{r}} + \tilde{\boldsymbol{q}}^{\mathsf{T}}\boldsymbol{L}_{1_q}^{-1}\tilde{\boldsymbol{w}} + \tilde{\boldsymbol{q}}^{\mathsf{T}}\boldsymbol{L}_{1_q}^{-1}\left(\hat{\boldsymbol{R}}_{\mathrm{IB}} - \boldsymbol{R}_{\mathrm{IB}}\right)\hat{\boldsymbol{v}}_{\mathrm{r}} \\
&+ \tilde{\boldsymbol{\lambda}}^{\mathsf{T}}\boldsymbol{L}_{1_\lambda}^{-1}\boldsymbol{S}(\tilde{\boldsymbol{\lambda}}+\boldsymbol{\lambda})\tilde{\boldsymbol{\omega}} - \tilde{\boldsymbol{\lambda}}^{\mathsf{T}}\boldsymbol{L}_{1_\lambda}^{-1}\boldsymbol{S}(\boldsymbol{\omega})\tilde{\boldsymbol{\lambda}} + \tilde{\boldsymbol{\zeta}}^{\mathsf{T}}\boldsymbol{L}_{1_\zeta}^{-1}\boldsymbol{S}(\tilde{\boldsymbol{\zeta}}+\boldsymbol{\zeta})\tilde{\boldsymbol{\omega}} - \tilde{\boldsymbol{\zeta}}^{\mathsf{T}}\boldsymbol{L}_{1_\zeta}^{-1}\boldsymbol{S}(\boldsymbol{\omega})\tilde{\boldsymbol{\zeta}} + \tilde{\boldsymbol{\omega}}^{\mathsf{T}}\boldsymbol{L}_{1_\omega}^{-1}\boldsymbol{I}^{-1}\boldsymbol{M}_v\tilde{\boldsymbol{v}}_{\mathrm{r}} \\
&\tilde{\boldsymbol{\omega}}^{\mathsf{T}}\boldsymbol{L}_{1_\omega}^{-1}\boldsymbol{I}^{-1}\boldsymbol{M}_v\boldsymbol{\Gamma}_{v,q}\boldsymbol{R}_{\mathrm{IB}}^{\mathsf{T}}\tilde{\boldsymbol{q}} + \tilde{\boldsymbol{\omega}}^{\mathsf{T}}\boldsymbol{L}_{1_\omega}^{-1}\boldsymbol{I}^{-1}\left(\boldsymbol{S}(\boldsymbol{I}(\tilde{\boldsymbol{\omega}}+\boldsymbol{\omega})) - \boldsymbol{S}(\boldsymbol{\omega})\boldsymbol{I} + \boldsymbol{M}_\omega + \boldsymbol{M}_v\boldsymbol{\Gamma}_{v,\omega}\boldsymbol{M}_v^{\mathsf{T}}\boldsymbol{I}\right)\tilde{\boldsymbol{\omega}} \qquad \text{(B.5)}
\end{aligned}
$$

Here we have color-coded terms by those that can be written as $\tilde{\boldsymbol{x}}_1^{\mathsf{T}}(\bullet)\tilde{\boldsymbol{x}}_1$ and those that can be written as $\tilde{\boldsymbol{x}}_2^{\mathsf{T}}(\bullet)\tilde{\boldsymbol{x}}_1$. The terms in violet are not immediately seen to follow either of these two forms. However, the common term

$$\left(\hat{\boldsymbol{R}}_{\mathrm{IB}} - \boldsymbol{R}_{\mathrm{IB}}\right)\hat{\boldsymbol{v}}_{\mathrm{r}}$$

may be re-written as

$$\left(\hat{\boldsymbol{R}}_{\mathrm{IB}} - \boldsymbol{R}_{\mathrm{IB}}\right)\hat{\boldsymbol{v}}_{\mathrm{r}} = \begin{bmatrix}\boldsymbol{M}_\lambda(\tilde{\boldsymbol{\lambda}},\tilde{\boldsymbol{\zeta}},\hat{\boldsymbol{v}}_{\mathrm{r}}) & \boldsymbol{M}_\zeta(\tilde{\boldsymbol{\lambda}},\tilde{\boldsymbol{\zeta}},\hat{\boldsymbol{v}}_{\mathrm{r}})\end{bmatrix}\begin{bmatrix}\tilde{\boldsymbol{\lambda}}\\ \tilde{\boldsymbol{\zeta}}\end{bmatrix}$$

where

$$\boldsymbol{M}_\lambda^{\mathsf{T}}(\tilde{\boldsymbol{\zeta}},\boldsymbol{\zeta},\hat{\boldsymbol{v}}_{\mathrm{r}}) = \begin{bmatrix}\hat{u}_{\mathrm{r}} & \hat{v}_{\mathrm{r}}(\tilde{\zeta}_3+\zeta_3) - \hat{w}_{\mathrm{r}}(\tilde{\zeta}_2+\zeta_2) & 0\\ \hat{v}_{\mathrm{r}} & -\hat{u}_{\mathrm{r}}(\tilde{\zeta}_3+\zeta_3) + \hat{w}_{\mathrm{r}}(\tilde{\zeta}_1+\zeta_1) & 0\\ \hat{w}_{\mathrm{r}} & \hat{u}_{\mathrm{r}}(\tilde{\zeta}_2+\zeta_2) - \hat{v}_{\mathrm{r}}(\tilde{\zeta}_1+\zeta_1) & 0\end{bmatrix} \qquad \text{(B.6a)}$$

$$\boldsymbol{M}_\zeta^{\mathsf{T}}(\boldsymbol{\lambda},\hat{\boldsymbol{v}}_{\mathrm{r}}) = \begin{bmatrix}0 & -\hat{v}_{\mathrm{r}}\lambda_3 + \hat{w}_{\mathrm{r}}\lambda_2 & \hat{u}_{\mathrm{r}}\\ 0 & \hat{u}_{\mathrm{r}}\lambda_3 - \hat{w}_{\mathrm{r}}\lambda_1 & \hat{v}_{\mathrm{r}}\\ 0 & -\hat{u}_{\mathrm{r}}\lambda_2 + \hat{v}_{\mathrm{r}}\lambda_1 & \hat{w}_{\mathrm{r}}\end{bmatrix} \qquad \text{(B.6b)}$$

Note that these choices of $\boldsymbol{M}_\lambda$ and $\boldsymbol{M}_\zeta$ are non-unique. Turning back to Eq. (B.5), we now have

$$
\begin{aligned}
&\tilde{\boldsymbol{v}}_{\mathrm{r}}^{\mathsf{T}}\boldsymbol{\Gamma}_{v,q}\boldsymbol{S}(\boldsymbol{\omega})\boldsymbol{R}_{\mathrm{IB}}^{\mathsf{T}}\tilde{\boldsymbol{q}} - \tilde{\boldsymbol{w}}^{\mathsf{T}}\boldsymbol{R}_{\mathrm{IB}}\left(\boldsymbol{S}(\boldsymbol{\omega})\boldsymbol{\Gamma}_{w,q} - \boldsymbol{\Gamma}_{w,q}\boldsymbol{S}(\boldsymbol{\omega})\right)\boldsymbol{R}_{\mathrm{IB}}^{\mathsf{T}}\tilde{\boldsymbol{q}} - \tilde{\boldsymbol{w}}^{\mathsf{T}}\boldsymbol{R}_{\mathrm{IB}}\boldsymbol{S}(\boldsymbol{\omega})\boldsymbol{\Gamma}_{w,\omega}\boldsymbol{M}_v^{\mathsf{T}}\boldsymbol{I}\tilde{\boldsymbol{\omega}} \\
&\quad\tilde{\boldsymbol{v}}_{\mathrm{r}}^{\mathsf{T}}\left(\left(\frac{1}{m}\boldsymbol{F}_v - \boldsymbol{S}(\tilde{\boldsymbol{\omega}}+\boldsymbol{\omega})\right)\boldsymbol{\Gamma}_{v,q} - \boldsymbol{\Gamma}_{v,q}\boldsymbol{R}_{\mathrm{IB}}^{\mathsf{T}}\hat{\boldsymbol{R}}_{\mathrm{IB}}\boldsymbol{\Gamma}_{v,q} - \boldsymbol{\Gamma}_{v,q}\boldsymbol{\Gamma}_{w,q} - \boldsymbol{\Gamma}_{v,\omega}\boldsymbol{M}_v^{\mathsf{T}}\boldsymbol{M}_v\boldsymbol{\Gamma}_{v,q}\right)\boldsymbol{R}_{\mathrm{IB}}^{\mathsf{T}}\tilde{\boldsymbol{q}} \\
&\quad+\tilde{\boldsymbol{v}}_{\mathrm{r}}^{\mathsf{T}}g\tilde{\boldsymbol{\zeta}} + \tilde{\boldsymbol{v}}_{\mathrm{r}}^{\mathsf{T}}\left(\left(\frac{1}{m}\boldsymbol{F}_v - \boldsymbol{S}(\tilde{\boldsymbol{\omega}}+\boldsymbol{\omega})\right)\boldsymbol{\Gamma}_{v,\omega}\boldsymbol{M}_v^{\mathsf{T}}\boldsymbol{I} - \boldsymbol{\Gamma}_{v,q}\left(\boldsymbol{R}_{\mathrm{IB}}^{\mathsf{T}}\hat{\boldsymbol{R}}_{\mathrm{IB}}\boldsymbol{\Gamma}_{v,\omega} + \boldsymbol{\Gamma}_{w,\omega}\right)\boldsymbol{M}_v^{\mathsf{T}}\boldsymbol{I}\right. \\
&\quad\left.+\frac{1}{m}\boldsymbol{F}_\omega + \boldsymbol{S}(\hat{\boldsymbol{v}}_{\mathrm{r}}) - \boldsymbol{\Gamma}_{v,\omega}\boldsymbol{M}_v^{\mathsf{T}}\left(\boldsymbol{S}(\boldsymbol{I}(\tilde{\boldsymbol{\omega}}+\boldsymbol{\omega})) - \boldsymbol{S}(\boldsymbol{\omega})\boldsymbol{I} + \boldsymbol{M}_\omega + \boldsymbol{M}_v\boldsymbol{\Gamma}_{v,\omega}\boldsymbol{M}_v^{\mathsf{T}}\boldsymbol{I}\right)\right)\tilde{\boldsymbol{\omega}} \\
&\quad-\tilde{\boldsymbol{v}}_{\mathrm{r}}^{\mathsf{T}}\boldsymbol{\Gamma}_{v,q}\boldsymbol{R}_{\mathrm{IB}}^{\mathsf{T}}\boldsymbol{M}_\lambda(\tilde{\boldsymbol{\lambda}},\tilde{\boldsymbol{\zeta}},\hat{\boldsymbol{v}}_{\mathrm{r}})\tilde{\boldsymbol{\lambda}} - \tilde{\boldsymbol{v}}_{\mathrm{r}}^{\mathsf{T}}\boldsymbol{\Gamma}_{v,q}\boldsymbol{R}_{\mathrm{IB}}^{\mathsf{T}}\boldsymbol{M}_\zeta(\tilde{\boldsymbol{\lambda}},\tilde{\boldsymbol{\zeta}},\hat{\boldsymbol{v}}_{\mathrm{r}})\tilde{\boldsymbol{\zeta}} + \tilde{\boldsymbol{w}}^{\mathsf{T}}\boldsymbol{R}_{\mathrm{IB}}\left(-\boldsymbol{\Gamma}_{w,\omega}\boldsymbol{M}_v^{\mathsf{T}}\boldsymbol{M}_v\boldsymbol{\Gamma}_{v,q}\right. \\
&\quad\left.-\boldsymbol{\Gamma}_{w,q}\left(\boldsymbol{R}_{\mathrm{IB}}^{\mathsf{T}}\hat{\boldsymbol{R}}_{\mathrm{IB}}\boldsymbol{\Gamma}_{v,q} + \boldsymbol{\Gamma}_{w,q}\right)\right)\boldsymbol{R}_{\mathrm{IB}}^{\mathsf{T}}\tilde{\boldsymbol{q}} + \tilde{\boldsymbol{w}}^{\mathsf{T}}\boldsymbol{R}_{\mathrm{IB}}\left(-\boldsymbol{\Gamma}_{w,q}\left(\boldsymbol{R}_{\mathrm{IB}}^{\mathsf{T}}\hat{\boldsymbol{R}}_{\mathrm{IB}}\boldsymbol{\Gamma}_{v,\omega} + \boldsymbol{\Gamma}_{w,\omega}\right)\boldsymbol{M}_v^{\mathsf{T}}\boldsymbol{I}\right. \\
&\quad\left.-\boldsymbol{\Gamma}_{w,\omega}\boldsymbol{M}_v^{\mathsf{T}}\left(\boldsymbol{S}(\boldsymbol{I}(\tilde{\boldsymbol{\omega}}+\boldsymbol{\omega})) - \boldsymbol{S}(\boldsymbol{\omega})\boldsymbol{I} + \boldsymbol{M}_\omega + \boldsymbol{M}_v\boldsymbol{\Gamma}_{v,\omega}\boldsymbol{M}_v^{\mathsf{T}}\boldsymbol{I}\right)\right)\tilde{\boldsymbol{\omega}} - \tilde{\boldsymbol{w}}^{\mathsf{T}}\boldsymbol{R}_{\mathrm{IB}}\boldsymbol{\Gamma}_{w,q}\boldsymbol{R}_{\mathrm{IB}}^{\mathsf{T}}\boldsymbol{M}_\lambda(\tilde{\boldsymbol{\lambda}},\tilde{\boldsymbol{\zeta}},\hat{\boldsymbol{v}}_{\mathrm{r}})\tilde{\boldsymbol{\lambda}} \\
&\quad-\tilde{\boldsymbol{w}}^{\mathsf{T}}\boldsymbol{R}_{\mathrm{IB}}\boldsymbol{\Gamma}_{w,q}\boldsymbol{R}_{\mathrm{IB}}^{\mathsf{T}}\boldsymbol{M}_\zeta(\tilde{\boldsymbol{\lambda}},\tilde{\boldsymbol{\zeta}},\hat{\boldsymbol{v}}_{\mathrm{r}})\tilde{\boldsymbol{\zeta}} + \tilde{\boldsymbol{q}}^{\mathsf{T}}\boldsymbol{L}_{1_q}^{-1}\left(\boldsymbol{R}_{\mathrm{IB}}\boldsymbol{\Gamma}_{w,q}\boldsymbol{R}_{\mathrm{IB}}^{\mathsf{T}} + \hat{\boldsymbol{R}}_{\mathrm{IB}}\boldsymbol{\Gamma}_{v,q}\boldsymbol{R}_{\mathrm{IB}}^{\mathsf{T}}\right)\tilde{\boldsymbol{q}} + \tilde{\boldsymbol{q}}^{\mathsf{T}}\boldsymbol{L}_{1_q}^{-1}\left(\boldsymbol{R}_{\mathrm{IB}}\boldsymbol{\Gamma}_{w,\omega}\right. \\
&\quad\left.+\hat{\boldsymbol{R}}_{\mathrm{IB}}\boldsymbol{\Gamma}_{v,\omega}\right)\boldsymbol{M}_v^{\mathsf{T}}\boldsymbol{I}\tilde{\boldsymbol{\omega}} + \tilde{\boldsymbol{q}}^{\mathsf{T}}\boldsymbol{L}_{1_q}^{-1}\boldsymbol{R}_{\mathrm{IB}}\tilde{\boldsymbol{v}}_{\mathrm{r}} + \tilde{\boldsymbol{q}}^{\mathsf{T}}\boldsymbol{L}_{1_q}^{-1}\tilde{\boldsymbol{w}} + \tilde{\boldsymbol{q}}^{\mathsf{T}}\boldsymbol{L}_{1_q}^{-1}\boldsymbol{M}_\lambda(\tilde{\boldsymbol{\lambda}},\tilde{\boldsymbol{\zeta}},\hat{\boldsymbol{v}}_{\mathrm{r}})\tilde{\boldsymbol{\lambda}} + \tilde{\boldsymbol{q}}^{\mathsf{T}}\boldsymbol{L}_{1_q}^{-1}\boldsymbol{M}_\zeta(\tilde{\boldsymbol{\lambda}},\tilde{\boldsymbol{\zeta}},\hat{\boldsymbol{v}}_{\mathrm{r}})\tilde{\boldsymbol{\zeta}} \\
&\quad+\tilde{\boldsymbol{\lambda}}^{\mathsf{T}}\boldsymbol{L}_{1_\lambda}^{-1}\boldsymbol{S}(\tilde{\boldsymbol{\lambda}}+\boldsymbol{\lambda})\tilde{\boldsymbol{\omega}} - \tilde{\boldsymbol{\lambda}}^{\mathsf{T}}\boldsymbol{L}_{1_\lambda}^{-1}\boldsymbol{S}(\boldsymbol{\omega})\tilde{\boldsymbol{\lambda}} + \tilde{\boldsymbol{\zeta}}^{\mathsf{T}}\boldsymbol{L}_{1_\zeta}^{-1}\boldsymbol{S}(\tilde{\boldsymbol{\zeta}}+\boldsymbol{\zeta})\tilde{\boldsymbol{\omega}} - \tilde{\boldsymbol{\zeta}}^{\mathsf{T}}\boldsymbol{L}_{1_\zeta}^{-1}\boldsymbol{S}(\boldsymbol{\omega})\tilde{\boldsymbol{\zeta}} + \tilde{\boldsymbol{\omega}}^{\mathsf{T}}\boldsymbol{L}_{1_\omega}^{-1}\boldsymbol{I}^{-1}\boldsymbol{M}_v\tilde{\boldsymbol{v}}_{\mathrm{r}} \\
&\quad+\tilde{\boldsymbol{\omega}}^{\mathsf{T}}\boldsymbol{L}_{1_\omega}^{-1}\boldsymbol{I}^{-1}\boldsymbol{M}_v\boldsymbol{\Gamma}_{v,q}\boldsymbol{R}_{\mathrm{IB}}^{\mathsf{T}}\tilde{\boldsymbol{q}} + \tilde{\boldsymbol{\omega}}^{\mathsf{T}}\boldsymbol{L}_{1_\omega}^{-1}\boldsymbol{I}^{-1}\left(\boldsymbol{S}(\boldsymbol{I}(\tilde{\boldsymbol{\omega}}+\boldsymbol{\omega})) - \boldsymbol{S}(\boldsymbol{\omega})\boldsymbol{I} + \boldsymbol{M}_\omega + \boldsymbol{M}_v\boldsymbol{\Gamma}_{v,\omega}\boldsymbol{M}_v^{\mathsf{T}}\boldsymbol{I}\right)\tilde{\boldsymbol{\omega}}
\end{aligned}
\tag{B.7}
$$

Let the $p \times p$ matrix-valued function $\boldsymbol{A}$ be

$$
\boldsymbol{A}(\tilde{\boldsymbol{x}}_1, \boldsymbol{x}_1, \hat{\boldsymbol{x}}_2) = \begin{bmatrix} \boldsymbol{A}_{q,q} & \boldsymbol{A}_{q,\lambda} & \boldsymbol{A}_{q,\zeta} & \boldsymbol{A}_{q,\omega} \\ \boldsymbol{0} & \boldsymbol{A}_{\lambda,\lambda} & \boldsymbol{A}_{\lambda,\zeta} & \boldsymbol{A}_{\lambda,\omega} \\ \boldsymbol{0} & \boldsymbol{0} & \boldsymbol{A}_{\zeta,\zeta} & \boldsymbol{A}_{\zeta,\omega} \\ \boldsymbol{0} & \boldsymbol{0} & \boldsymbol{0} & \boldsymbol{A}_{\omega,\omega} \end{bmatrix} \tag{B.8}
$$

where

$$
\begin{aligned}
\boldsymbol{A}_{q,q} &= \boldsymbol{L}_{1_q}^{-1}\left(\boldsymbol{R}_{\mathrm{IB}}\boldsymbol{\Gamma}_{w,q}\boldsymbol{R}_{\mathrm{IB}}^{\mathsf{T}} + \hat{\boldsymbol{R}}_{\mathrm{IB}}\boldsymbol{\Gamma}_{v,q}\boldsymbol{R}_{\mathrm{IB}}^{\mathsf{T}}\right) \\
\boldsymbol{A}_{q,\lambda} &= \boldsymbol{L}_{1_q}^{-1}\boldsymbol{M}_\lambda(\tilde{\boldsymbol{\lambda}},\tilde{\boldsymbol{\zeta}},\hat{\boldsymbol{v}}_{\mathrm{r}}), \qquad \boldsymbol{A}_{q,\zeta} = \boldsymbol{L}_{1_q}^{-1}\boldsymbol{M}_\zeta(\tilde{\boldsymbol{\lambda}},\tilde{\boldsymbol{\zeta}},\hat{\boldsymbol{v}}_{\mathrm{r}}) \\
\boldsymbol{A}_{q,\omega} &= \boldsymbol{L}_{1_q}^{-1}\left(\boldsymbol{R}_{\mathrm{IB}}\boldsymbol{\Gamma}_{w,\omega} + \hat{\boldsymbol{R}}_{\mathrm{IB}}\boldsymbol{\Gamma}_{v,\omega}\right)\boldsymbol{M}_v^{\mathsf{T}}\boldsymbol{I} + \boldsymbol{R}_{\mathrm{IB}}\boldsymbol{\Gamma}_{v,q}^{\mathsf{T}}\boldsymbol{M}_v^{\mathsf{T}}\boldsymbol{I}^{-1}\boldsymbol{L}_{1_\omega}^{-\mathsf{T}} \\
\boldsymbol{A}_{\lambda,\lambda} &= -\boldsymbol{L}_{1_\lambda}^{-1}\boldsymbol{S}(\boldsymbol{\omega}), \qquad \boldsymbol{A}_{\lambda,\zeta} = \boldsymbol{0}, \qquad \boldsymbol{A}_{\lambda,\omega} = \boldsymbol{L}_{1_\lambda}^{-1}\boldsymbol{S}(\tilde{\boldsymbol{\lambda}}+\boldsymbol{\lambda}) \\
\boldsymbol{A}_{\zeta,\zeta} &= -\boldsymbol{L}_{1_\zeta}^{-1}\boldsymbol{S}(\boldsymbol{\omega}), \qquad \boldsymbol{A}_{\zeta,\omega} = \boldsymbol{L}_{1_\zeta}^{-1}\boldsymbol{S}(\tilde{\boldsymbol{\zeta}}+\boldsymbol{\zeta}) \\
\boldsymbol{A}_{\omega,\omega} &= \boldsymbol{L}_{1_\omega}^{-1}\boldsymbol{I}^{-1}\left(\boldsymbol{S}(\boldsymbol{I}(\tilde{\boldsymbol{\omega}}+\boldsymbol{\omega})) - \boldsymbol{S}(\boldsymbol{\omega})\boldsymbol{I} + \boldsymbol{M}_\omega + \boldsymbol{M}_v\boldsymbol{\Gamma}_{v,\omega}\boldsymbol{M}_v^{\mathsf{T}}\boldsymbol{I}\right)
\end{aligned}
$$

Also, define the $(n-p) \times p$ matrix-valued function $\boldsymbol{B}$ as

$$
\boldsymbol{B}(\tilde{\boldsymbol{x}}_1, \boldsymbol{x}_1, \hat{\boldsymbol{x}}_2) = \begin{bmatrix} \boldsymbol{B}_{v_{\mathrm{r}},q} & \boldsymbol{B}_{v_{\mathrm{r}},\lambda} & \boldsymbol{B}_{v_{\mathrm{r}},\zeta} & \boldsymbol{B}_{v_{\mathrm{r}},\omega} \\ \boldsymbol{B}_{w,q} & \boldsymbol{B}_{w,\lambda} & \boldsymbol{B}_{w,\zeta} & \boldsymbol{B}_{w,\omega} \end{bmatrix} \tag{B.9}
$$

where

$$
\begin{aligned}
\boldsymbol{B}_{v_\mathrm{r},q} &= \Big(\boldsymbol{\Gamma}_{v,q}\boldsymbol{S}(\boldsymbol{\omega}) + \Big(\frac{1}{m}\boldsymbol{F}_v - \boldsymbol{S}(\tilde{\boldsymbol{\omega}}+\boldsymbol{\omega}) - \boldsymbol{\Gamma}_{v,q}\boldsymbol{R}_{\mathrm{IB}}^{\mathsf{T}}\hat{\boldsymbol{R}}_{\mathrm{IB}} - \boldsymbol{\Gamma}_{v,\omega}\boldsymbol{M}_v^{\mathsf{T}}\boldsymbol{M}_v\Big)\boldsymbol{\Gamma}_{v,q} \\
&\qquad - \boldsymbol{\Gamma}_{v,q}\boldsymbol{\Gamma}_{w,q}\Big)\boldsymbol{R}_{\mathrm{IB}}^{\mathsf{T}} + \boldsymbol{R}_{\mathrm{IB}}^{\mathsf{T}}\boldsymbol{L}_{1_q}^{-\mathsf{T}} \\
\boldsymbol{B}_{v_\mathrm{r},\lambda} &= -\boldsymbol{\Gamma}_{v,q}\boldsymbol{R}_{\mathrm{IB}}^{\mathsf{T}}\boldsymbol{M}_\lambda(\tilde{\boldsymbol{\lambda}},\tilde{\boldsymbol{\zeta}},\hat{\boldsymbol{v}}_\mathrm{r}) \\
\boldsymbol{B}_{v_\mathrm{r},\zeta} &= g\mathbb{I} - \boldsymbol{\Gamma}_{v,q}\boldsymbol{R}_{\mathrm{IB}}^{\mathsf{T}}\boldsymbol{M}_\zeta(\tilde{\boldsymbol{\lambda}},\tilde{\boldsymbol{\zeta}},\hat{\boldsymbol{v}}_\mathrm{r}) \\
\boldsymbol{B}_{v_\mathrm{r},\omega} &= \Big(\frac{1}{m}\boldsymbol{F}_v - \boldsymbol{S}(\tilde{\boldsymbol{\omega}}+\boldsymbol{\omega})\Big)\boldsymbol{\Gamma}_{v,\omega}\boldsymbol{M}_v^{\mathsf{T}}\boldsymbol{I} - \boldsymbol{\Gamma}_{v,q}\left(\boldsymbol{R}_{\mathrm{IB}}^{\mathsf{T}}\hat{\boldsymbol{R}}_{\mathrm{IB}}\boldsymbol{\Gamma}_{v,\omega} + \boldsymbol{\Gamma}_{w,\omega}\right)\boldsymbol{M}_v^{\mathsf{T}}\boldsymbol{I} + \frac{1}{m}\boldsymbol{F}_\omega + \boldsymbol{S}(\hat{\boldsymbol{v}}_\mathrm{r}) \\
&\quad - \boldsymbol{\Gamma}_{v,\omega}\boldsymbol{M}_v^{\mathsf{T}}\Big(\boldsymbol{S}(\boldsymbol{I}(\tilde{\boldsymbol{\omega}}+\boldsymbol{\omega})) - \boldsymbol{S}(\boldsymbol{\omega})\boldsymbol{I} + \boldsymbol{M}_\omega + \boldsymbol{M}_v\boldsymbol{\Gamma}_{v,\omega}\boldsymbol{M}_v^{\mathsf{T}}\boldsymbol{I}\Big) + \boldsymbol{M}_v^{\mathsf{T}}\boldsymbol{I}^{-1}\boldsymbol{L}_{1_\omega}^{-\mathsf{T}} \\
\boldsymbol{B}_{w,q} &= \boldsymbol{R}_{\mathrm{IB}}\Big(\boldsymbol{\Gamma}_{w,q}\boldsymbol{S}(\boldsymbol{\omega}) - \boldsymbol{S}(\boldsymbol{\omega})\boldsymbol{\Gamma}_{w,q} - \boldsymbol{\Gamma}_{w,\omega}\boldsymbol{M}_v^{\mathsf{T}}\boldsymbol{M}_v\boldsymbol{\Gamma}_{v,q} - \boldsymbol{\Gamma}_{w,q}\left(\boldsymbol{R}_{\mathrm{IB}}^{\mathsf{T}}\hat{\boldsymbol{R}}_{\mathrm{IB}}\boldsymbol{\Gamma}_{v,q} + \boldsymbol{\Gamma}_{w,q}\right)\Big)\boldsymbol{R}_{\mathrm{IB}}^{\mathsf{T}} + \boldsymbol{L}_{1_q}^{-\mathsf{T}} \\
\boldsymbol{B}_{w,\lambda} &= -\boldsymbol{R}_{\mathrm{IB}}\boldsymbol{\Gamma}_{w,q}\boldsymbol{R}_{\mathrm{IB}}^{\mathsf{T}}\boldsymbol{M}_\lambda(\tilde{\boldsymbol{\lambda}},\tilde{\boldsymbol{\zeta}},\hat{\boldsymbol{v}}_\mathrm{r}) \\
\boldsymbol{B}_{w,\zeta} &= -\boldsymbol{R}_{\mathrm{IB}}\boldsymbol{\Gamma}_{w,q}\boldsymbol{R}_{\mathrm{IB}}^{\mathsf{T}}\boldsymbol{M}_\zeta(\tilde{\boldsymbol{\lambda}},\tilde{\boldsymbol{\zeta}},\hat{\boldsymbol{v}}_\mathrm{r}) \\
\boldsymbol{B}_{w,\omega} &= \boldsymbol{R}_{\mathrm{IB}}\Big(- \boldsymbol{S}(\boldsymbol{\omega})\boldsymbol{\Gamma}_{w,\omega}\boldsymbol{M}_v^{\mathsf{T}}\boldsymbol{I} - \boldsymbol{\Gamma}_{w,q}\left(\boldsymbol{R}_{\mathrm{IB}}^{\mathsf{T}}\hat{\boldsymbol{R}}_{\mathrm{IB}}\boldsymbol{\Gamma}_{v,\omega} + \boldsymbol{\Gamma}_{w,\omega}\right)\boldsymbol{M}_v^{\mathsf{T}}\boldsymbol{I} \\
&\quad - \boldsymbol{\Gamma}_{w,\omega}\boldsymbol{M}_v^{\mathsf{T}}\Big(\boldsymbol{S}(\boldsymbol{I}(\tilde{\boldsymbol{\omega}}+\boldsymbol{\omega})) - \boldsymbol{S}(\boldsymbol{\omega})\boldsymbol{I} + \boldsymbol{M}_\omega + \boldsymbol{M}_v\boldsymbol{\Gamma}_{v,\omega}\boldsymbol{M}_v^{\mathsf{T}}\boldsymbol{I}\Big)\Big)
\end{aligned}
$$

Therefore, the expression (B.7) may be written as

$$
\tilde{\boldsymbol{x}}_2^{\mathsf{T}}\boldsymbol{B}(\tilde{\boldsymbol{x}}_1,\boldsymbol{x}_1,\hat{\boldsymbol{x}}_2)\tilde{\boldsymbol{x}}_1 + \tilde{\boldsymbol{x}}_1^{\mathsf{T}}\boldsymbol{A}(\tilde{\boldsymbol{x}}_1,\boldsymbol{x}_1,\hat{\boldsymbol{x}}_2)\tilde{\boldsymbol{x}}_1
$$

Finally, let

$$
\boldsymbol{\Lambda} = \sqrt{\frac{1}{\gamma}}\boldsymbol{B} \qquad \text{and} \qquad \boldsymbol{\Psi} = \frac{1}{2}\left(\boldsymbol{A} + \boldsymbol{A}^{\mathsf{T}}\right) \tag{B.10}
$$

Using a series of sub-multiplicative properties, and the definition of φ^* in Eq. (8.45), we have

$$
\begin{aligned}
\tilde{\boldsymbol{x}}_2^{\mathsf{T}}\boldsymbol{B}(\tilde{\boldsymbol{x}}_1,\boldsymbol{x}_1,\hat{\boldsymbol{x}}_2)\tilde{\boldsymbol{x}}_1 + \tilde{\boldsymbol{x}}_1^{\mathsf{T}}\boldsymbol{A}(\tilde{\boldsymbol{x}}_1,\boldsymbol{x}_1,\hat{\boldsymbol{x}}_2)\tilde{\boldsymbol{x}}_1 &\leq \left|\tilde{\boldsymbol{x}}_2^{\mathsf{T}}\boldsymbol{B}(\tilde{\boldsymbol{x}}_1,\boldsymbol{x}_1,\hat{\boldsymbol{x}}_2)\tilde{\boldsymbol{x}}_1\right| + \tilde{\boldsymbol{x}}_1^{\mathsf{T}}\boldsymbol{A}(\tilde{\boldsymbol{x}}_1,\boldsymbol{x}_1,\hat{\boldsymbol{x}}_2)\tilde{\boldsymbol{x}}_1 \\
&= \left|\tilde{\boldsymbol{x}}_2^{\mathsf{T}}\sqrt{\gamma}\boldsymbol{\Lambda}(\tilde{\boldsymbol{x}}_1,\boldsymbol{x}_1,\hat{\boldsymbol{x}}_2)\tilde{\boldsymbol{x}}_1\right| + \tilde{\boldsymbol{x}}_1^{\mathsf{T}}\boldsymbol{\Psi}(\tilde{\boldsymbol{x}}_1,\boldsymbol{x}_1,\hat{\boldsymbol{x}}_2)\tilde{\boldsymbol{x}}_1 \\
&\leq \sqrt{\gamma}\|\tilde{\boldsymbol{x}}_2\|\|\boldsymbol{\Lambda}(\tilde{\boldsymbol{x}}_1,\boldsymbol{x}_1,\hat{\boldsymbol{x}}_2)\tilde{\boldsymbol{x}}_1\| + \tilde{\boldsymbol{x}}_1^{\mathsf{T}}\boldsymbol{\Psi}(\tilde{\boldsymbol{x}}_1,\boldsymbol{x}_1,\hat{\boldsymbol{x}}_2)\tilde{\boldsymbol{x}}_1 \\
&= \sqrt{\varphi^*(\tilde{\boldsymbol{x}}_2)}\,\|\boldsymbol{\Lambda}(\tilde{\boldsymbol{x}}_1,\boldsymbol{x}_1,\hat{\boldsymbol{x}}_2)\tilde{\boldsymbol{x}}_1\| + \tilde{\boldsymbol{x}}_1^{\mathsf{T}}\boldsymbol{\Psi}(\tilde{\boldsymbol{x}}_1,\boldsymbol{x}_1,\hat{\boldsymbol{x}}_2)\tilde{\boldsymbol{x}}_1
\end{aligned}
$$

which proves Proposition 8.1. □